

**Estimating the Volatility of Aerosol Components and Diffusion Through the
Particle-Phase**

A thesis submitted to the University of Manchester for the degree of Doctor of
Philosophy (PhD) in the Faculty of Science and Engineering

2016

Simon Patrick O'Meara

Contents

1	Introduction	9
1.1	Motivation	9
1.2	Physical States	11
1.3	Phase Partitioning	14
1.4	Aerosol Components	16
1.5	Partitioning Theory	20
1.6	Determination of Vapour Pressure	27
1.7	Activity Coefficient	34
1.8	Surface Accommodation Coefficient	38
1.9	Diffusion	42
1.9.1	Introduction	42
1.9.2	Relevance to Atmosphere	45
1.9.3	Methods to solve, estimate and measure particle-phase diffusion	50
1.10	Introduction Summary	57
2	Research Papers	58
2.1	Paper 1	58
2.2	Paper 2	84
2.3	Paper 3	101
3	Summary	132
3.1	Thesis Overview	132
3.2	Conclusion of An assessment of vapour pressure estimation methods	133
3.3	Conclusion of The rate of equilibration of viscous aerosol particles	135
3.4	Conclusion of Implementing a more realistic efficient model for particle-phase diffusion, limitations to a general approach	136
3.5	Future Work	137
3.6	Implications for Climate and Air Quality	139

List of Figures in Introduction

1	Effective radiative forcing probability density function for aerosol, greenhouse gases and total anthropogenic effect	10
2	Schematic phase diagram	12
3	Schematic thermograms from DSC	14
4	Example mass spectrum	19
5	Partitioning determinants schematic	20
6	Partitioning coefficient relationship with vapour pressure	24
7	Example volatility distribution	26
8	Measured vapour pressure comparison for dicarboxylic acids	30
9	SOA concentration sensitivity to vapour pressure estimation and non-ideality	33
10	Particle morphology microscope images	34
11	Non-ideality effect on particulate concentration with relative humidity relationship	37
12	Concentration profiles resulting from partitioning rate limitations	39
13	Estimated interfacial transport equilibration times	41
14	Difference between Fickian and Maxwell-Stefan diffusion coefficients	45
15	Estimated gas-phase diffusion equilibration times	47
16	Example viscosity measurement results	48
17	Estimated particle-phase diffusion equilibration times	49
18	Example diffusion measurement results	51
19	Particle-phase diffusion modelling flowchart	54
20	Analytical solution to particle-phase diffusion compared with numerical solution	56

Abstract

The University of Manchester

Simon O'Meara

Doctor of Philosophy (PhD)

Estimating the Volatility of Aerosol Components and Diffusion Through the Particle-Phase

2016

Accurate models of aerosol transformation including partitioning between the gas- and particle-phase are needed for estimating their effects on climate and air quality. In this thesis, the process of partitioning between phases and its determining factors are introduced and investigated. Three studies assess: the accuracy of estimation methods for aerosol component volatility and its effect on particulate concentration and composition; the consistency of different solutions to models of particle-phase diffusion; and, a method to analytically solve particle-phase diffusion. These studies contribute to the ongoing effort of improving aerosol models, such that their wide-ranging effects can be accurately estimated.

Declaration

I declare that no portion of the work referred to in the thesis has been submitted in support of an application for another degree or qualification of this or any other university or other institute of learning

Copyright Statement

- i. The author of this thesis (including any appendices and/or schedules to this thesis) owns certain copyright or related rights in it (the “Copyright”) and s/he has given The University of Manchester certain rights to use such Copyright, including for administrative purposes.
- ii. Copies of this thesis, either in full or in extracts and whether in hard or electronic copy, may be made only in accordance with the Copyright, Designs and Patents Act 1988 (as amended) and regulations issued under it or, where appropriate, in accordance with licensing agreements which the University has from time to time. This page must form part of any such copies made.
- iii. The ownership of certain Copyright, patents, designs, trade marks and other intellectual property (the “Intellectual Property”) and any reproductions of copyright works in the thesis, for example graphs and tables (“Reproductions”), which may be described in this thesis, may not be owned by the author and may be owned by third parties. Such Intellectual Property and Reproductions cannot and must not be made available for use without the prior written permission of the owner(s) of the relevant Intellectual Property and/or Reproductions.
- iv. Further information on the conditions under which disclosure, publication and commercialisation of this thesis, the Copyright and any Intellectual Property University IP Policy (see <http://documents.manchester.ac.uk/display.aspx?DocID=24420>), in any relevant Thesis restriction declarations deposited in the University Library, The University Library’s regulations (see <http://www.library.manchester.ac.uk/about/regulations/>) and in The University’s policy on Presentation of Theses.

Acknowledgement

I am grateful to my supervisors: Gordon McFiggans and Dave Topping, for ideas, challenges and support. The Natural Environment Research Council funded the PhD. Ruth, John and Holly for support, encouragement and holidays. Michael, Jon, George, Alehouse and friends in CAS for fun and games. Vicki for being amazing, an incredible listener and advisor.

“Observe what happens when sunbeams are admitted into a building and shed light on its shadowy places. You will see a multitude of tiny particles mingling in a multitude of ways... their dancing is an actual indication of underlying movements of matter that are hidden from our sight... It originates with the atoms which move of themselves (i.e., spontaneously). Then those small compound bodies that are least removed from the impetus of the atoms are set in motion by the impact of their invisible blows and in turn cannon against slightly larger bodies. So the movement mounts up from the atoms and gradually emerges to the level of our senses, so that those bodies are in motion that we see in sunbeams, moved by blows that remain invisible.”

Lucretius, *De rerum natura*, 99 BC - 55BC (Book II, verses 113-140)

1 Introduction

This thesis conforms to the alternative format, with research papers forming its core. Alternative format was chosen because the research involved in this particular doctorate fell into three distinct projects, all based on gaps in our understanding of how particulate matter in the atmosphere changes. The results of the projects were considered sufficiently useful to the atmospheric research community and of sufficient quality to be publishable. The first two papers presented here have been published in peer-reviewed journals, while the third and final is ready for journal submission.

The papers are preceded by an introduction that explains their motivation and the relevant science, and reviews related work. The breadth and depth of the introduction is necessarily limited to be relevant to the research results, however, references have been provided for further information. The thesis finishes with a conclusion where the contributions of the presented research to the scientific community are summarised and further work is suggested.

1.1 Motivation

An aerosol is a matrix of suspended particulate matter and gases. In Earth's atmosphere aerosols can influence climate (Boucher *et al.*, 2013) and air quality (Nel, 2005; Rückerl *et al.*, 2011; Heal *et al.*, 2012). Examples include the global cooling following the 1990 Mount Pinatubo eruption (McCormick *et al.*, 1995) (natural source of aerosol) and premature mortality attributed to anthropogenic emissions (Anenberg *et al.*, 2010) (man-made source).

Determining the climatic effect of changes to natural and anthropogenic aerosols is not straightforward. A major complication is the variety of effects they exert on the global radiative budget. These can be categorised as the direct effect, which occurs when aerosols interact with solar or terrestrial radiation directly, and the indirect effect, which arises when aerosols influence cloud properties, which in turn affect the radiative budget (Seinfeld & Pandis, 2006). Studies into climate drivers, including aerosol, are reviewed in the reports of the Intergovernmental Panel on Climate Change (IPCC). They use an effective radiative forcing (ERF) metric to quantify the degree to which a driver perturbs the radiative budget relative to a fixed date, which typically precedes the Industrial Revolution. The ERF is the combined effect of direct (e.g. reflectance of incoming solar radiation by certain particulate matter) and rapid indirect (including changes to cloud and land cover but not changes to sea and sea-ice conditions) radiation forcing. The uncertainty around the ERF of anthropogenic aerosol is large compared to other drivers due to the relatively great complexity of aerosol-radiation interactions. Indeed, the latest IPCC report (AR5)

(Myhre *et al.*, 2013) states “the large uncertainty in the aerosol forcing is the main cause of the large uncertainty in the total anthropogenic ERF”. The uncertainty can be expressed as a probability density function, as shown in Fig. 1, and is clearly considerably larger for anthropogenic aerosols, which are expected to have an overall cooling effect, than for greenhouse gases.

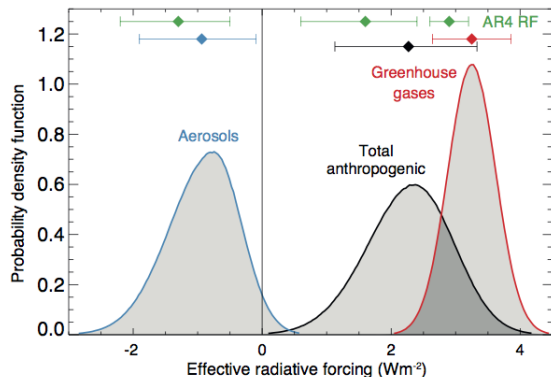


Figure 1: Probability density functions of the effective radiative forcing during the industrial period (1750-2005) for aerosols and greenhouse gases produced by human activity and the estimated total forcing due to anthropogenic changes to the Earth system. The upper and lower sets of whisker plots at the top represent the best estimate and 5-95 % confidence ranges from two successive IPCC reports: AR4 and the AR5 (most recent report), respectively. Taken from Myhre *et al.* (2013, sect. 8.5.1).

The uncertainty in the aerosol ERF is attributed to uncertainty in processes occurring over a wide-range of spatial and temporal scales (Boucher *et al.*, 2013). For example, at a single particle level (micrometre scale or below), the mixing state of aerosol containing black carbon influences its optical properties and, therefore, its direct effect (Lesins *et al.*, 2002; Shiraiwa *et al.*, 2010). While at the mesoscale (up to hundreds of kilometres), cloud formation must be accurately modelled to determine the indirect effect, and this depends on parameterisations of particulate growth into liquid droplets or ice particles (e.g. Simpson *et al.*, 2014).

The aerosol properties on which the direct and indirect effects depend are: particle number size distribution, chemical composition, mixing state and morphology, as these influence optical properties and ability to act as cloud condensation nuclei and ice nuclei (Boucher *et al.*, 2013). These characteristic aerosol properties are determined by fundamental properties of aerosol components (its chemical constituents), such as volatility. Uncertainty in radiative forcing may therefore result from three sources: fundamental properties, characteristic properties and relationships between aerosol and their dependent processes such as cloud formation (Myhre *et al.*, 2013; Seinfeld *et al.*, 2016). It is difficult to deconvolve the uncertainty arising from each source because their propagation of error is complex, however, as may be expected, poor constraint on fundamental properties generates significant uncertainty in effective radiative forcing estimates (Lee *et al.*, 2016).

There is strong evidence for a causal relationship between exposure to particulate matter and health (Dockery *et al.* , 1993; Pope *et al.* , 2002, 2004; Pöschl, 2005; Pope *et al.* , 2009; Rückerl *et al.* , 2011). Estimates of mortality due to exposure are typically based on the estimated concentration of particles (e.g. Anenberg *et al.* , 2010). However, uncertainty in particle concentration and its relationship with health can lead to large differences in estimated mortality, such as by a factor of five for U.S. mortality rates (Ford & Heald, 2016). Nevertheless, regulations and guidelines for maximum particulate concentrations have been set, such as by the World Health Organisation (Krzyzanowski & Cohen, 2008). Ethical considerations limit the empirical evidence that could improve the detail of our knowledge of aerosol-health relationships. Despite this, some components have been attributed with particularly strong effects, such as nickel and vanadium, while crustal aerosol have very weak effects (Heal *et al.* , 2012). As toxicological and epidemiological studies progress, along with biochemical models, greater detail on aerosol-health effects, such as size dependence is expected. Models of aerosol evolution that can estimate properties such as composition will then be informative and important tools in assessing the risk posed to health by particulate matter.

While measurements of aerosol properties allow for valuable improvement and validation of models, they are limited in temporal and spatial coverage. In principle, therefore, accurate aerosol models provide an invaluable tool by which climatic and health effects can be quantified. The fundamental drivers of aerosol properties are: the available components, thermodynamics and kinetics, and environmental variables such as temperature. With this information, models can estimate physicochemical processes such as nucleation, gas-particle partitioning, coagulation, and reaction. The aim of the research presented here is to improve models of some of these processes, which in turn improves our capability of modelling characteristic aerosol properties like size number distribution. With greater confidence in estimates of these characteristic properties, effects on climate and air quality can be quantified with greater certainty. The motivation behind this work is to contribute to the body of research necessary for decreasing the uncertainty around aerosol effects on climate and health. Consequently, actions to improve sustainability and human health can be better informed and more effective.

1.2 Physical States

The physical state (phase) of a component and those surrounding it is fundamental in determining how aerosols affect climate and health. Furthermore, it determines how an aerosol can transform with time. In this section, influences on phase and phase transitions relevant to ambient aerosol will be discussed. Unless otherwise stated, the reader is referred to P. Papon (2006) for further information.

The state of a component in either its pure form, or within a mixture depends on the environmental temperature, pressure and the effect of other components on its entropy. With decreasing entropy (molecular disorder), the component is more likely to form a regular molecular arrangement and crystallise. At a given temperature and pressure, the entropy of a component depends primarily on its ability to form intermolecular bonds homogeneously and heterogeneously. A phase diagram shows the conditions at which transitions to a stable phase occur. For example, Fig. 2 shows a typical form of phase transition dependence on temperature and pressure. At the triple point, the thermodynamically stable state can be solid, liquid or gas, it can be seen on Fig. 2 as the intersection of all three transition lines. The critical point is the condition at which further temperature or pressure increase leads to a supercritical fluid phase, with properties making it indistinct as a gas or liquid.

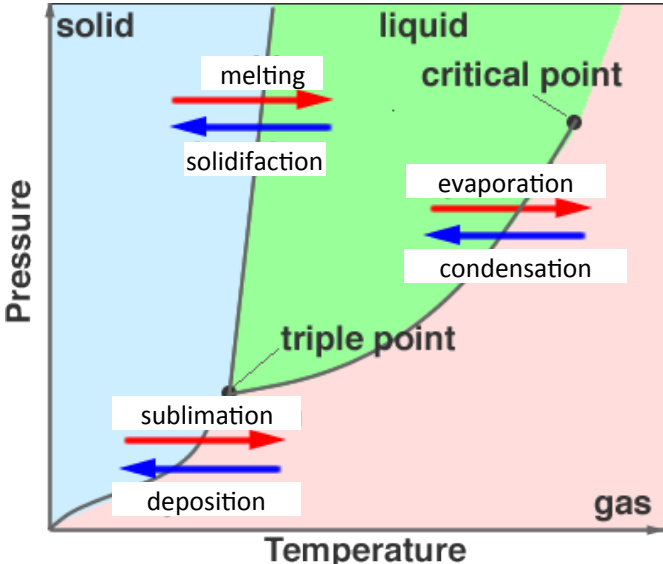


Figure 2: Schematic phase diagram of a component as a function of temperature and pressure. Lines represent the conditions at which transitions to a different phase are thermodynamically favoured. Note that the freezing process is more generally referred to as solidification. Adapted from Hepburn (2016).

A metastable phase occurs when conditions are such that a different phase is thermodynamically favoured, but is prevented due to an energy barrier. In the cases of condensation and crystallisation, the metastable states are termed supersaturated and supercooled, respectively. For decreasing entropy, transitions from gas or liquid to liquid or solid, respectively, requires nucleation, that is, the molecules must form a sufficiently ordered configuration to form and maintain the intermolecular bonds that maintain the stable phase. The transition to a more ordered molecular structure results in loss of molecular kinetic energy, which is transferred away from the molecules, and can be observed as a temperature increase (latent heat decrease). However, energy must also be input to form an interface between the two phases; this can be thought of as the energy required to pro-

duce surface tension. Only when the energy input is less than the energy output due to phase change does transition occur. Heterogenous nuclei or surfaces can assist nucleation because they decrease the energy required for interface formation from the component of interest.

Through maintenance of pressure, controlled heat flow and measured temperature change, one can measure the heat capacity of a component and therefore infer the melting temperature, a method called differential scanning calorimetry (DSC). Fig. 3 shows a schematic of a DSC thermogram, with plot (a) showing a spike in heat flow during cooling at the solidification point (representing a decrease in component latent heat). As discussed, this follows a temperature interval with a supercooled phase. On warming (entropy increase), the component must gain sufficient energy to break intermolecular bonds. The dip in heat flow in fig. 3a at the melting point indicates a spike in heat capacity: energy is used by component molecules to break intermolecular bonds rather than to increase thermal energy (latent heat increase).

In fig. 3b, during cooling, the component has transitioned into a glassy phase, rather than a solid. The glassy phase has mechanical (macroscopic) properties similar to a solid, and although some parts of a material may have molecular configurations similar to the solid, the long-range molecular structure is disordered, therefore it is described as an amorphous non-crystalline state (Debenedetti & Stillinger, 2001). In contrast to solidification/melting, there is no peak/dip in heat flow, representing a release/intake of latent heat, rather there is a stepwise change in heat capacity, representing the change to a different molecular order. Whether a component forms a glass during temperature change depends on a large number of variables including, the rate of temperature change and the concentration of other components. Relatively rapid cooling (quenching) increases the likelihood of glass formation, as does the presence of components that disrupt crystallisation. However, the required condition is that on cooling, glass formation rather than nucleation into a solid occurs if crystallisation can be prevented.

Another form of the phase diagram is to show transitions as a function of component mole fraction. The presence of other components can disrupt molecular bonding and structuring (depending on their mole fraction), thereby varying transition temperatures (Marcolli *et al.*, 2004b). For instance, at room temperature, the addition of water to solid salt can, with sufficient water, cause dissolution and therefore a transition to liquid (deliquescence). Similarly, as a salt-water solution is dried, eventually crystallisation can occur (efflorescence) (Martin, 2000). Similar to the change in phase due to temperature or pressure change, however, the mole fraction at which deliquescence and efflorescence can occur may be different. Again, it is during the change toward solidification that the difference arises: the salt can be supersaturated until the energy required to form a phase interface is less than the energy lost due to solidification.

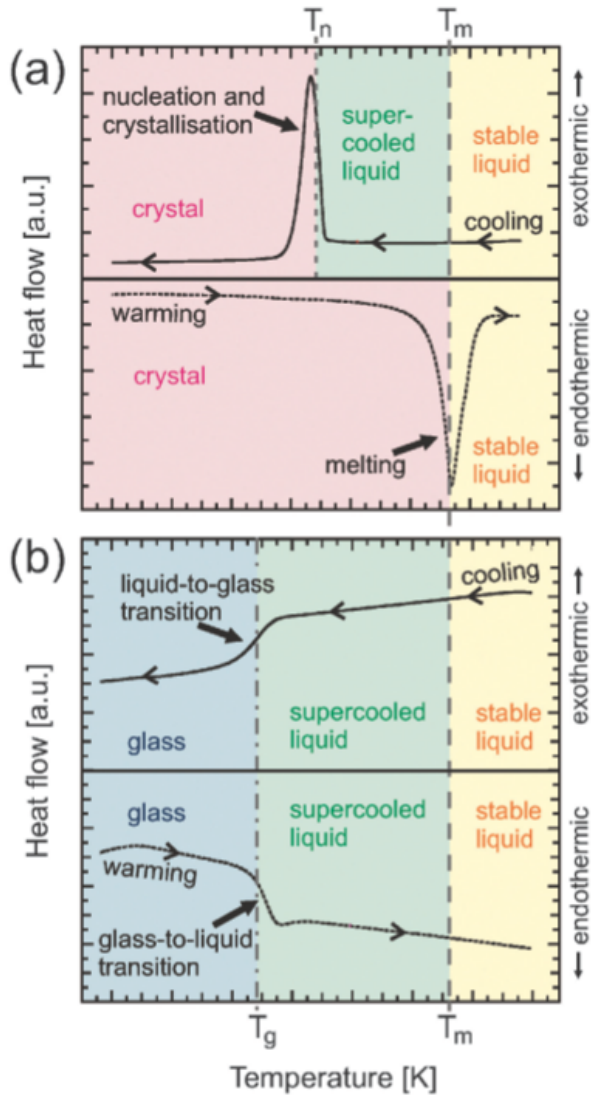


Figure 3: Schematic thermograms of (a), a component transitioning between liquid, supercooled liquid and solid phases and (b), a component transitioning between liquid, supercooled liquid and glass phases. Where T_m , T_n and T_g are melting, solidification and glass formation temperatures, respectively. Taken from Koop *et al.* (2011).

1.3 Phase Partitioning

In a closed system with constant temperature and pressure, a component may exist in equilibrium in more than one state. Indeed, for a supersaturated gas, the thermodynamically stable condition is for a component to attain its saturation vapour pressure, which requires partitioning between the gas- and condensed (liquid or solid)-phases. The saturation vapour pressure is the boundary above/below which the condensed/vapour phase is thermodynamically favoured. In the temperature-pressure phase diagram (e.g. Fig. 2), the boundary with the vapour phase represents the saturation vapour pressure (when this is equal to or greater than the ambient pressure boiling can occur). A component with a comparatively high saturation vapour pressure has a greater tendency to partition into

the vapour-phase than one with a lower saturation vapour pressure: at equilibrium the former component has a greater fraction in the vapour-phase than the latter component, all else being equal.

If there is insufficient component concentration available (in any phase) to attain the saturation vapour pressure, then at equilibrium all of the component will be in the gas-phase (a volatile component). If there is sufficient concentration to attain the saturation vapour pressure, at equilibrium the component will be partitioned between the vapour- and condensed-phase, and the fraction in each will depend on the saturation vapour pressure and component concentration. Components with very low saturation vapour pressures partition very little into the vapour-phase and can be considered effectively entirely in the condensed-phase and therefore nonvolatile.

For a component (i) at equilibrium between the condensed- and vapour-phase, its vapour pressure above a flat particle/gas interface is equal to its activity coefficient (γ_i) multiplied by its condensed-phase mole fraction (x_i) and pure component saturation vapour pressure (p_i^0) (Zuend *et al.*, 2010). For particles, the effect of surface tension due to curvature should also be incorporated (Riipinen *et al.*, 2010):

$$p_i = \gamma_i x_i p_i^0 \exp\left(\frac{2M_i\sigma}{RT_p\rho R_p}\right), \quad (1)$$

where M is molar mass, σ is surface tension, R is the ideal gas constant, T_p is particle temperature, ρ is particle density and R_p is particle radius. The curvature (or Kelvin effect) decreases with increasing particle size as the surface tension decreases and is negligible for supermicron size particles (McFiggans *et al.*, 2006; Krieger *et al.*, 2012).

For partitioning equilibrium, the vapour pressure must equal the effective saturation vapour pressure p_i , rather than p_i^0 . Eq. 1 demonstrates that, with decreasing mole fraction of i in the condensed phase, the equilibrium vapour pressure decreases also. This is an example of Le Chatelier's principle: when the concentration in one part of a system changes, the equilibrium position adjusts to counteract the change. An example is: for an ideal system ($\gamma_i = 1$) with initial relative humidity of 100 %, $x_i = 1$, where i represents water. A nonvolatile component enters the condensed-phase, instantaneously causing $x_i = 0.5$. Now the equilibrium has changed and according to eq. 1 the effective saturation vapour pressure of water is half the current vapour pressure, so water is supersaturated. Consequently, water condenses, and assuming the total concentrations of water and nonvolatile component stay constant, this acts to increase x_i to a new equilibrium value between 0.5 and 1.0 (and the effective saturation vapour pressure changes proportionally).

For solids and liquids at equilibrium, solid-liquid partitioning is only possible near the melting temperature. However, the temperature range at which a component may co-

exist as a solid and liquid at equilibrium is very small compared to the range observed in the atmosphere, and therefore this situation arises rarely. Whereas being away from the effective saturation vapour pressure for gas-condensed partitioning can be resolved by partitioning, being away from the equilibrium temperature for solid-liquid partitioning is resolved by thermal energy exchange. The low compressibility of liquids and solids means that the equilibrium entropy cannot be attained through partial pressure change, as in vapour-condensed partitioning, rather thermal energy must be exchanged with surroundings. This is indicated in Fig. 2 by the small dependence of the solid-liquid transition line on pressure. Consequently, if the equilibrium temperature lies on the other side of the solid-liquid transition line in Fig. 2 to the current phase, it is attained via a change in phase (due to thermal energy change). As a result of their different processes to equilibrate, while components in condensed- and gas-phases experience partitioning, solid and liquid phases (or an intermediate (e.g. glassy)), most often occur independently for a given component at equilibrium.

1.4 Aerosol Components

To estimate the phase of a particle, information on the chemical composition of the gas- and condensed-phase is required. Constituents of aerosol are often segregated into organic and inorganic fractions. The major identified components of the inorganic fraction are: black carbon, sulphate, iodine, potassium, sodium, chlorine, ammonium, nitrate, crustal minerals (e.g. quartz), halogens and trace metals, which may chemically react with one another (e.g. Hitchcock *et al.*, 1980; Dall’Osto & Harrison, 2006; Seinfeld & Pandis, 2006; Bi *et al.*, 2011; Allan *et al.*, 2015; Laskin *et al.*, 2016). Their concentrations can be measured through a variety of techniques, however, aerosol mass spectrometry allows measurement of a comparatively wide range of components (Canagaratna *et al.*, 2007; Lanz *et al.*, 2010; Nizkorodov *et al.*, 2011; Laskin *et al.*, 2016). Inorganic particle components may form through primary production, whereby the component is in the particle phase from emission (e.g. desert dust), or through secondary production, whereby the component or a precursor is initially in the gas-phase and following a change in environmental condition (e.g. temperature), or chemical transformation (e.g. oxidation of sulphur dioxide), partitions into the particle-phase (Charlson *et al.*, 1987; Heintzenberg, 1989; Pankow, 1994; Pöschl, 2005; Bi *et al.*, 2011).

Strictly speaking water is part of the inorganic fraction, however, because of its high abundance and solvating properties it is often discussed as a stand-alone fraction. In the ambient atmosphere the mixing ratio of water can vary between 10^{-6} and 10^{-2} mol/mol (Jacob, 1999), in contrast, isoprene and α -pinene, which are relatively abundant VOCs, have levels of $< 10^{-10}$ to 10^{-8} mol/mol (Holdren *et al.*, 1979; Yokouchi & Ambe, 1988;

Wagner & Kuttler, 2014). As with all atmospheric vapours, water vapour may partition between the gas- and particle-phase, however, the partitioning of water is particularly important for particulate removal from the atmosphere, through the formation of cloud droplets and their subsequent deposition. The lifecycle of water and other particulate components are therefore tightly coupled (Seinfeld & Pandis, 2006). Because of its high abundance, the effect of water on particulate properties such as deviations from ideality and diffusivity can be considerable and even dominating, as will be discussed in following sections.

The number of inorganic aerosol components is sufficiently small to make measurement of pure component properties such as vapour pressure practical. In contrast, there are expected to be of the order of millions of organic components present in the atmosphere, many of which have not been identified to date (Aumont *et al.*, 2005; Goldstein & Galbally, 2007).

Understanding the emissions of organic components and their precursors and the array of chemical reactions that affect them is an area undergoing significant development, with new findings reported regularly (e.g. Crouse *et al.*, 2013; Ehn *et al.*, 2014; Mutzel *et al.*, 2015; Tröstl *et al.*, 2016). As for inorganics, organic particle components may form through primary or secondary mechanisms; those in the latter group are referred to as SOA (secondary organic aerosol) (Bidleman, 1988; Pöschl, 2005; Jimenez *et al.*, 2009). SOA is estimated to comprise a substantial fraction of total global organic aerosol. For example, in a literature review, Kanakidou *et al.* (2005, sect. 1) find that organic material comprises 20-90 % of fine (aerodynamic diameter $\leq 2.5 \mu\text{m}$) particulate mass, and globally Hallquist *et al.* (2009, sect. 1) estimate that 70 % of organic material mass in particulates is SOA. It may be formed when a precursor volatile organic compound (VOC) like isoprene is emitted and oxidised in the atmosphere.

The ratio of organic to inorganic particulate concentration can vary in time and space due to variations in emissions and conditions for atmospheric chemistry. The mass fraction of organics is often around 50 % in urban environments (Zhang *et al.*, 2007), but increases to around 90 % in forested regions (Artaxo *et al.*, 1990). Such fractions belie, however, the composition differences between aerosol of different size, which can be large and is important when considering effects (Putaud *et al.*, 2004; Fuzzi *et al.*, 2007; Facchini *et al.*, 2008). Particles are described as externally mixed when each particle in an ensemble is composed of just one component, with more than one particle type (e.g. sulphuric acid and quartz) present. However, either through coagulation (sticking and merging) of particles or condensation of components from the vapour-phase, single particles are frequently composed of more than one component (internally mixed), as shown by theoretical studies and observations (Marcolli *et al.*, 2004a; Pierce & Adams, 2007; Twohy & Anderson, 2008; Pratt & Prather, 2010). While the inorganic component is clearly important in de-

termining aerosol effects, it is the less well understood composition and properties of the organic fraction that most frequently motivates research into physicochemical processes. Consequently, the focus of this thesis is on the organic fraction.

The thermodynamically preferred oxidation state of carbon is +4, however, organisms provide an abundant supply of reduced carbon (organic compounds) with varying lengths of carbon backbone. These may be emitted through a range of processes including biomass burning, hydrocarbon combustion or evaporation from plant leaves (Lamb *et al.* , 1987; Kerminen *et al.* , 1997; Reid *et al.* , 2005; Sharkey *et al.* , 2008). While in the atmosphere, reduced organic components are exposed to oxidising agents such as the hydroxyl (OH) and nitrate (NO₃) radicals, ozone (O₃) and halogen atoms. The initial and subsequent reactions can have two effects on component volatility: i) increased polarity, which acts to decrease vapour pressure, or ii) breaking of the carbon backbone, leading to a lower molecular weight component and acting to increase vapour pressure. An overview of organic chemistry in the atmosphere is given by Kroll & Seinfeld (2008) and Ziemann & Atkinson (2012).

The numerous VOCs, their oxidation products and products of further processes like polymerisation (Kalberer *et al.* , 2004) represent a challenging range of properties to measure and estimate. The lowest molar mass is 16 g mol⁻¹ for methane, while the maximum molar mass of organic components is around 1000 g mol⁻¹ (Gao *et al.* , 2010; Kalberer *et al.* , 2004). The oxidation state ranges from -4 for methane to +4 for carbon dioxide, with observations of elemental oxygen to carbon ratios in SOA components of 0.2-1.0 (Aiken *et al.* , 2008; DeCarlo *et al.* , 2008; Heald *et al.* , 2010; Ng *et al.* , 2010; Kroll *et al.* , 2011). A range of molecular structures, including branches and rings, and of functional groups have also been identified (Saxena & Hildemann, 1996; Graham *et al.* , 2002; Decesari *et al.* , 2006; Ziemann & Atkinson, 2012). These diverse molecular properties lead to a wide range of component properties such as vapour pressure, deviations from non-ideality and diffusivity (Hanford *et al.* , 2008; Zuend *et al.* , 2008; Barley & McFiggans, 2010; Donahue *et al.* , 2011; Price *et al.* , 2014; Davies & Wilson, 2016; Li *et al.* , 2016). Accurate measurement and estimation of these properties, which are fundamental in determining aerosol transformation, poses a significant challenge, as will be discussed in following sections.

High resolution mass spectrometry (HR-MS) allows the identification of some organic components present in a sample of SOA, demonstrating their number and range of molar mass. Soft ionisation methods (those that induce relatively little fragmentation of the target compound) such as electrospray ionisation (ESI) of a solvated sample can minimise fragmentation of components, but may not ionise all components, particularly those with low proton affinity and ability to bind to sodium cations (Nizkorodov *et al.* , 2011). Nevertheless, when combined with a HR-MS technique such as Fourier transform ion cy-

clotron resonance (FTICR), the accuracy and resolution with which components may be identified is high compared to earlier techniques that induced large fragmentation (making parent compound identification less accurate) and had lower resolving power (causing signals from fragments with similar mass:charge ratios to become indistinguishable). The ESI-FTICR method is used by Gao *et al.* (2010), in which α -pinene and β -pinene are reacted with ozone in a flow tube reactor, with the resulting SOA sampled and dissolved in an acetonitrile/water mixture before measurement in a mass spectrometer. The resulting negative ion mass spectrum is shown in fig. 4 and shows approximately 950 identifiable components. This illustrates the number and molar mass range of components with sufficiently low vapour pressure to partition into the particle-phase that may be produced from the ozonolysis of one monoterpene. As an indication of which of these products may be classed as semi-volatile or low volatility, molar mass relationships with volatility are discussed in Shiraiwa *et al.* (2014) and Li *et al.* (2016).

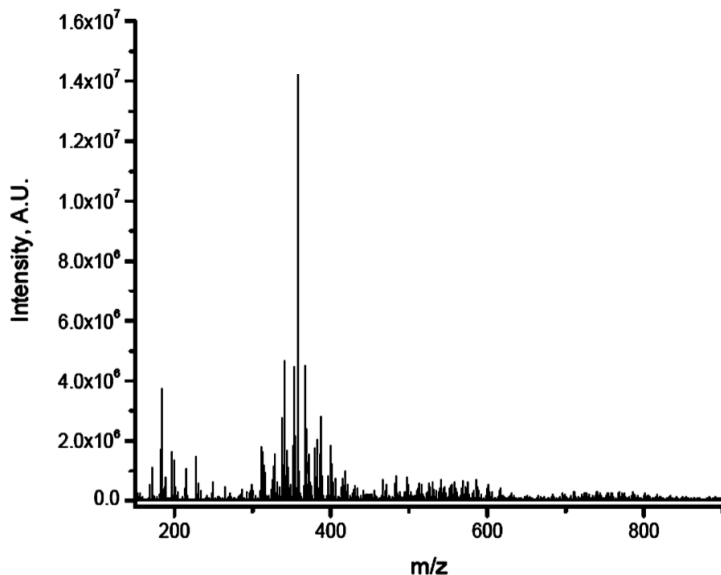


Figure 4: A negative ion mass spectrum of SOA produced from oxidation of α -pinene and β -pinene by ozone. The measurement method is described in the main text and in more detail by the source of the mass spectrum: Gao *et al.* (2010). m is molecular mass, z is charge, and intensity represents the number of counts of an ion in arbitrary units (A.U.).

As discussed in sect. 1.3, vapour pressures are important in determining the phases of components. In turn, the phase determines the fate of a component: if the vapour pressure is sufficiently high, the component will not condense and may eventually undergo complete cleavage and oxidation to CO_2 (if not deposited beforehand). However, if condensation does occur a component may be subject to different chemical processes, such as polymerisation (Kalberer *et al.*, 2004; Barsanti & Pankow, 2004; Kroll & Seinfeld, 2008), and different deposition mechanisms. A similar general mechanism applies to reactive inorganic components. For example, gas-phase sulphur dioxide and NO_x are oxidised

to sulphuric and nitric acid, respectively, which have sufficiently low vapour pressures to partition into the particle-phase (Jacob, 1999).

1.5 Partitioning Theory

The major variables in determining gas-particle partitioning are shown in a schematic in fig. 5. They will be described in this and following sections, however, partitioning is first discussed by distinguishing partitioning regimes that depend on the mean free path of a vapour molecule relative to the size of a particle.

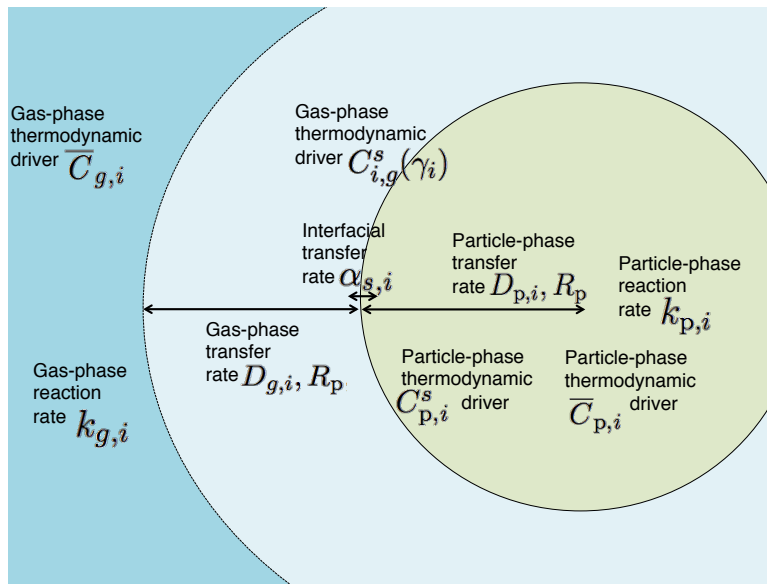


Figure 5: The major variables determining the degree (thermodynamic drivers) and rate of gas-particle partitioning for component i , where g and p represent the gas- and particle-phase, respectively, and \bar{C} is the concentration in the bulk of the respective phase (at the particle centre if there is a concentration gradient throughout the particle), C^s is concentration outside and inside the gas-particle interface for the gas- and particle-phase respectively, γ is the activity coefficient in the particle-phase, D is the diffusion coefficient, R_p is particle radius, k is reaction rate and α_s is the surface accommodation coefficient. The dark blue colour represents the bulk gas-phase, light blue is the gas-phase region with a concentration gradient when the system is in disequilibrium, and the green region represents the particle. Modified from similar plots in Davidovits *et al.* (2006) and Zaveri *et al.* (2014).

The mean free path of a vapour molecule of component i (λ_i) is the mean distance it travels in the gas-phase before impinging on another gas-phase molecule. The ratio of mean free path to particle radius (R_p) is called the Knudsen number (Kn), which indicates the controlling factor(s) in the rate of particle and molecule collision:

$$Kn_i = \frac{\lambda_i}{R_p}, \quad (2)$$

where

$$\lambda_i = \frac{3D_{g,i}}{\bar{v}_i}, \quad (3)$$

where $D_{g,i}$ is the gas phase diffusion coefficient and \bar{v} is the mean speed.

If $\lambda \ll R_p$ ($Kn_i \ll 1$) the rate of collision between molecule and particle depends on the initial distance between them and the gas-phase diffusivity of i . Under this scenario, the partitioning regime is called the continuum regime and the important variable in gas-particle partitioning is gas-phase diffusion, with a diffusion coefficient $D_{g,i}$. The partitioning equation then takes on a form similar to Fick's first law (Crank, 1975) for diffusion toward a sphere, in which the concentration difference between the bulk vapour phase ($\bar{C}_{g,i}$) and the vapour bordering the particle surface ($C_{g,i}^s$), and a measure of the diffusion distance and sphere surface area (both dependent on R_p) are determinants. Denoting the mean concentration of i in the particle-phase as $\bar{C}_{p,i}$, its rate of change is given by the partitioning equation (Wexler & Seinfeld, 1990, 1991; Zaveri *et al.*, 2008):

$$\frac{d\bar{C}_{p,i}}{dt} = 4\pi R_p D_{g,i} f(Kn_i, \alpha_{s,i}) (\bar{C}_{g,i} - C_{g,i}^s), \quad (4)$$

where f is the correction factor for non-continuum effects (described below, but =1 in the continuum regime), and $\alpha_{s,i}$ is the accommodation coefficient (described in sect. 1.8). It can be seen that the concentration difference drives particle growth (the thermodynamic drive), while the terms outside the brackets determine the rate at which equilibrium may be achieved (the kinetic determinants), these are collectively called the condensational sink (s^{-1}).

Partitioning kinetics change with increasing Kn_i , i.e., increasing mean free path relative to particle size. The kinetic regime occurs for $Kn_i \gg 1$. For this regime the dominating determinant on partitioning is the likelihood of a vapour molecule reaching the surface of the particle to transfer across its interface. This is quantified by the accommodation coefficient ($\alpha_{s,i}$), which, for condensation, is the fraction of incoming gas molecules that cross the gas-particle interface ($0 \leq \alpha_i \leq 1$). The partitioning regime under this scenario is called the kinetic regime and may be described by eq. 4, but now with $f \neq 1$. Several formulations for f have been suggested, such as Fukuta & Walter (1970) and Dahneke (1983). That of Fuchs & Sutugin (1971), however, has been validated against measurement for a range of Kn values (Qu & Davis, 2001; Fladerer & Strey, 2003):

$$f(Kn_i, \alpha_i) = \frac{0.75\alpha_{s,i}(1 + Kn_i)}{Kn_i(1 + Kn_i) + 0.283\alpha_{s,i}Kn_i + 0.75\alpha_{s,i}}, \quad (5)$$

Eqs. 4-5 may be applied under any Kn value, including the transition regime, which is when Kn is around 1. The accommodation coefficient is discussed in sect. 1.8. The partitioning regime may vary across particle sizes, however, when solving partitioning for a polydisperse size population of particulates, eqs. 4-5 provide a single, convenient, formulation.

The partitioning equation makes the following assumptions (Vesala *et al.* , 1997; Bilde *et al.* , 2015): no chemical reaction in either phase, ideality in the gas-phase, pressure is temporally and spatially uniform, no transport phenomena other than diffusion occur (e.g. convection), temperature is spatially uniform, the gas-phase concentration of the partitioning component is small compared to that of non-partitioning components, the system is in quasi-steady state (i.e. changes to, for example, the gas-phase concentration of partitioning component are small over the time interval used for solution), the system is quasi-stationary in that the particle surface is in thermodynamic equilibrium with the gas-phase neighbouring it, and droplets are spherical. In reality chemical reactions are likely to affect some partitioning components, however, this can be accounted for by choosing a suitable time interval to solve the partitioning equation over and then solving reaction equations separately. Beside chemical reaction, the least likely assumption to be valid is constant pressure with time. However, as with any other variable that may vary temporally, this can be accounted for by solving the partitioning equation over a suitable time interval and then finding the new variable value and its influence on the variables inside the partitioning equation before repeating the calculation process over the next time step.

$C_{g,i}^s$ in eq. 4 is analogous to the effective saturation vapour pressure in eq. 1:

$$C_{g,i}^s = \gamma_i x_i C_i^0 \exp\left(\frac{2M_i\sigma}{RT_p\rho R_p}\right), \quad (6)$$

where C_i^0 is the pure component saturation concentration (mass/unit volume (air)). Similarly, $\bar{C}_{g,i}$ is analogous to the bulk vapour-phase vapour pressure of i . Therefore, for thermodynamic equilibrium, the effective saturation vapour pressure of i must equal its vapour pressure in the bulk vapour-phase.

Eq. 4 traditionally assumes instantaneous diffusion through the particle-phase. If a component condensing onto a particle is unable to diffuse through, however, and instead remains at the surface, adsorption has occurred. While if it can fully diffuse (the thermodynamically favoured state for an ideal mixture) through the particle the process is called absorption. The distinction is important because the mole fraction of a component at the particle surface, not in the bulk, determines the effective saturation vapour pressure (eq. 1), and therefore whether partitioning equilibrium is reached.

In the condensing case therefore, if adsorption is dominant, sufficient condensation must occur to raise the mole fraction at the particle surface to attain partitioning equilibrium with the bulk vapour-phase (even though the mole fraction in the bulk particle can be much lower). However, if absorption is dominant, the mole fraction in the bulk particle equals that at the surface, requiring more partitioning to the particle-phase to attain partitioning equilibrium compared to the adsorption case (all else being equal). Therefore, the ability of the component to diffuse through the particle-phase will determine the fraction in each phase. In reality, particle-phase diffusivity and time available for diffusion will likely vary substantially between particles (e.g. a particle of elemental carbon vs. one of aqueous solution), therefore the definitions of absorption and adsorption above represent two possible extremes of partitioning.

Equations to describe absorptive and adsorptive partitioning are presented and discussed in Pankow (1994) and Pankow (1987), respectively. Here the discussion will focus on the absorptive approach because, as detailed later, when coupled with particle-phase diffusion considerations, adsorption can be treated as a limiting case of absorptive partitioning. The partitioning constant for the absorptive process is the ratio of rates of sorption and desorption to/from the condensed phase (Pankow, 1994; Kamens *et al.*, 1999):

$$K_{p,i} = \frac{w_j RT}{M_j \gamma_i p_i^0 10^6}, \quad (7)$$

where i and j represent the partitioning component and the organic absorbing medium, respectively. w is weight fraction (of the organic absorbing medium over the total (organic and inorganic) absorbing medium), R is the ideal gas constant ($8.2057 \times 10^{-5} \text{m}^3 \text{atm mol}^{-1} \text{K}^{-1}$), T is temperature and M is molar mass. p_i^0 must have units in atm to be compatible with R , otherwise a conversion factor is required. When considering purely organic aerosol, $w_j = 1$, and the inverse of $K_{p,i}$ gives the effective saturation concentration (mass/unit volume(air)):

$$C_i^* = \frac{1}{K_{p,i}} = \frac{M_j \gamma_i p_i^0 10^6}{RT}. \quad (8)$$

A further simplification is to assume that the absorbing organic medium j has the same molar mass as the partitioning component i , producing:

$$C_i^* = \frac{M_i \gamma_i p_i^0 10^6}{RT}, \quad (9)$$

which is the definition given by Donahue *et al.* (2006). The study of Barley *et al.* (2009) demonstrates that for simple cases with less than ten organic components, using eq. 9 rather than eq. 8 may produce erroneous estimates of partitioning because the constant

molar mass assumption is not valid. The assumption was shown to breakdown when relatively low molecular weight water was included in models of aqueous organic particles, as would be expected in the ambient atmosphere. When used accurately, C_i^* is a useful metric for partitioning because it can be combined with the total mass concentration of particle-phase (C_{aer}) to give the partitioning coefficient:

$$\xi_i = \left(1 + \frac{C_i^*}{C_{aer}}\right)^{-1}, \quad (10)$$

ξ_i is the fraction of i in the particle-phase at equilibrium. Eq. 10 shows that for a given total concentration of condensing component i , as the concentration of particle-phase increases, the fraction of i in the particle-phase at equilibrium increases. This is consistent with eqs. 1 and 6, which show for increased particle-phase concentration (and constant total concentration of i) a decreased mole fraction of i results, which decreases its effective saturation vapour pressure/concentration, thereby increasing its tendency to condense. According to eq. 10, components with a C_i^* value equal to the total particle phase loading (C_{aer}) will partition 50:50 between phases at equilibrium.

To illustrate the relationship of partitioning coefficient and total particle-phase concentration, the saturation curve described by eq. 10 can be plotted for several total particle-phase concentrations (C_{aer}), as in fig. 6. While, volatile and nonvolatile components have been described above, those components with a vapour pressure within the shaded region of fig. 6 may be called semi-volatile, as they may (depending on C_{aer}) have considerable fractions in both the condensed and gas phase. The C_{aer} values used in fig. 6 are representative of the range expected in the troposphere away from emission sources (Chung & Seinfeld, 2002; Cabada *et al.*, 2004; Seinfeld & Pandis, 2006).

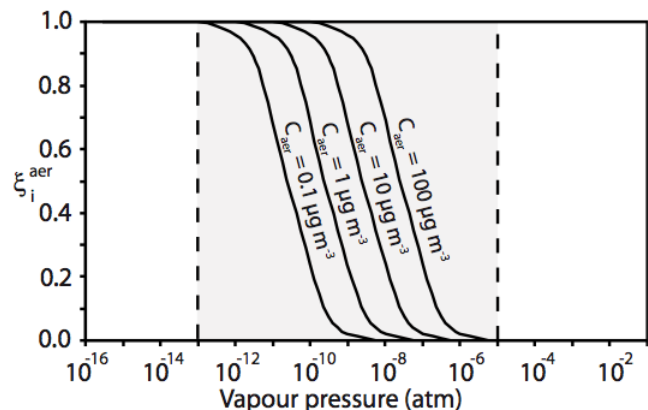


Figure 6: The partitioning coefficient (equilibrium fraction in the particle-phase) as a function of pure component saturation vapour pressure and total particle-phase concentration (given beside curves as C_{aer}). The shaded region shows the effective vapour pressure range of semi-volatile components. Taken from Valorso *et al.* (2011).

Estimating the partitioning of components between phases, even when diffusion through both phases is assumed instantaneous, has proved a considerable challenge. In part this is because C_{aer} can vary substantially in space and time in the ambient atmosphere, as shown in the representative values used in fig. 6. Considering this variation, fig. 6 shows that for components of a vapour pressure around 10^{-9} atm, the condensed fraction could be close to 100 % or 0 %. A second complication is the large number and diversity of organic compounds in the atmosphere, with individual vapour pressure dependencies on temperatures.

To address partition estimation three main methods have been proposed. The first was the two-product model of Odum *et al.* (1996), in which the semi-volatile organic group is treated as two surrogate compounds, with prescribed mass fractions and C^* values. These values are found by fitting to empirical relationships of particle-phase yields and total particle-phase concentration, and can give very good fits to laboratory observations of partitioning (Odum *et al.*, 1996; Shrivastava *et al.*, 2006). The weakness in this approach is its general applicability to the ambient atmosphere where concentrations of oxidants, component precursors and initial particle-phase compositions and concentrations vary substantially. Constants derived empirically are therefore unlikely to provide reliable estimates of partitioning behaviour under the full range of ambient conditions.

An alternative approach is lumping components by volatility. This separates partitioning from factors like atmospheric oxidative capability, in principle allowing a more general estimation of partitioning (Bian & Bowman, 2002). This approach has been developed and called the “Volatility Basis Set” (VBS) (Donahue *et al.*, 2006; Robinson *et al.*, 2007; Donahue *et al.*, 2009). Individual components or surrogates representing groups of components are split into volatility bins represented by C_i^* , enabling a concentration volatility distribution to be created, as in fig. 7. Typically decadal volatility bins are used. The concentration volatility distributions can be inferred from laboratory or field observation of volatility (Grieshop *et al.*, 2009; Shilling *et al.*, 2009; Cappa & Jimenez, 2010). Although also based on empirical evidence, the important distinction between the VBS and the two-product model is the ability to combine distributions of concentration with volatility from different regions and sources, affording a much greater generality than the latter, which is limited to four degrees of freedom. Using the two-product model, for example, in an air mass that has passed over several different emission sources, requires an estimate of two mass fractions and two C^* values that attempt to represent the partitioning behaviour of the resulting complex combination of components. These values will be drawn from empirical data of comparatively simple simulations of the atmosphere (e.g. a given emission source, atmospheric oxidative capacity, temperature and relative humidity). An increased likelihood of accurately estimating the partitioning of this complex component mixture would be to combine the volatility distributions from each emission source, since

this allows a much more detailed estimate of partitioning, rather than relying on the four values of the two-product approach. This is the advantage of the VBS approach. The arrow in fig. 7 indicates the volatility bin where 50:50 partitioning between phases occurs at equilibrium (eq. 10).

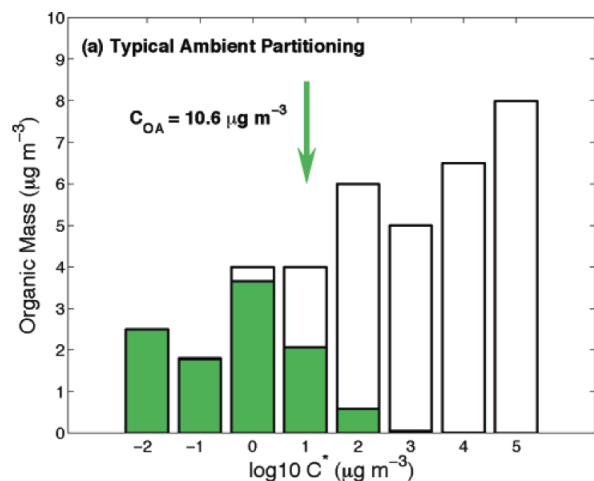


Figure 7: Example concentration volatility distribution. Bars represent the total loading per volatility bin and green segments represent the particle-phase concentration at equilibrium according to eq. 10. The C_{OA} is the total particle-phase mass loading, and the arrow points to the volatility bin with the same value for effective saturation concentration (thereby giving 50:50 partitioning between phases (eq. 10)). The plot is intended to exemplify the background distribution, and the derivation is described in Donahue *et al.* (2006) from which it is taken.

Recently the VBS has been used to simulate partitioning inside a regional model including meteorology and gas-phase chemistry: the Weather Research and Forecasting Model Coupled to Chemistry (WRF-CHEM) (Ahmadov *et al.*, 2012). It was found to give much better agreement with observations of SOA concentrations compared to the original model that used the two-product approach to partitioning described above.

The VBS approach, however, is still limited by empirical evidence and therefore potentially restricted in its generality (Bergström *et al.*, 2012; Li *et al.*, 2015). In principle the most general modelling approach to partitioning is mechanistic modelling, by which partitioning components are individually identified and their vapour pressure dependency on temperature is either estimated or drawn from a database (e.g. Li *et al.*, 2015). Toward this end, comprehensive gas- and particle-phase chemical mechanisms relevant for the atmosphere have been created and continue to be developed. For the gas-phase, the Master Chemical Mechanism (MCM) (Jenkin *et al.*, 2003; Saunders *et al.*, 2003; Bloss *et al.*, 2005) is a near-explicit description of the reaction of VOCs and their reaction products. It has been found, however, to underestimate SOA loading when compared to laboratory and field measurements (Jenkin, 2004; Johnson *et al.*, 2004, 2005, 2006). Possible reasons for the underestimate are missing reactions in the gas-phase leading to comparatively low

vapour pressure products, systematic overestimation of pure component vapour pressure, or neglect of particle-phase reactions.

Using a similar reaction generation mechanism for reactions as in the MCM, The Generator of Explicit Chemistry and Kinetics of Organics in the Atmosphere (GECKO-A) (Aumont *et al.* , 2005) attempts to explicitly account for all gas-phase reactions. While, the MCM intentionally omits reactions thought to produce low yields, GECKO-A does not. It was employed in a model for phase partitioning over Mexico City in Lee-Taylor *et al.* (2011) and found to give good reproduction of the diurnal variation in SOA concentration when compared with observations. When compared against reaction chamber results, however, the explicit approach was found to overestimate SOA concentration, by up to a factor of five (Valorso *et al.* , 2011). Further comparison with chemical characterisation indicated this could be due to missing or biased mechanisms within GECKO-A, inaccurate partitioning modelling or even unaccounted for loss of components to chamber walls. Regardless of its accuracy, the explicit or near-explicit approaches to gas-phase reaction are comparatively computationally expensive. They are the first examples, in this thesis, of a complex benchmark method that may be used to identify a simpler, less computationally expensive method. For example, results from a verified GECKO-A model could be compared with those from a chemistry model containing certain fractions of the complete reaction set (i.e. those thought to be most important) to determine whether a simpler model is realistic.

While lumped volatility is inferred from measurements when employing the VBS or two-product approaches, for the mechanistic representation of semi-volatile components, the volatility of each component must be known. The following sections describe methods to measure and estimate pure component vapour pressures so that this information may be available to mechanistic partition modelling.

1.6 Determination of Vapour Pressure

Studies involving models of varying complexity, from simple absorptive partitioning (McFiggans *et al.* , 2010) to regional simulations coupled with meteorology (Simpson *et al.* , 2007; Bergström *et al.* , 2012; Li *et al.* , 2015), have reported uncertainty in vapour pressure to be a major contributor to uncertainty in estimated aerosol concentrations. The complexity of these models also varies in terms of the representation of organic components. In the McFiggans *et al.* (2010) study for example, up to 1×10^4 components are used with an atmospherically representative range of estimated volatilities, whereas in the Simpson *et al.* (2007) study, 8 components represent the organic semi-volatile group. Regardless of this range, uncertainty in the vapour pressures of partitioning components is a major, if not dominant, source of uncertainty in results. Current measurement capability

means that only a small fraction ($< 1\%$) of the many organic compounds expected in the atmosphere (Aumont *et al.* , 2005; Goldstein & Galbally, 2007) have been measured for pure component vapour pressure (Barley & McFiggans, 2010; Bilde *et al.* , 2015). Consequently, it is necessary to employ estimation methods for vapour pressure, though these require validation against measurements.

The differential equation for dependence of pure component saturation vapour pressure (eq. 1) on temperature (T) is expressed in the Clausius-Clapeyron equation (Schwarzenbach *et al.* , 1993):

$$\frac{dp_i^0}{dT} = \frac{\Delta H_{pv}}{T\Delta V_{pv}}, \quad (11)$$

where ΔH_{pv} and ΔV_{pv} are the changes in molar enthalpy and molar volume between the particle- (p) and vapour-phase (v), respectively. In principle, this could be used to produce the transition line between the vapour- and particle-phase in a phase diagram, such as fig. 2. However, the equation can only be solved by approximation. A commonly employed approximation is (Schwarzenbach *et al.* , 1993):

$$\ln p_i^0 = -\frac{B}{T} + A; B = \frac{\Delta H_{pv}}{R}; A = \frac{\Delta S_{pv}}{R}, \quad (12)$$

where ΔH_{pv} is assumed to be constant with temperature and ΔS_{pv} is the change in entropy between the phases. In reality, ΔH_{pv} is dependent on temperature, and this may be accounted for by a more complex approximation.

Several measurement techniques have been used for pure component vapour pressures. Those that are relevant to atmospheric organic compounds have been reviewed in Bilde *et al.* (2015). Knudsen-cell based methods entail placing a macroscopic sample of the component of interest inside a container with a hole in the ceiling. Loss of vapour-phase component occurs by effusion through the hole at a rate proportional to the component vapour pressure as long as sufficient time has been allowed for partitioning equilibrium inside the container to be reached. For effusion to be the dominant transfer process the ratio of the mean free path of vapour phase molecules inside the container to size of the container aperture must be sufficiently high (eq. 2). The rate of effusion is then measured either through measurement of the concentration of effusing molecules (Booth *et al.* , 2009), or by the change in mass of the sample (da Silva & Monte, 1990).

Single particle methods operate through measuring the rate of size change of a single particle held in place either by an electrodynamic balance (Zardini *et al.* , 2006) or optical tweezers (Hopkins *et al.* , 2004). Growth or shrinkage can be induced through controlled change of the bulk vapour-phase concentration of the component being studied. Particle

size distribution methods also infer vapour pressure from measurement of the rate of size or volume change of an aerosol population when subject to controlled temperature and relative humidity conditions that induce partitioning (Koponen *et al.* , 2007b; Saleh *et al.* , 2008; Salo *et al.* , 2010). Finally, the thermal desorption methods begin by collection of the component onto a relatively cold surface. The surface is then heated and the evaporation rate measured and used to infer vapour pressure (Chattopadhyay & Ziemann, 2005; Cappa *et al.* , 2007; Bruns *et al.* , 2012).

Certain methods are advantageous over others regarding factors such as measurable vapour pressure range and operational temperature, however all require certain assumptions and have sources of error. In the Knudsen-cell technique, for example, a calibration is required using a sample of previously measured vapour pressure. Therefore, there is an assumption that the target component behaves similarly to the calibration compound with regard to fragmentation upon ionisation and that the signal-vapour pressure relationship of the calibration component is applicable to the target component, even though their vapour pressures may not overlap. In the single particle methods, it is assumed that there is zero concentration of the partitioning component in the gas-phase, however this may not be true if some adsorbs to the walls of the measurement apparatus. For thermal desorption, it is assumed that the surface on which the component is first adsorbed and then warmed does not impede evaporation, however it is possible that intermolecular bonds form between the instrument surface and sample.

Carboxylic acids have been popular compounds for vapour pressure measurements because of their presence at many sites and comparatively high atmospheric abundance (Kawamura & Sakaguchi, 1999; Kawamura *et al.* , 2007; Fuzzi *et al.* , 2007; Miyazaki *et al.* , 2009; Stone *et al.* , 2010) and because of their comparatively easy acquisition from chemical suppliers. They have been measured by all of the techniques mentioned above, providing a means for measurement comparison. In fig. 8 the published measurements for vapour pressures of the first ten straight-chain dicarboxylic acids are shown. It clearly demonstrates large discrepancies between measurements, frequently of two orders of magnitude, but sometimes reaching three or even four.

The cause of these discrepancies is subject to continuing investigation, however, a large source of uncertainty appears to be the purity of the sample being measured. Impurities may disrupt the formation of intermolecular bonds between molecules of the sample under investigation, therefore affecting tendency to partition to the gas-phase (Bilde *et al.* , 2015).

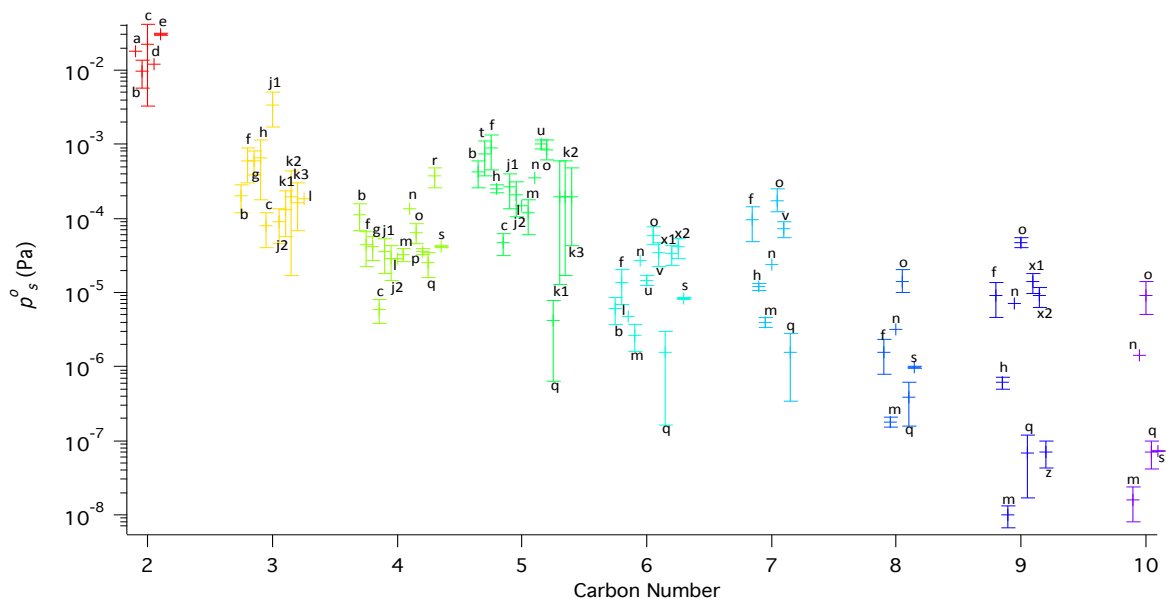


Figure 8: Published solid vapour pressures for the first ten straight-chain dicarboxylic acids at 298 K. Letters represent publications whilst numbers indicate different methods within a publication: a =de Wit *et al.* (1983), b=Booth *et al.* (2010), c=Soonsin *et al.* (2010), d=Bradley & Cotson (1953), e=Noyes & Wobbe (1926), f=Bilde *et al.* (2003), g=Mønster *et al.* (2004), h=da Silva *et al.* (1999), j1/2=Koponen *et al.* (2007a, using Van Laar activity coefficient (γ)/using UNIFAC γ), k1/2/3=Pope *et al.* (2010, using fitted γ /UNIFAC γ /UNIFAC (Peng modified) γ), l=Riipinen *et al.* (2007), m=Cappa *et al.* (2007), n=Chattopadhyay & Ziemann (2005), o=Salo *et al.* (2010), p=da Silva *et al.* (2001), q=Bruns *et al.* (2012), r=Saleh *et al.* (2009), s=Davies & Thomas (1960), t=Bilde & Pandis (2001), u=Tao & McMurry (1989), v=Saleh *et al.* (2008), x1/x2=Saleh *et al.* (2010, atomization generation/homogenous condensation generation), z=Yatavelli & Thornton (2010). The reader is referred to the cited articles for further details on measurement method, including activity coefficient (γ) estimation methods.

The current time and accuracy limitations of measuring semi-volatile component vapour pressures means that only a tiny fraction of atmospheric organic components have measured vapour pressures, and of these the accuracy is often questionable. For explicit modelling of phase partitioning, therefore, estimation methods of pure component vapour pressures are employed (e.g. Valorso *et al.*, 2011; Lee-Taylor *et al.*, 2011; Li *et al.*, 2015). Numerous vapour pressure estimation methods have been published, which may be categorised as either: structure activity relationships (SAR) or fundamental models.

For the majority of SARs, chemical groups, such as a methyl group, are valued by their effect (or contribution) on vapour pressure. Therefore, by defining the constituent groups

of a given component, vapour pressure may be estimated. The contributions of groups to vapour pressure are estimated through “training” (a fitting procedure) to measured vapour pressures. The training set is then the particular database of measured vapour pressures used for contribution estimation. Consequently, the accuracy of the SAR is dependent on the accuracy of the training set. Furthermore, the range of components a SAR is applicable to is dependent on the range in the training set. While some SARs report very good accuracy in their original publications, when applied to a different test set of measurements, accuracy can vary considerably. Only recently have SARs trained on atmospherically relevant components been produced (Capouet & Müller, 2006; Pankow & Asher, 2008; Compernelle *et al.*, 2011). Alternative SARs are intended for chemical engineering purposes, and consequently trained on comparatively high vapour pressure, less multifunctional components (Reid *et al.*, 1987; Myrdal & Yalkowsky, 1997; Nannoolal *et al.*, 2008; Moller *et al.*, 2008).

Fig. 8 shows that for the SARs with atmospheric relevance, the training set itself is a source of large vapour pressure uncertainty. Furthermore, the number of components with measured vapour pressures and range of their functional groups is far less than those available to methods pertaining to chemical engineering. For example, in a literature review, Barley & McFiggans (2010) found 45 components with published measured vapour pressures that were expected to be classifiable as SVOC, whereas the training set of the Nannoolal *et al.* (2008) SAR comprised 1663 components.

The final objective for measurements is a sufficient accuracy and number covering a sufficient range of components to produce a useful training and test set for SARs. This will allow mechanistic modelling of partitioning with a known uncertainty generated by vapour pressure estimation. However, defining the sufficient accuracy, number and range of components needed to produce and test estimation methods is not straightforward. It is informed, however, by assessing estimates against measurements. The benefits of assessment are manifold; firstly, it may determine the range of components a method is applicable to (not always clearly stated in the original publication). Secondly, of the applicable components, it shows which estimation method is most accurate, in turn indicating deficiencies and strengths in method structure and parameterisation. Such assessments can determine to what extent the larger size of chemical engineering-based training sets compensates for their lower relevance to the atmosphere. Finally, if coupled with eqs. 9 and 10, the vapour pressure estimates may be used to estimate SOA loading, and therefore assess the sensitivity of loading to estimate variation.

Ultimately, if loading and composition can be estimated to within a satisfactory accuracy, vapour pressure measurements and estimation methods have achieved their objective. An estimation method assessment, including SOA loading sensitivity, is the topic of the first paper in this thesis. The satisfactory accuracy will vary depending on the application,

however, studies to date indicate a certainty in mass concentration of organic aerosol of at best a factor of 2 to 3 (McFiggans *et al.*, 2010; Barley & McFiggans, 2010; Valorso *et al.*, 2011; Li *et al.*, 2015). For predicting particulate matter concentration and resulting air quality standards, this uncertainty is insufficient to distinguish between moderate or heavy pollution (Seinfeld & Pandis, 2006), and therefore not a satisfactory accuracy.

In a series of papers: McFiggans *et al.* (2010), Topping *et al.* (2011) and Barley *et al.* (2011), the sensitivity of partitioning was investigated with regard to vapour pressure and nonideality. The study focussed on the mechanistic approach to partitioning, with Barley *et al.* (2011) using 2742 atmospherically relevant compounds to represent airborne components. Sensitivity was tested through choosing a base case model setup, which was the Nannoolal *et al.* (2008) vapour pressure estimation method, which required a normal boiling point estimation method, chosen as Nannoolal *et al.* (2004). For activity coefficients (γ), the base case assumed ideality ($\gamma = 1$). Several variants of this setup were chosen to produce comparable estimates produced for numerous scenarios of emissions, temperature, relative humidity and concentrations of nonvolatile particle core.

Partitioning sensitivity was presented as the \log_{10} of the ratio of estimated SOA mass concentrations between model setups and the base case. Results are given in fig. 9 as box-whisker plots. This shows a systematic discrepancy between different estimation methods, with some methods averaging one order of magnitude difference with the base case, but under some atmospheric variable scenarios, reaching two or more orders of magnitude. Two orders of magnitude difference is observed between rural and heavily polluted urban sites (Seinfeld & Pandis, 2006). These discrepancies therefore indicate mechanistic partitioning modelling to be practically useless unless vapour pressure estimation methods are reliably assessed against measurements to determine the most accurate and its uncertainty.

The disagreement in SOA mass in fig. 9 is small compared to the maximum disagreement in measured vapour pressures shown in fig. 8. It may be expected that since estimation methods are trained on such measurements there would be similar disagreement between estimated SOA masses and training set measurements. The majority of vapour pressure measurements used in estimation method training sets are of $p^0 > 10^{-3}$ Pa, since these are most abundant. At these higher vapour pressures, measurement accuracy is relatively good, as indicated in fig. 8. Consequently, the estimation methods typically agree on vapour pressures within an order of magnitude (Barley & McFiggans, 2010).

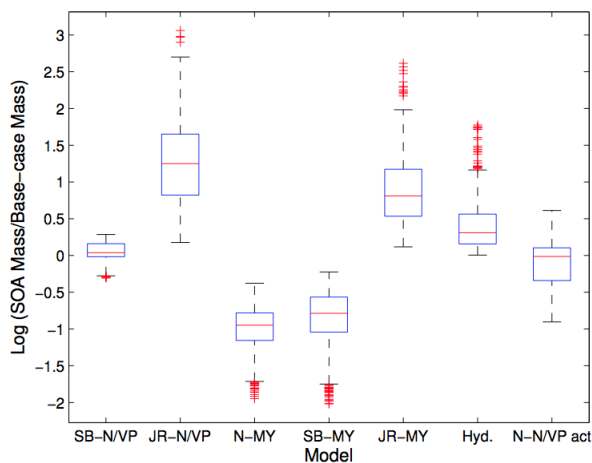


Figure 9: Sensitivities (expressed as box-whisker plots) of SOA mass loading to variation in model setup. In the first 5 plots (from left) vapour pressure estimation method is given by the second set of letters: N/VP for Nannoolal *et al.* (2008), MY for Myrdal & Yalkowsky (1997); normal boiling point estimation (an input to vapour pressure estimation methods) is represented by the first set of letters: SB for Stein & Brown (1994), JR for Joback & Reid (1987) and N for Nannoolal *et al.* (2004). Plots 6 and 7 vary from the base-case through the inclusion of hydrolysis of acid anhydrides and non-ideality, respectively.

In a regional model with a mechanistic approach to partitioning, Li *et al.* (2015) test particulate loading sensitivity to estimated vapour pressure by decreasing all estimated vapour pressures by a factor of 100. In Barley & McFiggans (2010, their fig. 2) the greatest average disagreement between estimation methods was around two orders of magnitude. Therefore a factor of 100 represents a conservative estimate of average discrepancy in vapour pressure estimates. Li *et al.* (2015) observe maximum changes to the daily average of a factor of 2.3, much less than the sensitivity observed by Barley *et al.* (2011). It is not possible to determine the cause of the differences in the studies here, though a major difference is the inclusion of chemical reactions in Li *et al.* (2015), indicating that chemical ageing may reduce loading sensitivity to vapour pressure estimates.

The vapour pressure assessment paper presented in this thesis is concerned with SAR methods, however computational quantum mechanic models like COSMO-RS (conductor-like screening model for real solvents) and quantitative structure-property relationship methods like SPARC (Hilal & Karickhoff, 2003) offer an estimation method independent of vapour pressure measurement accuracy. In general the mechanism behind these methods is to first estimate the intermolecular interactions of a component, and, based on this, estimate its vapour pressure. They have shown encouraging accuracy when compared against measurements (Asher & Pankow, 2006; Arp & Goss, 2009; Schnitzler & McDonald, 2012). A recent analysis by Schröder *et al.* (2016) provides the most complete and rigorous assessment of COMSO-RS vapour pressure assessment to date. It indicates similar accuracy to the EVAPORATION group contribution method, which showed comparatively high accuracy in its original publication (Compernelle *et al.*, 2011). In both assessments,

however, relevance to atmospheric components is questionable since most vapour pressure measurements being tested against are too high to induce a considerable condensable fraction.

Although the mechanistic approach to gas-particle partitioning is attractive for its general applicability and independence from the limitations and potential biases of empirical approaches (e.g. volatility basis set), it appears to be in its infancy. A major limiting factor to progress is the accuracy of vapour pressure measurements of components relevant to SVOC. This restricts the accuracy of estimation methods trained on such measurements and the ability to validate both structure activity relationship and more fundamental approaches to vapour pressure estimation.

1.7 Activity Coefficient

The activity coefficient (γ) of a component (i) represents its nonideality relative to a pure liquid reference state ($\gamma_i = 1$ when $x_i = 1$), where 1 is an ideal mixture and increasing/decreasing values are increasingly nonideal. It is indicative of the miscibility of a partitioning component in a sorbate (the absorbing medium) (Saxena & Hildemann, 1996). Eq. 8 demonstrates that the effective saturation ratio is proportional to γ , thus decreasing γ below one acts to increase the likelihood of condensation.

In certain systems activity coefficients are expected to be sufficiently low in the particle-phase that phase separation occurs: when immiscible components with the same phase form aggregates. Liquid-liquid phase separation has been predicted and observed for particles (Erdakos & Pankow, 2004; Marcolli & Krieger, 2006; Zuend *et al.*, 2008; Ciobanu *et al.*, 2009). The effect of phase separation is particularly important if it results in one phase partitioning to the surface since the surface composition determines thermodynamic drivers (eqs. 4-6) (Krieger *et al.*, 2012, , and discussed in sect. 1.5). Optical microscope images in fig. 10, taken from Ciobanu *et al.* (2009), show the morphology that may result from liquid-liquid phase separation.

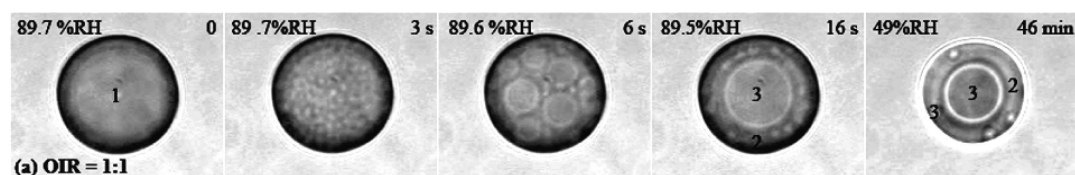


Figure 10: Optical microscope images of particle morphology during drying and showing phase separation, with relative humidity given in the top left of each plot, time in the top right and for an organic to inorganic dry mass ratio (OIR) of 1:1. Labels on particles represent phases: 1, aqueous ammonium sulphate (AS) and poly(ethylene glycol)-400 (PEG-400) solution; 2, aqueous PEG-400; 3, aqueous AS. Taken from Ciobanu *et al.* (2009).

Regardless of whether phase separation occurs, for accurate estimation of gas-particle partitioning γ must be accurately known. For aqueous systems it may be measured using, for example, a dew point-based technique, which measures the relative humidity of a sample of known mole fraction of water. Relative humidity can be calculated more accurately than the vapour phase saturation ratios of most organic components because the relationship of water saturation vapour pressure with temperature is known comparatively accurately. With RH and mole fraction known, eq. 1 can be used to calculate γ of a system (Marcolli & Peter, 2005). There are a multitude of measurements available for systems with variable ratios of organic:inorganic:water concentrations, some of which are reported in Zuend *et al.* (2008) and Zuend *et al.* (2011). As an example of the accuracy attainable for γ measurements, ± 0.015 is given by Marcolli & Peter (2005) and Marcolli & Krieger (2006), representing a fractional accuracy of 3 % for a γ value of 0.5. This is considerably better accuracy than has been obtained for vapour pressures measurements of semi-volatile components (discussed in 1.6).

Several methods have been suggested for the estimation of γ . Those that can treat mixtures of organic and inorganic components (and are therefore atmospherically relevant (sect. 1.4)) may be divided into two categories: coupled models that explicitly account for organic-ion interactions and decoupled models that treat electrolytes and non-electrolytes separately and use a mixing rule to determine the overall γ . In the first category, the AIOMFAC (Aerosol-Inorganic-Organic Mixtures Functional groups Activity Model) extends the LIFAC model for activity coefficients (Yan *et al.*, 1999) to improve applicability to the atmosphere. This has been done through the addition of contributions from organic functional groups, accounting for high concentrations of electrolytes, and for new electrolytes, using better suited reference and standard states and parameterising against relatively low temperature measurements (Zuend *et al.*, 2008, 2011; Ganbavale *et al.*, 2015). In the second category, either the Zdanovskii-Stokes-Robinson (ZSR) relationship (Stokes & Robinson, 1966; Topping *et al.*, 2005a,b; Clegg & Seinfeld, 2006) or a Pitzer-type relationship (Pitzer, 1991; Carslaw *et al.*, 1995) may be used to combine the effects of electrolytes and non-electrolytes on γ . The activity contribution from each constituent of a mixture in this second category may be estimated by a UNIFAC (Fredenslund *et al.*, 1975, 1977; Marcolli & Peter, 2005) approach (Clegg *et al.*, 2001; Clegg & Seinfeld, 2004, 2006), or the Pitzer, Simonson and Clegg (PSC) model for inorganic-water interaction (Clegg *et al.*, 1998; Clegg & Brimblecombe, 1998).

Comparison with laboratory measurements show that both coupled and decoupled models can achieve good accuracy when predicting particle hygroscopicity for ternary systems including water, an inorganic salt and soluble or partly-soluble organic component at a range of relative humidities (Hanford *et al.*, 2008; Tong *et al.*, 2008). In Lei *et al.* (2014) AIOMFAC and ZSR relation models were shown to accurately predict hygroscop-

icity measurements of mixtures of ammonium sulphate and levoglucosan, a major component of biomass burning emissions. However, for the organic component (also found in biomass burning emissions) that showed no hygroscopic growth, 4-hydroxybenzoic acid, these models were forced to assume an insoluble organic phase to gain measurement agreement, which was not predicted in the models. Several of the activity coefficient models may predict liquid-liquid phase separation and crystallisation. These include the AIOM-FAC model (Zuend *et al.*, 2008, 2010, 2011), the PSC-based model (Clegg *et al.*, 2001), and a comparatively computationally efficient model (Topping *et al.*, 2013) that may be applied to an arbitrary number of components. The framework for modelling the activity coefficients and any resulting phase separation, therefore appears to be in place, and to perform well for specific, relatively simple systems.

As for vapour pressures, however, model development and testing is hindered by measurement availability. Measurement of activity coefficients is in fact limited by the large uncertainty of vapour pressure estimates because for a n component mixture, the vapour pressures of $n - 1$ components must be known to infer γ from vapour phase concentration measurements (Zuend *et al.*, 2011; Bilde *et al.*, 2015) (eqs. 4-6). The large uncertainty in measured p^0 of organics (sect. 1.6), therefore means there are very few measurements of γ for mixtures of more than 3 components. This severely limits the applicability of measurements to atmospheric conditions where multiple components are found within one particle (Laskin *et al.*, 2016).

The effect of including nonideality in an explicit partitioning model has been compared against the assumption of ideality in Compernelle *et al.* (2009), McFiggans *et al.* (2010), Barley *et al.* (2011), Topping *et al.* (2013) (which also modelled liquid-liquid phase separation) and Li *et al.* (2015). These studies used >1000 components to represent organic constituents. All indicated that inclusion of nonideality can alter the estimated particulate mass loading by up to ± 50 %.

Disagreement between nonideal and ideal models was found to be dependent on relative humidity because water has a comparatively high polarity and high abundance. It therefore exerts a dominating effect on the estimated activity coefficient, with lower polarity molecules having larger deviations from ideality and greater likelihood to enter a low polarity organic-rich phase (Zuend *et al.*, 2011). The effect is exemplified in fig. 11, which are Topping *et al.* (2013) model estimates for a relatively strong biogenic VOC emission case. It shows that for this particular scenario, assuming ideality overestimates particle-phase mass loading by a maximum of 50 % at low RH. Components with higher oxygen to carbon elemental ratios (O:C) have greater polarity, and are therefore found in the aqueous-phase, whereas lower O:C compounds form a separate liquid- (or amorphous-) phase.

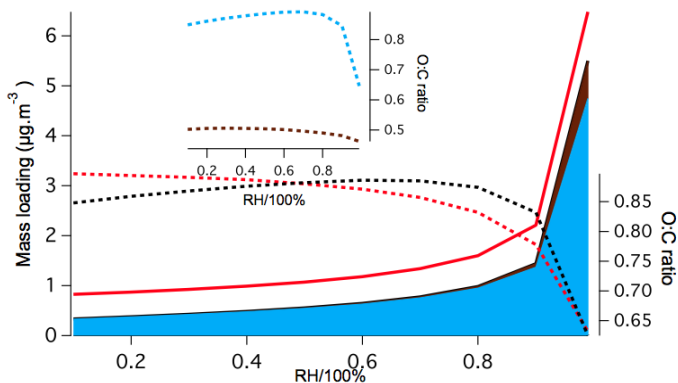


Figure 11: The particle-phase mass loading as a function of relative humidity estimated by the partitioning model given in Topping *et al.* (2013) (from which this figure is taken). Red lines are with ideality assumed, black lines are for non-ideality and liquid-liquid phase separation turned on. Solid lines correspond to the left axis and dashed lines to the right axis. Blue and brown represent the two phases: high O:C (aqueous) phase and low O:C phase, respectively. The subplot shows the O:C ratio of these two phases.

The sensitivity of explicit partitioning models to the inclusion of nonideality was studied in Barley *et al.* (2011). A description of their approach is given in sect. 1.6 here, and the seventh plot from left in fig. 9 here shows how estimated mass loading of SOA varies between an ideal assumption of mixing and inclusion of nonideality. The median estimated loading is in good agreement between the treatments, though under certain atmospheric scenarios disagreement between treatments can reach a factor of 10. As shown in fig. 11, however, although loading estimates may be similar, estimated composition may vary, and indeed, Barley *et al.* (2011) find that composition change when using nonideality is greater than for using different vapour pressure estimation methods (when compared against a base case), despite the latter variation leading to a generally much greater effect on estimated SOA mass concentration (fig. 9). Furthermore, the variation in composition for ideal vs. nonideal models causes greater sensitivity of estimated hygroscopicity to nonideality compared to vapour pressure estimation technique (Compernelle *et al.*, 2009; Topping *et al.*, 2011).

Since SOA composition and resulting hygroscopicity is indicated to be sensitive to estimation of the component activity coefficients, it is a variable in gas-particle partitioning that requires accurate estimation. However, it is widely agreed that the major limitation to improving mechanistic partitioning models is the measurement and estimation of vapour pressure (Clegg *et al.*, 2008; Barley *et al.*, 2011; Topping *et al.*, 2013; Bilde *et al.*, 2015). Additionally, as discussed above, vapour pressure accuracy limits further improvement in understanding (measurement and estimation) of activity coefficients.

1.8 Surface Accommodation Coefficient

Whereas vapour pressure and activity coefficient determine the thermodynamic drivers for partitioning, the introduction will now look at some of the kinetic determinants. The first is the accommodation coefficient (α_i), which was introduced in eq. 5. On collision with a particle surface, a molecule may scatter away or be accommodated (after which it may desorb, absorb, or remain at the surface (adsorb)). Accommodation results from intermolecular bonding such as van der Waals interactions (Pöschl *et al.* , 2007). α_i is therefore the fraction of partitioning molecules of component i impinging on the particle surface that are accommodated to the surface.

Condensation may be split into three chronological stages: gas-phase diffusion, accommodation onto the gas-particle interface (interfacial transport) and particle-phase diffusion. When treating the latter two stages separately, the distinction between surface accommodation coefficient ($\alpha_{s,i}$) and bulk accommodation coefficient ($\alpha_{b,i}$) is important. The latter is the fraction of molecules of component i impinging on the particle surface that are accommodated in the particle bulk. It is therefore inextricably linked to the particle-phase diffusion coefficient (Pöschl *et al.* , 2007; Kolb *et al.* , 2010). Only in particles where particle-phase diffusion can be considered instantaneous, and i is nonreactive does $\alpha_{s,i} = \alpha_{b,i}$.

$\alpha_{s,i}$ determines the rate of interfacial transport. A plot representing partitioning via the three stages of condensation (and evaporation when the stage order is reversed) is shown in fig. 12, which are model results from (Mai *et al.* , 2015). Each plot in the figure was produced with different model inputs that induced mass transfer limitation by a different partitioning stage: either the gas-phase diffusion coefficient ($D_{g,i}$) (plot (a)), surface accommodation coefficient (plot (b)) or particle-phase diffusion coefficient ($D_{p,i}$) (plot (c)) were set relatively low.

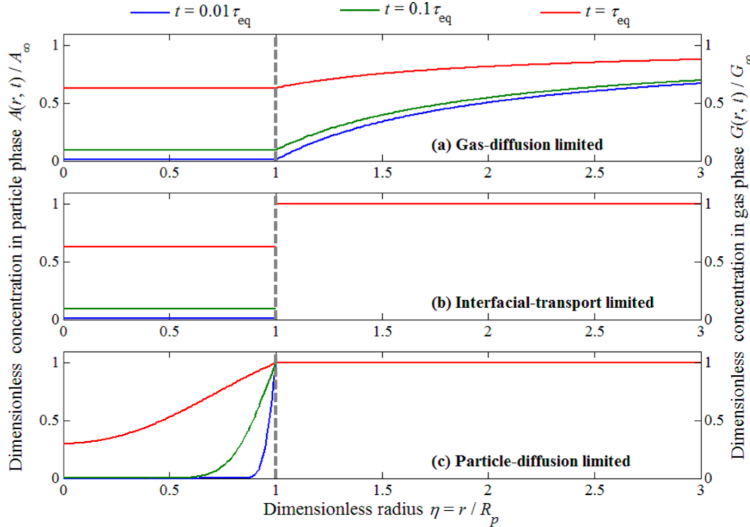


Figure 12: The concentration (normalised to concentration in the bulk gas-phase and equilibrium particle-phase concentration for the right and left axis, respectively) profiles with distance (normalised to the particle radius, where 0 is the particle centre) for three cases of partitioning, each kinetically limited by the partitioning stage given in plot labels. Taken from Mai *et al.* (2015). As shown in the legend, curves are results at three fractions of the equilibrium time (which is defined in Mai *et al.* (2015)).

Measurement of $\alpha_{s,i}$ faces several complications, depending on the system. When attempting to infer $\alpha_{s,i}$ from measurements, at least five factors must be considered: $\alpha_{s,i}$, γ_i , p_i^0 , $D_{g,i}$ and $D_{p,i}$ as shown in eqs. 4-6 (the effect of diffusion is discussed in sect. 1.9). Although several measurement techniques are available, the key variable measured is either the change in gas-phase concentration of the component of interest, or the size or mass change of the absorbing part (Davidovits *et al.*, 2006; Krieger *et al.*, 2012). This allows estimation of the uptake coefficient, which is the ratio of number of vapour phase molecules partitioning to the condensed phase to the number of vapour phase molecules colliding with the particle surface (Kolb *et al.*, 2010).

Since measurement of only one variable (e.g. gas phase concentration) is obtained, $\alpha_{s,i}$ must be the only unknown for its value to be constrained. However, as discussed, there are major uncertainties around the estimation and measurement of both γ and p_i^0 , leading to uncertainty around $\alpha_{s,i}$ estimates (Miles *et al.*, 2012). Further complexity is introduced by chemical reaction, since uncertainty around rate of reaction propagates into $\alpha_{s,i}$ estimates (Shiraiwa *et al.*, 2013).

Any liquid-liquid phase separation in measurement systems must also be well defined, because $\alpha_{s,i}$ is determined by phases at the particle surface only. Thus phase separation models such as Topping *et al.* (2013) can be useful for experiment design and, if phase separation is expected, for inference of $\alpha_{s,i}$. Alternatively, the experiment may be coupled with magnified images of particles to determine morphology as long as any phase separa-

tion is known to be distinguishable by the chosen wavelength of radiation (Krieger *et al.* , 2012; Julin *et al.* , 2014).

Measurement methods for $\alpha_{b,i}$ are discussed in Davis (2006) and Davidovits *et al.* (2006). Attempts to measure pure samples of organic compounds include the expansion chamber method, which infers $\alpha_{b,i}$ from size measurements (Julin *et al.* , 2014). An alternative technique is the integrated volume-tandem differential mobility analysis method, which is also based on size change (Saleh *et al.* , 2009). Neither approach, however, allows for direct decoupling of diffusion from accommodation, therefore this must be estimated or measured separately, or experiments done under conditions when accommodation is known to be limiting (Mai *et al.* , 2015). Results from Saleh *et al.* (2009) show $\alpha_{b,i}$ well below unity for pure dicarboxylic acids: 0.07, 0.08 and 0.24 of succinic, adipic and pimelic acids respectively, however, no attempt was made to determine the relative contributions of particle-phase diffusion and $\alpha_{s,i}$ on these values. In contrast, Julin *et al.* (2014) estimated $\alpha_{b,i}$ values of 1.0 using molecular dynamic simulations for adipic acid, succinic acid, naphthalene and nonane. Expansion chamber results for nonane corroborated this finding. The discrepancy between the measured $\alpha_{b,i}$ in Saleh *et al.* (2009) and molecular dynamic estimates in Julin *et al.* (2014) continues the discrepancies observed between earlier measurements and model estimates, discussed in Davidovits *et al.* (2006) and Davis (2006). Julin *et al.* (2014) say, however, that the model run time is too short for particle phase-diffusion to occur, thus their estimates are effectively for surface, not bulk, accommodation coefficients. If particle-phase diffusion limits movement of partitioning molecules into the particle bulk this would decrease the measured $\alpha_{b,i}$ compared to the estimates of molecular dynamics. Another possible cause for the disagreement is inaccurate input to the simulations. For example, models were found to be very sensitive to the input interaction potentials that are used to quantify intermolecular bond strength and the accuracy of these potentials has been questioned (Davidovits *et al.* , 2006).

Recent progress in measurement of particle-phase diffusion coefficients (discussed in sect. 1.9) should allow deconvolution of diffusion and accommodation contributions to $\alpha_{s,i}$ measurements. In turn, this will enable accommodation models to be validated and improved. While in principal the molecular dynamics model allows for the most rigorous simulation of surface processes, alternative (potentially less computationally expensive) models have been proposed, such as the collision model of Clement *et al.* (1996) and the critical cluster model (Davidovits *et al.* , 2006; Kolb *et al.* , 2010). The need for accurate $\alpha_{s,i}$ estimates for organic systems, is considered a top priority in gas-particle partitioning by Kolb *et al.* (2010), Topping *et al.* (2013), and Bilde *et al.* (2015).

The timescale of partitioning equilibrium determined by interfacial transport is given by (Mai *et al.* , 2015):

$$\tau_{i,eq} = \frac{4R_p^2\rho_p}{3\alpha\bar{v}C_i^*}, \quad (13)$$

where R_p is particle radius, ρ_p is particle density and C^* is the effective saturation ratio (sect. 1.5). \bar{v} is the mean molecular speed of the partitioning component i in the gas-phase, given by (Serway & Vuille, 2014, pp. 352):

$$\bar{v} = \left(\frac{3Tk_B}{m} \right)^{1/2}, \quad (14)$$

where T is temperature (K), k_B is the Boltzmann constant ($1.381 \times 10^{-23} \text{ kg m}^2 \text{ s}^{-2} \text{ K}^{-1}$) and m is mass of the molecule (kg). With $m = 1.96 \times 10^{-25} \text{ kg/molecule}$ (that of succinic acid), the mean molecular speed is $2.51 \times 10^2 \text{ m s}^{-1}$ at 298.15 K. Assuming a molecular weight of 200.0 g mol^{-1} (typical of SVOC (Barley *et al.*, 2011)), activity coefficient of 1.0 and temperature of 298.15 K, C^* was found using eq. 9 across a range of vapour pressures expected for semi-volatile organic compounds (fig. 6). With this \bar{v} and C^* input to eq. 13, along with $\rho_p = 1.4 \times 10^{12} \mu\text{g m}^{-3}$ (typical for SVOC (Topping *et al.*, 2011)), the equilibrium time for interfacial transport for a range of atmospherically relevant vapour pressures (Valorso *et al.*, 2011) and particle radii (Seinfeld & Pandis, 2006) were found, and are shown in fig. 13. Fig. 13 demonstrates equilibrium times for $\alpha = 1$ in plot a) and $= 1 \times 10^{-2}$ in plot b) (as expected from eq. 13, the timescale is linearly proportional to α).

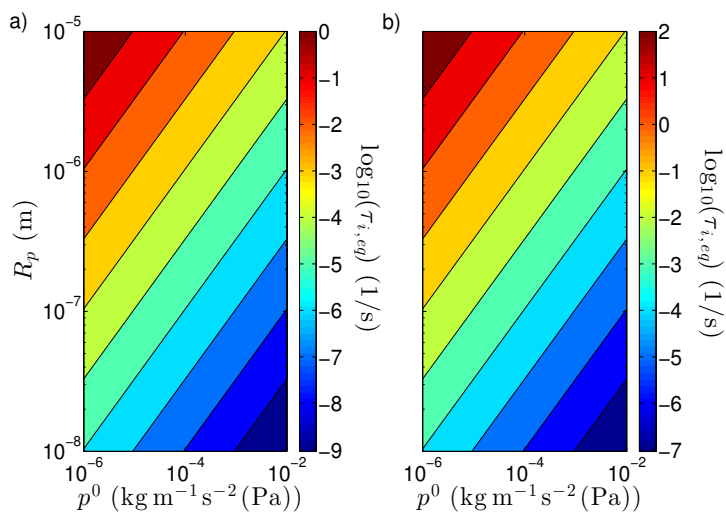


Figure 13: Estimated interfacial transport equilibration times (using eq. 13) as a function of partitioning component volatility and absorbing particle radius, for a) $\alpha = 1$ and b) $\alpha = 1 \times 10^{-2}$. Both variables are plotted on logarithmic scales.

An α value of 1×10^{-2} represents a conservative estimate based on the measurements and

model estimates discussed above. With this in mind, comparison of the typical lifetime of a particle, which is a few days to a few weeks (Jacob, 1999), to the equilibration times in fig. 13 indicate that interfacial transport is unlikely to prevent partitioning equilibration over the atmospheric lifetime of a particle. It may, however, limit chemical reaction, for example, if a component is reacting inside a particle at a rate greater than the interfacial transport equilibration time. In the next section, the equilibrium kinetics imposed by gas- and particle-phase diffusion are discussed, allowing a comparison with the limitations imposed by interfacial transport.

1.9 Diffusion

1.9.1 Introduction

The ability of a molecule to move through a medium due to its Brownian motion and that of nearby molecules is its diffusivity. It can be expressed as a diffusion coefficient, which is the mean-square distance moved over time. Brownian motion may be viewed as the method by which a system attains maximum entropy with regards to molecular spatial distribution within a given phase state, and therefore attains equilibrium. For an ideal system, equilibrium is reached when the molecules of all components are uniformly distributed.

Diffusion occurs in systems at disequilibrium, it is the net movement of molecules down a chemical potential gradient due to their Brownian motion. Looking along this gradient, the likelihood of a molecule diffusing to a given point is proportional to the concentration gradient: the relationship is an error function, resulting in an asymptotic approach to equilibrium. The basis of diffusion equations is therefore the concentration gradient and the diffusion coefficient. Diffusion rate may be expressed using two similar formulas, which are presented next. Both equations assume conditions are isobaric and isothermal since temperature and pressure can affect diffusion rate. The first is Fickian diffusion, which, for a steady state (where the flux is constant), can be expressed as (Crank, 1975):

$$(\mathbf{J}) = -C_t[D](\nabla x), \quad (15)$$

where \mathbf{J} is molar flux ($\text{mol m}^{-2} \text{s}^{-1}$), C_t is total concentration (mol m^{-3}), D is the diffusion coefficient ($\text{m}^2 \text{s}^{-1}$), x is mole fraction, and ∇ represents gradient with respect to distance (m). Round brackets represent a column of length $n - 1$, where n is the number of components, whereas square brackets represent a matrix. For a system of n components, a $(n - 1)^2$ matrix of D values is required (Mutoru & Firoozabadi, 2011).

The second is Maxwell-Stefan diffusion, which may be expressed as (Krishna & Wesselingh,

1997):

$$(\mathbf{J}) = -C_t[B]^{-1}[\Gamma](\nabla x), \quad (16)$$

where Γ is a function of the activity coefficient (sect. 1.7) (Krishna & Wesselingh, 1997) and the elements of B are given by:

$$B_{ii} = \frac{x_i}{D_{in}} + \sum_{k=1, k \neq i}^n \frac{x_k}{D_{ik}}, \quad B_{ij(i \neq j)} = -x_i \left(\frac{1}{D_{ij}} - \frac{1}{D_{in}} \right), \quad (17)$$

where i and j are row and column indices, respectively, k represents a particular component, and D is the Maxwell-Stefan diffusion coefficient. It can be seen from this equation that $[B]$ is dependent on mole fractions and binary diffusion coefficients (diffusion coefficient when i passes either itself or another component (j)). The Fickian diffusion coefficient matrix ($[D]$) in eq. 15 is similarly composed of binary diffusion coefficients.

For a non-ideal system, the deviation from ideality is implicit in the Fickian diffusion coefficient (eq. 15), but is treated separately from the Maxwell-Stefan diffusion coefficient through Γ (eqs. 16 to 17). The two coefficients have the following relationships for a binary and multicomponent system, respectively (Krishna & Wesselingh, 1997):

$$D = D\Gamma, \quad [D] = [B]^{-1}[\Gamma], \quad (18)$$

While eqs. 15 and 16 may be used for multicomponent systems, often the simpler binary system is assumed. In part this is because measurement of binary diffusion coefficients in multicomponent systems, which are needed for eqs. 15 to 16 are challenging. In addition, the binary system assumption is valid when the binary diffusion coefficients (in a multicomponent system) are equal and the system is ideal. It is also valid when one component is significantly more abundant than any other, and may therefore be considered a solvent (Krishna & Wesselingh, 1997). If these conditions are not met, then using the binary approximation for a multicomponent system implies an effective diffusion coefficient, representing an average over all components.

For a binary system with components i and j , the diffusion coefficient is the same for both components at a given mole fraction of i , and is therefore referred to as mutual. This is because molecular movements are coupled, for example, water molecules moving in the direction of decreasing water chemical potential gradient in a sucrose-water solution create spaces that may be filled by sucrose molecules, which therefore move in the opposite direction (the same direction as the decreasing sucrose chemical potential gradient) (Heitjans & Kärger, 2005, ch. 14).

The mutuality should hold even for two components with very different molecular sizes and self-diffusion coefficients at the same temperature, such as sucrose (low diffusivity) and water (high diffusivity). If sucrose is very concentrated at one end of the diffusion gradient (extreme case is solid phase state), then, despite its high self-diffusion coefficient, water is unable to diffuse down its concentration gradient as it cannot penetrate the sucrose molecular matrix. If, however, the sucrose is less concentrated (i.e. greater concentration of water, leading to a glassy or liquid phase), then, despite, the low diffusivity of sucrose, the high rate of Brownian motion in the water molecules increases the frequency at which molecular spaces became available, enabling diffusion of each component down their chemical potential gradients. The overall diffusion rate is then a result of the combined diffusivities of sucrose and water. This is not to say, however, that the molecules have the same rate of Brownian motion; the Stokes-Einstein relation (given below) indicates that for a given viscosity (which may be viewed as an average diffusion coefficient in a mixture), individual components will have diffusion coefficients dependent on their molecule size. Indeed, if there is no concentration gradient, it is possible to measure the separate diffusivities of each component (Price *et al.* , 2016; Chenyakin *et al.* , 2016). It is only when a concentration gradient is present that overall diffusion can be described by a mutual diffusion coefficient. The Stokes-Einstein relation is (Booth *et al.* , 2014):

$$D = \frac{k_B T}{6\pi\eta r_m}, \quad (19)$$

where k_B is the Boltzmann constant, η is viscosity (pressure time) and r_m is hydrodynamic radius of the diffusant.

Several methods for estimating the mutual diffusion coefficient from the self-diffusion coefficients of constituent components (the diffusion coefficient through itself) have been proposed. For an ideal binary system, the method of Vignes (1966) appears to work well:

$$D = (D_i^0)^{x_i} (D_j^0)^{x_j}, \quad (20)$$

where x is mole fraction, and D^0 is the self-diffusion coefficient. The defining feature of the Vignes relation is the linear plot of the logarithm of D against mole fraction ($x_i = 1 - x_j$).

Fig. 14 demonstrates several features of the above discussion on diffusion using the methanol-*n* hexane system. In fig. 14a) is the empirically-derived activity coefficient relationship with mole fraction of methanol, showing the system is non-ideal, while in b) is the predicted diffusion coefficient using eq. 20, the empirically-derived D , and \bar{D} calculated by eq. 18. Fig. 14 demonstrates how D implicitly accounts for non-ideality, and therefore

contrasts greatly with \bar{D} , which has a mole fraction dependence similar to D for an ideal system.

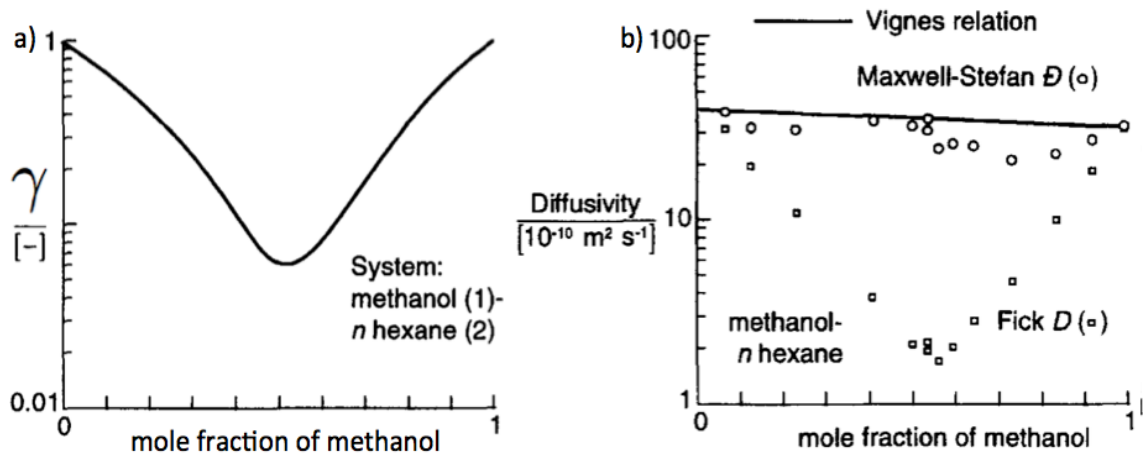


Figure 14: a) empirical activity coefficients for the methanol- n hexane system, and b) the predicted diffusion coefficient using eq.20, the empirical D and \bar{D} calculated using eq. 18. Adapted from Krishna & Wesselingh (1997), with data from Clark & Rowley (1986).

The deviation from non-ideality can be sufficiently great for diffusion to occur against the concentration gradient, a process known as uphill diffusion. While for most diffusion processes, if equation inputs are known correctly the Fickian and Maxwell-Stefan approaches are in agreement, it has been proposed that Fickian diffusion is unable to accurately model some scenarios of uphill diffusion (Krishna & Wesselingh, 1997). It has also been shown, however, that uphill diffusion is not incompatible with Fickian diffusion, as negative Fickian diffusion coefficients are valid (Mutoru & Firoozabadi, 2011).

1.9.2 Relevance to Atmosphere

As for the accommodation coefficient, diffusion in either the gas- or particle-phase may impose a kinetic limitation on partitioning equilibration (fig. 5, fig. 12, eq. 4). Furthermore, as discussed in sect. 1.5, diffusion through the particle-phase determines whether partitioning is absorptive or adsorptive, and therefore, the total partitioning possible. Consequently, estimates of diffusivity in both phases are required for estimating equilibration time.

Diffusion in the gas-phase is a key component of the partitioning equation (eq. 4). The timescale for partitioning equilibration between the gas-phase and a particle surface is (Mai *et al.* , 2015):

$$\tau_{g,eq} = \frac{R_p^2 \rho_p}{3D_g C_i^*}, \quad (21)$$

where D_g is the gas-phase diffusion coefficient, ρ_p is the density of the particle, and C_i^* is given in eq. 9. This equation shows that gas-phase diffusion has a square dependence on particle size, an inverse dependence on the gas-phase diffusion coefficient and an inverse dependence on the vapour pressure of component i (through C_i^*). Assuming ideality, D_g is given by (Poling *et al.* , 2004, pp. 9.3):

$$D_g = \frac{\bar{v}\lambda}{3}, \quad (22)$$

where \bar{v} is the mean molecular speed in the gas-phase, estimated using eq. 14. λ is the mean free path of the molecule estimated by (Chapman *et al.* , 1970, pp. 88):

$$\lambda = \frac{0.707}{\pi n \sigma^2}, \quad (23)$$

where n is number density of molecules, and σ is the molecular diameter (m).

Therefore, taking the example of succinic acid, for a $T = 298.15$ K, $P = 1013.25$ kgm⁻¹s⁻² and $R = 8.31$ kgm²s⁻²mol⁻¹K⁻¹, n has a value of 2.47×10^{23} m⁻³. With a σ value of 9.75×10^{-10} m, the estimated λ is 9.62×10^{-7} m. With $m = 1.96 \times 10^{-25}$ kg/molecule, the mean molecular speed is then 2.51×10^2 ms⁻¹, and D_g is 8.05×10^{-5} m²s⁻¹. Assuming a molecular weight of 200.0 g/mol (typical of SVOC (Barley *et al.* , 2011)), activity coefficient of 1.0 and temperature of 298.15 K, C^* was found using eq. 9 across a range of vapour pressures expected for semi-volatile organic compounds fig. 6. Then, assuming a density of 1.4×10^{12} μ g m⁻³ (typical of SVOC (Topping *et al.* , 2011)), and the diffusion coefficient found above for succinic acid, the gas-phase diffusion equilibrium time was found for a range of particle radii relevant to the atmosphere. Results are shown in fig. 15 and indicate that gas-phase diffusion equilibration can vary by 9 orders of magnitude, with relatively high volatility components in the vicinity of relatively small particles diffusing quickest.

Most tropospheric particulates have lifetimes between a few days and a few weeks (Jacob, 1999), therefore, fig. 15 indicates that for relatively large particles and relatively low volatility compounds, equilibrium will not be attained due to gas-phase diffusion limitation. All else being equal, fig. 15 shows that smaller particles will grow in preference to larger particles, thus gas-phase diffusion is a key determinant in number size distribution dynamics. It should be noted that with decreasing particle size, the Kelvin or curvature effect becomes increasingly important and acts to increase the effective vapour pressure of components (eq. 1). To determine the rate of equilibration of a given component with the Kelvin effect accounted for we therefore have to consider increasing values of the x-axis in fig. 15 as particle size decreases. It can be seen that the Kelvin effect acts to increase the rate of equilibration and therefore increase the difference in equilibration rates between

small and large particles for a given component.

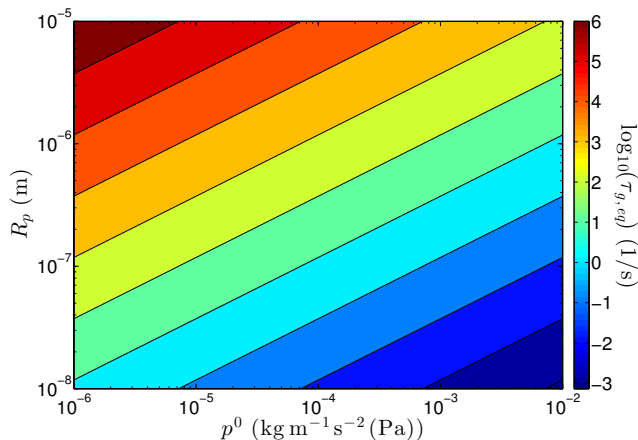


Figure 15: Estimated gas-phase diffusion equilibration times as a function of partitioning component volatility and absorbing particle radius. Both variables are plotted on logarithmic scales.

The particulate loading, gas temperature and pressure, and molecular diameter can also affect gas-phase diffusion, but are unlikely to vary by as many orders of magnitude as the partitioning component vapour pressure and particle radius. An important distinction with particle-phase diffusion is the variation in composition of diffusing medium: whereas the particle composition is expected to vary substantially in space and time, because $> 99.0\%$ mole fraction of air consists of N_2 , O_2 and Ar, its' composition is effectively constant.

For the particle-phase, the distinction between partitioning onto solid particles with negligible diffusivity and onto liquid particles with assumed instantaneous diffusion has long been recognised, and called adsorptive and absorptive partitioning, respectively (Pankow, 1987, 1994; Donahue *et al.*, 2006; Zuend *et al.*, 2010) (sect. 1.5). However, there had until recently been very limited investigation into partitioning with particles that had an intermediate diffusivity, and therefore potentially pose a kinetic limitation to absorptive partitioning.

Thermodynamic calculations and measurements by Marcolli *et al.* (2004b) indicated that even at relatively low relative humidities, mixtures of several organic components and inorganic salts are expected to form an amorphous solid or liquid phase at atmospheric temperatures. This was despite most of the compounds having pure component melting temperatures above room temperature. In part this was due to the depression of the melting temperature through mixing, but in addition, mixing of components was found to depress the deliquescence points, increasing the likelihood that water would be incorporated to the particle and be able to exert a plasticising effect. Roth *et al.* (2005) were among the first to report partitioning observations indicating particle-phase diffusion

limitation in samples from the ambient atmosphere. Using differential scanning calorimetry (sect. 1.2) on aqueous solutions of organic compounds Zobrist *et al.* (2008) found that their glass transition temperatures were above temperatures observed in the upper troposphere, indicating either a glass or solid phase.

Field and laboratory experiments have since presented strong evidence for the presence of particles with diffusivities sufficiently low to impede partitioning (Virtanen *et al.*, 2010; Vaden *et al.*, 2011; Saukko *et al.*, 2012; Pajunoja *et al.*, 2014; Järvinen *et al.*, 2016). For example, in Järvinen *et al.* (2016), α -pinene and ozone were emitted into a reaction chamber to undergo ozonolysis. Some of the reactants condensed and either formed new particles or partitioned to existing ones. If the particles were highly viscous, they were observed to coagulate and form non-spherical or structurally inhomogeneous bodies. In contrast, low viscosity particles are expected to form the thermodynamically favourable shape of a sphere. Deviations from the equilibrium shape were found to be proportional to the extent of depolarisation of backscattered light, allowing inference of viscosity from depolarisation. They found that at -10 and -34 °C, the particles were in a highly viscous state up to a relative humidity of around 35 and 75 %, respectively, above which they equilibrated and formed homogeneous spheres. Results for -10 °C are shown in fig. 16. Viscosities are generally easier to measure/infer than diffusion coefficients and have therefore been traditionally more popular, particularly for multicomponent mixtures. Viscosity and diffusion are proportional (as suggested by the Stokes-Einstein equation (eq. 19)), though their proportionality coefficient may change near the glass transition temperature (Power *et al.*, 2013; Booth *et al.*, 2014; Price *et al.*, 2016).

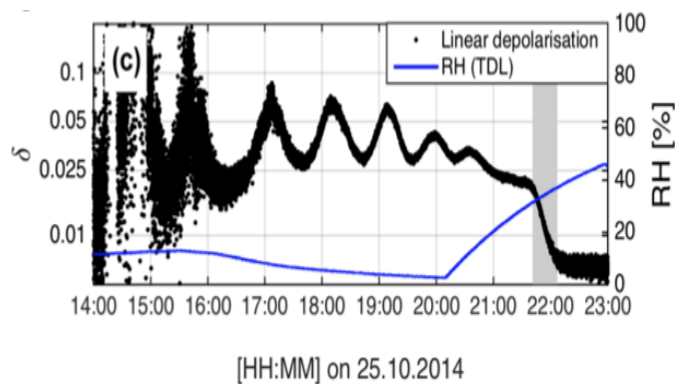


Figure 16: The temporal change of relative humidity and depolarisation of light backscattered from SOA particles (δ) inside the reaction chamber of the Järvinen *et al.* (2016) experiment described in the text. The grey region indicates the transition from low to high viscosity particles when the temperature was constant at -10 °C. The depolarisation values before 22:00 indicate non-spherical (and therefore relatively highly viscous) particles, whereas after the grey region values indicate (through calibration) spherical (and therefore less viscous) particles. Taken from Järvinen *et al.* (2016).

The equilibrium time for particle-phase diffusion as a function of the particle-phase Fickian

diffusion coefficient (D_p) and particle radius is given by (Shiraiwa *et al.* , 2011; Mai *et al.* , 2015):

$$\tau_{p,eq} = \frac{R_p^2}{\pi^2 D_p}, \quad (24)$$

Note that eq. 24 assumes that either D_p is constant, or it represents an average over the diffusion process that produces the same equilibration time as a composition dependent D_p . Using eq. 24 , equilibrium time may be plotted as a function of D_p and particle diameter, as in fig. 17. Also shown in fig. 17 are the viscosities related to the shown diffusivities through the Stokes-Einstein equation (Koop *et al.* , 2011) (assuming a molecular radius of 1 nm), the typical viscosity ranges of different phases and the viscosities of well known materials at room temperature. The blue bar shows the observed temperature dependence of diffusion coefficient of water through a glassy matrix, indicating the potential plasticising effect, particularly at higher temperatures. The grey region indicates where the Stokes-Einstein relation is not valid (near the glass transition temperature).

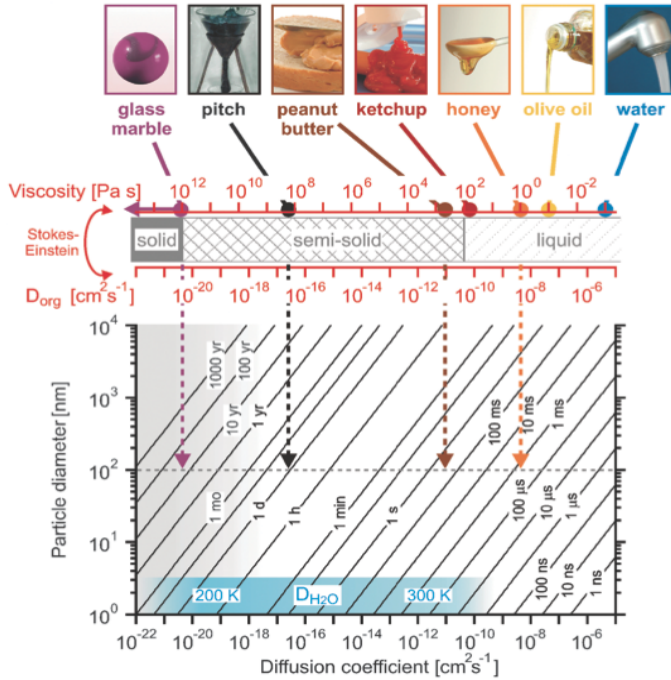


Figure 17: In the main contour plot are equilibrium times estimated using eq. 24. The blue region indicates observed water diffusion coefficients through glassy matrices, and the grey region indicates where the Stokes-Einstein relation may breakdown. The top bar shows how diffusion coefficients and viscosities are related through the Stokes-Einstein relation assuming a molecular diameter of 1 nm, and the phase states and familiar materials (at room temperature) associated with these viscosities. Taken from Koop *et al.* (2011).

Comparison of eqs. 13, 21 and 24 show that the stage of partitioning (gas-phase diffusion, interfacial transport or particle-phase transport) that limits partitioning rate is dependent

on several variables. The most important variables are vapour pressure, particle radius, accommodation coefficient and diffusion coefficients in either phase. While Mai *et al.* (2015) present results delimiting the variable ranges when each stage is limiting, this is for a simplified scenario without the complications of chemical reaction, varying concentrations of components due to emission, partitioning and deposition, and particle population changes such as emission, nucleation, deposition and coagulation. Since all these processes can affect partitioning rates, it seems that only a comprehensive mechanistic model of aerosol is capable of identifying the relative importance of each partitioning stage (i.e., which is rate limiting at a given space and time). If, for example, relative humidity and component water solubilities are sufficiently high across spatial and temporal ranges, it is conceivable that the particle-phase diffusion rate is constantly toward the right side of fig. 17, and therefore can be assumed to be instantaneous.

In order to produce a mechanistic partitioning model, reliable solutions to all three partitioning stages are required. While gas-phase diffusion and interfacial transport are already incorporated into the partitioning equation (eq. 4), particle-phase diffusion has not been. The next subsection therefore discusses methods to solve particle-phase diffusion. Furthermore, whilst an accepted method to estimate the gas-phase diffusion coefficient has been discussed above, methods to estimate and measure the particle-phase diffusion coefficient will also be discussed in the following subsection.

1.9.3 Methods to solve, estimate and measure particle-phase diffusion

Measurements of particle-phase binary diffusion coefficients are rarely conducted on systems with more than three components because it becomes difficult to identify the diffusion coefficient of component i with respect to each component (Mutoru & Firoozabadi, 2011). In non-ideal systems, the accurate deconvolution of activity coefficients and Maxwell-Stefan diffusion coefficients introduces a further challenge. Consequently, most measurements are in binary systems and are of the Fickian diffusion coefficient (eq. 15).

Direct diffusion measurements (not based on viscosity measurements) have been made using a variety of techniques, of which a sample are presented here. D has been inferred from measured size change of droplets (the mass transfer method) in Zobrist *et al.* (2011) for aqueous sucrose, in Lienhard *et al.* (2014) for aqueous citric acid, in Steimer *et al.* (2015) for aqueous shikimic acid and in Lienhard *et al.* (2015) for α -pinene derived SOA. Isothermal desorption (measurement of evaporation rate) was used to infer the self-diffusion coefficient of *o*-terphenyl by Mapes *et al.* (2006) and α -pinene ozonolysis derived SOA (Abramson *et al.* , 2013). The fluorescence recovery after photobleaching (FRAP) technique was used by Corti *et al.* (2008) for aqueous trehalose, Deschout *et al.* (2010) for a biopolymer mixture and Chenyakin *et al.* (2016) for aqueous sucrose. A Raman

isotope tracer method was used on several aqueous organics by Price *et al.* (2014) and Davies & Wilson (2016), on α -pinene derived SOA by Price *et al.* (2015) and on aqueous sucrose by Price *et al.* (2016).

For investigations that measure diffusion of water through a mixture of organics, such as SOA the organic mix is considered as one single component and the water another, allowing a single binary diffusion coefficient to be measured rather than attempting to infer the diffusion of water past each SOA constituent. While simplifying the calculation of diffusion coefficients, the resulting diffusion coefficient dependence on water mole fraction and temperature may not be sufficiently general for application to a model that considers large variations in particle compositions, as discussed below.

Food and chemical engineering research has studied particle-phase diffusion for a longer time than atmospheric science, and may provide valuable ideas for diffusion investigation. For example, Nowakowski *et al.* (2015) use Fourier Transform Near-Infrared hyperspectral imaging to measure diffusion of water through organics and the concentration gradient with distance, which should allow a comprehensive comparison against a model. An image of water mole fraction with distance through a syrup/sucrose mixture taken from Nowakowski *et al.* (2015) is shown in fig. 18. It shows the water to have a relatively high mole fraction from the water-exposed edge of the sample (left side) to a diffusion “front” about midway through the sample. The “front” consists of a peak in water mole fraction followed (to the right) by a steep decrease in mole fraction. To the right is a region of lower water mole fraction (representative of the initial sample state). For the most part this mole fraction profile is consistent with a Fickian diffusion model where the diffusion coefficient is dependent on mole fraction (increasing with increasing water mole fraction) (Zobrist *et al.* , 2011). However, the peak in water mole fraction at the “front” is not predicted by such a model. Nowakowski *et al.* (2015) propose this could be related to the low diffusion barrier (akin to a liquid wave breaking against a solid barrier) or to crystallisation of sucrose once water mole fraction increases (though not sufficiently to dissolve all sucrose).

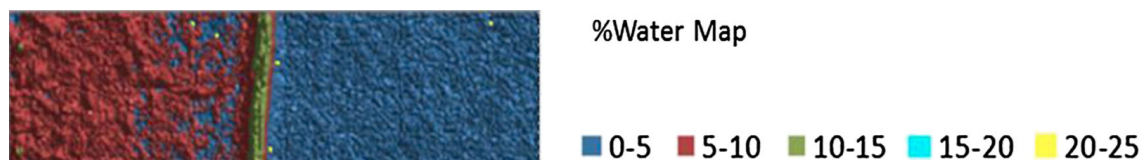


Figure 18: Example water concentration distribution with distance along a sample with initially low water mole fraction (e.g. right side of sample), exposed to a higher water mole fraction on the left edge of the sample. Mole fractions are colour coded according to the legend. The total length of sample is 3mm, and distance is represented linearly. Taken from Nowakowski *et al.* (2015).

The monosaccharide sucrose has been a comparatively popular choice of organic compo-

ment for diffusion coefficient measurement. It has several properties that make it advantageous. First, it has an oxygen-to-carbon elemental ratio (O:C) of 0.92, which is in the range reported for atmospheric SOA (approximately 0.2-1.0) (Aiken *et al.*, 2008; DeCarlo *et al.*, 2008; Heald *et al.*, 2010; Ng *et al.*, 2010), second, it has published measurements of viscosities over a wide range of water activities (Chenlo *et al.*, 2002; Quintas *et al.*, 2006; Telis *et al.*, 2007; Migliori *et al.*, 2007; Power *et al.*, 2013), and finally, it has measured viscosities within the range expected for SOA at room temperature (Booth *et al.*, 2014; Song *et al.*, 2015, 2016; Grayson *et al.*, 2016).

Measurements of diffusion coefficient on the same mixture (e.g. aqueous sucrose) at the same temperature (or range of temperatures) by different measurements is required to ensure consistency between measurement methods. Davies & Wilson (2016) provide their own measurements, but also compare with others. They find good agreement between their observations of water diffusion through aqueous sucrose solutions using raman spectroscopy of a levitated particle and those of Price *et al.* (2014) using raman spectroscopy on a sample in a cover slide. However, they find disagreement with the result of Zobrist *et al.* (2011) that used the mass transfer method. Marshall *et al.* (2016) suggest this discrepancy could arise from uncertainty in the water activity coefficient (γ_w), which is required for conversions of concentration (or mole (x_w) or mass fractions) with water activity (a_w):

$$a_w = \gamma_w x_w, \quad (25)$$

The raman spectroscopy method is based on diffusion of isotopes through a matrix of constant and homogenous composition (with the exception of an isotope concentration gradient). Whereas the mass transfer method involves changing of the boundary concentration (through changed gas-phase composition) to create a component concentration gradient. The resulting diffusion coefficient from the mass transfer method is the binary diffusion coefficient of the solution, whereas D from the isotope measurement method is the single component diffusion coefficient (whichever component has the isotopic tracer). All else being equal (e.g. temperature, water activity), the two should agree if diffusion of water dominates over that of sucrose, as it seems to (Price *et al.*, 2014, 2016). If the disagreement is not due to uncertainty in the activity coefficient, it may be because of a process resulting from the concentration gradient in the mass transfer method that does not occur in the constant concentration approach and is not modelled (D in the mass transfer method is inferred from measurements using a diffusion model). Such a feature may be the effect of sucrose crystallisation as water concentration decreases (Nowakowski *et al.*, 2015).

What is the objective of diffusion measurements relevant to atmospheric particles? Mea-

measurements on complex mixtures of components representing SOA, such as in Abramson *et al.* (2013), Price *et al.* (2015) and Lienhard *et al.* (2015) are certainly useful for indicating the conditions under which particle-phase diffusion may limit partitioning and therefore number size distribution changes and chemical reaction. However, as with the VBS approach to component volatility, they do not provide useful input to a mechanistic determination of the diffusion coefficient, e.g. through a multicomponent Fickian or Maxwell-Stefan diffusion equation. A mechanistic approach may be desirable because of variations in relative humidity, temperature and gas-phase composition, which, in addition to time available for chemical reaction and particle history, determines the particle-phase composition (e.g. Vaden *et al.* (2011), Pfrang *et al.* (2011), Abramson *et al.* (2013) and Hosny *et al.* (2016) observe diffusion and viscosity dependencies on particle age).

While it seems that studies measuring diffusion in VOC derived SOA have proven particle-phase diffusion limitation to partitioning under certain conditions (Virtanen *et al.* , 2010; Vaden *et al.* , 2011; Saukko *et al.* , 2012; Abramson *et al.* , 2013; Booth *et al.* , 2014; Pajunoja *et al.* , 2014; Price *et al.* , 2015; Song *et al.* , 2015, 2016; Grayson *et al.* , 2016; Järvinen *et al.* , 2016), an objective must be to define the range of values expected due to particle composition variation in the atmosphere. If the results of these studies indicate good agreement of diffusion coefficient dependence on water activity and temperature across particle compositions, or a strong correlation with, for example, oligomer concentration, or inorganic component concentration, then a mechanistic approach to diffusion modelling may be overcomplicated, and a simpler model should be formed. A diagram illustrating the mechanistic and simple approach to particle-phase diffusion modelling is given in fig. 19.

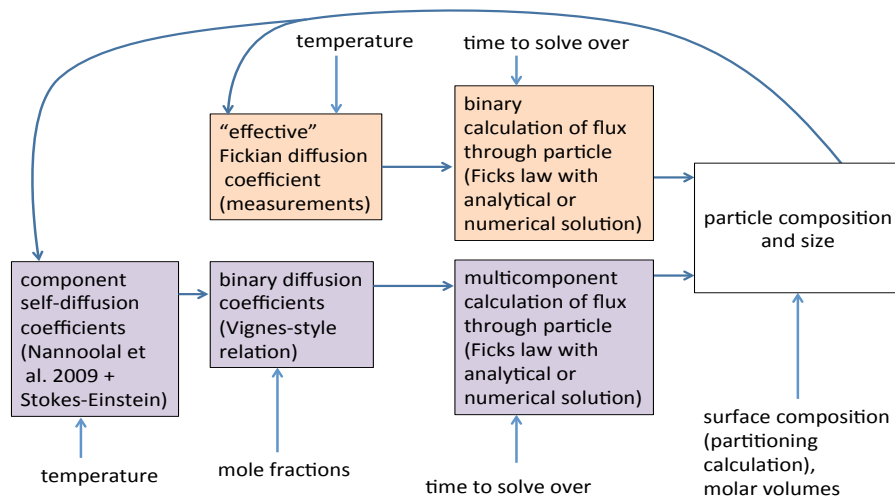


Figure 19: The steps required for modelling single particle composition and size change due to particle-phase diffusion, with arrows showing the sequence of steps, which are in black boxes. Calculation inputs are linked to the step by a blue arrow. In brackets are example methods to complete the step (the partitioning calculation refers to eq. 4). The orange and purple boxes show the simple and mechanistic approaches to diffusion coefficient estimation, respectively.

If a mechanistic model were to be used a diffusion coefficient estimation method would likely be required for the first calculation step (fig. 19) since diffusion measurements of all expected components in particulates is currently impractical. For the second step a vignes-type relation for binary diffusion coefficients and mole fractions has been found to fit measured diffusion coefficients reasonably well for binary systems (eq. 20) (Vignes, 1966; Lienhard *et al.*, 2014; Davies & Wilson, 2016). Furthermore, measurements of diffusion coefficient dependence on both temperature and water activity have found the Vogel-Fulcher-Tamman equation to agree with observations on binary systems (Debenedetti & Stillinger, 2001; Zobrist *et al.*, 2011; Matthiesen *et al.*, 2011).

In order to apply the Vignes relation, self-diffusion coefficients of components are required and may not have been measured (fig. 19). Several methods to estimate these, including the Stokes-Einstein relation are presented in Taylor & Krishna (1993, ch. 4) and Abbasi & Eslamloueyan (2014). The majority of these require pure-component viscosities, which also require estimation. A range of pure component viscosity estimation methods are described in Nannoolal *et al.* (2009).

If self-diffusion coefficients could be accurately estimated, and the Vignes equation accurately applied, in theory, the multicomponent diffusion calculation could be made using either eq. 15 or 16 (Taylor & Krishna, 1993) (fig. 19). This has not yet been attempted on a multicomponent system of atmospheric relevance, for example, for an α -pinene de-

rived SOA sample (in part because the composition is uncertain). The resource required to design, make and test a mechanistic approach to particle-phase diffusion is potentially substantial (i.e. an approach where binary diffusion coefficients for all components are first estimated). Its necessity is currently uncertain. First, measurements studies are required that define the range of diffusion rates in atmospherically relevant particles. These should provide input to models that test the sensitivity of particle properties, such as number size distribution, to particle-phase diffusion. Such models may initially use an “effective” Fickian diffusion coefficient that depends on composition and temperature and solves diffusion assuming a binary system (fig. 19). The models should provide an indication of property sensitivity to diffusion rate, indicating the accuracy of diffusion coefficient required to estimate particle properties to a satisfactory accuracy.

The second and third paper presented in this thesis investigate methods to solve Fickian diffusion when the diffusion coefficient is dependent on composition (fig. 19). Here a brief overview of the available methods is given, while a more detailed analysis is provided in the papers.

Strictly speaking eq. 15 is valid for a steady state system where the flux is constant. This is rarely the case in atmospheric particles equilibrating with a (potentially variable) gas-phase concentration of partitioning component. For an unsteady state, with diffusion coefficient dependent on composition, Fick’s second law is applicable (Crank, 1975, ch. 7):

$$\frac{\partial C}{\partial t} = \nabla(D\nabla C), \quad (26)$$

which is a partial differential equation without a general analytical solution. Three numerical methods have been used to solve unsteady state composition dependent diffusion for a particle. An initial-boundary problem approach to eq. 26 (Smith *et al.* , 2002, 2003), a Runge-Kutta (finite-difference) numerical solution to eq. 15 (Shiraiwa *et al.* , 2012) and a Euler forward step method (Zobrist *et al.* , 2011). These have been used for the inference of D from mass transfer diffusion coefficient experiments, such as in Zobrist *et al.* (2011); Lienhard *et al.* (2014); Steimer *et al.* (2015); Lienhard *et al.* (2015) and for simulations of diffusion, for example with regard to atmospheric ice formation (Berkemeier *et al.* , 2014; Lienhard *et al.* , 2015; Price *et al.* , 2015) and gas-uptake and chemical ageing (Smith *et al.* , 2003; Shiraiwa *et al.* , 2011; Hosny *et al.* , 2016).

The three approaches treat the particle as spherical and formed of concentric shells, each with assumed uniform concentration. The shell representation allows radial heterogeneity of concentration and diffusion coefficient to be explicitly represented. The second paper in this thesis investigates whether, despite their different approaches to solving Fickian diffusion, these methods do give consistent estimates of diffusion rate, all else being

equal.

Analytical solutions to diffusion assuming a constant diffusion coefficient have also been presented in Zaveri *et al.* (2014) and Liu *et al.* (2014). Zaveri *et al.* (2014) show that the analytical solution can give good reproduction of numerical solution estimates. In their model comparison the following conditions were set: a constant diffusion coefficient of $1 \times 10^{-19} \text{ m}^2 \text{ s}^{-1}$ (representative of an amorphous solid (fig. 17)), an initial gas-phase concentration of partitioning component (i) of zero, a constant emission rate of i of $0.1 \mu\text{g m}^{-3} \text{ h}^{-1}$, an initial particle diameter of $0.2 \mu\text{m}$ and particle number concentration $5 \times 10^9 \text{ m}^{-3}$. Analytical estimates were compared with numerical ones for a range of volatilities of i and its reaction rate in the particle-phase, with results given in fig. 20 and showing very good agreement.

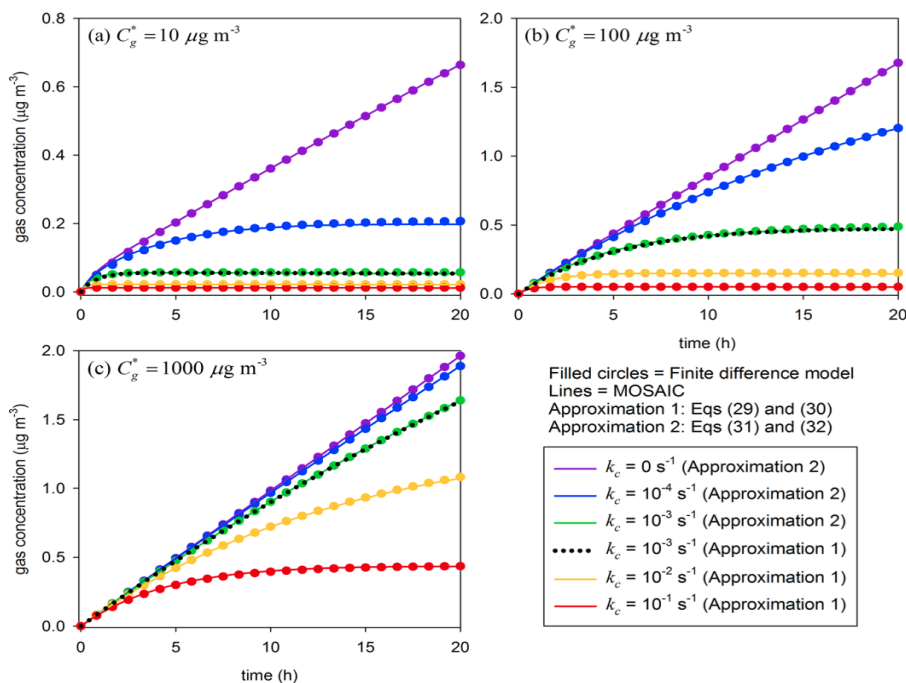


Figure 20: Comparison between the analytical solution to particle-phase diffusion (solid lines) and the finite-difference approach (circles) for the conditions: constant diffusion coefficient of $1 \times 10^{-19} \text{ m}^2 \text{ s}^{-1}$ (representative of an amorphous solid (fig. 17)), initial gas-phase concentration of partitioning component (i) of zero, constant emission rate of i of $0.1 \mu\text{g m}^{-3} \text{ h}^{-1}$, initial particle diameter of $0.2 \mu\text{m}$ and particle number concentration $5 \times 10^9 \text{ m}^{-3}$. Particle-phase reaction rates are given in the legend, and the volatility of i is given by its effective saturation concentration in each plot. Approximation 1 refers to the solution derived from the analytical solution presented in Crank (1975), while approximation 2 was derived from two-film theory (Lewis & Whiteman, 1924). Both solutions and their derivation are described in Zaveri *et al.* (2014), from which this figure was taken.

The great advantage of the analytical solution over a numerical solution is reduced demand on computer power, leading to reduced calculation times. The analytical solution presented in Zaveri *et al.* (2014) is readily incorporated into the Model for Simulating

Aerosol Interactions and Chemistry (MOSAIC). In turn, MOSAIC has been implemented in regional models in which it is combined with chemical and meteorological simulations to describe aerosol transformations (Fry & Sackinger, 2012; Baklanov *et al.*, 2014). However, it is clear from the diffusion studies discussed above that a chemical-composition diffusion coefficient is required to accurately simulate particle-phase diffusion (e.g. Lienhard *et al.*, 2015). The third paper of this thesis therefore investigates a correction to the analytical solution of Zaveri *et al.* (2014) that would make it applicable to composition dependent diffusion. The initial aim of a realistic and computationally efficient solution to particle-phase diffusion would be to conduct sensitivity studies of particle properties, such as number size distribution, to particle-phase diffusion (with diffusion coefficient estimates informed by measurement studies). This would enable a rigorous assessment of the accuracy to which diffusion coefficients need to be known to accurately estimate particulate effects on the radiation budget, air quality and atmospheric chemistry.

1.10 Introduction Summary

This introduction has established the basis, including motivation and previous work, for the studies presented here. It explained that particulate properties and their underlying mechanisms need to be known to evaluate particulate effects on climate and health. While measurements are invaluable means to improve models, simulations are essential for providing a general prediction tool for particulate effects. The properties determining the phase state of a pure component or mixture were discussed. This led onto partitioning between the gas- and particle-phase and its determinants. The composition of aerosol was discussed, drawing on observations from varying environments. It was shown that while the inorganic group was comparatively well understood, the much greater number of components in the organic group and their broad range of molecular properties means they are much more complicated to model.

The theory behind partitioning between the gas- and particle-phases was explained, laying the foundation for later sections that discussed properties determining partitioning, along with their measurement and estimation methods: volatility, deviations from ideality, surface accommodation and diffusion rates. The requirement for accurate estimates of volatility and particle-phase diffusion have been explained. To address the volatility issue, the first of the three papers presented here assesses vapour pressure estimation methods and their effects on estimated SOA concentration and composition. This gives an indication of how close current methods are of providing reliable volatility estimates in a mechanistic model of partitioning. The second and third papers investigate the diffusion issue. In the second, published numerical solutions to diffusion with and without dependence on composition are compared for consistency. This paper determines whether one or

all solutions can be reliably used for Fickian diffusion simulations, which are used in atmospheric models, inference of diffusion coefficients from measurements and as benchmarks for analytical solutions. Finally, the third paper investigates a correction to a previously presented analytical solution to particle-phase diffusion (Zaveri *et al.* , 2014) to make it applicable to composition dependent diffusion. Such a generally applicable analytical solution is required for realistically implementing particle-phase diffusion in regional models, from which sensitivities to diffusion can be assessed and inform further work.

The aims and objectives of the research papers are summarised in the list below:

- Identify the most accurate vapour pressure estimation method with regards to vapour pressures of atmospherically relevant components
- Identify the most accurate vapour pressure estimation method with regards to secondary organic aerosol loading and composition
- Determine the areas of vapour pressure research that require greatest attention (e.g. improvement of a particular estimation method or measurement of a particular chemical class)
- Determine whether the three numerical methods currently used to solve particle-phase diffusion in atmospheric research are consistent
- Identify the most effective measurement method to infer diffusivity dependence on particle composition
- Derive and test a correction to the analytical solution of diffusion to account for composition dependent diffusion
- Determine the applicability of such a correction to various atmospheric scenarios

2 Research Papers

In this section the research papers containing the methodology, results, discussion and conclusions carried out during the PhD will be presented. Before each paper a brief introduction will be given, while more detailed introductions are given within the papers.

2.1 Paper 1

The requirement for accurate pure component saturation vapour pressures was a recurring theme throughout the introduction. Beside accurate estimation of the partitioning coefficients of semi-volatile components, they are required for the accurate measurement

of activity coefficients, surface accommodation coefficients and some measurement methods of diffusion coefficients. While vapour pressure measurements of organic components remain restricted to a small fraction (<1 %) of the estimated number in the atmosphere, estimation methods of vapour pressure are required for mechanistic modelling of partitioning.

As discussed in sect. 1.6, estimates of semi-volatile component vapour pressure can lead to disagreement in estimated particulate concentration of up to two orders of magnitude (Barley *et al.* , 2011). It is therefore necessary to assess estimation methods against measurements to determine the most accurate with regards to vapour pressure and resulting partitioning. This has been done in several previous publications, the most recent and atmospherically relevant (in terms of components) was Barley & McFiggans (2010). However, new vapour pressure measurements of comparatively low volatility components were released after this assessment. This first paper combines these new measurements with previously published results to provide a new, more rigorous, assessment of vapour pressure estimation methods.

Paper 1

An assessment of vapour pressure estimation methods



Cite this: *Phys. Chem. Chem. Phys.*,
2014, 16, 19453

An assessment of vapour pressure estimation methods†

Simon O'Meara,* Alastair Murray Booth,* Mark Howard Barley,* David Topping* and Gordon McFiggans*

Laboratory measurements of vapour pressures for atmospherically relevant compounds were collated and used to assess the accuracy of vapour pressure estimates generated by seven estimation methods and impacts on predicted secondary organic aerosol. Of the vapour pressure estimation methods that were applicable to all the test set compounds, the Lee–Kesler [Reid *et al.*, *The Properties of Gases and Liquids*, 1987] method showed the lowest mean absolute error and the Nannoolal *et al.* [Nannoolal *et al.*, *Fluid Phase Equilib.*, 2008, **269**, 117–133] method showed the lowest mean bias error (when both used normal boiling points estimated using the Nannoolal *et al.* [Nannoolal *et al.*, *Fluid Phase Equilib.*, 2004, **226**, 45–63] method). The effect of varying vapour pressure estimation methods on secondary organic aerosol (SOA) mass loading and composition was investigated using an absorptive partitioning equilibrium model. The Myrdal and Yalkowsky [Myrdal and Yalkowsky, *Ind. Eng. Chem. Res.*, 1997, **36**, 2494–2499] vapour pressure estimation method using the Nannoolal *et al.* [Nannoolal *et al.*, *Fluid Phase Equilib.*, 2004, **226**, 45–63] normal boiling point gave the most accurate estimation of SOA loading despite not being the most accurate for vapour pressures alone.

Received 27th February 2014,
Accepted 28th July 2014

DOI: 10.1039/c4cp00857j

www.rsc.org/pccp

1 Introduction

Aerosol influences the Earth's radiative budget through the scattering and absorption of radiation.¹ Additionally it can adversely affect health^{2,3} (Pope and Dockery, 2006; Heal *et al.*, 2012), and atmospheric trace gas constitution by providing reagents for chemical reactions and providing sites for chemical reaction.⁴

Quantification of these effects is limited, in part, by our inability to predict aerosol composition^{1,5} and microphysics. This is complicated by the large number of organic compounds present in the atmosphere, whose explicit automatic generation mechanism technique estimate to be of the order 10⁶.⁶ The mass fraction of aerosol formed of organic material varies by the location, but it is frequently significant and can be dominant.^{7,8} Once emitted, volatile organic compounds (VOCs) can undergo chemical reactions, leading to products of generally lower volatility and greater propensity to condense.

Organic products with volatilities that allow fractions to exist in both the condensed (particle) and gas phase are referred to as semi-volatile organic compounds (SVOCs). In this paper SVOCs are defined as compounds able to partition

(under any condition) between 99.9% and 0.1% into the condensed phase, the remainder being in the gas phase (based on volatility considerations only).

In addition to the oxidation of VOCs, SVOCs may also enter the gas phase by the evaporation or sublimation of compounds already in the particulate phase. Examples include chemicals within particles being warmed and/or diluted.⁹ The volatility of a given SVOC, given by its saturation vapour pressure (p^0), is one thermodynamic property determining the condensable fraction. SVOCs can constitute a major fraction of total organic aerosol,⁸ therefore (p^0) values are required to accurately estimate particulate composition and mass loading when using a mechanistic approach.

Fig. 1 illustrates how the condensable fraction of a compound varies with p^0 , the particulate mass and temperature (when p^0 is the only thermodynamic property considered). The C^* metric in Fig. 1 is the effective saturation coefficient defined in ref. 9 and calculated by:

$$C_i^* = \frac{10^6 M_i p_i^0}{RT} \quad (1)$$

where M_i is the molar mass of compound i , R is the ideal gas constant ($8.2057 \times 10^{-5} \text{ m}^{-3} \text{ atm mol}^{-1} \text{ K}^{-1}$) and T is the temperature. $\log_{10}(C^*)$ is used as the abscissa in the volatility basis set (VBS) method of partitioning estimation, in which compounds are typically aggregated into unit bins.⁹ This method can be constrained using experimental data from chamber

Centre for Atmospheric Sciences, School of Earth, Atmospheric and Environmental Sciences, University of Manchester, Manchester, M13 9PL, UK.

E-mail: g.mcfiggans@manchester.ac.uk; Tel: +44 (0)1613063954

† Electronic supplementary information (ESI) available. See DOI: 10.1039/c4cp00857j

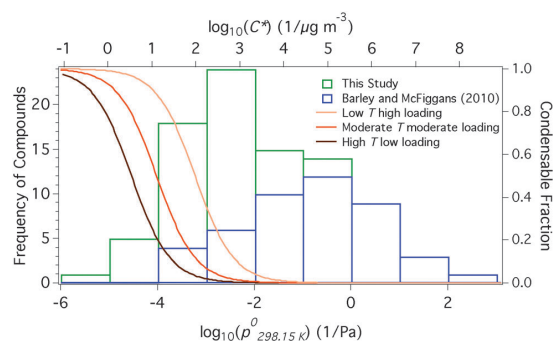


Fig. 1 Histogram (left axis) for the vapour pressure (bottom axis) of compounds in this study and those used in ref. 10. Orange curves correspond to the right axis and represent the condensable fraction change with the effective saturation coefficient (top axis), where 1 means entirely partitioned into the condensed phase. Condensable fractions were obtained for different scenarios, varying by temperature (T) and particulate loading: low temperature = 273.15 K, low loading = $3.0 \mu\text{g m}^{-3}$, moderate temperature = 293.15 K, moderate loading = $12.0 \mu\text{g m}^{-3}$ and high temperature = 313.15 K, high loading = $96 \mu\text{g m}^{-3}$.

experiments or as a technique for grouping more detailed single component representations of condensation/evaporation. It is included in Fig. 1 since it is a familiar measure, however, as discussed in Barley *et al.*¹¹ a molar based approach is more reliable. Molar based calculations are described in eqn (13) and (14) below. For Fig. 1 an average molar mass of 200 g mol^{-1} was assumed.

For estimating particulate mass loading in atmospheric scenarios, transport models may use the VBS. This semi-empirical approach, however, relies on a simplified treatment of the chemical composition of SVOCs. The alternative mechanistic approach is to predict the chemicals present through a chemical degradation model followed by estimation of their vapour pressures using a p^0 estimation method such as one of those assessed below.¹² Assessment of the sensitivity of such a mechanistic approach to estimate p^0 and other inputs is required to quantify uncertainties in particulate loading and prioritise development of model components. For instance, loadings were noted to be particularly sensitive to vapour pressure estimates in McFiggans *et al.*¹³

Laboratory measurements of saturation vapour pressure have been made using several methods.^{14,15} Due to their large number, measurement of the vapour pressure of all atmospheric organic compounds is currently impractical, necessitating p^0 estimation methods. Multiple estimation methods have been proposed, varying structurally and by their parameterisations. Seven estimation methods, chosen for their relatively high accuracy (as shown in prior assessments), are assessed here for accuracy.

The assessment of vapour pressure estimation methods by Barley and McFiggans¹⁰ compared estimates against vapour pressure measurements. The current study follows an identical approach but doubles the number of test set compounds from Barley and McFiggans¹⁰ (90 vs. 45). The average measured p^0 of test set compounds is lowered, as shown in Fig. 1 (average p^0 at 298.15 K here is 2.7 Pa compared to 5.3 Pa in the earlier study).

Fig. 1 shows that even at a comparatively high particulate loading and low temperature (conditions that act to increase the condensable fraction of a given compound), the majority of compounds used in the test set of Barley and McFiggans¹⁰ would not partition >10% into the condensed phase. In contrast, approximately half of the compounds in the new study would partition at least 20% into the condensed phase. The test set of compounds used here is therefore more representative of SVOCs than the previous assessment.

Camredon and Aumont¹⁶ and Mbienda *et al.*¹⁷ assessed vapour pressure estimation methods using larger test sets of measurements than our study, however, some of their measurements are collated from secondary sources, such as data books. Such sources can be unclear as to the primary source of the measurement values and whether an extrapolation has been applied from a different temperature, thereby introducing uncertainty. Consequently, all measurements used here are from the primary literature. Furthermore, as with the Barley and McFiggans¹⁰ study, the majority of measurements were above 10^{-1} Pa. For Camredon and Aumont¹⁶ only 18 of a total 850 measurements fall below this pressure, and there is a similar proportion in the Mbienda *et al.*¹⁷ study, therefore for testing compounds relevant to SVOC with low p^0 the current study is advantageous. Unlike these past assessments, the current study also evaluates the sensitivity of SOA loading and composition to vapour pressure estimation methods.

Both Camredon and Aumont¹⁶ and Mbienda *et al.*¹⁷ assessed the Lee–Kesler¹⁸ and Myrdal and Yalkowsky¹⁹ methods, which are also assessed here. Camredon and Aumont¹⁶ showed these two methods to have similar estimation accuracy, but Myrdal and Yalkowsky¹⁹ showed greater potential for accurate estimates at lower p^0 . Mbienda *et al.*¹⁷ reported that the accuracy for both methods tends to decrease with an increasing number of oxygenated functional groups per compound, but that this trend was stronger for Lee–Kesler.

The estimates of several estimation methods were compared against those of the EVAPORATION method in Compennolle *et al.*²⁰ The method of Nannoolal *et al.*²¹ had the strongest agreement, and since this shows comparatively high accuracy in the Barley and McFiggans¹⁰ assessment, this suggests that EVAPORATION could also produce accurate estimates. Here EVAPORATION²⁰ is assessed against measurements for the first time (to the author's knowledge).

This study reports the results of the comparison of estimated p^0 (from seven estimation methods) against measured p^0 for a test set of compounds. To assess the wider significance of these results, measured and estimated p^0 are also applied to an absorptive partitioning model. We present the SOA loading and composition sensitivity to varying p^0 estimates, and, through comparison with measured vapour pressure values, identify the estimation method predicting the most accurate SOA loading and composition.

2 Method

2.1 Test set compilation

Laboratory measurements of vapour pressure for 90 compounds were collated. Recent studies have presented evidence of

laboratory and ambient particulates taking a non-crystalline solid state,^{22,23} though the actual phase state of complex mixtures remains debatable. We use the sub-cooled liquid vapour pressure for two reasons. Estimation methods for a non-crystalline solid state are not, as far as the authors are aware, specifically presented in the literature. Consequently, the current modeling approach to highly viscous mixtures is to use the sub-cooled liquid p^o reference state and account for the influence of viscosity through diffusion limitations in the condensed phase. Therefore, the presented assessment of sub-cooled liquid p^o methods is relevant to SOA formation models. There remains substantial debate around the phase of organic components in particulates. According to thermodynamic theory²⁴ mixing of different compounds in the condensed phase depresses the melting point of each species, with the degree of depression correlated with the number of species. Given that the estimated number of atmospheric organic compounds contributing to the condensed phase might be of the order of 10^5 (ref. 6) there is theoretical support for the organic component of particles to be in a liquid-like state. Furthermore, a liquid-like state has been observed under laboratory conditions.²⁵ More work is needed to decipher the true phase state and subsequent influence on gas/particle mass transfer.

Where necessary solid state vapour pressure measurements were converted to sub-cooled liquid vapour pressures using the equation of Prausnitz *et al.*:²⁶

$$\ln(p_l^o) = \ln(p_s^o) + \frac{\Delta H_{\text{fus}}}{RT_m} \left(\frac{T_m}{T} - 1 \right) - \frac{\Delta c_{p,\text{sl}}}{R} \left(\frac{T_m}{T} - 1 \right) + \frac{\Delta c_{p,\text{sl}}}{R} \ln \left(\frac{T_m}{T} \right) \quad (2)$$

where p_l^o and p_s^o are the sub-cooled liquid and solid vapour pressures, respectively, the latter obtained at temperature T . ΔH_{fus} is enthalpy of fusion, R is the ideal gas constant ($8.314 \text{ J mol}^{-1} \text{ K}^{-1}$), T_m is the melting temperature and $\Delta c_{p,\text{sl}}$ is the heat capacity change between the solid and liquid state. If $\Delta c_{p,\text{sl}}$ measurements were not available the assumption $\Delta H_{\text{fus}}/T = \Delta S_{\text{fus}} = \Delta c_{p,\text{sl}}$ was used. Sources of ΔH_{fus} , $\Delta c_{p,\text{sl}}$ and T_m are given in Table S1 of the ESI.† Measurements were selected if they met the following criteria:

(1) Compounds were required to have at least one non-hydrocarbon functional group, since oxidation is the major mechanism by which VOCs are converted to SVOCs.^{27,28}

(2) The non-hydrocarbon functional group(s) borne by compounds had to be reported as having been observed in the atmosphere. The selected atmospherically relevant functional groups and their associated publications are listed in Table 1.

(3) Measurements had to be below 10^3 Pa , since compounds with vapour pressures above this are expected to be too volatile to contribute to the condensed phase.

(4) For measurements of solid vapour pressure, there had to be a measurement of $\Delta c_{p,\text{sl}}$ or ΔH_{fus} and T_m available in the primary literature to apply the conversion to sub-cooled p^o (eqn (2)).

The selected measurements and their associated publications are presented in Table S1 of the ESI.† To describe the test set compounds, their average carbon molecule oxidation state³⁷

Table 1 The functional groups included in the test set

Functional group	Number of compounds with group	Publication supporting ambient presence
Carboxyl	51	Pietrogrande <i>et al.</i> ²⁹
Hydroxyl	29	Decesari <i>et al.</i> ³⁰
Amine	11	Beddows <i>et al.</i> ³¹
Ketone	7	Hamilton <i>et al.</i> ³²
Aldehyde	5	Hamilton <i>et al.</i> ³²
Nitro	9	Rogge <i>et al.</i> ³³
Ester	3	Helmig <i>et al.</i> ³⁴
Ether	7	Kalberer <i>et al.</i> ³⁵
Methoxy	12	Decesari <i>et al.</i> ³⁰
Nitrate	1	Day <i>et al.</i> ³⁶

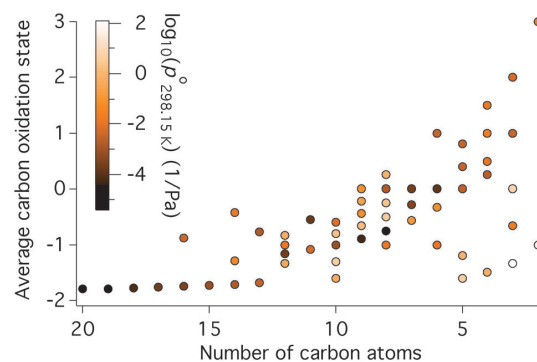


Fig. 2 The average carbon oxidation state and the carbon number for each compound in the test set. Colours represent the sub-cooled liquid vapour pressure at 298.15 K, as described on the colour scale.

and the number of carbon atoms per compound are presented in Fig. 2. Also in this figure are the sub-cooled liquid vapour pressures at 298.15 K (extrapolated where necessary). Lower volatility compounds are expected toward the top left corner of the Fig. 2 plot, *i.e.*, a high oxidation state and a high carbon number. Although existent compounds do fit this space,³⁷ their vapour pressures have not been measured, owing to the difficulty of their measurement.^{14,15,38} The reader is referred to the original publications of measurements, given in Table S1 of the ESI,† for a description of measurement methods.

Unfortunately, varying fractions of test set measurements have been used in the parameterisation of the different estimation methods, introducing some bias. As shown in Table 1 and Table S1 of the ESI,† dicarboxylic acids constitute a substantial fraction of the test set. Because of this, the EVAPORATION method, in particular, is likely to have a favourable bias, since this was created most recently, and was therefore able to use the recent widespread availability of p^o measurements for dicarboxylic acids, most of which are also part of the assessment test. 13 of the 14 primary literature sources of dicarboxylic acid p^o measurements used for EVAPORATION have been published since 2000. The methods of Lee–Kesler and Myrdal and Yalkowsky, however, were produced before then, and are therefore expected to perform less well for this class of compound. A further limitation of the test set concerns its representativeness of the atmosphere.

Ideally all functional groups observed in ambient SVOCs would be represented. Table 1 shows that although a reasonably representative range of atmospherically relevant functional groups are covered, peroxyacyl nitrate, hydroperoxide and percarboxylic acid groups are not, resulting from a scarcity of p° measurements. Preferably we would be able to assess against more measurements of nitrates, since these can constitute a substantial fraction of organics in the condensed phase.³⁶ The high reactivity of nitrate compounds, however, often makes their handling unsafe and therefore greatly limits vapour pressure measurements. This is also an important factor restricting measurement of peroxyacyl nitrate, hydroperoxide and percarboxylic acid compounds, in addition to their thermal instability. Further welcome additions to the test set to improve atmospheric representativeness would be: methanesulfonic acid,³⁹ organic salts,^{40,41} organosulfates⁴² and compounds where the only non-hydrocarbon functional group is amines⁴¹ or ketones/aldehydes.³⁵ Generally, multi-functional compounds with low vapour pressures ($<1 \times 10^{-3}$) other than substituted dicarboxylic acids (which have had comparatively large numbers of measurements) would be useful additions.

With regard to the ratios of numbers of compounds bearing particular functional groups, observational studies show there to be large variation in space and time.^{43,44} Furthermore, much of the condensed organic component is yet to be identified at a molecular level,⁸ limiting judgment on the atmospheric relevance of the test set with regard to the proportions of compounds with certain functional groups. The assessment was not only conducted on the entire test set, but also for low volatility compounds, with $p^\circ < 10^{-2}$ Pa, only. As can be seen from Fig. 1, below this vapour pressure, notable fractions of compounds will condense, making them most relevant to secondary organic aerosol. Compounds with particularly poor or good vapour pressure estimation were also evaluated in greater detail.

p° measurements were taken at a range of temperatures between 263 and 405 K. At values outside the ambient temperature range, relevance to the atmosphere is somewhat decreased. Furthermore, the difference between estimated and experimental p° at the measurement temperature and at ambient temperatures is likely to vary. However, through extrapolating p° values to ambient temperature using, for example, an Antoine equation, error is introduced by uncertainty in the equation parameters. For the assessment of compound vapour pressure estimation there was no benefit in extrapolation to ambient temperature, as it would have increased the uncertainty in the measurement values, thereby complicating the source of errors (*i.e.*, from measurement values or estimation methods). The majority of compounds (66) did have measured vapour pressures at ambient temperatures.

For the same reason, for the low volatility subset of compounds, although they were selected based on their vapour pressure at 298.15 K (extrapolated to where necessary), their vapour pressures at measurement temperatures were used for the assessment. In contrast, where necessary, vapour pressures were extrapolated to 298.15 K for the SOA loading assessment, in order to best simulate ambient conditions.

2.2 Estimation methods

The seven estimation methods assessed were chosen for having shown comparatively high accuracy in previous assessments.^{10,45}

The majority of methods tested take a group contribution approach, where functional groups (*e.g.* $-\text{CH}_3$) are first defined, followed by estimation of their contribution to p° through a minimisation procedure using a set of measured p° for a variety of compounds (often referred to as the training set). The constitution of the training set and subsequent parameterisation is therefore of fundamental importance to the accuracy of the resulting estimates (this point is also true for the non-group contribution methods). To estimate p° , group contributions are multiplied by the frequency of the corresponding functional group in a given compound and these products are summed. The functional groups of a given method determine the compound classes it is applicable to.

Four of the estimation methods: Nannoolal *et al.*,²¹ Myrdal and Yalkowsky,¹⁹ Moller *et al.*⁴⁶ and Lee-Kesler¹⁸ are combined methods, requiring T_b as input. T_b was found using the group contribution estimation methods of Nannoolal *et al.*⁴⁷ and Stein and Brown.⁴⁸ The former had a correction applied to improve accuracy for small dicarboxylic acids, as described in the ESI† of Barley *et al.*⁴⁹ The popular T_b method of Joback and Reid⁵⁰ was not used as it has been shown to produce comparatively low accuracy estimates.^{10,48}

The input T_b , however, is a potential source of error. For methods that extrapolate p° from T_b , the magnitude of propagated error increases with increasing difference between T_b and the temperature to be estimated at. If any error in the p° estimation, however, acts to compensate the propagated error in T_b , a reasonably accurate result can be obtained. This has been observed when the Myrdal and Yalkowsky¹⁹ p° estimation method is combined with the Joback and Reid⁵⁰ T_b estimation method, with the latter's tendency to overestimate T_b often negated by the former's tendency to underestimate the slope of the vapour pressure line.^{10,51} Nevertheless, this combination was not tested here, since the assessment was not concerned solely with identifying the estimation method generating the highest accuracy p° , but the one that best modeled the dependence of p° on temperature.

The Nannoolal *et al.*²¹ method was found to give comparatively high accuracy p° in the Barley and McFiggans¹⁰ assessment. It relies on the normal boiling temperature (T_b) of a compound from which it extrapolates the p° vs. T curve. The curve's gradient is estimated using a group contribution approach. For compound i :

$$\log_{10}(p_{i,l}^\circ) = (4.1012 + dB) \left(\frac{T_r - 1}{T_r - \frac{1}{8}} \right) \quad (3)$$

where dB is the group contribution and $T_r = T/T_b$. dB is found using group contribution values. In addition to functional groups, some steric effects and group interactions are considered in estimating dB ; these are often referred to as second-order effects.

Moller *et al.*⁴⁶ noted that the Nannoolal *et al.*²¹ method performed comparatively poorly for aliphatic compounds containing carboxyl and alcohol groups. They applied a correction

term to resolve this. Additionally, the training set of experimental results was expanded from Nannoolal *et al.*, generating a different parameterisation:

$$\ln(p_{i,l}^o) = (9.42208 + dB)\left(\frac{T - T_b}{T - C}\right) + D'\ln\left(\frac{T}{T_b}\right) \quad (4)$$

where the second term is the correction term and only used for compounds containing carboxyl and alcohol groups. C is given by:

$$C = 2.65 + \frac{T_b^{1.485}}{135} \quad (5)$$

Despite these modifications Compernelle *et al.*⁴⁵ and Booth *et al.*⁵¹ observed that this method estimated unrealistic vapour pressures for molecules with high numbers of hydrogen bonding groups.

Of the group contribution methods assessed here, Nannoolal *et al.* and Moller *et al.* have the highest number of groups: 132 for the former and 212 for the latter. Although this complexity has the potential to enable better accuracy through greater specificity, groups trained on too few measurements are liable to over-fitting. To an extent, this problem has been mitigated by the relatively large size of the training set for these methods: approximately 1660 and 2330 compounds for the Nannoolal *et al.* and Moller *et al.* methods, respectively.

Like the previous two, the Myrdal and Yalkowsky¹⁹ method is a combined method, requiring T_b for input. It is not a group contribution method however, rather intermolecular bonds and molecular flexibility are considered:

$$\log_{10}(p_{i,l}^o) = -\frac{(86.0 + 0.4\tau + 1421(\text{HBN}))(T_b - T)}{19.1T} + \frac{(-90.0 - 2.1\tau)\left(\frac{T_b - T}{T} - \ln\left(\frac{T_b}{T}\right)\right)}{19.1} \quad (6)$$

where HBN denotes the hydrogen bond number and τ is the effective torsional bond number. Both Compernelle *et al.*²⁰ and Barley and McFiggans¹⁰ observed a systematic increase in overestimation with decreasing volatility for this method. However, a comparatively low standard deviation around its line of best fit was also noted.

The method of Capouet and Muller⁵² uses the vapour pressure of the parent hydrocarbon ($p_{\text{hc},l}^o$) (the molecule left when all oxygenated functional groups are replaced by a H atom):

$$\log_{10}(p_{i,l}^o) = \log_{10}(p_{\text{hc},l}^o) + \sum_{k=1}^n N_{k,i}(B + CT) \quad (7)$$

where N is the number of group k in the compound and B and C are group contributions. n is the total number of groups. Where possible parent hydrocarbon vapour pressures were found from the primary literature (the sources are listed besides their compounds in Table S1 of the ESI†). Where literature values could not be found $p_{\text{hc},l}^o$ was estimated using the Lee–Kesler method,¹⁸ following the recommendation of Capouet and Muller.⁵² This method was only applicable to 9 compounds in the Barley and McFiggans¹⁰ assessment due to the limited

number of functional groups it accounts for. For these 9 it showed a comparatively low standard deviation and bias. In this study the method is applicable to 42 compounds, allowing a more robust assessment of its accuracy.

Compernelle *et al.*²⁰ proposed the EVAPORATION method:

$$\log_{10}(p_{i,l}^o) = A_i + \frac{B_i}{T^{1.5}} \quad (8)$$

where A and B are found from group contributions. 788 compounds were used in the training set of EVAPORATION. Like Nannoolal *et al.*²¹ and Moller *et al.*⁴⁶ it attempts to account for second-order effects, though it uses 5 second-order groups compared to approximately 60 in Moller *et al.*⁴⁶ Compounds with relevance to the atmosphere were targeted in the minimisation process used to quantify group contributions. This is not the case for all the methods described here, for example Nannoolal *et al.*²¹ was produced with a view to applications in chemical engineering, though its functional groups cover those observed in the atmosphere very well. Several functional groups present in our test set compounds are not covered by the EVAPORATION method, including aromatics, thereby restricting it to 46 compounds. EVAPORATION has not been assessed against measured p^o other than in its original publication where it was shown to have a strong correlation to the Nannoolal *et al.*²¹ method. This indicates potential to produce good estimates since Nannoolal *et al.*²¹ demonstrated comparatively high accuracy in the Barley and McFiggans¹⁰ assessment.

The SIMPOL.1 method by Pankow and Asher⁵³ is similar to EVAPORATION, though with a more complex temperature dependence:

$$\log_{10}(p_{i,l}^o) = A(T) + \sum_{k=1}^n N_{k,i}\left(\frac{C_{1,k}}{T} + C_{2,k} + C_{3,k} + C_{4,k}\ln(T)\right) \quad (9)$$

where A is the constant (at a given temperature) across all compounds. C values are group contributions for group k . Halogen containing groups, nitrile and carbonate groups are not included in SIMPOL.1, making it applicable to 81 of our test set compounds.

Although SIMPOL.1 has greater degrees of freedom compared to EVAPORATION, its training set contained less compounds (272), making it more liable to over-fitting. Despite showing relatively inaccurate p^o in Barley and McFiggans¹⁰ SIMPOL.1 continues to be a common choice of estimation method in studies considering SVOCs (*e.g.* Fry and Sackinger⁵⁴), therefore it was chosen for further testing here.

The corresponding state method of Lee–Kesler¹⁸ takes critical temperature (T_c) and pressure (p_c) as input:

$$\ln(p_{i,r}^o) = f^{(0)}(T_r) + \omega f^{(1)}(T_r) \quad (10)$$

where

$$f^{(0)} = 5.92714 - \frac{6.09648}{T_r} - 1.28862\ln(T_r) + 0.169347(T_r)^6 \quad (11)$$

and

$$f^{(1)} = 15.2518 - \frac{15.6875}{T_r} - 13.472 \ln(T_r) + 0.43577(T_r)^6 \quad (12)$$

T_r is the reduced temperature: T/T_c , p_r is the reduced pressure: p/p_c , ω is the acentric factor, which depends on the critical properties as well as the boiling point. Critical properties were estimated using the group-contribution method of Ambrose¹⁸ using T_b estimated by Nannoolal *et al.*⁴⁷ as primary input. Reasonable performance in comparison with other methods was observed for Lee–Kesler in Barley and McFiggans,¹⁰ though with a poorer fit to measured values than Nannoolal *et al.*²¹ Booth *et al.*,⁵¹ however, observed that Nannoolal *et al.*²¹ poorly estimated p^o for compounds with 3 oxygenated groups or more. The average number of oxygenated functional groups per compound is increased in this study over Barley and McFiggans,¹⁰ giving a more representative sample of semi-volatile organics and a more robust test of estimation methods.

Table 2 lists all estimation methods and the number of test set compounds each could be applied to given functional groups they covered. The full 90 compounds will be referred to as the complete test set, while the 42 compounds, which all methods could be applied to, will be referred to as the reduced test set. Similarly, for the subset of compounds with $p_{298.15K}^o < 10^{-2}$ Pa, Nannoolal *et al.*,²¹ Lee–Kesler, Myrdal and Yalkowsky¹⁹ and Moller *et al.*⁴⁶ were applicable to all 50 compounds fitting these criteria, while SIMPOL.1, EVAPORATION and Capouet and Muller⁵² were only applicable to 49, 34 and 33 compounds of this subset, respectively.

2.3 SOA model

The molar based absorptive partitioning model of Pankow⁵⁵ was used to estimate SOA mass loading using measured and estimated vapour pressures. Central to the model is calculation of the condensable fraction of a given compound (i), called the partitioning coefficient:

$$\xi_i = \left(1 + \frac{C_{M_i}^*}{C_{MOA}}\right)^{-1} \quad (13)$$

where $C_{M_i}^*$ is the molar based effective saturation coefficient, found by removing M_i from eqn (1). C_{MOA} is the total molar concentration ($\mu\text{mol m}^{-3}$) of condensed material and non-volatile mass:

$$C_{MOA} = \frac{\sum_i C_i \xi_i + C_{nv}}{\bar{M}} \quad (14)$$

where C_i and C_{nv} are the mass concentrations of SVOCs (including water) and the non-volatile part respectively. \bar{M} is

the average molar mass of material in the condensed phase. Eqn (13) and (14) were run iteratively using a first-guess for the C_{MOA} value to initialise the calculation.

Similar studies of modeled SOA loading employ chemical mechanism models to estimate the atmospheric compounds present. Such studies rely on estimation methods for compound vapour pressures since measured vapour pressures for all the compounds predicted to be present are not available. There is no reason the values used in those studies are correct, as we have shown below in the comparison with pure component values. In addition, as other studies have also shown, sensitivity is dependent on the gas phase mechanism used and the number of compounds included in those schemes.^{49,56} Here, compounds of the complete and reduced test sets that had measured vapour pressure values were used as two sets of SVOC input to the partitioning model. Although this provides a simplified model of atmospheric particulate production, our ability to estimate loading using measured and estimated vapour pressures allows the error in loading when using estimation methods to be quantified. This is a major advantage over studies without measured vapour pressures. For this part of the assessment measured p^o were extrapolated to 298.15 K (where necessary). Concentrations of each compound were fitted to observations, providing the following constraints:

(1) when measured p^o values were used the total aerosol mass concentration was either 3.0 or 96.0 $\mu\text{g m}^{-3}$, simulating a remote and a polluted environment, respectively⁵⁷

(2) compounds were segregated into unit bins of $\log_{10}(C^*)$ depending on their measured p^o . The relative amounts of aerosol mass per bin were fitted to the observations of total organic aerosol mass concentration in the field study of Cappa and Jimenez (their Fig. 5a).⁵⁸

The resulting concentrations for compounds in each volatility bin for the remote environment are shown in Table 3.

The total number of organic compounds in the atmosphere is several orders of magnitude higher than the number in the test set. However, the test set compounds have been fitted with concentrations to reproduce observed concentrations of organic aerosol. Consequently, the fitted concentrations are unrealistically high. Nevertheless, this approach provides the most realistic interpretation of SOA formation using available measurements of compounds pertinent to SVOCs.

Cappa and Jimenez⁵⁸ found that the global minimum C^* for SVOCs is $10^{-3} \mu\text{g m}^{-3}$ by considering the lowest aerosol mass

Table 2 The assessed estimation methods and the number of test set compounds they were applicable to

Estimation method	Applicable compounds
Nannoolal <i>et al.</i> ²¹	90
Moller <i>et al.</i> ⁴⁶	90
Myrdal and Yalkowsky ¹⁹	90
Capouet and Muller ⁵²	42
Compernelle <i>et al.</i> ²⁰	46
Pankow and Asher ⁵³	81
Lee–Kesler ¹⁸	90

Table 3 The total (sum of the condensed and gas phase) concentration allocated to each compound in a $\log_{10}(C^*)$ bin. Bins are given by their central value, e.g., -2.5 represents the range $-3 \leq \log_{10}(C^*) < -2$

Number of compounds in test set	Total concentration per $\log_{10}(C^*)$ bin ($\mu\text{g m}^{-3}$) ($\times 10^{-1}$)									
	-2.5	-1.5	-0.5	0.5	1.5	2.5	3.5	4.5	5.5	6.5
90	3.7	4.0	4.3	0.79	0.46	0.66	3.9	8.7	35	290.0
42	3.6	3.8	4.1	1.1	6.4	1.1	41.0	27.0	99.0	820.0
Number of compounds per $\log_{10}(C^*)$ bin ($\mu\text{g m}^{-3}$)										
90	1	1	1	7	19	27	11	13	9	3
42	1	1	1	5	13	16	1	4	3	1

loading and highest temperatures realistic for Earth (conditions acting to promote evaporation of SVOC). This was taken to be the minimum volatility for SVOCs in the current study, however, the minimum C^* of the test set compounds was $10^{-1} \mu\text{g m}^{-3}$. To fill the 10^{-3} and $10^{-2} \mu\text{g m}^{-3}$ C^* bins a concentration was assigned to each, fitted as for the test set compounds. A molar mass of 200 g mol^{-1} was assumed for these bins.

The concentrations of test set compounds were held constant when p° estimation methods were applied. If test set compounds had a p° predicted by an estimation method that placed them in the lowest two volatility bins their concentration was summed with the concentrations assigned to these bins in the measured p° case.

To represent the non-volatile fraction a non-volatile mass concentration was introduced with an assumed molar mass of 200 g mol^{-1} . The ratio of non-volatile to condensed organic aerosol mass concentrations was set to 1:1 for the measured p° , and the resulting non-volatile mass was maintained throughout the model runs using estimated p° . This ratio is typical of observations, though it can vary substantially.^{57,58} Relative humidities between 20–90% were tested to determine the effect on SOA loading for a given estimation method. The variation was found to be negligible in comparison to the variation between estimation methods. A single relative humidity of 60% was therefore used to obtain the results shown below.

The partitioning model had several assumptions: ideality, no diffusion limitations and no consideration of phase separation, therefore volatility was the sole determinant of gas/condensed partitioning. Despite these limitations the model is thought to be sufficient to gain a primary indication of the sensitivity of aerosol loading and composition to vapour pressure.

3 Results and discussion

3.1 Vapour pressure estimates compared to measurements

The mean absolute error (MAE) and mean bias error (MBE) for each method are presented in Table 4. In order to weight errors equally between compounds with varying numbers of measurements, the average error was first found for a given compound (averaging over multiple measurements (j)), before the average over all compounds (i) was found:

$$\text{MAE} = \frac{1}{n_i} \sum_{i=1}^{n_i} \left(\frac{1}{n_j} \sum_{j=1}^{n_j} \left| \log_{10} \frac{p_{\text{est}}^\circ}{p_{\text{exp}}^\circ} \right| \right) \quad (15)$$

and

$$\text{MAE} = \frac{1}{n_i} \sum_{i=1}^{n_i} \left(\frac{1}{n_j} \sum_{j=1}^{n_j} \log_{10} \frac{p_{\text{est}}^\circ}{p_{\text{exp}}^\circ} \right) \quad (16)$$

Fig. 3 compares the MAE and MBE for the p° estimation methods that require T_b when the Nannoolal *et al.*⁴⁷ and the Stein and Brown⁴⁸ T_b estimation methods were used. Whiskers in Fig. 3 show the variance of compounds at the 5% confidence interval. Therefore, if whiskers of a given p° estimation method overlap we can be 95% sure that there is no significant

Table 4 Performance indicators of vapour pressure estimation methods for all test set sizes: method acronyms are the same as in Fig. 4. Statistics are: regression coefficients for the least square fit of $\log_{10}(\text{estimated } p^\circ)$ vs. $\log_{10}(\text{measured } p^\circ(x))$; one standard deviation of $\log_{10}(\text{estimated } p^\circ)$ from the least-squares regression line, the mean absolute error (MAE) and mean bias error (MBE) of estimates from measurements

Number of compounds	Estimation method	Regression coefficient	σ	MAE	MBE
90	N	$0.16 + 1.02x$	0.76	0.89	-0.01
	LK	$0.15 + 1.04x$	0.75	0.83	-0.03
	MY	$0.53 + 0.83x$	0.60	0.93	0.67
	M	$-0.32 + 1.34x$	1.10	1.46	-1.06
81	N	$0.16 + 1.04x$	0.80	0.93	0.01
	LK	$0.15 + 1.05x$	0.79	0.85	0.00
	MY	$0.54 + 0.83x$	0.64	0.98	0.74
	M	$-0.33 + 1.38x$	1.17	1.56	-1.15
46	S	$-0.32 + 1.03x$	0.98	0.87	-0.29
	N	$0.37 + 1.04x$	0.93	1.03	0.08
	LK	$0.54 + 1.07x$	0.82	0.90	0.90
	MY	$0.77 + 0.85x$	0.65	1.03	1.03
	M	$-0.41 + 1.32x$	1.41	1.90	-1.57
42	S	$-0.04 + 0.97x$	0.84	0.72	0.72
	E	$0.04 + 1.09x$	0.51	0.54	0.50
	N	$0.38 + 1.06x$	0.99	1.05	0.05
	LK	$0.58 + 1.11x$	0.85	0.84	0.12
	MY	$0.76 + 0.86x$	0.67	1.12	0.90
	M	$-0.62 + 1.32x$	1.41	1.90	-1.76
	S	$-0.01 + 0.99x$	0.89	0.73	-0.17
	E	$0.07 + 1.11x$	0.51	0.55	-0.25
	CM	$0.10 + 0.95x$	0.79	0.91	-0.15

difference in its accuracy between the T_b estimation methods. The only pair of whiskers that do not overlap are for the MBE of the Myrdal and Yalkowsky¹⁹ method, though they are very close. It was therefore concluded that there was no significant difference between the T_b estimation methods. The results presented below all use the Nannoolal *et al.*⁴⁷ T_b estimation. This method was also used to estimate T_b for the calculation of the acentric factor and critical properties in the Lee–Kesler method.

Plots of estimated p° against measured p° are shown in Fig. 4. Plots for Capouet and Muller,⁵² SIMPOL.1 and EVAPORATION have fewer points because their group contributions limited them to fewer compounds, as described in Table 2. The least-squares regression line, the 1:1 line and standard deviations of estimates around the least-squares regression line are also shown in Fig. 4. Regression coefficients, standard deviations, MAE and MBE are given in Table 4. The regression coefficients (A and B) of the least-squares fit apply to the equation $\log_{10}(p_{\text{est}}^\circ) = A + B(\log_{10}(p_{\text{exp}}^\circ))$.

Of the four methods that cover the complete test set, Lee–Kesler shows the minimum MAE for the complete test set, with 0.83, while the Nannoolal *et al.*²¹ method is the next best performing with an MAE of 0.89. With regard to MBE for 90 compounds, Nannoolal *et al.*²¹ method has the minimum with -0.01, while Lee–Kesler is the second best with 0.03. Indeed, from Table 4 alone there is little to distinguish the performance of these two methods.

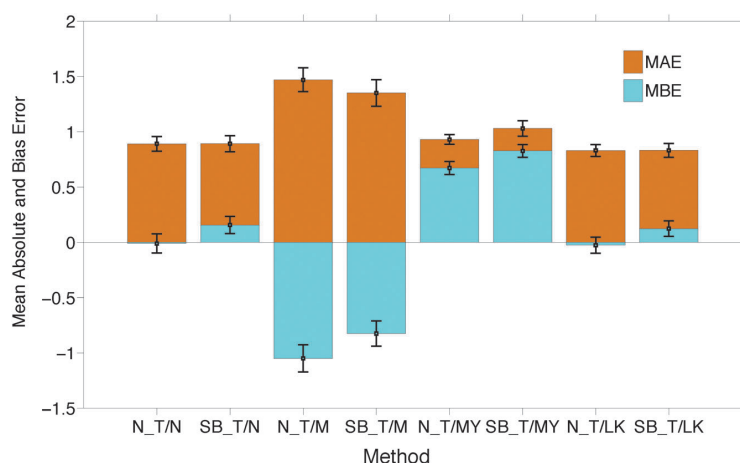


Fig. 3 The mean absolute (orange) and mean bias (blue) error. Method codes have the normal boiling point method first followed by the vapour pressure estimation method, where: N_T = Nannoolal *et al.*,⁴⁷ SB_T = Stein and Brown,⁴⁸ and for p° methods: (N) = Nannoolal *et al.*,²¹ (M) = Moller *et al.*,⁴⁶ (MY) = Myrdal and Yalkowsky¹⁹ and (LK) = Lee–Kesler. Whiskers show confidence intervals.

Compared to other methods Nannoolal *et al.*,²¹ Moller *et al.*⁴⁶ and SIMPOL show particularly poor estimation for the only two compounds with four hydrogen bonding functional groups: citric and tartaric acid (bounded by green in Fig. 4). The maximum error by any method for each compound was ranked, and plotted on the graph shown in Fig. 5, along with the errors of other methods for that compound. The estimation methods are colour coded in Fig. 5, and show a tendency for Moller *et al.*⁴⁶ to underestimate p° , while Myrdal and Yalkowsky¹⁹ tend to overestimate. For the compounds to which it is applicable, EVAPORATION has a notably good fit to the zero error line in Fig. 5.

Boxes numbered 1, 2 and 3 in Fig. 5 enclose compounds with a maximum error in the range, error ≥ 4 , $4 > \text{error} \geq 3$ and error < 1 , respectively, where the error is calculated by: $\log_{10}(p_{\text{est}}^\circ) - \log_{10}(p_{\text{exp}}^\circ)$ (1/Pa). Therefore, boxes 1, 2 and 3 enclose compounds with relatively very poor estimation, poor estimation and relatively good estimation, respectively. To determine chemical properties that influence the accuracy of estimation, the number of groups with hydrogen bonds per compound (Hb_n), which has been observed to affect the Nannoolal *et al.*²¹ and Moller *et al.*⁴⁶ estimation accuracy previously,⁵¹ and the number of carbon atoms (C_n) per compound were plotted in the same order as maximum error ranking. A metric (\hat{u}) accounting for both these properties was also calculated and plotted in this order, using the equation:

$$\hat{u} = \left(\frac{\text{Hb}_n}{\max(\text{Hb}_n)} + \frac{C_n}{\max(C_n)} \right) / 2 \quad (17)$$

where max represents the maximum number out of all compounds. Thus this equation normalises each compound's Hb_n and C_n by the maximum of each value in the test set and sums the results. The effect of the final division ($/2$) is to restrict results to the convenient range of 0 to 1; if a compound had

both the highest number of hydrogen bonding groups and carbon atoms, its \hat{u} value would be 1.

This combined metric showed a substantially better correlation with the maximum MAE ranking order ($R^2 = 0.4$, Fig. S1 of ESI[†]) than the number of hydrogen bonds ($R^2 = 0.2$) and the number of carbon atoms ($R^2 = 0.0$) alone, indicating that both factors combined affect estimation accuracy more strongly than separately. It is noted that increased hydrogen bonding and the number of carbon atoms generally act to decrease vapour pressure. As discussed, lower vapour pressure compounds are challenging to measure, leading to measurement error and relative scarcity of measurements. Both these factors will lower the ability of estimation methods, trained on measurements, to estimate accurately. The source of inaccuracy is likely to be both errors in training set measurements (or even the lack of comparable compounds in the training set) and in the functional form of estimation methods, *i.e.* how intermolecular forces are accounted for. The inaccuracies introduced by each will likely increase with lower volatility compounds, such that the observed trend of increased p° inaccuracy with an increased number of hydrogen bonds and carbon atoms is expected.

Seven compounds lie inside box 1 of Fig. 5, six of these are aliphatic carboxylic acids, of which five are substituted dicarboxylic acids and one is citric acid (a tricarboxylic acid). The other compound is nitrocatechol, and is easily distinguished from the others, as it tends to have an overestimated p° , compared to the other compounds, which are mostly underestimated. Therefore, it is recommended that estimation methods focus on improving their performance for dicarboxylic acids and their oxygenated products and that more measurements of similar compounds are made to improve future assessments. It is noted, however, that p° measurements of such compounds can be widely divergent,¹⁵ which, until resolved, will limit the extent to which estimation methods can improve through refitting.

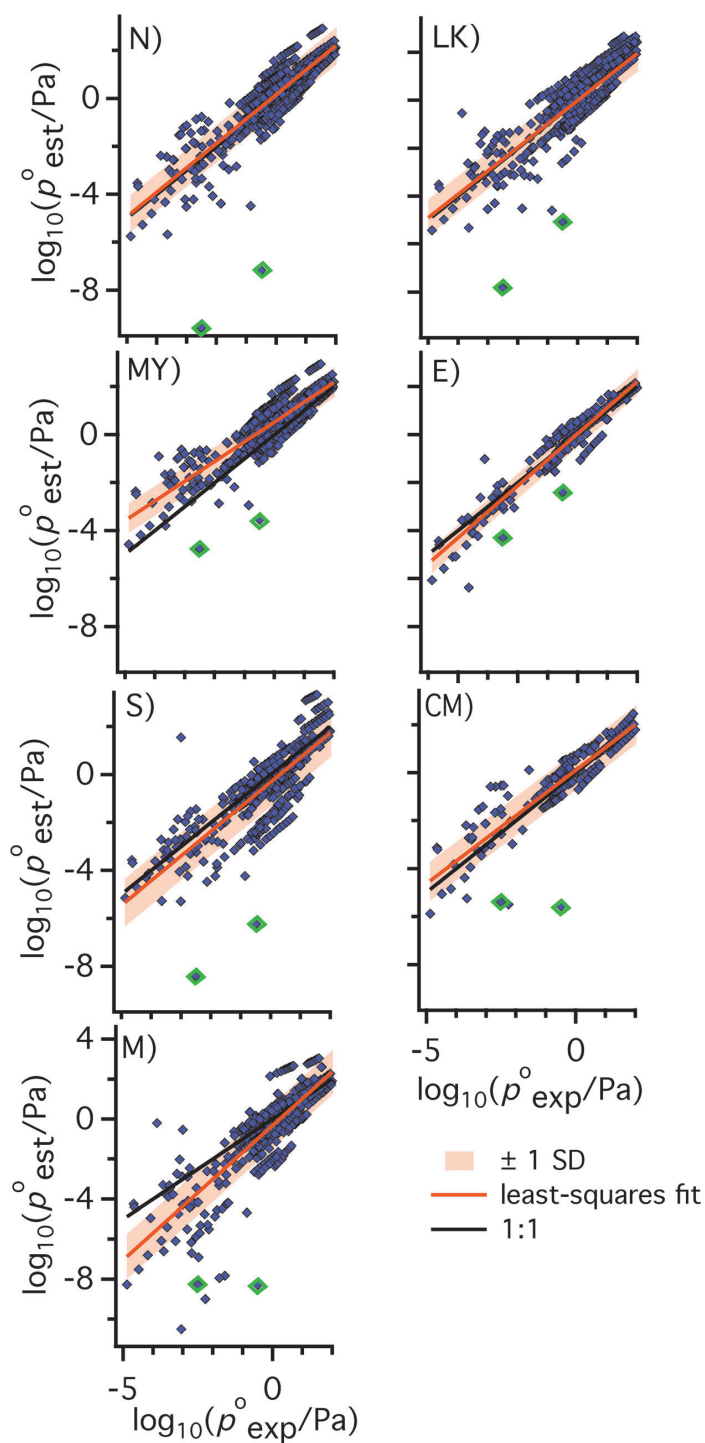


Fig. 4 Estimated vapour pressures against measured vapour pressures, where (N) = Nannoolal *et al.*,²¹ (LK) = Lee-Kesler, (MY) = Myrdal and Yalkowsky,¹⁹ (E) = EVAPORATION, (S) = SIMPOL, (CM) = Capouet and Muller⁵² and (M) = Moller *et al.*⁴⁶ Orange lines are least-squares linear regression lines, shaded regions are ± 1 standard deviation (SD), black lines are 1 : 1 fits. All abscissa ranges are consistent across plots and all ordinate ranges, except for the Moller *et al.*⁴⁶ plot, are consistent. Green bounded markers represent citric and tartaric acid.

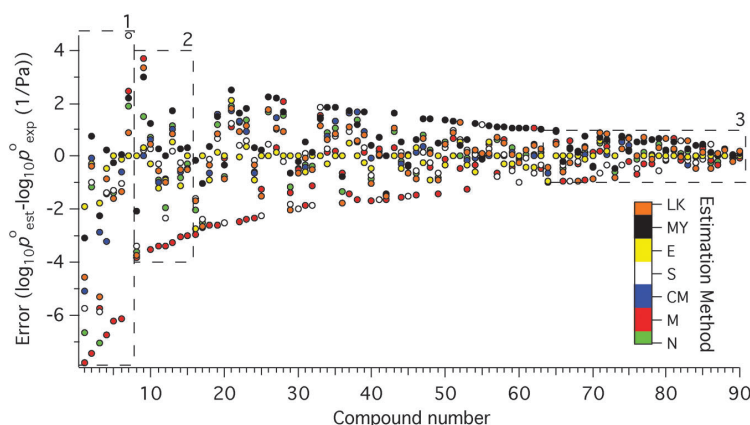


Fig. 5 The vapour pressure error of each compound for each estimation method (averaged where necessary over multiple measurement temperatures). Estimation methods are colour coded, as shown in the legend. Boxes segregate compounds falling into error ranges as discussed in the main text. Compounds have been ordered according to their maximum error.

Box 2 of Fig. 5 contains eight compounds with comparatively poorly estimated vapour pressures, and for which similar compounds should also therefore be targeted for further measurement and estimation method refitting. Of the eight compounds six are carboxylic acids (4 dicarboxylic and 2 long chain monocarboxylic). Dibutyl phthalate is also included, which is the worst estimated compound without a hydrogen bonding group. Other aromatic compounds are estimated relatively well, indicating that this property is not the cause for dibutyl phthalate's poor estimation. It may be the combination of an aromatic ring with comparatively long branches in dibutyl phthalate that causes poor estimation. Levoglucosan is the final compound in box 2. It has a far higher maximum error than another compound with three hydroxyl groups (1,2,3-trihydroxypropane with a maximum error of 1.27), therefore its combination of hydroxyl groups with a bicyclic structure and/or ether groups may cause its high inaccuracy.

The 27 compounds in box 3 of Fig. 5 have their vapour pressures estimated relatively accurately by all methods. These compounds are relatively simple, with an average number of hydrogen bonding groups of 0.9 compared to the entire test set average of 1.5. Six compounds have 2 hydrogen bonding groups (the maximum number for box 3 compounds), and of these five are dihydroxyl compounds. Although there are four monocarboxylic compounds in box 1 there are no polycarboxylics. Thus, the estimation methods perform much better for dihydroxyl compounds than dicarboxylic ones. Despite the low number of hydrogen bonding groups, all but one of the 27 compounds has multiple oxygenating groups, including ketones, amines and halogen groups. 2-Phenylbromide-TEGMME, for example, contains four ether groups and a bromine group. The relatively good estimation of these compounds is further evidence that estimation methods perform comparatively poorly for compounds with an increased number of hydrogen bonding groups, and therefore decreased volatility.

The results of the assessment of estimates against measurements for compounds with $p_{298.15K}^0 < 10^{-2}$ Pa only are given in Table 5.

Table 5 Performance indicators for estimation methods applied to compounds with $p_{298.15K}^0 < 10^{-2}$ Pa. See Table 4 and Fig. 4 for the definitions of indicators and method acronyms, respectively. Results are first given for the maximum number of low volatility compounds estimation methods were applicable to. Below these results are given for the subset of 33 compounds that the Capouet and Muller⁵² method was applicable to

Number of compounds	Estimation method	Regression coefficients	σ	MAE	MBE
50	N	$0.54 + 1.14x$	0.84	0.97	0.03
50	LK	$0.38 + 1.08x$	0.69	0.82	0.08
50	MY	$0.94 + 0.94x$	0.58	1.06	0.95
50	M	$-0.31 + 1.36x$	1.41	1.67	-1.16
49	S	$-0.10 + 0.97x$	0.76	0.78	-0.19
34	E	$-0.07 + 1.08x$	0.53	0.60	-0.35
33	CM	$0.00 + 0.91x$	0.81	0.77	-0.07
33	N	$0.61 + 1.15x$	1.00	1.04	-0.13
33	LK	$0.52 + 1.10x$	0.75	0.79	-0.02
33	MY	$1.03 + 0.95x$	0.65	1.05	0.88
33	M	$-0.93 + 1.19x$	1.46	1.94	-1.80
33	S	$0.09 + 1.02x$	0.80	0.71	-0.27
33	E	$-0.07 + 1.09x$	0.53	0.61	-0.37

Of the methods that cover all 50 of these compounds, Lee-Kesler again has the lowest MAE, and Nannoolal *et al.*²¹ the lowest MBE. Focusing on these lower volatility compounds increases the MAE for Nannoolal *et al.*²¹ and Myrdal and Yalkowsky.¹⁹ In contrast, the MAE for Lee-Kesler is constant between the low volatility subset and the complete test set. Meanwhile, the positive bias of Myrdal and Yalkowsky¹⁹ increases substantially from the complete test set to the low volatility subset, which can also be seen in Fig. 4. However, for both test sets, it shows a notably lower standard deviation around its least square regression line than the other methods.

For the combined methods inaccuracies result from either the vapour pressure or the normal boiling point equation. There is a scarcity of T_b estimation method assessments relevant to SVOC, indeed the authors are not aware of any. This may be due to measurement difficulties, as these compounds have a tendency to

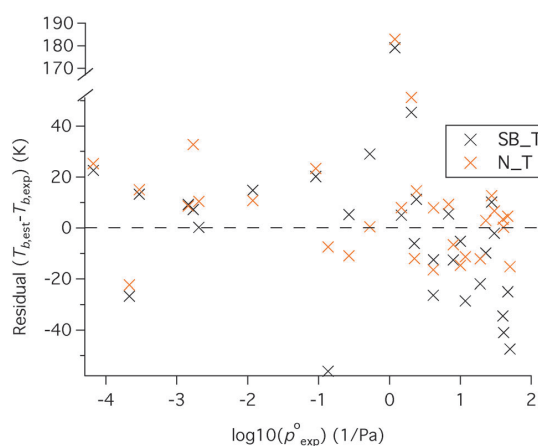


Fig. 6 The residual of Stein and Brown⁴⁸ (black crosses) and Nannoolal *et al.*⁴⁷ (orange crosses) from measured normal boiling points against the vapour pressures of the corresponding compounds. The dotted line represents zero disagreement between the estimate and the measurement.

decompose at temperatures approaching their boiling point. Here we briefly assessed T_b estimates by collating normal boiling points from the online chemistry databases of ChemSpider⁵⁹ and NIST.⁶⁰ Of the 90 compounds in our vapour pressure test set 30 had experimental T_b values in at least one database. Similar to vapour pressures, the primary source can be difficult to determine, and the claim of an experimental value difficult to verify as measurements are frequently unaccompanied by error margins. The NIST database reports the range of values around an average if several sources are available for a T_b value. The largest range was ± 70 K for triacetin, however, a more typical range around single values (where available) was ± 3 K.

The Stein and Brown⁴⁸ and Nannoolal *et al.*²¹ T_b estimates for the 30 compounds had the experimental values substituted and the resulting residuals were plotted against measured compound p^o in Fig. 6. If a compound had measurements at multiple temperatures, p^o at the median temperature was taken, so that the plot was most easily comparable to those in Fig. 4. The majority of residuals are within ± 50 K, but 2-methyl succinic acid has a value of ~ 180 K for both estimates. A similar compound, succinic acid, which we expect to have a T_b within 20 K of 2-methyl succinic acid (based on experience and estimates), has a database T_b of 508 K, compared to 380 K for the latter. The residual for succinic acid is within the typical range for both estimates. Thus the 2-methyl succinic acid appears to be due to measurement error, or derived erroneously by estimation. Consequently, the residual for 2-methyl succinic acid was omitted from calculations of average absolute errors; these were 19 K and 13 K for Stein and Brown⁴⁸ and Nannoolal *et al.*,⁴⁷ respectively.

The experimental T_b values were input to the combined p^o estimation methods and the resulting errors from experimental p^o values were found. No method showed an improvement in p^o accuracy for all compounds using experimental T_b . The error using experimental T_b was divided by that using estimated T_b

values, so that a value of 1 represented no change and a value of 0.5, for example, represented a halving of error. The median values for Nannoolal *et al.*²¹ and Myrdal and Yalkowsky¹⁹ were 1.3 and 1.4, respectively, and those for Moller *et al.*⁴⁶ and Lee–Kesler were 0.7 and 0.8, respectively. For the majority of the 30 compounds, the former two methods, therefore, had a lower error using estimated T_b than experimental, whilst for the latter two methods p^o accuracy improved for the majority of compounds when experimental T_b was used.

Decoupling the contribution of error from the T_b estimation and the p^o equation is not straightforward since, as the previous paragraph shows, inaccuracy in estimated T_b can actually improve estimated p^o accuracy if it offsets the inaccuracy of the p^o equation. In effect, the contribution of inaccuracy from the T_b estimation is a function of the p^o estimation method and the compound in question, since it depends on how the method treats a given compound. The relative contributions of error will therefore vary by the p^o estimation method and compound.

Were one of the combined methods to be used for p^o estimation in a chemical transport model using a mechanistic approach to organic aerosol partitioning the T_b of SVOCs would also have to be estimated. Therefore the results of this study are pertinent to such models.

Moller *et al.*⁴⁶ vapour pressure results show a notably larger standard deviation than any other method. A large deviation of Moller *et al.*⁴⁶ p^o estimates from Capouet and Muller⁵² estimates was observed in Compemolle *et al.*,⁴⁵ in addition to unrealistically high estimates for molecules with more than three oxygenated functional groups. In our assessment major errors arise from underestimation, with a tendency to increasingly underestimate p^o with decreasing measured p^o . Generally, lower vapour pressures occur at temperatures comparatively far from the compound's normal boiling point. Under this situation error introduced by either (or both of) the estimation of T_b or the p^o curve is likely to be magnified since the Moller *et al.*⁴⁶ method works by extrapolating the p^o vs. T curve from the normal boiling point.

Myrdal and Yalkowsky¹⁹ has a lower standard deviation than Nannoolal *et al.*²¹ and Lee–Kesler, however, it shows an increasing tendency to overestimate with decreasing p^o , as also observed in Compemolle *et al.*⁴⁵ and Barley and McFiggans.¹⁰ Compemolle *et al.*⁴⁵ suggest that this could be due to the assumption of a constant change in heat capacity from gas to liquid with temperature. Since the tendency is also observed in the current assessment we recommend this assumption be tested using measurement data. Myrdal and Yalkowsky¹⁹ estimates for citric and tartaric acid p^o show the best agreement with measurements (of the methods covering the complete test set), suggesting that it could produce relatively accurate estimates for compounds with high numbers of hydrogen bonding groups. Fig. 5 supports this advantageous property of Myrdal and Yalkowsky,¹⁹ since this method shows relatively low errors for compounds in the high maximum error boxes (box numbers 1 and 2). It seems likely, however, that this relatively good accuracy is partly attributable to an offset by its systematic overestimation of p^o . Fig. 6 shows no systematic bias in T_b estimates with compound vapour pressure,

indicating that the main cause of the overestimation in Myrdal and Yalkowsky¹⁹ is the p° equation.

Based on the above results, of the methods assessed here that cover the complete test set, the Lee–Kesler or the Nannoolal *et al.*²¹ method is recommended. Compared to Nannoolal *et al.*,²¹ Lee–Kesler shows very similar mean absolute error (0.83 : 0.89), standard deviation (0.75 : 0.76) and regression coefficients values ($0.15 + 1.04x : 0.16 + 1.02x$) for 90 compounds (Table 4). There is more distinction between the performances of these methods when subsets of the data are analysed. For the low volatility subset (Table 5), the Nannoolal *et al.*²¹ MAE rises to 0.97, while Lee–Kesler changes little from the complete test set, with 0.82. Nannoolal *et al.*,²¹ however, still outperforms Lee–Kesler on MBE (0.03 : 0.08). Regarding Fig. 5 and the compounds in boxes 1 and 2, which have the highest maximum estimation error and tend to have the highest number of hydrogen bonding groups and/or carbon atoms, Lee–Kesler generally performs better than Nannoolal *et al.*²¹ Fig. 4 shows for the two compounds with 4 hydrogen bonding groups that it has a lower MAE by about 2 error units. Therefore, based on these results, Lee–Kesler is recommended over Nannoolal *et al.*²¹

This contrasts with the conclusion of Barley and McFiggans,¹⁰ which recommended Nannoolal *et al.*²¹ over Lee–Kesler. The reason for this change is the expanded test set. As shown in Fig. 1, the main difference between this test set and 2010 study is the decrease in mean average compound vapour pressure. Table 5 and Fig. 4 show that Lee–Kesler produces more accurate results for these lower volatility compounds, most likely because it accounts for the effect of their increased oxygenation and/or chain length better. Therefore it is the inclusion of lower volatility compounds that has favoured Lee–Kesler in this study.

Our recommendation is coupled with a request for further assessment following further vapour pressure measurements. As discussed, the full test set is biased toward carboxylic acids, and is without some functional groups known to be present in the atmosphere (such as hydroperoxide⁶¹). The low volatility test set is particularly skewed toward methods that accurately estimate for carboxylic acids, with 42 of the 50 compounds containing a carboxylic acid group. Thus, further measurements, particularly for non-carboxylic compounds, are required for more rigorous future assessment.

Were the systematic overestimation by the Myrdal and Yalkowsky¹⁹ extrapolation method to be rectified this would likely be recommended due to its relatively low standard deviation: approximately 20% lower than that of Lee–Kesler and Nannoolal *et al.*²¹ for the 90 compound test set, and the same improvement over Lee–Kesler for the low volatility subset also.

EVAPORATION shows clear superiority of all methods in standard deviation and MAE for the test sets with 46 and 42 compounds. For 46 compounds the intercept for its least-squares fit line is equal with SIMPOL.1 is being the closest to 0. Its gradient is within 0.05 and 0.02 of Nannoolal *et al.*²¹ and Lee–Kesler, respectively, therefore showing a comparatively good fit to the 1 : 1 line. For the low volatility subset, EVAPORATION again shows superiority in MAE when compared against other

methods for the same set of compounds (Table 5). It is notable, however, that its bias is comparatively low for this subset, and its regression coefficients in both Tables 4 and 5 and its least square line in Fig. 3 indicate a tendency to increasingly underestimate vapour pressure with decreasing vapour pressure. Nevertheless, these results show that over all compounds to which it is applicable EVAPORATION provides the most accurate p° values of the estimation methods assessed here. It is recommended that this method be extended to cover all functionalities found in SVOC since its good accuracy here suggests potential to estimate p° with improved accuracy for all SVOC. Additional work may be required, however, to rectify its tendency to underestimate vapour pressure for lower volatility compounds.

As discussed in Section 2.1, the EVAPORATION method was produced using some of the measurements it is assessed against. This is likely to give it an advantage over methods produced earlier, such as Lee–Kesler, particularly for carboxylic acids, for which there has been a concerted measurement effort recently. Therefore, the comparatively high accuracy of EVAPORATION is, to an extent, artificial. Consequently, it is strongly recommended to test EVAPORATION against further measurements, particularly for compounds other than carboxylic acids, but relevant to the atmosphere.

A further consideration is reliability in the measured p° . Although we have assumed zero error in measurements since our objective was to assess estimates, uncertainties in measurements can span orders of magnitude. There is a wide range in reported values for many compounds (for example 4 orders of magnitude for azelaic acid between Salo *et al.*⁶² and Cappa *et al.*⁶³). Experimental issues arise from the following: extrapolation to 298 K from higher temperatures; an unknown or a poorly controlled sample state (*e.g.* amorphous or hydrated material); contamination of samples with higher volatility material; contamination or saturation of the instrument; availability of low vapour pressure calibration compounds. The measurement of low volatility compounds remains an active area of research and is the subject of a recent review paper.³⁸

3.2 Sensitivity of particulate mass loading and composition to estimation methods

Measured and estimated p° for the test set compounds were input to a molar-based absorptive partitioning model⁵⁵ as described in Section 2.3. Results were converted to mass loadings to allowing comparison of simulated particulate concentrations. Compounds were fitted with concentrations based on the organic aerosol concentration distribution with volatility reported in the ambient field study of Cappa and Jimenez.⁵⁸ The results for a low (remote scenario) and high (polluted scenario) particulate loading case at 60% relative humidity are shown in Fig. 7. When using measured p° values, the low and high cases had secondary organic aerosol mass loadings (SOA) of $1.5 \mu\text{g m}^{-3}$ and $48 \mu\text{g m}^{-3}$, respectively, and the SOA : non-volatile mass ratio was 1 : 1.

Table 6 presents the fraction change in SOA mass loading relative to the measured p° case for the different methods.

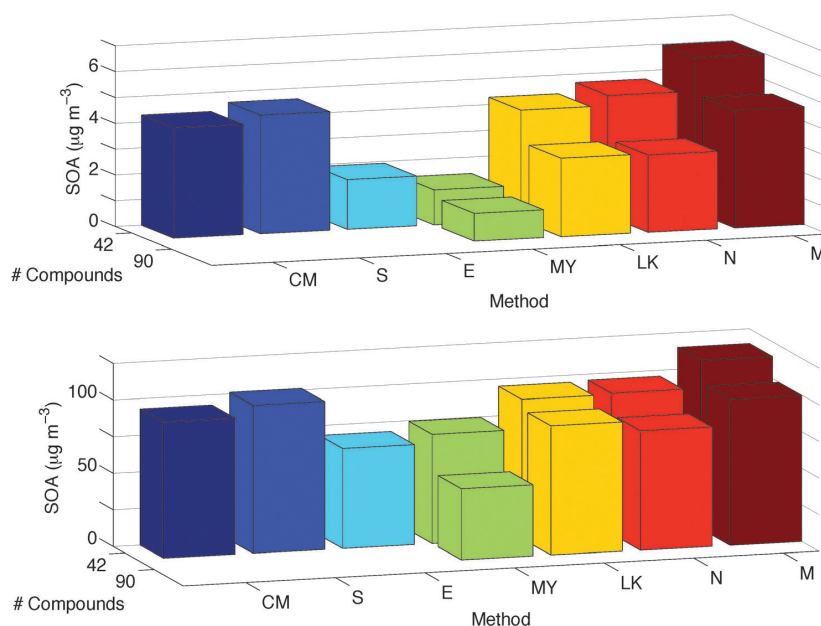


Fig. 7 Modeled secondary organic aerosol mass loading (SOA) using different vapour pressure estimation methods. Method acronyms are the same as in Fig. 4. The upper and lower plots are for compound concentrations that yielded 1.5 and 48 $\mu\text{g m}^{-3}$ SOA (when measured vapour pressures were used), respectively. Both simulations were at a relative humidity of 60% and when measured p° were used the non-volatile:SOA mass concentration ratio was 1:1.

Table 6 The fraction change from using the measured p° to estimated p° to obtain SOA mass loading, where fraction change = SOA loading using estimated p° /SOA loading using measured p° (e.g. 0.5 equates to a factor of 2 decrease). See Fig. 4 for method acronyms

Measured p° case SOA ($\mu\text{g m}^{-3}$)	Number of compounds	Method	Fraction change
1.5	42	N	3.1
		M	4.0
		LK	2.9
		MY	0.9
		EVA	1.3
	90	SIM	3.1
		CM	2.8
		N	2.0
		M	3.0
		LK	2.0
48.0	42	MY	0.7
		N	2.0
		M	2.4
		LK	2.0
		MY	1.6
	90	EVA	1.4
		SIM	2.1
		CM	1.9
		N	1.7
		M	2.1
		LK	1.8
		MY	1.0

Fig. 7 and Table 6 show that the performance of estimation methods to predict pure compound vapour pressures is not linearly related to their performance to predict SOA loading

when their estimated vapour pressures are input to an absorptive partitioning model. Most estimation methods overestimate SOA mass loading. This is true even for methods giving a net positive bias in Table 4, and which one might therefore expect to underestimate SOA. The cause is the fitting of compound concentrations to field observations of increasing concentration with increasing p° . To exemplify the effect of this, consider the case where a negligible bias is produced through the same number of compounds having vapour pressure underestimated as overestimated by the same amount. The underestimated compounds generate more condensed mass than the overestimated compounds they have replaced in p° space would have done (with measured p°) since they have the greater total concentration. Consequently there has to be a relatively major systematic overestimation of p° for SOA to be underestimated, as seen with Myrdal and Yalkowsky¹⁹ in Table 6.

The variation in SOA mass loading accuracy between the complete and reduced test sets is likely due to an average change in the composition of compounds between the sets. For certain classes of compound a given method's accuracy will vary (e.g. Asher *et al.*⁶⁴). The variation in SOA accuracy between the remote and polluted scenarios is due to a change in the average chemical composition of SVOC. This is because the vapour pressure range in which SVOC reside shifts depending on the particulate loading (C_{MOA} (eqn (13))). The issue of changing chemical composition between the reduced and complete test set is therefore an artefact of the assessment. In contrast, the issue of changing composition with volatility is

expected in the atmosphere: lower volatility compounds are expected to be more oxidised and/or have higher molecular weights.

Despite comparatively low MAE and MBE values for the vapour pressure comparisons Nannoolal *et al.*²¹ and Lee–Kesler show relatively poor accuracy for SOA mass loading. This is because of the increasing total mass of compounds with increasing volatility (as discussed above), combined with the lack of any compensating effect such as a positive p^0 bias. They show an improved SOA accuracy for the polluted case, indicating a decreasing MAE for compounds with higher volatilities since these contribute more to the condensed phase under a higher particulate loading. Fig. 4 demonstrates this is indeed the case.

Myrdal and Yalkowsky¹⁹ and EVAPORATION generate the most accurate SOA mass loading estimates. The positive p^0 bias of the former causes an underestimation of the SOA in the low loading scenario. In the high loading scenario the upward shift of the volatility range of SVOC results in a lower average overestimation of SVOC p^0 by Myrdal and Yalkowsky¹⁹ (Fig. 4). This leads to a very accurate loading estimation for the complete test set and an overestimation of loading in the reduced test set (Table 6).

Despite EVAPORATION having a negative MBE for the reduced test set (Table 4), the relatively low MAE of this method means that the movement of compounds in volatility space between the measured and estimated p^0 case is relatively minimal.

The composition and not only mass of the modeled SOA is also important. To characterise composition, the average carbon oxidation state and the number of carbon atoms of compounds in the condensed phase were found and are shown in Fig. 8. The average is weighted by the condensed concentration of each compound. The first feature to note in Fig. 8 is that markers of the same shape (marker shape represents scenarios) generally congregate together. The clustering of the 90 compound results vs. those of the 42 compounds is, like the SOA loading accuracy results, an artefact of the test set (*i.e.*, due to the sample of

compounds in each set). Secondly, the estimation methods show a strong tendency to overestimate the mean carbon oxidation state and underestimate the number of carbon atoms per compound compared to the base case (in which measured vapour pressures are used). This tendency is generally reduced, to an extent, when the loading is increased, indicating less sensitivity of composition to vapour pressure estimation when partitioning coefficients increase, as for SOA loading. The direction of points along this plot approximately follows the trajectory of where biomass burning organic aerosol (BBOA) (lower average oxidation state, higher number of carbon atoms), SVOC and low-volatility oxidised organic aerosol (LV-OOA) (higher oxidation state, lower number of carbon atoms) would be expected to be found.³⁷ The base case points fall within the BBOA region, whereas the majority of estimation method points fall within the SVOC or even the LV-OOA region. Thus, the differences between the base case and the majority of estimation methods in Fig. 8 represent major differences in the SOA composition.

There is little variation between the combined methods in Fig. 8, though, for the low loading scenarios, Myrdal and Yalkowsky¹⁹ show notably better agreement with the base case in the number of carbon atoms and slightly better agreement in the average oxidation state. This appears to reinforce its choice as the most useful method for estimating SOA loading and composition (despite it showing comparatively poor accuracy for pure compound p^0). EVAPORATION has very good agreement in both dimensions for the low loading scenario. For the high loading scenario its agreement is worse but notably better than the other methods. The utility of EVAPORATION is, however, limited by the number of functional groups it covers.

There has to be a clear distinction on method recommendation based on (1) pure component comparisons and (2) atmospheric SOA predictions using empirically constrained volatility profiles. Overall EVAPORATION and Myrdal and Yalkowsky¹⁹ have been shown as the preferred methods for estimating SOA (point 2). As discussed, Myrdal and Yalkowsky¹⁹ generates the most accurate loading through the offsetting effect of its overestimation of p^0 for most compounds. Despite this, it also boasts comparatively good estimates of the average oxidation state and the number of carbon atoms for low loading scenarios. The Myrdal and Yalkowsky¹⁹ method, however, requires further assessment against SVOCs with measured $p^0 < 10^{-1}$ Pa. Its systematic overestimation of p^0 on SOA when these compounds are included is expected to produce even greater underestimation of loading than seen here. For the other estimation methods, when applied to a test set more representative of the atmosphere, the greatest change is likely to be the introduction of more oxygenated compounds. As discussed, the methods tend to show increasing error for compounds of an increasing number of hydrogen bonds, thus a greater mean absolute error of vapour pressure and overestimation of SOA loading would be expected from inclusion of more oxygenated compounds.

The above discussion demonstrates that absolute accuracy as well as bias influence the accuracy of SOA mass loading estimates. Sensitivity of predicted SOA mass, and composition, to the choice of estimation method depends on the abundance and volatility of each compound. For example, estimation methods

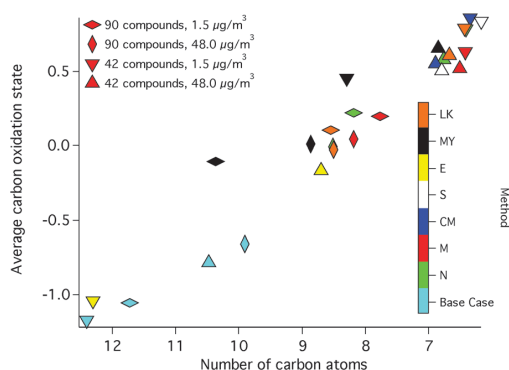


Fig. 8 The weighted average number of carbon atoms and the average oxidation state in the condensed phase. Marker shapes represent different scenarios (number of compounds in the test set and loading), while marker colours represent the method used to obtain vapour pressures (as shown on the colour scale).

have been applied to predicted compounds generated by near-explicit models of VOC oxidation: the Master Chemical Mechanism in Barley *et al.*⁴⁹ and GECKO-A in Valorso *et al.*⁵⁶ In the former study a factor of 10 difference was noted in SOA between Myrdal and Yalkowsky¹⁹ and Nannoolal *et al.*²¹ when both used Nannoolal *et al.*⁴⁷ T_b estimates. Valorso *et al.*⁵⁶ found that the difference in SOA is greatest when the aerosol loading is low, varying by a maximum factor of 3.5 between Myrdal and Yalkowsky¹⁹ with Joback and Reid⁵⁰ T_b and Nannoolal *et al.*²¹ with Nannoolal *et al.*⁴⁷ T_b . When aerosol loading is low, compounds with relatively lower vapour pressures are able to condense whereas those with higher vapour pressures cannot. As others and we have shown, the discrepancy between estimation methods increases as vapour pressure decreases so this is expected. As Barley *et al.*⁴⁹ found, as the number of compounds increases, sensitivity to estimation method decreases.

4 Conclusion

This study compared the vapour pressures generated by seven estimation methods against measurements to assess their accuracy. Compared to the assessment of Barley and McFiggans¹⁰ the number of test set compounds was doubled and the types and frequency of functional groups per compound were increased, thereby providing a more thorough assessment. Three of the methods were not applicable to all the functional groups present in the test set of compounds, meaning that a reduced test set was also needed. EVAPORATION gave the minimum MAE for the reduced test set, while Lee–Kesler gave the minimum MAE for the complete set. The MBE was lowest for Nannoolal *et al.*,²¹ however this method showed comparatively poor accuracy for compounds with lower volatility. Similarly, the Myrdal and Yalkowsky¹⁹ method increasingly overestimated vapour pressures for compounds with decreasing volatility.

Using a simple absorptive equilibrium model, the sensitivity of predicted SOA loading to the choice of estimation technique was assessed by mapping concentrations of compounds within the test set to a volatility profile derived from an ambient study. By comparing predictive saturation vapour pressures with measured vapour pressures, the majority of methods, including Lee–Kesler and Nannoolal *et al.*,²¹ showed overestimation of SOA by factors of between 1.8 and 3.

Myrdal and Yalkowsky¹⁹ and EVAPORATION showed the highest accuracy for SOA loading estimates using our methodology as well as the highest accuracy for SOA composition (represented by the average carbon oxidation state and the number of carbon atoms per compound). The effect of the increasing overestimation of vapour pressure with decreasing volatility by Myrdal and Yalkowsky¹⁹ on SOA loading, however, requires testing, since none of the compounds here had volatilities toward the lower end of the SVOC volatility region. The EVAPORATION method cannot be used on compounds containing certain functional groups. If it could be extended to cover all groups present in the atmosphere and maintain its comparatively high accuracy it would be the preferable method for both vapour pressure estimation and SOA modeling.

The recommended method is dependent on its application: for a single organic compound EVAPORATION has been shown as most accurate and consistent. However, if it is not applicable to the compound in question due to missing functional group information, Lee–Kesler is recommended. In contrast, based on SOA mass loading sensitivities, the Myrdal and Yalkowsky¹⁹ method has been shown as the best. A future study should consider whether the Myrdal and Yalkowsky¹⁹ method coupled with a chemical degradation model or the volatility basis set provides the better estimation of mass distribution by volatility in a chemical transport model.

Acknowledgements

The Natural Environment Research Council funded this work through the studentship of Simon O'Meara and grant numbers: NE/J02175X/1, NE/J009202/1 and NE/H002588/1.

References

- 1 P. Forster, V. Ramaswamy, P. Artaxo, T. Berntsen, R. Betts, D. W. Fahey, J. Haywood, J. Lean, D. C. Lowe, G. Myhre, J. Nganga, R. Prinn, G. Raga, M. Schulz and R. Van Dorland, in *Climate Change 2007: The Physical Science Basis. Contribution of Working Group I to the Fourth Assessment Report of the Intergovernmental Panel on Climate Change*, ed. S. Solomon, D. Qin, M. Manning, Z. Chen, M. Marquis, K. B. Averyt, M. Tignor and H. L. Miller, Cambridge University Press, Cambridge, United Kingdom and New York, NY, USA, 2007, ch. 2, pp. 129–234.
- 2 C. Pope and D. Dockery, *J. Air Waste Manage. Assoc.*, 2006, **56**, 709–742.
- 3 M. R. Heal, P. Kumar and R. M. Harrison, *Chem. Soc. Rev.*, 2012, **41**, 6606–6630.
- 4 M. Andreae and P. J. Crutzen, *Science*, 1997, **276**, 1052–1058.
- 5 S. Fuzzi, M. Andreae, B. Huebert, M. Kulmala, T. Bond, M. Boy, S. Doherty, A. Guenther, M. Kanakidou, K. Kawamura, V. Kerminen, U. Lohmann, L. Russell and U. Poschl, *Atmos. Chem. Phys.*, 2006, **6**, 2017–2038.
- 6 B. Aumont, S. Szopa and S. Madronich, *Atmos. Chem. Phys.*, 2005, **5**, 2497–2517.
- 7 Q. Zhang, J. L. Jimenez, M. R. Canagaratna, J. D. Allan, H. Coe, I. Ulbrich, M. R. Alfarra, A. Takami, A. M. Middlebrook, Y. L. Sun, K. Dzepina, E. Dunlea, K. Docherty, P. F. DeCarlo, D. Salcedo, T. Onasch, J. T. Jayne, T. Miyoshi, A. Shimono, S. Hatakeyama, N. Takegawa, Y. Kondo, J. Schneider, F. Drewnick, S. Borrmann, S. Weimer, K. Demerjian, P. Williams, K. Bower, R. Bahreini, L. Cottrell, R. J. Griffin, J. Rautiainen, J. Y. Sun, Y. M. Zhang and D. R. Worsnop, *Geophys. Res. Lett.*, 2007, **34**, L13801.
- 8 M. Hallquist, J. C. Wenger, U. Baltensperger, Y. Rudich, D. Simpson, M. Claeys, J. Dommen, N. M. Donahue, C. George, A. Goldstein, J. Hamilton, H. Herrmann, T. Hoffmann, Y. Iinuma, M. Jang, M. Jenkin, J. Jimenez, A. Kiendler-Scharr, W. Maenhaut, G. McFiggans, T. F. Mentel,

- A. Monod, A. Prevot, J. Seinfeld, J. Surratt, R. Szmigielski and J. Wildt, *Atmos. Chem. Phys.*, 2009, **9**, 5155–5236.
- 9 N. M. Donahue, A. L. Robinson, C. O. Stanier and S. N. Pandis, *Environ. Sci. Technol.*, 2006, **40**, 2635–2643.
- 10 M. H. Barley and G. McFiggans, *Atmos. Chem. Phys.*, 2010, **10**, 749–767.
- 11 M. Barley, D. O. Topping, M. E. Jenkin and G. McFiggans, *Atmos. Chem. Phys.*, 2009, **9**, 2919–2932.
- 12 A. Baklanov, K. Schlünzen, P. Suppan, J. Baldasano, D. Brunner, S. Aksoyoglu, G. Carmichael, J. Douros, J. Flemming, R. Forkel, S. Galmarini, M. Gauss, G. Grell, M. Hirtl, S. Joffre, O. Jorba, E. Kaas, M. Kaasik, G. Kallos, X. Kong, U. Korsholm, A. Kurganskiy, J. Kushta, U. Lohmann, A. Mahura, A. Manders-Groot, A. Maurizi, N. Moussiopoulos, S. T. Rao, N. Savage, C. Seigneur, R. S. Sokhi, E. Solazzo, S. Solomos, B. Sørensen, G. Tsegas, E. Vignati, B. Vogel and Y. Zhang, *Atmos. Chem. Phys.*, 2014, **14**, 317–398.
- 13 G. McFiggans, D. O. Topping and M. H. Barley, *Atmos. Chem. Phys.*, 2010, **10**, 10255–10272.
- 14 A. Delle Site, *J. Phys. Chem. Ref. Data*, 1997, **26**, 157.
- 15 A. J. Huisman, U. K. Krieger, A. Zuend, C. Marcolli and T. Peter, *Atmos. Chem. Phys. Discuss.*, 2013, **13**, 1133–1177.
- 16 M. Camredon and B. Aumont, *Atmos. Environ.*, 2006, **40**, 2105–2116.
- 17 A. K. Mbienda, C. Tchawoua, D. Vondou and F. M. Kamga, *Int. J. Geophys.*, 2013, **2013**(612375), 13.
- 18 R. Reid, J. Prausnitz and B. Poling, *The Properties of Gases and Liquids*, McGraw-Hill, New York and London, 4th edn, 1987.
- 19 P. Myrdal and S. Yalkowsky, *Ind. Eng. Chem. Res.*, 1997, **36**, 2494–2499.
- 20 S. Compernelle, K. Ceulemans and J.-F. Müller, *Atmos. Chem. Phys.*, 2011, **11**, 9431–9450.
- 21 Y. Nannoolal, J. Rarey and D. Ramjugernath, *Fluid Phase Equilib.*, 2008, **269**, 117–133.
- 22 B. J. Murray and A. K. Bertram, *Phys. Chem. Chem. Phys.*, 2008, **10**, 3287–3301.
- 23 A. Virtanen, J. Joutsensaari, T. Koop, J. Kannosto, P. Yli-Pirilä, J. Leskinen, J. M. Mäkelä, J. K. Holopainen, U. Pöschl, M. Kulmala, D. R. Worsnop and A. Laaksonen, *Nature*, 2010, **467**, 824–827.
- 24 C. Marcolli, B. Luo and T. Peter, *J. Phys. Chem. A*, 2004, **108**, 2216–2224.
- 25 C. D. Cappa, E. R. Lovejoy and A. R. Ravishankara, *Proc. Natl. Acad. Sci. U. S. A.*, 2008, **105**, 18687–18691.
- 26 J. Prausnitz, R. Lichtenhaler and E. de Azevedo, *Molecular Thermodynamics of Fluid-Phase Equilibria*, Prentice-Hall, Englewood Cliffs, NJ, USA, 2nd edn, 1986.
- 27 N. L. Ng, M. R. Canagaratna, Q. Zhang, J. L. Jimenez, J. Tian, I. M. Ulbrich, J. H. Kroll, K. S. Docherty, P. S. Chhabra, R. Bahreini, S. M. Murphy, J. H. Seinfeld, L. Hildebrandt, N. M. Donahue, P. F. DeCarlo, V. a. Lanz, A. S. H. Prévôt, E. Dinar, Y. Rudich and D. R. Worsnop, *Atmos. Chem. Phys.*, 2010, **10**, 4625–4641.
- 28 N. M. Donahue, S. a. Epstein, S. N. Pandis and A. L. Robinson, *Atmos. Chem. Phys.*, 2011, **11**, 3303–3318.
- 29 M. C. Pietrogrande, D. Bacco, M. Visentin, S. Ferrari and V. Poluzzi, *Atmos. Environ.*, 2014, **86**, 164–175.
- 30 S. Decesari, S. Fuzzi, M. Facchini, M. Mircea, L. Emblico, F. Cavalli, W. Maenhaut, X. Chi, G. Schkolnik, A. Falkovich, Y. Rudich, M. Claeys, V. Pashynska, G. Vas, I. Kourtchev, R. Vermeylen, A. Hoffer, M. Andreae, E. Tagliavini, F. Moretti and P. Artaxo, *Atmos. Chem. Phys.*, 2006, **6**, 375–402.
- 31 D. C. S. Beddows, R. J. Donovan, R. M. Harrison, M. R. Heal, R. P. Kinnersley, M. D. King, D. H. Nicholson and K. C. Thompson, *J. Environ. Monit.*, 2004, **6**, 124–133.
- 32 J. Hamilton, P. Webb, A. Lewis, J. Hopkins, S. Smith and P. Davy, *Atmos. Chem. Phys. Discuss.*, 2004, **4**, 1393–1423.
- 33 W. F. Rogge, M. A. Mazurek and L. M. Hildemannt, *Atmos. Environ.*, 1993, **27A**, 1309–1330.
- 34 D. Helmig, A. Bauer, J. Müller and W. Klein, *Atmos. Environ.*, 1990, **24**, 179–184.
- 35 M. Kalberer, D. Paulsen, M. Sax, M. Steinbacher, J. Dommen, A. S. H. Prevot, R. Fisseha, E. Weingartner, V. Frankevic, R. Zenobi and U. Baltensperger, *Science*, 2004, **303**, 1659–1662.
- 36 D. a. Day, S. Liu, L. M. Russell and P. J. Ziemann, *Atmos. Environ.*, 2010, **44**, 1970–1979.
- 37 J. H. Kroll, N. M. Donahue, J. L. Jimenez, S. H. Kessler, M. R. Canagaratna, K. R. Wilson, K. E. Altieri, L. R. Mazzoleni, A. S. Wozniak, H. Bluhm, E. R. Mysak, J. D. Smith, C. E. Kolb and D. R. Worsnop, *Nat. Chem.*, 2011, **3**, 133–139.
- 38 M. Bilde, Overview of Equilibrium Vapour Pressures and Vaporization Enthalpies of Low Volatility Organic Molecules of Atmospheric Relevance, *Chem. Rev.*, to be submitted.
- 39 A. Kettle and M. Andrea, *J. Geophys. Res.*, 2000, **105**, 26793–26808.
- 40 K. Barsanti, P. McMurry and J. Smith, *Atmos. Chem. Phys.*, 2009, **9**, 2949–2957.
- 41 M. C. Facchini, S. Decesari, M. Rinaldi, C. Carbone, E. Finessi, M. Mircea, S. Fuzzi, F. Moretti, E. Tagliavini, D. Ceburnis and C. D. O'Dowd, *Environ. Sci. Technol.*, 2008, **42**, 9116–9121.
- 42 J. D. Surratt, Y. Gómez-González, A. W. H. Chan, R. Vermeylen, M. Shahgholi, T. E. Kleindienst, E. O. Edney, J. H. Offenberg, M. Lewandowski, M. Jaoui, W. Maenhaut, M. Claeys, R. C. Flagan and J. H. Seinfeld, *J. Phys. Chem. A*, 2008, **112**, 8345–8378.
- 43 S. Decesari, M. Mircea, F. Cavalli, S. Fuzzi, F. Moretti, E. Tagliavini and M. C. Facchini, *Environ. Sci. Technol.*, 2007, **41**, 2479–2484.
- 44 P. Saxena and L. M. Hildemann, *J. Atmos. Chem.*, 1996, **24**, 57–109.
- 45 S. Compernelle, K. Ceulemans and J.-F. Müller, *Atmos. Chem. Phys.*, 2010, **10**, 6271–6282.
- 46 B. Moller, J. Rarey and D. Ramjugernath, *J. Mol. Liq.*, 2008, **143**, 52–63.
- 47 Y. Nannoolal, J. Rarey, D. Ramjugernath and W. Cordes, *Fluid Phase Equilib.*, 2004, **226**, 45–63.
- 48 S. Stein and R. Brown, *J. Chem. Inf. Comput. Sci.*, 1994, 581–587.
- 49 M. H. Barley, D. Topping, D. Lowe, S. Utembe and G. McFiggans, *Atmos. Chem. Phys.*, 2011, **11**, 13145–13159.
- 50 K. Joback and R. Reid, *Chem. Eng. Commun.*, 1987, **57**, 233–243.

- 51 A. M. Booth, M. H. Barley, D. O. Topping, G. McFiggans, A. Garforth and C. J. Percival, *Atmos. Chem. Phys.*, 2010, **10**, 4879–4892.
- 52 M. Capouet and J.-F. Muller, *Atmos. Chem. Phys.*, 2006, **6**, 1455–1467.
- 53 J. F. Pankow and W. E. Asher, *Atmos. Chem. Phys.*, 2008, **8**, 2773–2796.
- 54 J. L. Fry and K. Sackinger, *Atmos. Chem. Phys.*, 2012, **12**, 8797–8811.
- 55 J. Pankow, *Atmos. Environ.*, 1994, **28**, 185–188.
- 56 R. Valorso, B. Aumont, M. Camredon, T. Raventos-Duran, C. Mouchel-Vallon, N. L. Ng, J. H. Seinfeld, J. Lee-Taylor and S. Madronich, *Atmos. Chem. Phys.*, 2011, **11**, 6895–6910.
- 57 J. H. Seinfeld and S. N. Pandis, *Atmospheric Chemistry and Physics*, John Wiley & Sons Inc., Hoboken, NJ, USA, 2nd edn, 2006.
- 58 C. D. Cappa and J. L. Jimenez, *Atmos. Chem. Phys.*, 2010, **10**, 5409–5424.
- 59 R. S. of Chemistry, *ChemSpider: Search and share chemistry*, 2014, <http://www.chemspider.com>.
- 60 N. I. for Science and Technology, *NIST Chemistry WebBook: NIST Standard Reference Database Number 69*, 2014, <http://webbook.nist.gov/chemistry/name-ser.html>.
- 61 N. M. Donahue, A. L. Robinson and S. N. Pandis, *Atmos. Environ.*, 2009, **43**, 94–106.
- 62 K. Salo, A. M. Jonsson, P. U. Andersson and M. Hallquist, *J. Phys. Chem. A*, 2010, **114**, 4586–4594.
- 63 C. D. Cappa, E. R. Lovejoy and A. R. Ravishankara, *J. Phys. Chem. A*, 2007, **111**, 3099–3109.
- 64 W. E. Asher, J. F. Pankow, G. B. Erdakos and J. H. Seinfeld, *Atmos. Environ.*, 2002, **36**, 1483–1498.

1

Supplementary Material for An Assessment of Vapour Pressure Estimation Methods

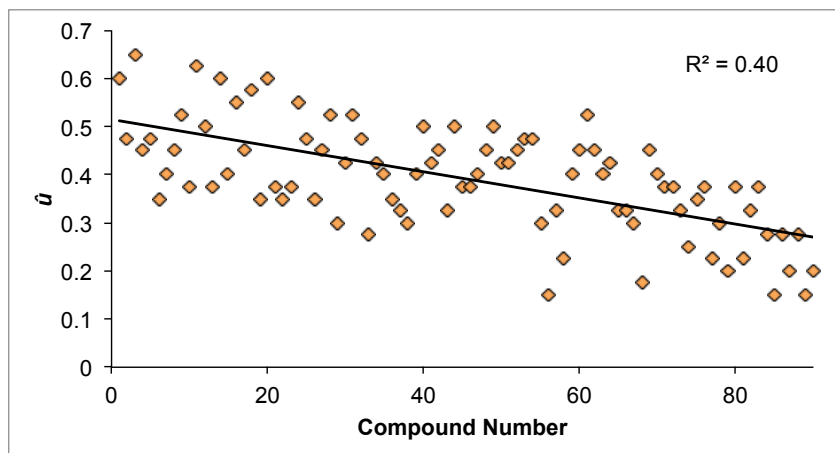


Figure S1: The combined metric for hydrogen bond number and carbon number as described in the main text (eq.17 of main text), plotted in the order of decreasing (from left to right) maximum vapour pressure error by any estimation method for the 90 test set compounds. Line represent the least-squares best fit.

90 compounds comprised the test set, they are listed in table 1, along with their CAS code, literature source, vapour pressure, temperature range and the source for their parent hydrocarbon vapour pressure, if this were found in the literature. Also listed are the sources for enthalpies of fusion, heat capacities for the solid and liquid state, and melting temperature, when these were found in the literature.

Compound	CAS code	P_{hc}^{ref} Source	P^{ref} (Pa) range	T range (K)	P_{hc}^{ref} (Pa) Δ	ΔH_{fus}	ΔC_p	T_m
Tridecanoic acid	638-53-9	a	2.87E-3	298.15	b	c	c	d
Tetradecanoic acid	544-63-8	a	1.46E-3	298.15	e	c	c	d
Pentadecanoic acid	1092-84-2	a	6.98E-4	298.15	b	c	f	d
Hexadecanoic acid	57-10-3	a	2.97E-4	298.15	e	f	f	d
Heptadecanoic acid	506-12-7	a	1.88E-4	298.15	b	c	c	d
Octadecanoic acid	57-11-4	a	6.61E-5	298.15	g	f	f	d
Nonadecanoic acid	646-30-0	a	3.32E-5	298.15	e/b	c	c	d
Eicosanoic acid	506-30-9	a	1.34E-5	298.15	g/h	c	c	i
Oxalic acid	144-62-7	j	2.74E-2	298.00	k	j	j	j
Malonic acid	141-82-2	j/l/m	3.19E-3/3.73E-1-357.494/2.07E-3	298.00/339.299-357.494/296.00	n	j	j	j
2-methyl malonic acid	516-05-2	j/o	5.34E-3/1.44E-1	298.00/298.00	p	j	j	j
2-hydroxy malonic acid	88-69-3	j	5.64E-3	298.00	n	j	j	j
Succinic acid	110-15-6	j/q/m	3.86E-3/1.21-4.30/1.39E-3	298.00/360.106-375.135/296.00	r/s	j	j	j
2-methyl succinic acid	498-21-5	j/q/o	5.58E-4/2.40E-1-1.76/3.51E-3	298.00/343.119-360.112/298.00	t	j	j	j
2-methyl, 2-hydroxy succinic acid	6236-10-8	j	7.48E-3	298.00	t	j	j	j
2-hydroxy succinic acid	6915-15-7	j	8.72E-4	298.00	r/s	j	j	j
2,3-dihydroxy succinic acid	133-37-9	j	3.23E-1	298.00	r/s	j	j	j
2-amino succinic acid	56-84-8	j	2.56E-2	298.00	N/A	j	j	j
2-keto succinic acid	328-42-7	j	1.67E-2	298.00	r/s	j	j	j
Glutaric acid	110-94-1	j/l/m	1.96E-3/0.3404-1.334/3.3E-3	298.00/348.150-363.149/296.00	u	v	v	j
2-methyl glutaric acid	617-62-9	j/q	9.63E-4/1.28E-1-4.299E-1	298.00/338.378-347.643	LK,P	j	j	j
3-methyl glutaric acid	626-51-7	j/o	9.19E-4/3.8E-3	298.00/298.00	LK,P	j	j	j
3-carboxylic, 3-hydroxy glutaric acid	77-92-9	j	3.10E-3	298.00	LK,P	j	j	j
2-amino glutaric acid	56-86-0	j	2.05E-3	298.00	N/A	j	j	j
2-keto glutaric acid	328-50-7	j	2.02E-3	298.00	u	j	j	j
3-keto glutaric acid	542-05-2	j	3.22E-3	298.00	u	j	j	j
Adipic acid	124-04-9	j/m/o	2.14E-4/3.7E-4/5.7E-4	298.00/296.00/298.00	u	v	v	j
Suberic acid	505-48-6	v/m	2.23E-5/2.4E-5	298.00/296.00	b	w	w	w
ortho-phthalic acid	88-99-3	x	1.68E-3	298.00	N/A	x	x	x
meta-isophthalic acid	121-91-5	x	1.40E-2	298.00	N/A	x	x	x
para-terephthalic acid	100-21-0	x	1.38E-1	298.00	N/A	y	y	y
1,1-cyclopropane dicarboxylic acid	598-10-7	v	3.10E-3	298.00	LK,P	v	v	v
1,1-cyclobutane dicarboxylic acid	5445-51-2	v	6.47E-3	298.00	LK,P	v	v	v
1,2-cyclopentane dicarboxylic acid	1461-96-7	v	3.47E-4	298.00	LK,P	v	v	v
1,3-cyclohexane dicarboxylic acid	3971-31-1	v	4.60E-4	298.00	LK,P	v	v	v
Azelaic acid	123-99-9	l/m	1.287E-1-3.722E-1/8.1E-5	367.062-377.038/296.00	b	z	z	l
Undecanedioic acid	1852-04-6	l	7.933E-2-2.146E-1	371.184-380.925	b	z	z	l
Dodecanedioic acid	1852-04-6	a	2.27E-4	298.00	b	z	z	z
cis-pinonic acid	473-72-3	v	7.78E-4	298.00	LK,P	v	v	v
para-anisic acid	100-09-4	x	4.76E-3	298.00	N/A	x	x	x
Vanillic acid	121-34-6	x	1.42E-3	298.00	N/A	x	x	x
Syringic acid	530-57-4	x	9.80E-4	298.00	N/A	x	x	x
Nitrocatechol	3316-09-4	x	9.99E-4	298.00	N/A	x	x	x
Levoglucosan	498-07-7	v	1.35E-4	298.00	N/A	v	v	v
ortho-dimethyl amino benzoic acid	610-16-2	x	1.07E-2	298.00	N/A	x	x	x
meta-dimethyl amino benzoic acid	99-64-9	x	6.42E-4	298.00	N/A	x	x	x
1,2-pentanediol	5345-92-0	a1	1.35-98.44	289.2-336.2	u	N/A	N/A	N/A
1,2,3-trihydroxypropane	56-81-5	a2	0.0249-1.97	298.75-341.35	n	N/A	N/A	N/A
1,4-butanediol	110-63-4	a3	13.85-84.55	329.2-351.2	r/s	N/A	N/A	N/A
2-(methylamino)ethanol	109-83-1	a4	13.94 - 92.12	274.9-296.3	N/A	N/A	N/A	N/A
2,4-pentanediol	625-69-4	a5	4.8-87.35	297.2-330.5	u	N/A	N/A	N/A
2,6-dinitrotoluene	696-20-2	a6	0.0127-1.974	277.15-323.15	N/A	a7	a7	a7
2-aminoethanol	141-43-5	a4	8.48-83.66	279.0-306.3	N/A	N/A	N/A	a4
2-aminonitrobenzene	88-74-4	a8	1.20-12.37	313.5-342.3	N/A	a9	a9	a9
2-chloro-3,5-dimethoxy-4-HBA	76341-69-0	a10	0.046-0.9	293.15-323.15	N/A	N/A	N/A	N/A
2-chloropropionic acid	598-78-7	a11	13.36-82.72	287.4-308.4	N/A	N/A	N/A	N/A
2-hydroxybenzoic acid	69-72-7	a12	0.443-2.434	307.05-323.71	N/A	a9	a9	a9
2-phenylbromide-TEGMME	929259-37-0	a13	0.061-1.446	333.2-369.9	N/A	N/A	N/A	N/A
3-(2-methoxyphenyl)PA	6342-77-4	a14	0.329-1.514	331.156-347.165	N/A	a14	N/A	a14
3-(3,4-dimethoxyphenyl)PA	2107-70-2	a14	0.1159-0.4707	352.178-366.163	N/A	a13	N/A	a14
3,4-dichloronitrobenzene	99-54-7	a15	9.1-74.69	316.3-346.5	N/A	N/A	N/A	a15
3,4-dihydroxycyclohexene	99-54-7	a10	0.6-8.7	293.15-323.15	N/A	N/A	N/A	a16
3,5-di-tert-butylcatechol	1020-31-1	a17	0.270-5.58	313.2-346.2	N/A	a17	est	a17
3,7-dimethyl-7-hydroxyoctanol	107-75-5	a17, a18	0.117-15.87	283.355-332.65	LK,P	N/A	N/A	N/A
3-chloro-2,6-dimethoxyphenol	18113-22-9	a10	0.52-7.1	293.15-323.15	N/A	N/A	N/A	a19
3-chloroaniline	108-42-9	a15	6.02-76.82	291.2-325.3	N/A	N/A	N/A	a15
3-hydroxypropanenitrile	109-78-4	a20	15.64-91.47	306.3-331.4	N/A	N/A	N/A	a21
3-nitro-3-(4-nitrophenyl)-pentane	204189-06-0	a8	0.063-1.920	321.4-358.1	N/A	N/A	N/A	N/A
3-nitrobenzoic acid	121-92-6	a22	0.604-2.03	347.16-361.16	N/A	a9, a23	a24, est	a9
3-nitrophenol	554-84-7	a25	14.74-35.51	357.2-369.3	N/A	a25	N/A	a25
4-aminobenzoic acid	150-13-0	a26	0.28-2.31	359.14-382.56	N/A	a9	est.	a9, a27
Anisole	123-11-5	a17, a18	1.32-30.4	283.95-322.95	N/A	N/A	N/A	a28
Benzyl salicylate	118-58-1	a17, a18	0.016-1.24	295.45-342.95	N/A	N/A	N/A	a17
Diethyl phthalate	84-74-2	a29	0.00191-0.0335	293.05-317.15	N/A	N/A	N/A	a30
Ethyl vanillin	121-32-4	a18, a31	0.96-3.78	323.35-337.45	N/A	a32	N/A	a32
Eugenol	97-53-0	a18, a33	0.64-20.00	285.45-326.75	N/A	N/A	N/A	a21
Glycerine carbonate	931-40-8	a34	0.29-46.94	330.2-398.5	N/A	N/A	N/A	N/A
Heliotropin	120-57-0	a18, a31	0.58-11.60	293.45-326.85	N/A	est	N/A	a18
Isoamyl salicylate	87-20-7	a17, a18	0.22-8.93	287.95-328.55	N/A	N/A	N/A	N/A
1'-hydroxy-1,1'-bis(cyclohexyl)-2-one	28746-99-8	a35	1.23-6.64	308.22-330.4	LK,P	N/A	N/A	a35
Methyl anthranilate	134-20-3	a18, a36	2.32-13.73	299.45-319.15	N/A	N/A	N/A	a18, a36
Musk Ambrette	83-96-9	a18, a31	0.303-1.33	328.55-345.45	N/A	est	N/A	a18, a31
N-methylidethanolamine	105-59-9	a37	0.61-80.9	293.69-333.0	N/A	N/A	N/A	N/A
1-(4-Methoxyphenyl)ethanone	100-06-1	a36	5.60-25.5	313.55-333.45	N/A	N/A	N/A	a36
1,3,5-benzenetriol	108-73-6	a38	0.82-5.06	381.31-404.58	N/A	a1	est	a1
Pimelic acid	111-16-0	v/l/m	2.6E-4/1.928E-1-7.761E-1/3.4E-4	298.00/358.149-371.656/296.00	b	w, a39	w, a39	l, a39
Pinonaldehyde	2704-78-1	a40	0.09-0.6	263.15-278.15	LK,P	N/A	N/A	N/A
Tetraethylene glycol	112-60-7	a41	0.173-44.7	323.23-398.23	N/A	N/A	N/A	a21
Triacetin	102-76-1	a42	0.0512-2.081	284.2-318.2	N/A	N/A	N/A	a21
Triethylene glycol dinitrate	111-22-8	a42	0.025-2.21	303.4-348.0	N/A	N/A	N/A	N/A

Table S1: u = Chattopadhyay and Ziemann (2005), b = Ambrose and Walton (1989), c = Schaake et al. (1982a), d = Gaikwad and Subrahmanyam (1985), e = Morgan and Kobayashi (1994), f = Schaake et al. (1982b), g = Macknick and Pransnitz (1979), h = Chirico et al. (1989), i = Adriaanse et al. (1964), j = Booth et al. (2010), k = Straty and Tsunuma (1976), l = da Silva et al. (1999b), m = Biale et al. (2003), n = Kratzke (1989), o = Munster et al. (2004), p = Aston et al. (1940), q = da Silva et al. (2001), r = Flebbe et al. (1982), s = Martinez-Ortiz and Manley (1978), t = Schumann et al. (1942), v = Ewing and Ochoa (2006), w = Booth et al. (2011), LK,P = Reid et al. (1987), u = Roux et al. (2005), x = Booth et al. (2012), y = Huang et al. (2009), z = Cingolani and Berchiesi (1974), $a1$ = Verevkin (2004), $a2$ = Cammenga et al. (1977), $a3$ = Vasilisova et al. (2005), $a4$ = Kapteina et al. (2005), $a5$ = Verevkin (2007), $a6$ = Pella (1977), $a7$ = Finch and Payne (1990), $a8$ = Verevkin (1997), $a9$ = Domalski and Hearing (2006), $a10$ = Lei et al. (1999), $a11$ = Lagoa et al. (2002), $a12$ = Colomina (1981), $a13$ = Dabrowska et al. (2006), $a14$ = Monte and Hillesheim (2001), $a15$ = Verevkin and Schick (2003), $a16$ = Parke and Williams (1955), $a17$ = Serpinski et al. (1955), $a18$ = Serpinski et al. (1958), $a19$ = Varshnicikova et al. (1958), $a20$ = Roux et al. (2007), $a21$ = Dykyi and Repas (1979), $a22$ = da Silva et al. (1999a), $a23$ = Rai and Mandal (1990), $a24$ = Andrews (1926), $a25$ = Heintz et al. (2007), $a26$ = Dekruif et al. (1979), $a27$ = Andrews et al. (1926), $a28$ = Kendall and Gibbons (1915), $a29$ = Birks and Bradley (1949), $a30$ = Song et al. (2003), $a31$ = Serpinski et al. (1953), $a32$ = Sierget et al. (2005), $a33$ = Serpinski et al. (1957), $a34$ = Verevkin et al. (2008), $a35$ = Shevelova et al. (2006), $a36$ = Serpinski et al. (1954), $a37$ = Noll (1998), $a38$ = de Wit et al. (1983), $a39$ = Steele et al. (2002), $a40$ = Hallquist et al. (1997), $a41$ = Hales et al. (1981), $a42$ = Woodman and Adicoff (1963). \star N/A denotes chemicals that have a group not specified in the Caponet and Muller (2006) method and thus do not require P_{hc}^{ref} .

References

- N. Adriaanse, H. Dekker, and J. Coops. Some physical constants of normal, saturated fatty acids and their methyl esters. *Recl. Trav. Chim. Pays-Bas*, 83:557, 1964.
- D. Ambrose and J. Walton. Vapour pressures up to their critical temperatures of normal alkanes and 1-alkanols. *Pure & Appl. Chem.*, 61:8:1395–1403, 1989.
- D.H. Andrews. The specific heats of some isomers of the type ortho, meta and para c₆h₄xy from 110 to 340 k. *Bulletin of the American Chemical Society*, 48:1287–1299, 1926.
- D.H. Andrews, G. Lynn, and J. Johnson. The heat capacities and heat of crystallisation of some isomeric aromatic compounds. *J. Am. Chem. Soc.*, 48(5):1274–1287, 1926.
- J.G. Aston, R.M. Kennedy, and S.C. Schumann. The heat capacity and entropy, heats of fusion and vaporisation and the vapor pressure of isobutane. *J. American Chem. Soc.*, 62:2059–2063, 1940.
- M. Bilde, B. Svenningsson, J. Mønster, and T. Rosenørn. Even-odd alteration of evaporation rates and vapor pressures of c₃-c₉ dicarboxylic acid aerosols. *Environ. Sci. Technol.*, 37:1371–1378, 2003.
- J. Birks and R.S. Bradley. The rate of evaporation of droplets .2. the influence of changes of temperature and of the surrounding gas on the rate of evaporation of drops of di-normal-butyl phthalate. *Proceedings of the Royal Society of London Series a-Mathematical and Physical Sciences*, 198(1053):226–239, 1949.
- A. M. Booth, M. H. Barley, D. O. Topping, G. McFiggans, A. Garforth, and C. J. Percival. Solid state and sub-cooled liquid vapour pressures of substituted dicarboxylic acids using Knudsen Effusion Mass Spectrometry (KEMS) and Differential Scanning Calorimetry. *Atmospheric Chemistry and Physics*, 10(10):4879–4892, May 2010. ISSN 1680-7324. doi: 10.5194/acp-10-4879-2010. URL <http://www.atmos-chem-phys.net/10/4879/2010/>.
- A.M. Booth, W.J. Montague, M.H. Barley, D.O. Topping, G. McFiggans, A. Garforth, and C.J. Percival. Solid state and sub-cooled liquid vapour pressures of cyclic aliphatic dicarboxylic acids. *Atmos. Chem. Phys.*, 11:655–665, 2011.
- A.M. Booth, T. Bannan, M.R. McGillen, M.H. Barley, D.O. Topping, G. McFiggans, and C.J. Percival. The role of ortho, meta, para, isomerism in measured solid state and derived sub-cooled liquid vapour pressures of substituted benzoic acids. *RSC Advances*, 2:4430–4443, 2012.
- H.K. Cammenga, F.W. Schulze, and W. Theuerl. Vapor pressure and evaporation coefficient of glycerol. *J. Chem. Eng. Data*, 22(2):131–134, 1977.
- M. Capouet and J.-F. Muller. A group contribution method for estimating the vapour pressures of α -pinene oxidation products. *Atmospheric Chemistry and Physics*, 6:1455–1467, 2006.
- S. Chattopadhyay and P.J. Ziemann. Vapor pressures of substituted and unsubstituted monocarboxylic and dicarboxylic acids measured using an improved thermal desorption particle beam mass spectrometry method. *Aerosol Science and Technology*, 39:11:1085–1100, 2005.
- R.D. Chirico, A. Nguyen, W.V. Steele, and M.M. Strube. Vapor pressure of *n*-alkanes revisited. new high-precision vapor pressure data on *n*-decane, *n*-eicosane, and *n*-octacosane. *J. Chem. Eng. Data*, 34:149–156, 1989.
- A. Cingolani and G. Berchiesi. Thermodynamic properties of organic compounds. *J. Thermal Analysis*, 6:87–91, 1974.
- M. Colomina. Propiedades termoquímicas de derivados del ácido benzoico. *Anales de Química*, 177:114–117, 1981.
- M.A.V. Ribeiro da Silva, M.A.R. Matos, M.J.S. Monte, D.M. Hillesheim, M.C.P.O. Marques, and N.F.T.G. Vieira. Enthalpies of combustion, vapour pressures, and enthalpies of sublimation of three methoxy-nitrobenzoic acids. vapour pressures and enthalpies of sublimation of the three nitrobenzoic acids. *J. Chem. Thermodynamics*, 31: 1429–1441, 1999a.
- M.A.V. Ribeiro da Silva, M.J.S. Monte, and J.R. Ribeiro. Vapour pressures and the enthalpies and entropies of sublimation of five dicarboxylic acids. *J. Research of the National Bureau of Standards - A. Physics and Chemistry*, 80A(1):35–39, 1999b.
- M.A.V. Ribeiro da Silva, M.J.S. Monte, and J.R. Ribeiro. Thermodynamic study on the sublimation of succinic acid and of methyl- and dimethyl-substituted succinic and glutaric acids. *J. Chem. Thermodynamics*, 33:23–31, 2001.
- A. Dabrowska, A. Sporzynski, and S.P. Verevkin. Vapour pressures and enthalpies of vaporisation of a series of aromatic ethers of mono-, di- and triethylene glycol. *Fluid Phase Equilibria*, 249(1-2):115–119, 2006.
- H.G.M. de Wit, J.A. Bouwstra, J.G. Blok, and C.G. de Kruif. Vapor pressures and lattice energies of oxalic acid, mesotartaric acid, phloroglucinol, myoinositol, and their hydrates. *J. Chem. Physics*, 78(3):1470–1475, 1983.
- C.G. Dekruif, J. Voogd, and J.C.A. Offringa. Enthalpies of sublimation and vapor-pressures of 14 amino-acids and peptides. *J. Chem. Thermodynamics*, 11(7):651–656, 1979.

- E.S. Domalski and E.D. Hearing. Heat capacities and entropies of organic compounds in the condensed phase. volume iii. *J. Physical and Chemical Reference Data*, 25:1–525, 2006.
- J. Dykyi and M. Repas. *Saturation Vapor Pressure of Organic Compounds*. Veda Vydavatelstvo Slovenskej Akademie Vied, Bratislava, 1979.
- M.B. Ewing and J.C. Sanchez Ochoa. Vapor pressures of *n*-pentane determined by comparative ebulliometry. *J. Chem. Thermodynamics*, 38:289–295, 2006.
- A. Finch and J. Payne. Thermochemical study of 2,6-dinitrotoluene. *Thermochimica Acta*, 164:55–63, 1990.
- J.L. Flebbe, D.A. Barclay, and D.B. Manley. Vapor pressures of some C₄ hydrocarbons and their mixtures. *J. Chem. Eng. Data*, 27:405–412, 1982.
- B.R. Gaikwad and V.V. Subrahmanyam. Melting behavior of fatty alcohols and their binary blends. *J. Indian Chem. Soc.*, 62:513, 1985.
- J.L. Hales, R.C. Cogman, and W.J. Frith. A transpiration-glc apparatus for measurement of low vapor concentration. *J. Chem Thermodynamics*, 13(6):591–601, 1981.
- M. Hallquist, I. Wängberg, and E. Ljungström. Atmospheric fate of carbonyl oxidation products originating from α -pinene and Δ^3 -carene: Determination of rate of reaction with OH and NO₃ radicals, UV absorption cross sections, and vapor pressures. *Environ. Sci. Technol.*, 31:3166–3172, 1997.
- A. Heintz, S. Kapteina, and S.P. Verevkin. Pairwise-substitution effects and intramolecular hydrogen bonds in nitrophenols and methylnitrophenols. thermochemical measurements and ab initio calculations. *Journal of Physical Chemistry A*, 111(28):6552–6562, 2007.
- H. Huang, Z. Zeng, W. Xue, and W. Zhu. Solubility of terephthalic acid in the reaction system oligomeric bishydroxybutyl terephthalates-1,4-butanediol. *Polymer Engineering and Science*, 49:819–823, 2009.
- S. Kapteina, K. Slowik, S.P. Verevkin, and A. Heintz. Vapor pressures and vaporization enthalpies of a series of ethanalamines. *J. Chem. Eng. Data*, 50:398–402, 2005.
- J. Kendall and W.A. Gibbons. The addition compounds of aldehydes and ketones with organic acids. *J. Am. Chem. Soc.*, 37:149–162, 1915.
- H. Kratzke. Thermodynamic quantities for propane 1. the vapour pressure of liquid propane. *J. Chem. Thermodynamics*, 12:305–309, 1980.
- A.L.C. Lagoa, H.P. Diogo, and M.E. Minas da Piedade. Energetics of the C-Cl bond in CH₃CH(Cl)COOH. enthalpy of formation of (S)-(-)-2-chloropropionic acid and of the 1-carboxyethyl radical. *J. Phys. Chem. A*, 106:9855–9861, 2002.
- Y.D. Lei, F. Wania, W.Y. Shiu, and D.G.B. Boocock. Temperature dependent vapor pressures of chlorinated catechols, syringols, and syringaldehydes. *J. Chem. Eng. Data*, 44:200–202, 1999.
- A.B. Macknick and J.M. Prausnitz. Vapor pressures of high-molecular-weight hydrocarbons. *J. Chem. Eng. Data*, 24(3):175–178, 1979.
- J.A. Martínez-Ortiz and D.B. Manley. Vapor pressures for the system isobutane-isobutylene-*n*-butane. *J. Chem. Eng. Data*, 23(2):165–167, 1978.
- J. Mønster, T. Rosenørn, B. Svenningsson, and M. Bilde. Evaporation of methyl- and dimethyl-substituted malonic, succinic, glutaric and adipic acid particles at ambient temperatures. *J. Aerosol Science*, 35:1453–1465, 2004.
- M.J.S. Monte and D.M. Hillesheim. Thermodynamic study on the sublimation of 3-phenylpropionic acid and of three methoxy-substituted 3-phenylpropionic acids. *J. Chem. Thermodynamics*, 33(8):837–847, 2001.
- D.L. Morgan and R. Kobayashi. Direct vapor pressures measurements of ten *n*-alkanes in the C₁₀-C₂₈ range. *Fluid Phase Equilibria*, 97:211–242, 1994.
- O. Noll. Vapor pressures and liquid densities of *n*-methylethanolamine, diethanolamine, and *n*-methyldiethanolamine. *ELDATA: The International Electronic Journal of Physico-Chemical Data*, 4(3):105–120, 1998.
- D.V. Parke and R.T. Williams. Studies in detoxication. 63. metabolism of halogenbenzenes .a. meta-dichlorobenzene .b. further observations on the metabolism of chlorobenzene. *Biochemical Journal*, 59(3):415–422, 1955.
- P.A. Pella. Measurement of the vapour pressures of TNT, 2,4-dnt, 2,6-dnt, and egdn. *J. Chem. Thermodynamics*, 9:301–305, 1977.
- U.S. Rai and K.D. Mandal. Chemistry of organic eutectics - para-phenylenediamine-*m*-nitrobenzoic acid system involving the 1-2 addition compound. *Bulletin of the Chemical Society of Japan*, 63(5):1496–1502, 1990.

- R.C. Reid, J.M. Prausnitz, and B.E. Poling. *The Properties of Gases and Liquids*. McGraw-Hill, New York and London, 4 edition, 1987.
- M.V. Roux, M. Temprado, and J.S. Chickos. Vaporization, fusion and sublimation enthalpies of the dicarboxylic acids from C₄ to C₁₄ and C₁₆. *J. Chem. Thermodynamics*, 37:941–953, 2005.
- M.V. Roux, R. Notario, E. Velez, M. Temprado, A. Guerrero, S.P. Verevkin, J. Quijano, and J. Gaviria. Experimental and computational thermochemical study of 3-hydroxypropanenitrile. *J. Chem. Thermodynamics*, 39(10):1377–1383, 2007.
- R.C.F. Schaake, J.C. van Miltenburg, and C.G. de Kruif. Thermodynamic properties of the normal alkanolic acids i. molar heat capacities of seven odd-numbered normal alkanolic acids. *J. Chem. Thermodynamics*, 14:763–769, 1982a.
- R.C.F. Schaake, J.C. van Miltenburg, and C.G. de Kruif. Thermodynamic properties of the normal alkanolic acids i. molar heat capacities of seven even-numbered normal alkanolic acids. *J. Chem. Thermodynamics*, 14:771–778, 1982b.
- S.C. Schumann, J.G. Aston, and M. Sagenkahn. The heat capacity and entropy, heats of fusion and vaporization and the vapor pressures of isopentane. *J. American Chem. Soc.*, 64:1039–1043, 1942.
- V.V. Serpinskiĭ, S.A. Voitkevich, and N.Y. Lyuboshitz. Determination of saturated vapour pressures of fragrances. *Zhurnal Fizicheskoi Khimii*, 27:1032–1038, 1953.
- V.V. Serpinskiĭ, S.A. Voitkevich, and N.Y. Lyuboshitz. Opredelenie davleniya nasyschennogo para nekotorykh dushistykh veshchestv .3. *Zhurnal Fizicheskoi Khimii*, 28(11):1969–1974, 1954.
- V.V. Serpinskiĭ, S.A. Voitkevich, and N.Y. Lyuboshits. Determination of saturated vapour pressure of some aromatic principles. *Zhurnal Fizicheskoi Khimii*, 29(4):653–657, 1955.
- V.V. Serpinskiĭ, S.A. Voitkevich, and N.Y. Lyuboshitz. Determination of the saturated vapor pressures of some odorous substances .6. *Zhurnal Fizicheskoi Khimii*, 31(6):1278–1284, 1957.
- V.V. Serpinskiĭ, S.A. Voitkevich, and N.Y. Lyuboshits. Results of determination of pressures of saturated vapour of 36 aromatic substances. *Trudy Vsesoyuz. Nauch.-Issledovatel. Inst. Sintet.i Natural. Dushistykh Veshchestv*, 4: 125–130, 1958.
- M.P. Shevelyova, D.H. Zaitsau, Y.U. Paulechka, and G.J. Kabo. Thermodynamics of 2-(1'-hydroxycyclohexyl)cyclohexane: Vaporization, sublimation, and the ideal gas state thermodynamic properties. *J. Chem. Eng. Data*, 51:1946–1952, 2006.
- M. Skerget, L. Cretnik, Z. Knez, and M. Skrinjar. Influence of the aromatic ring substituents on phase equilibria of vanillins in binary systems with CO₂. *Fluid Phase Equilibria*, 231(1):11–19, 2005.
- W.L. Song, A. Li, and X.Q. Xu. Water solubility enhancement of phthalates by cetyltrimethylammonium bromide and beta-cyclodextrin. *Industrial & Engineering Chemistry Research*, 42(5):949–955, 2003.
- W.V. Steele, R.D. Chirico, A.B. Cowell, S.E. Knipmeyer, and A. Nguyen. Thermodynamic properties and ideal-gas enthalpies of formation for 1,4-diisopropylbenzene, 1,2,4,5-tetraisopropylbenzene, cyclohexane oxime, dimethyl malonate, glutaric acid, and pimelic acid. *J. Chem. Eng. Data*, 47:725–739, 2002.
- G.C. Straty and R. Tsumura. Pvt and vapor pressure measurements on ethane. *J. Research of the National Bureau of Standards - A. Physics and Chemistry*, 80A(1):35–39, 1976.
- D. Varhanickova, S.C. Lee, W. Shiu, and D. Mackay. Aqueous solubilities of chlorocatechols, chlorovanillins, chlorosyringols, and chlorosyringaldehydes at 25-degrees-c. *J. Chem. Eng. Data*, 40:620–622, 1958.
- T.V. Vasil'tsova, S.P. Verevkin, E. Birch, and A. Heintz. Thermodynamic properties of mixtures containing ionic liquids. activity coefficients of ethers and alcohols in 1-methyl-3-ethyl-imidazolium bis(trifluoromethyl-sulfonyl) imide using the transpiration method. *J. Chem. Eng. Data*, 50:142–148, 2005.
- S.P. Verevkin. Thermochemistry of nitro compounds. experimental standard enthalpies of formation and improved group-additivity values. *Thermochimica Acta*, 307:17–25, 1997.
- S.P. Verevkin. Determination of vapour pressures and enthalpies of vaporisation of 1,2-alkanediols. *Fluid Phase Equilibria*, 224:23–29, 2004.
- S.P. Verevkin. Vapor pressures and enthalpies of vaporization of a series of the 1,3-alkanediols. *J. Chem. Eng. Data*, 52:301–308, 2007.
- S.P. Verevkin and C. Schick. Determination of vapour pressures, enthalpies of sublimation, enthalpies of vaporisation, and enthalpies of fusion of a series chloro-aminobenzenes and chloro-nitrobenzenes. *Fluid Phase Equilibria*, 211(2): 161–177, 2003.

S.P. Verevkin, A.V. Toktonov, Y. Chernyak, B. Schäfer, and A. Börner. Vapour pressure and enthalpy of vaporization of cyclic alkaline carbonates. *Fluid Phase Equilibria*, 268(1-2):1–6, 2008.

A.L. Woodman and A. Adicoff. Vapor pressure of triacetin, triethylene glycol denigrate and metriol trinitrate. *J. Chem. Eng. Data*, 8:241–242, 1963.

2.2 Paper 2

As discussed in sect. 1.9, observations of field and laboratory particulates show that under certain scenarios, particle-phase diffusion can limit gas-particle partitioning. Modelling studies are therefore required to determine whether particle-phase diffusion can impose a significant influence on aerosol transformation in the ambient atmosphere. In addition, some diffusion measurement techniques rely on diffusion models to infer diffusion coefficients (Zobrist *et al.*, 2011; Lienhard *et al.*, 2014; Steimer *et al.*, 2015). Three numerical methods for solving unsteady state diffusion have been proposed, each with a different framework (Smith *et al.*, 2003; Zobrist *et al.*, 2011; Shiraiwa *et al.*, 2012). However, despite the potentially important role of particle-phase diffusion and indeed, some modelling sensitivity studies already conducted into its effect on particulate transformation (e.g. Lienhard *et al.*, 2015), the numerical solutions to diffusion had not been compared. In this second paper, the solutions are compared across a variety of scenarios to assess their consistency. The result is intended to inform modellers of the reliability and required model setup of each numerical solution.

Paper 2

The rate of equilibration of viscous aerosol particles



The rate of equilibration of viscous aerosol particles

Simon O'Meara¹, David O. Topping^{1,2}, and Gordon McFiggans¹

¹Centre for Atmospheric Science, School of Earth, Atmospheric & Environmental Sciences, University of Manchester, Manchester, M13 9PL, UK

²National Centre for Atmospheric Science (NCAS), University of Manchester, Manchester, M13 9PL, UK

Correspondence to: Gordon McFiggans (g.mcfiggans@manchester.ac.uk)

Received: 14 December 2015 – Published in Atmos. Chem. Phys. Discuss.: 18 January 2016

Revised: 4 April 2016 – Accepted: 5 April 2016 – Published: 28 April 2016

Abstract. The proximity of atmospheric aerosol particles to equilibrium with their surrounding condensable vapours can substantially impact their transformations, fate and impacts and is the subject of vibrant research activity. In this study we first compare equilibration timescales estimated by three different models for diffusion through aerosol particles to assess any sensitivity to choice of model framework. Equilibration times for diffusion coefficients with varying dependencies on composition are compared for the first time. We show that even under large changes in the saturation ratio of a semi-volatile component (e_s) of 1–90% predicted equilibration timescales are in agreement, including when diffusion coefficients vary with composition. For condensing water and a diffusion coefficient dependent on composition, a plasticising effect is observed, leading to a decreased estimated equilibration time with increasing final e_s . Above 60% final e_s maximum equilibration times of around 1 s are estimated for comparatively large particles (10 μm) containing a relatively low diffusivity component ($1 \times 10^{-25} \text{ m}^2 \text{ s}^{-1}$ in pure form). This, as well as other results here, questions whether particle-phase diffusion through water-soluble particles can limit hygroscopic growth in the ambient atmosphere. In the second part of this study, we explore sensitivities associated with the use of particle radius measurements to infer diffusion coefficient dependencies on composition using a diffusion model. Given quantified similarities between models used in this study, our results confirm considerations that must be taken into account when designing such experiments. Although quantitative agreement of equilibration timescales between models is found, further work is necessary to determine their suitability for assessing atmospheric impacts, such as their inclusion in polydisperse aerosol simulations.

1 Introduction

Recent attention on the phase state of atmospheric particles has motivated questions about the means to model diffusion through them. It had been conventionally assumed that particles possess a liquid phase state, such that timescales of diffusion were much less than their atmospheric residence times. However, several recent studies present evidence that particles can exist in an amorphous solid state (Smith et al., 2002; Murray and Bertram, 2008; Virtanen et al., 2010; Vaden et al., 2011). Viscosities for amorphous solid particles will be higher than for liquid ones, resulting in lower condensed phase diffusion coefficients and potentially limiting the rate of gas-particle partitioning for condensing or evaporating components. For such particles it is important to critically assess models that attempt to predict or infer the effects of diffusion limitations in order to report findings with confidence.

Fick's first and second laws of diffusion state that the rate of transport of a given component through a given area is proportional to the concentration gradient normal to the area. The Fickian diffusion coefficient (D_i) is the proportionality constant between the diffusive flux and the concentration gradient (Eq. 1).

Recent attempts at modelling diffusion through particles have centred on Fick's second law, which in spherical coordinates is

$$\frac{\partial C_i(r, t)}{\partial t} = \frac{1}{r^2} \frac{\partial}{\partial r} \left(r^2 D_i \frac{\partial C_i(r, t)}{\partial r} \right), \quad (1)$$

where C is the concentration of species i , r is the radius from the particle centre and t is time. Fick's second law is applied when the concentration gradient, and therefore flux, changes

with time and distance, i.e. non-steady state. This study analyses and compares three approximations of Eq. (1) used to model diffusion through particles:

- i. The ETH model presented by Zobrist et al. (2011), based on the Euler forward step method;
- ii. The “kinetic multi-layer model of gas-particle interactions in aerosol and clouds” (KM-GAP) (Shiraiwa et al., 2012), based on coupled differential equations;
- iii. The Fick's Second Law solved by partial differential equation model (hereafter referred to as Fi-PaD), a formulation of which was used in Smith et al. (2003).

A description of each model is provided in the method below. For a system with D_i independent of composition, it has been reported that Fi-PaD and KM-GAP give very similar results (Shiraiwa et al., 2010). To our knowledge however, no detailed comparison of all three approaches, including cases of D_i dependent on composition, has yet been published. Despite this, a recent study by Lienhard et al. (2015) linked the impact of particulate viscosity on ice nucleation using a composition dependent D_i . A critical review of these models is intended to guide those with an interest in simulating particle evolution inside instruments, chamber experiments, and the ambient atmosphere. For non-equilibrium viscous particles, diffusivity (along with other properties such as volatility) determines the temporal evolution of particle composition and size- and number-distributions (Zaveri et al., 2014). These are key factors determining aerosol impact on climate and health, therefore the choice of diffusion model could have far-reaching consequences (Pöschl, 2005). In addition to differences in modelled particle size and composition change, inappropriate choice of model formulation and assumptions therein could lead to differences in inferred properties, such as diffusion coefficients from single particle levitation measurements (Lienhard et al., 2014; Zobrist et al., 2011).

The numerical methods employed by all three models involve discretisation in time and space. However, subtle differences in how they define concentration gradients may induce variations in estimated diffusion rate. Therefore, it is expected that any differences in rate will increase with greater heterogeneity in the concentration-radius profile, i.e. an increasingly steep diffusion front. Such fronts have been observed when water and glassy organics diffuse through one another (Nowakowski et al., 2015). It is currently unclear which of the models investigated here, if any, is suitable to such a situation, given the paucity of experimental data available.

Indeed, the Fickian framework may not be appropriate for some systems; in polymer studies it is well known that non-Fickian diffusion occurs for many examples of liquids diffusing through glassy polymers (Thomas and Windle, 1982; Kee et al., 2005), and in such systems a narrow diffusion front is often observed (e.g. Thomas and Windle, 1982). Non-Fickian diffusion results from structural changes following

diffusion and the resultant composition change. It arises when the rate of deformation is comparable to that of diffusion (Crank, 1975). Alternative models have been proposed, such as the free volume model (He et al., 2006; Price et al., 2014) and the Maxwell-Stefan model (Krishna and Wesselingh, 1997). The aim of this study, however, is to compare the estimated equilibration timescales of the Fickian diffusion models that are used in atmospheric aerosol science and, in turn, assess sensitivities of derived diffusion coefficients in such particles. In most test cases below the diffusing semi-volatile component has the self-diffusion coefficient of water at room temperature, and the resulting diffusion timescales are most relevant to water and water-soluble particles, however, the findings regarding consistency between models are applicable to components with self-diffusion coefficients across the investigated range (2×10^{-9} – 1×10^{-25} m² s⁻¹).

2 Method

2.1 Model description

The ETH model, KM-GAP and Fi-PaD used the same representation of an aerosol particle: it was assumed spherical, and split into concentric shells. A comparatively thin surface shell was assumed to equilibrate instantly with the gas-phase in all simulations (for the purpose of comparing particle-phase diffusion models and gaining insight into the limitation imposed by particle-phase diffusion on mass-transfer this assumption is reasonable). The initial concentration profile in bulk shells (those below the surface) was homogeneous, and in equilibrium with the initial gas phase concentration. Figure 1a demonstrates how the particle is represented in a 2-D view. Figure 1b illustrates the concentration-radius profiles of a semi-volatile component at several time steps using the ETH model in the case of an instantaneous increase in saturation ratio from 1 to 90% when the diffusion coefficient is independent of composition. In contrast, Fig. 1c shows the same information but when the diffusion coefficient has a logarithmic dependence on composition and the self-diffusion coefficients of the two components are very different, that of the non-volatile ($D_{\text{nv}}^0 = 1 \times 10^{-21}$ m² s⁻¹) and for the semi-volatile ($D_{\text{sv}}^0 = 2 \times 10^{-9}$ m² s⁻¹). The “diffusion front” is clear in this example and arises from the very different diffusion coefficient values in neighbouring shells that result from variations in shell composition.

The e -folding time for the difference in concentration of the semi-volatile component at the surface ($[\text{sv}]_{\text{eq}}$) and of its average concentration across the particle bulk ($\overline{[\text{sv}]_b}$) was used as a metric for diffusion time by Zaveri et al. (2014). It is readily transferable to other studies, and is the chosen metric for diffusion timescale here. The ratio of the concentration difference in the surface and bulk-average of the semi-volatile component at any time (t) to that difference at $t = 0$

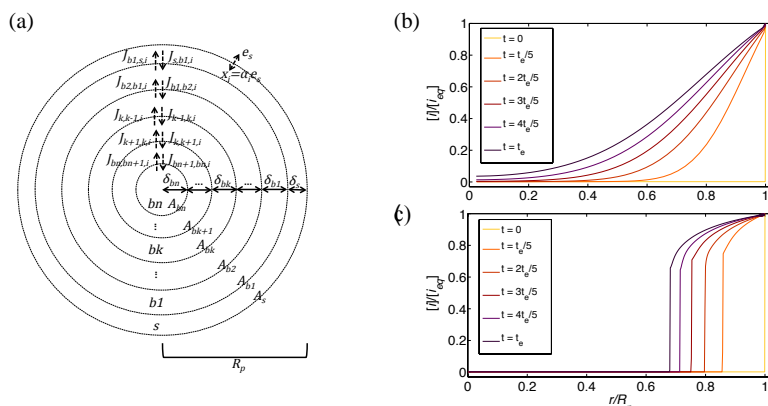


Figure 1. (a) A schematic of a particle split into shells, as used in the diffusion models, with shell boundaries represented by lines, and symbols relating to those used in the model equations (α_i , X_i and e_s are the accommodation coefficient, particle-phase mole fraction and vapour-phase saturation ratio of the semi-volatile, respectively). The relative width of the surface shell is shown larger than that used in models for clarity. (b, c) The concentration-radius profiles estimated using the ETH model at various times during diffusion for a semi-volatile component diffusing inwards with an initial mole fraction of 0.01 and equilibrium mole fraction of 0.90 (instantaneous change in saturation ratio of 1–90% assuming ideality), where t_e is the e -folding time. Note that the axes are relative, and normalised by the total radius (R_p) of the particle on the abscissa and by the equilibrium concentration ($[i]_{\text{eq}}$) on the ordinate. (b) is for the diffusion coefficient independent of composition and (c) is for the diffusion coefficient with a logarithmic dependence on mole fraction ($D_{\text{nv}}^0 = 1 \times 10^{-25}$, $D_{\text{sv}}^0 = 2 \times 10^{-9} \text{ m}^2 \text{ s}^{-1}$).

is

$$Q = \frac{[\text{SV}]_{\text{eq}} - \overline{[\text{SV}]_{\text{b}, t \geq 0}}}{[\text{SV}]_{\text{eq}} - \overline{[\text{SV}]_{\text{b}, t = 0}}} \quad (2)$$

The e -folding time was therefore the time taken for Q to increase/decrease by a factor of e^1 . Figure 1b and c therefore demonstrate the concentration-radius profiles at several steps between $Q = 1$, which occurs at $t = 0$, and $Q = e^{-1}$, which marks the e -folding time. Comparing e -folding times between models strictly only tests model consistency at this particular stage of diffusion and not before this. However, e -folding time agreement would indicate agreement at previous times (and future ones), because the underlying equations are identical. For reassurance on this, concentration-radius profiles at times prior to the e -folding time were compared. All models were run on a 12 core Intel Core i7 processor with a speed of 3.2 GHz.

Fick's first law, which assumes a constant concentration gradient and therefore flux, with time, is the basis of the ETH model. However, following the Euler forward step method, if time steps are sufficiently short this model should be able to capture changes in concentration gradient, and therefore flux, and therefore replicate the second law. The flux between shells is thus found by

$$J_{\text{bk}, \text{bk}-1, i} = -A_{\text{bk}} D_{\text{bk}, \text{bk}-1, i} \frac{([i]_{\text{bk}} - [i]_{\text{bk}-1})}{0.5(\delta_{\text{bk}} + \delta_{\text{bk}-1})}, \quad (3)$$

where J is the flux (mol s^{-1}) between bulk (b) shell numbers k and $k-1$ (ascending from $k=1$ for the near-surface shell to $k=n$ at the centre). If $k=1$, then $k-1$ is the surface layer (s). A is the surface area of the shell's outer surface. $D_{\text{bk}, \text{bk}-1, i}$ is the diffusion coefficient at the shell boundary and here is found using one of the dependencies on composition given in Sect. 2.3. $[i]$ is concentration of component i at the shell centre and δ is shell width. Figure 1a demonstrates how these terms relate to the physical representation of the particle. From Eq. (3) the change in number of moles in a shell is found by:

$$\Delta N_{\text{bk}, i} = (J_{\text{bk}, \text{bk}-1, i} - J_{\text{bk}+1, \text{bk}, i}) \Delta t, \quad (4)$$

where Δt is the time interval (setting of Δt is described in Sect. 2.2). The version of the ETH model we have written was tested against the model output in Zobrist et al. (2011), and found to replicate their results accurately (Fig. A1 in the Appendix for the replica plot).

In KM-GAP the number of moles of a component in a shell is found by integrating the following coupled ordinary differential equations (ode) with respect to time:

$$\frac{dN_{\text{s}, i}}{dt} = (J_{\text{b1}, \text{s}, i} - J_{\text{s}, \text{b1}, i}), \quad (5)$$

$$\frac{dN_{b1,i}}{dt} = (J_{s,b1,i} - J_{b1,s,i}) + (J_{b2,b1,i} - J_{b1,b2,i}), \quad (6)$$

$$\frac{dN_{bk,i}}{dt} = (J_{bk+1,bk,i} - J_{bk,bk+1,i}) + (J_{bk-1,bk,i} - J_{bk,bk-1,i}), \quad (k = 2, \dots, n-1), \quad (7)$$

$$\frac{dN_{bn,i}}{dt} = (J_{bn-1,bn,i} - J_{bn,bn-1,i}). \quad (8)$$

The flux is found by

$$J_{bk,bk\pm 1,i} = K_{bk,bk\pm 1,i} [i]_{bk} A_{bk}, \quad (9)$$

where K is the transport rate coefficient (m s^{-1}):

$$K_{bk,bk\pm 1,i} = \frac{2D_{bk,bk\pm 1,i}}{(\delta_{bk} + \delta_{bk\pm 1})}, \quad (10)$$

where δ is shell width. $D_{bk,bk\pm 1,i}$ is the diffusion coefficient at the shell boundary (Sect. 2.3). Note that in Eqs. (9) and (10), if $k = 1$, then $k - 1$ is the surface shell (s).

Equations (5)–(10) were solved in Matlab software using the ode23tb numerical solver, which has an adaptive time step. It was found that the solver became increasingly unstable as the gradient of D_i with r increased, thus error tolerances (given in the Appendix) were increased appropriately. ode23tb uses a Runge–Kutta method of two stages: a trapezoidal rule followed by a backward differentiation formula stage.

Fi-PaD treats Eq. (1) as an initial-boundary problem, with initial conditions:

$$C_{bk,i}(r < R_p, 0) = C_{i,\text{eq}}^0, \quad (11)$$

$$C_{s,i}(R_p, 0) = C_{i,\text{eq}}, \quad (12)$$

where eq represents the equilibrium condition. Equation (11) states that initial concentrations in the bulk shells are in equilibrium with the original e_s value, whilst Eq. (12) states that the initial concentration at the surface is in equilibrium with the new e_s . The boundary conditions were

$$\frac{\partial N_i(0, t)}{\partial t} = 0, \quad (13)$$

$$\frac{\partial C_i(R_p, t)}{\partial t} = 0, \quad (14)$$

where R_p is the particle radius. Equation (13) states that there is no flux at the centre of the particle and Eq. (14) states that the concentration of components at the surface is constant. For Fi-PaD the numerical solver pdepe in Matlab software was used. The solver uses the method of lines, which discretises the problem in space to gain a system of ordinary differential equations that are then solved using the numerical solver ode15s in Matlab. ode15s is similar to ode23tb in that both are designed for stiff systems, however, ode15s has a high order of accuracy for a given error tolerance. The default error tolerances for pdepe were found to provide stable solutions across the range of parameter spaces used here; the contrast to the variable error tolerances used in KM-GAP is attributed to the difference in the accuracy of their ode solvers.

2.2 Particle representation

Particles were assumed to consist of two components: a non-volatile (nv) and semi-volatile (sv), which were assigned the molar mass and density of sucrose and water, respectively. In general, components with relatively high molar masses are expected to have comparatively low diffusion coefficients (Haynes, 2015). To test the effect of using a high molar mass component against using sucrose on equilibration times, a molar mass (M) of 700 g mol^{-1} (M of sucrose = $342.296 \text{ g mol}^{-1}$) and density (p) of $2.0 \times 10^3 \text{ kg m}^{-3}$ (p of sucrose = $1.5805 \times 10^3 \text{ kg m}^{-3}$) was assigned to the non-volatile component and its self-diffusion coefficient was set relatively low: $1.0 \times 10^{-25} \text{ m}^2 \text{ s}^{-1}$. When the saturation ratio of the semi-volatile component (e_s) increased from 1–90 % the e -folding times for all three models increased between 13–16 % from those using sucrose values (since the molar volume of the non-volatile component increased a decreased semi-volatile component concentration was required to attain equilibrium, leading to a decreased concentration gradient for the same change in e_s). Since these changes to e -folding times are similar across the models and are for a comparatively large change in e_s , our conclusions are expected to be applicable to a broad range of component M and p values.

All models assumed ideality for most simulations (see later) so that at equilibrium the value of e_s equalled the mole fraction of the semi-volatile component in the condensed phase. While estimates of accommodation coefficients for semi-volatiles cover a wide range, for the purposes of this study we have held it constant at unity (as has been found reasonable for that of water vapour on liquid water in multiple studies, e.g. Kolb et al., 2010). Assuming ideality, the volume of a component was equal to the product of its number of moles (N) and molar volume. The volume of a shell was therefore given by

$$V_{bk} = N_{\text{nv},bk} \left(\frac{M_{\text{nv}}}{p_{\text{nv}}} \right) + N_{\text{sv},bk} \left(\frac{M_{\text{sv}}}{p_{\text{sv}}} \right), \quad (15)$$

where M is molar mass and p is density.

To accurately simulate the size change in particles resulting from condensation (growth) or evaporation (shrinkage), at the end of each time interval, shell volumes were recalculated using the new values of $N_{i,bk}$. In KM-GAP and Fi-PaD, a maximum change to the particle radius of 0.1 % was allowed per time step; if the radius change exceeded 0.1 % the interval was iteratively shortened until the change was acceptable. Decreasing this maximum acceptable change did not change e -folding times significantly (< 2 % for both KM-GAP and Fi-PaD when a maximum radius change of 0.01 % was used instead), thus it was considered sufficient to account for volume change. For the ETH model, it has been recommended that to ensure model stability, the number of moles inside any shell should not change by more than 2 % over a single time interval (Zobrist et al., 2011). The same

condition was used here because values below 2% did not change predicted e -folding times significantly (< 1% change when maximum change in number of moles was 0.01% instead).

Bulk shells (those below the surface) were initially set to have equal widths. The surface shell represents the sorption layer, where transfer between the condensed and gas-phase occurs. Since the surface shell is contained within the initial particle diameter, the width should be sufficiently thin to not significantly affect the e -folding time, i.e. one must not decrease the width of bulk shells such that diffusion is accelerated. A factor of 1×10^{-3} of the particle radius was chosen to calculate the surface shell width because using lower factors resulted in no significant change to estimated e -folding time.

During condensation the surface shell expands; however, since this shell simulates the boundary between the shell and the gas-phase it should remain comparatively thin. Therefore, if the surface shell grew to double its initial width, it was reduced back to its initial width by transferring the excess volume to the near-surface shell, or, if this near-surface shell had a width greater than the total radius divided by the number of shells, the transferred material was used to make a new near-surface shell. The concentration of components in the transferred material was the same as in the surface shell (i.e. at equilibrium with the gas phase). This approach had potential to introduce numerical diffusion by decreasing the distance for diffusion in the case of introducing a new shell and decreasing the concentration gradient in the case of transfer.

To gain an indication of whether numerical diffusion influenced one model more than another, e -folding times were found with this approach (transfer on) and without it (transfer off). For the latter case the surface shell was allowed to grow without adjustment, leading to an unrealistically wide shell and comparatively longer equilibration times, but eliminating the possibility of numerical diffusion. If numerical diffusion affected one model more than another we would expect the difference in e -folding times between the transfer on and transfer off cases to vary between them. However, there was no substantial difference between models: for a change in e_s of 1–90% all models had an increase of 20–30% in e -folding times from the transfer on to the transfer off case; and for a change in e_s of 60–80% the increase was between 6 and 10%. These differences are negligible in comparison to the several orders of magnitude change in e -folding times seen across the range of non-volatile component diffusivity used below.

During evaporation the width of the surface shell decreased and the mass of non-volatile component in the surface shell tended toward zero. If the surface shell decreased below a factor of 1×10^{-1} of its initial width it was returned to its initial width by transferring a sufficient volume from the near-surface shell. The concentration of components in the transferred material was equal to that in the surface shell, thus the concentration in the surface shell was maintained

and any excess semi-volatile component was presumed to evaporate. Similarly, if the near-surface shell shrank to below a factor of 1×10^{-1} of the initial width of the surface shell, then the two shells were coalesced into a new surface shell at equilibrium concentration. It was found that decreasing the width at which transfer and coalescence were invoked led to a decrease and convergence of predicted e -folding times, indicating decreasing numerical diffusion (which could occur due to steepening of the concentration gradient through either coalescence or transfer). A decrease of no more than 1% was seen across models and changes in e_s when using lower factors than 1×10^{-1} of the initial width of the surface shell, thus this factor was concluded to be sufficiently low to effectively prevent numerical diffusion.

2.3 D Dependence

At any point in the particle the diffusion coefficient of both components was the same, i.e., we assumed symmetrical diffusion coefficients, which is valid for an ideal binary mixture (Wesselingh and Bollen, 1997). We compared models using three functions of D_i :

- i. D_i independent of the semi-volatile mole fraction (x_{sv}) and therefore fixed throughout the simulation;
- ii. D_i with a logarithmic dependence on semi-volatile mole fraction, which has been observed for ideal systems by Vignes (1966):

$$D_i(x_{sv}) = D_{sv}^{0x_{sv}} D_{nv}^{0(1-x_{sv})}, \quad (16)$$

where D_{sv}^0 is the self-diffusion coefficient of the semi-volatile component and D_{nv}^0 is the self-diffusion coefficient of the non-volatile component;

- iii. D_i with a sigmoidal dependence on x_{sv} , which was observed for the citric acid-water system by Lienhard et al. (2014):

$$D_i(x_{sv}) = D_{sv}^{0x_{sv}\alpha} D_{nv}^{0(1-x_{sv}\alpha)}, \quad (17)$$

where α is a correction parameter given by

$$\ln(\alpha) = (1 - x_{sv})^2 [C + 3D - 4D(1 - x_{sv})]. \quad (18)$$

Where the values of C and D were chosen as -3.105 and 3.300 respectively. These provided a relatively steep “cliff-edge” sigmoidal dependence and therefore a substantial variation from the logarithmic dependence, enabling a test of consistency between models across a wide range of dependencies. Examples of these dependencies are shown in Fig. 2.

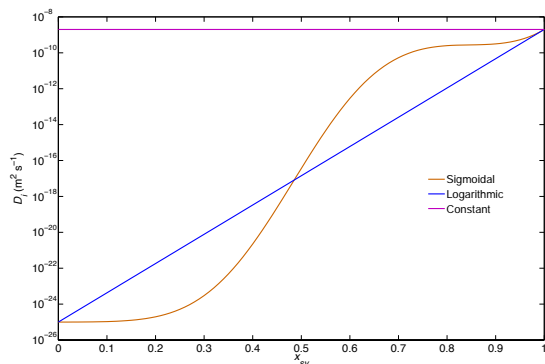


Figure 2. Example dependencies of D_i on the mole fraction of the semi-volatile component. For the constant case both components have a value of $2 \times 10^{-9} \text{ m}^2 \text{ s}^{-1}$ and for the other cases the self-diffusion coefficient of the semi-volatile component is set to $2 \times 10^{-9} \text{ m}^2 \text{ s}^{-1}$ and that of the non-volatile is $1 \times 10^{-25} \text{ m}^2 \text{ s}^{-1}$.

For the latter two cases $D_i(x_{sv})$ was calculated within the numerical solvers of KM-GAP and Fi-PaD, whilst for the ETH model it was calculated at the start of each time step. x_{sv} at a shell boundary was found using the arithmetic mean concentration of the semi-volatile component across the bounding shells.

In the first part of the study we compare the equilibration timescales estimated by models when the diffusion coefficient is constant and when it follows the logarithmic and sigmoidal dependencies on composition given above. Self-diffusion coefficients of the non-volatile and semi-volatile components range between that of water at room temperature, $2.0 \times 10^{-9} \text{ m}^2 \text{ s}^{-1}$ (Starr et al., 1999), and a comparatively low value of $1.0 \times 10^{-25} \text{ m}^2 \text{ s}^{-1}$, which according to the Stokes–Einstein relationship between diffusivity and viscosity, is representative of a glassy material (Debenedetti and Stillinger, 2001). e -folding times are found for several changes in the vapour-phase saturation ratio of a semi-volatile component, and across a range of particle sizes and differences in the self-diffusion coefficient of components.

Finally, we present an example of the differences in modelled particle size change with time when different dependencies of D_i on composition are assumed, thereby providing guidance on the most effective experimental procedure for inference of diffusion coefficient dependencies on composition. For actual inferences one would preferably have good knowledge of the system's deviation from ideality. In an attempt to replicate a real system, we therefore use the estimation for water activity and density as a function of sucrose weight fraction presented in Zobrist et al. (2011). The initial and surface shell water activity were set equal to the initial and current gas-phase saturation ratio of water (the saturation ratio changed with time), respectively, with the accommodation coefficient of water assumed to be one.

3 Results

Numerical convergence of e -folding times was observed with increasing spatial resolution for all three models due to improved resolution of concentration gradients and therefore changes in D_i (when dependent on composition) and flux with space. e -folding times showed an exponential relationship with shell number (e.g. Fig. A2), thus the criteria for shell number was that at which the e -folding time was within 10 % of the asymptote. Generally as the gradient of D_i with particle radius increased, the shell number increased to maintain convergence (Table A2). However, increasing the shell number increases the possibility of accumulating significant round-off error, in addition to requiring greater computer time. The round-off error at the chosen resolution was investigated by halving the number of significant numbers assigned to variable values. The difference in predicted e -folding times between the two precisions was found to be negligible, with a maximum of 2 %, indicating that round-off error was not a substantial source of inaccuracy.

Zobrist et al. (2011) reported requiring up to several thousand shells in the ETH model to resolve concentration gradients. However, we found that using of the order of hundreds gave convergence for the cases with steepest concentration gradients (Fig. A2). The difference in required shell resolution between the studies could be due to differences in D_i dependence on composition. Using the Matlab software it was found that computational time for the case of diffusion coefficient independent of composition was quickest, gradually increasing as the steepness of the diffusion coefficient dependence on composition increased, largely due to the greater spatial resolution. For D_i independent of composition the ETH model took of the order 1 s to reach the e -folding state while KM-GAP and Fi-PaD were of the order 10^2 s. For a steep diffusion coefficient dependence, the chosen example was the logarithmic dependence, with $D_{nv}^0 = 1 \times 10^{-25}$ and $D_{sv}^0 = 2 \times 10^{-9} \text{ m}^2 \text{ s}^{-1}$ and e_s instantaneously increased from 1 to 90 %: to reach e -folding states the ETH model took of the order 10^2 s while both KM-GAP and Fi-PaD took of the order 10^4 s.

In the first model comparison, e -folding times were found when D_i was independent of x_{sv} . For a complete analysis of model output, initial particle diameters ($D_{p,t=0}$) were varied between 1×10^{-5} and 1×10^{-8} m, which covers most of the size range observed in the ambient atmosphere (Seinfeld and Pandis, 2006) and D_i ranged between 2.0×10^{-9} and $1.0 \times 10^{-25} \text{ m}^2 \text{ s}^{-1}$. e -folding times were found across this parameter space for a change in e_s of 1–90 and 90–1 % for all three models. This relatively large change in e_s was chosen to create a large concentration gradient, as this would most likely induce disagreement between models. However, all models agreed very well across the whole range of particle size and D_i (Fig. A3).

In the next case D_i varied logarithmically with mole fraction of the semi-volatile, between a maximum of

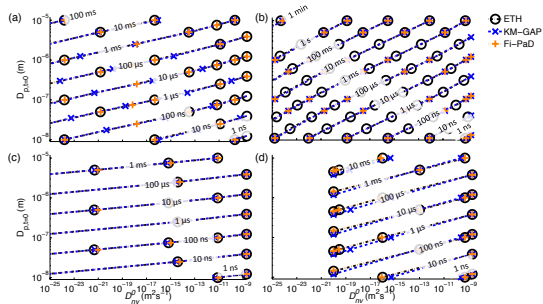


Figure 3. e -folding time contour plots for different changes to the saturation ratio of the semi-volatile component (Δe_s) and different diffusion coefficient dependencies: (a) $\Delta e_s = 1\text{--}90\%$ logarithmic dependence, (b) $\Delta e_s = 90\text{--}1\%$, logarithmic dependence, (c) $\Delta e_s = 1\text{--}90\%$, sigmoidal dependence, and (d) $\Delta e_s = 90\text{--}1\%$ sigmoidal dependence. D_{nv}^0 is the diffusion coefficient at a semi-volatile mole fraction of 0, while D_{sv}^0 (diffusion coefficient at a semi-volatile mole fraction of 1) was fixed at $2.0 \times 10^{-9} \text{ m}^2 \text{ s}^{-1}$.

$2.0 \times 10^{-9} \text{ m}^2 \text{ s}^{-1}$ at $x_{sv} = 1$ and a minimum given by D_{nv}^0 (i.e. D_i at $x_{sv} = 0$). D_{nv}^0 ranged between 2.0×10^{-9} and $1.0 \times 10^{-25} \text{ m}^2 \text{ s}^{-1}$. Contour plots of e -folding times as a function of D_{nv}^0 and $D_{p,t=0}$ and for a 1–90 and a 90–1 % change in e_s are shown in Fig. 3a and b, respectively.

For both changes in e_s there is good agreement of e -folding times between all models, with a maximum variation of 10 %, which is well within the uncertainty caused by varying degrees of numerical convergence and potential numerical diffusion. Diffusion times are much shorter than in the constant D_i case due to the high diffusivity of the semi-volatile component. Figure 3a shows that even when starting with a glassy particle, if the saturation ratio of a plasticising semi-volatile component increases sufficiently, the e -folding state can be reached in less than 1 s. For the decreasing e_s used in Fig. 3b a low diffusivity outer casing will form on the particle, impeding diffusion and evaporation. However, Fig. 3b shows that if a particle initially of water-like diffusivity is quickly dried, the e -folding state is reached within 10 s, even when the non-volatile component has a relatively low diffusivity.

e -folding times for 1–90 and 90–1 % changes in e_s were also found using the sigmoidal dependence of D_i on x_{sv} ; the results are given in Fig. 3c and d, respectively. In the 90–1 % case an unpractical computer time ($> 12 \text{ h}$) was required to attain numerical convergence at low values of D_{nv}^0 , therefore the minimum D_{nv}^0 is $1 \times 10^{-20} \text{ m}^2 \text{ s}^{-1}$. For this relatively large change in e_s the sigmoidal dependence induces a steeper diffusion front than the logarithmic dependence. Despite this, the models show good agreement here also. In the 1–90 % case, a maximum variation in e -folding times of 5 % is seen while for 90–1 % this value is 30 %. This latter variation is between KM-GAP and the other two models and

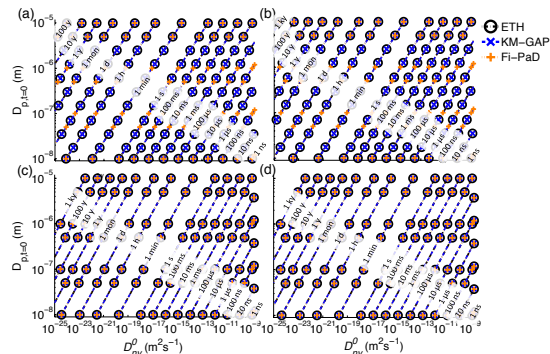


Figure 4. e -folding time contour plots for different changes to the saturation ratio of the semi-volatile component (Δe_s) and different diffusion coefficient dependencies: (a) $\Delta e_s = 10\text{--}20\%$ logarithmic dependence, (b) $\Delta e_s = 20\text{--}10\%$, logarithmic dependence, (c) $\Delta e_s = 10\text{--}20\%$, sigmoidal dependence, and (d) $\Delta e_s = 20\text{--}10\%$ sigmoidal dependence. D_{nv}^0 is the diffusion coefficient at a semi-volatile mole fraction of 0, while D_{sv}^0 (diffusion coefficient at a semi-volatile mole fraction of 1) was fixed at $2.0 \times 10^{-9} \text{ m}^2 \text{ s}^{-1}$.

is greater than expected from different degrees of numerical convergence. However, given the gradual divergence of the e -folding isolines in Fig. 3d, we do not attribute the discrepancy to model framework differences, but to an insufficient shell resolution in KM-GAP. Diffusion is quicker using the sigmoidal dependence than the logarithmic dependence, particularly for the 90–1 % scenario. This is explained by the higher D_i values at $x_{sv} > 0.5$ (Fig. 2).

e_s changes more realistic of the atmosphere were also tested. Results for 60–80 and 80–60 % (Fig. A4) are similar to those for 1–90 and 90–1 % for their respective D_i dependency; there is good model agreement, and across the $D_{p,t=0}$ and D_{nv}^0 range and for both dependencies, e -folding time is less than 1 s. Results for 10–20 and 20–10 %, given in Fig. 4, also show agreement between models. For both dependencies diffusion is much slower than in the 1–90 and 60–80 % simulations, approaching 1 ky at low D_{nv}^0 and high $D_{p,t=0}$. This shows that at low saturation ratios of semi-volatile component, gas-particle partitioning can be limited by condensed-phase diffusion in viscous particles.

e -folding times between models were also found to be in good agreement for these changes in e_s when D_{nv}^0 was fixed at $1.0 \times 10^{-25} \text{ m}^2 \text{ s}^{-1}$ and D_{sv}^0 was varied between 1.0×10^{-25} and $2 \times 10^{-9} \text{ m}^2 \text{ s}^{-1}$. As discussed, the agreement between models in estimating e -folding times indicates that the estimated profiles of concentration with particle radius prior to the e -folding state are consistent between models because the underlying equations are the same. By comparing concentration-radius profiles at various stages of diffusion we indeed found good model agreement across all cases. In Fig. 5 we show the example of the logarithmic

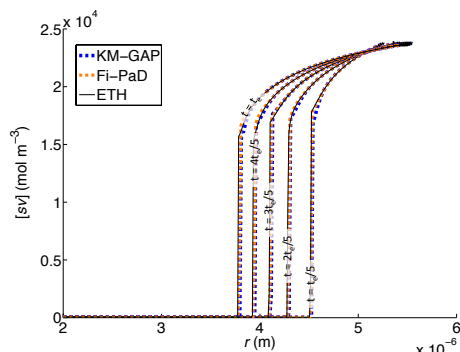


Figure 5. The concentration ($[sv]$)-radius (r) profiles of the semi-volatile component at times (t) preceding and including the e -folding time (t_e) as estimated by the three models given in the legend, for the case of logarithmic dependence of D_i on x_{sv} , an instantaneous increase in e_s from 1 to 90 % and with $D_{nv}^0 = 1 \times 10^{-25}$ and $D_{sv}^0 = 2 \times 10^{-9} \text{ m}^2 \text{ s}^{-1}$. Note that for clarity the radius axis begins at $2 \times 10^{-6} \text{ m}$ and not 0 m.

mic dependence of D_i on x_{sv} , an instantaneous change in saturation ratio of 1–90 % and with $D_{nv}^0 = 1 \times 10^{-25}$ and $D_{sv}^0 = 2 \times 10^{-9} \text{ m}^2 \text{ s}^{-1}$. At several times preceding and including e -folding time the concentration-radius profiles are in good agreement.

In the final part of this study the estimated temporal profile of particle radius was compared between the sigmoidal and logarithmic D_i dependencies. We have used the water activity and density dependence on sucrose weight fraction as described in Zobrist et al. (2011) for the sucrose-water system in an attempt to replicate a non-ideal system. The ETH model was employed, though the results above indicate that KM-GAP and Fi-PaD would produce identical profiles. For the inference of D_i dependency from radius measurements the signal to noise ratio is minimised by inducing a large change in radius relative to the measurement accuracy over a timespan that is large compared to the measurement frequency.

Taking the case of water as the semi-volatile component, from Fig. 3 it is clear that for certain values of D_{nv}^0 and certain changes in e_s attaining a large ratio of equilibrium time to measurement frequency may be difficult, even if the change in radius is large. Indeed, the radius-time profiles in Figs. 6 and 7 for instantaneous changes in e_s and a $D_{nv}^0 = 1 \times 10^{-25} \text{ m}^2 \text{ s}^{-1}$ confirm that for changes with a high final e_s , significant radius change is estimated to occur over less than 1 s, while the measurement frequency reported in the studies of Zobrist et al. (2011) and Lienhard et al. (2014) is approximately 15 s. Nevertheless, for the e_s change of 1–90 % in Fig. 5, there is a notable difference in the radius profiles between the dependencies. Despite having lower D_i at low x_{sv} , the radius change from the sigmoidal dependence is more rapid than the logarithmic, in-

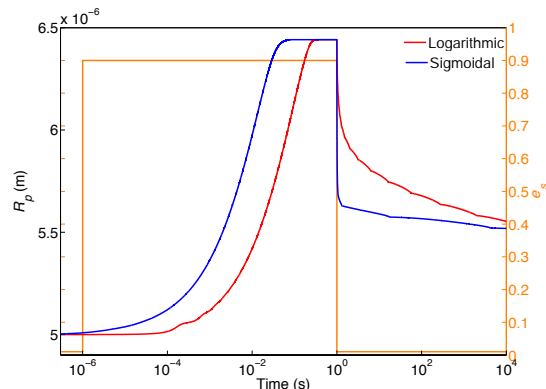


Figure 6. The radius (R_p) change with time for a single particle subject to the changes in e_s shown by the orange curve and right vertical axis. Here $D_{sv}^0 = 2 \times 10^{-9}$ and $D_{nv}^0 = 1 \times 10^{-25} \text{ m}^2 \text{ s}^{-1}$ using the D_i dependencies given in the legend.

dicating that the D_i at higher x_{sv} has a dominating effect on the profile. The inference of D_i dependency using such a large change in e_s is therefore poorly constrained for lower x_{sv} . For better constraint smaller changes in e_s are required, such as those used in Lienhard et al. (2014). An example of the radius profiles following incremental changes in e_s , $D_{nv}^0 = 1 \times 10^{-25}$, $D_{sv}^0 = 2 \times 10^{-9} \text{ m}^2 \text{ s}^{-1}$ and using both dependencies is shown in Fig. 7. This plot demonstrates the need for consideration of the time a given e_s is maintained in measurement experiments, since the difference in the equilibrium timescales between the e_s increments covers several orders of magnitude. Indeed, over low changes in e_s such as between 1–10 %, equilibration time may be too long to be practical for gaining a useful measurement of radius change. It is worthwhile to note that the rate of change of e_s over an increment is preferably much greater than the rate of equilibration, as this provides the greatest potential for a clear signature of the D_i dependence and therefore greatest constraint on inference.

4 Discussion and conclusion

The results above show that despite variations in their numerical methods, all three Fickian-based diffusion models tested here: the ETH model, KM-GAP and Fi-PaD give good agreement of estimated e -folding timescales over a wide range of changes to the saturation ratio of the semi-volatile component and over a wide range of differences in the self-diffusion coefficient of the semi-volatile and non-volatile components. Furthermore, there is good agreement between models when different dependencies of diffusion coefficient on composition are used. This result has not been reported before to our knowledge and verifies consistency between existing Fickian

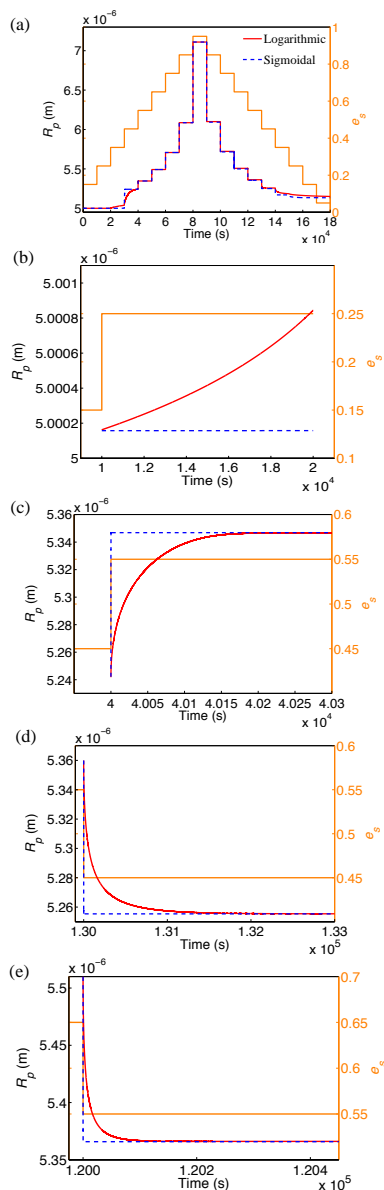


Figure 7. (a) Radius (R_p) change with time for a single particle experiencing the changes in saturation ratio of the semi-volatile component (e_s) shown by the orange curve (allied with the right vertical axis), for $D_{sv}^0 = 2 \times 10^{-9}$ and $D_{nv}^0 = 1 \times 10^{-25} \text{ m}^2 \text{ s}^{-1}$ and using the D_i dependencies given in the legend. (b–e) Time intervals of (a) over select changes in e_s (as shown by their orange curve and right vertical axes).

diffusion models. The maximum disagreement in e -folding times for results gained with satisfactory shell resolution is 10 %, which is within the uncertainty generated by varying degrees of numerical convergence and potential numerical diffusion. The consistency in modelled concentration-radius profiles at times preceding and including the e -folding state (Fig. 5) shows that if used for a polydisperse aerosol population, the models would give agreement in changes to the size distribution. In addition, if the diffusing component were reactive the rate of particle-phase reaction would depend on its concentration; therefore model agreement in concentration-radius profiles would give consistent reaction rates across the particle (which in turn could affect diffusion rate).

Using the three diffusion models as described above and with the spatial resolutions presented in the Appendix, the ETH model takes approximately 2 orders of magnitude less computer time than Fi-PaD or KM-GAP for a given diffusion scenario. With the models giving consistent estimates of diffusion, the ETH model therefore appears to be favourable.

The e -folding times given in Fig. 3 for changes in e_s of 1–90 and 90–1 %, and in Fig. A4 for changes of 60–80 and 80–60 %, show that for a semi-volatile component with water-like (at room temperature) diffusivity, given a sufficiently high starting/finishing e_s , attainment of the e -folding state is effectively instant compared to residence times in the atmosphere and chamber experiments. This is due to the plasticising effect of water (and applies to any semi-volatile component with a sufficiently high self-diffusion coefficient). At lower values of e_s diffusion time can be much longer (Fig. 4), consistent with measurement studies (e.g. Zobrist et al., 2011; Lienhard et al., 2014). The question therefore arises that for a given D_{sv}^0 , at what e_s can equilibration be assumed instant? Figure 7 indicates that for water condensing at room temperature equilibration time is less than 1 s when the final e_s is greater than 50 % for the sigmoidal dependence used here and when it is greater than 60 % for the logarithmic dependence. These results indicate no limitation on mass transfer of water from particle-phase diffusion at high relative humidity and at ambient temperature, and therefore no impediment to the formation of cloud droplets. Experimental results from Lienhard et al. (2014) and Zobrist et al. (2011) indicate that this is also true down to ~ 250 K.

For a hygroscopicity tandem differential mobility analyser (HTDMA), which has a typical residence time of 20–25 s (Zardini et al., 2008) and e_s increase of ~ 90 % from an initial value < 10 %, Figs. 3 and 5 show that equilibration is attained even when sampling relatively large ($\sim 1 \times 10^{-5}$ m) particles containing components of relatively low diffusivity (self-diffusion coefficients $\sim 1 \times 10^{-25} \text{ m}^2 \text{ s}^{-1}$).

Note, however, that we have not considered extreme dependencies of D_i on composition. If, for example, a very high mole fraction of water were required before the “cliff-edge” in the sigmoidal dependence (Fig. 2) was reached, longer diffusion times than those shown here would be expected.

Regarding the inference of diffusion coefficient dependence on composition from particle radius measurements, we have shown that incremental changes in e_s provide the best constraint, and note that changes should occur over a short time compared to the equilibration time. The consistency between the diffusion models shown here indicates that the choice of model does not affect the accuracy of the inferred dependence (as long as sufficient spatial and temporal resolution is used).

In a follow-up study we intend to investigate the implementation of composition-dependent D_i in the Model for Simulating Aerosol Interactions and Chemistry (MOSAIC) (Zaveri et al., 2008). MOSAIC is used for chamber and ambient studies and can therefore include, among other factors, multiple components, chemistry and volatility. Furthermore, it can model polydisperse aerosol, providing insight into how composition-dependent diffusion coefficients affect the evolution of size distributions.

As mentioned, Fickian-diffusion is, strictly speaking, limited to ideal-systems. Thus, for cases where dissolution occurs, for example, the employed or derived diffusion coefficients are actually effective values of D_i . As we mention briefly in the introduction, numerous alternative theories to Fickian diffusion exist. Although an analysis of such frameworks is beyond the scope of this study, a similar critical analysis may be useful in the future when data from more complex multicomponent systems exist.

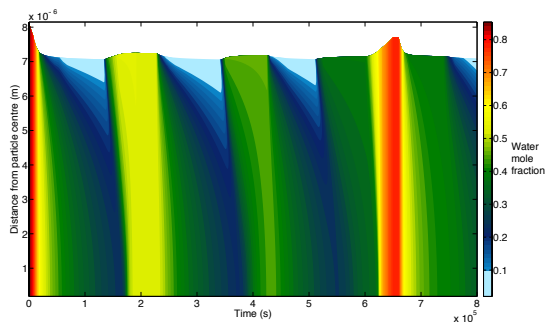


Figure A1. The water mole fraction as a function of time and distance through a single particle using the ETH model and the same inputs as for Fig. 3 of Zobrist et al. (2011).

Appendix A

To validate our version of the ETH model Fig. 3d of Zobrist et al. (2011) was reproduced using our version of the model and the relative humidity measurements presented in their Fig. 3a. Note that in reproducing this figure the dependence of diffusion coefficient on water activity given in Zobrist et al. (2011) was used. Furthermore, water activity and density estimated as a function of sucrose weight fraction, as described in Zobrist et al. (2011), was used. Our reproduction is given in Fig. A1.

Figure A2 shows the convergence of e -folding times with increasing shell number for the ETH model. Results are for self-diffusion coefficients of the semi-volatile and non-volatile components of $2.0 \times 10^{-9} \text{ m}^2 \text{ s}^{-1}$, respectively, with a logarithmic dependence of D_i on composition and change to the vapour-phase saturation ratio of the semi-volatile of 1–90 (Fig. A2a) and 90–1% (Fig. A2b). These cases were chosen because they are expected to have the strongest concentration and diffusion coefficient gradients through the particle (compared to other cases in this study) and should therefore require greatest spatial resolution. The exponential fits in Fig. A2 were obtained using Igor Pro software.

The absolute tolerances that were required to attain stability in the KM-GAP model are given in Table A1. The tolerance was dependent on the self-diffusion coefficient of the non-volatile and the initial particle diameter. The relative tolerance was kept fixed at 1.0×10^{-12} . These tolerances were used for changes to the semi-volatile saturation ratio of 1–90 and 90–1%. Since these represent the largest changes in saturation ratio used in this study, the tolerances in Table A1 are conservative values for all other cases presented in the study.

The number of shells used for each model is given in Table A2. The optimum number of shells required for acceptable numerical convergence was found to be dependent on

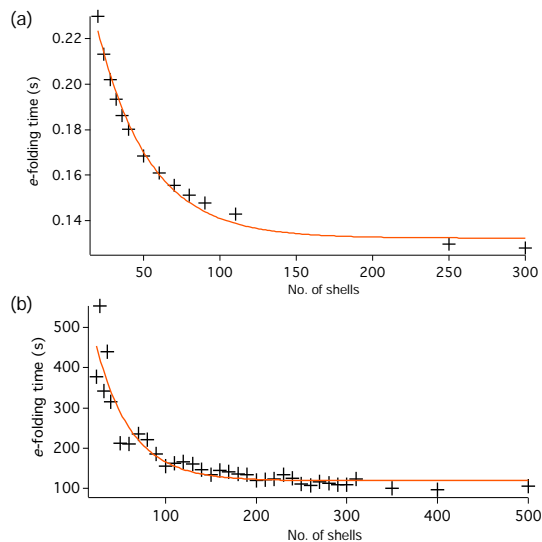


Figure A2. The e -folding time convergence with increasing shell number for the ETH model: change in the semi-volatile component saturation ratio in (a) was 1–90% and in (b) was 90–1%. The self-diffusion coefficient of the semi-volatile was $2.0 \times 10^{-9} \text{ m}^2 \text{ s}^{-1}$ and that of the non-volatile was $1.0 \times 10^{-25} \text{ m}^2 \text{ s}^{-1}$. Orange curves are the exponential best fits.

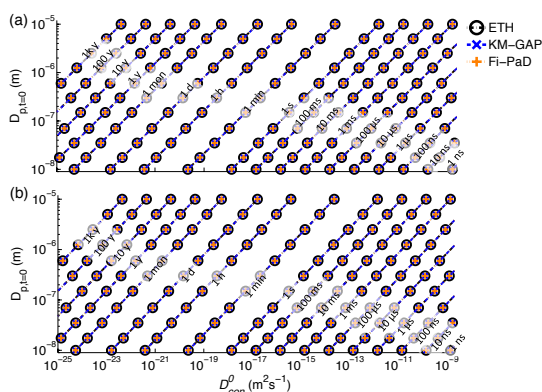


Figure A3. e -folding times (isolines) for the three models given in the legend. Where D_{con}^0 is the constant diffusion coefficient used throughout the simulation. $D_{p,t=0}$ is the initial particle diameter. In (a) the saturation ratio of the semi-volatile is increased from 1 to 90% instantaneously, whilst in (b) it is decreased from 90 to 1% instantaneously.

the change in semi-volatile saturation ratio and the difference in the self-diffusion coefficients of the components.

Results for model estimates of e -folding times when the diffusion coefficient was kept constant are given in Fig. A3. Good agreement can be seen between all three models across

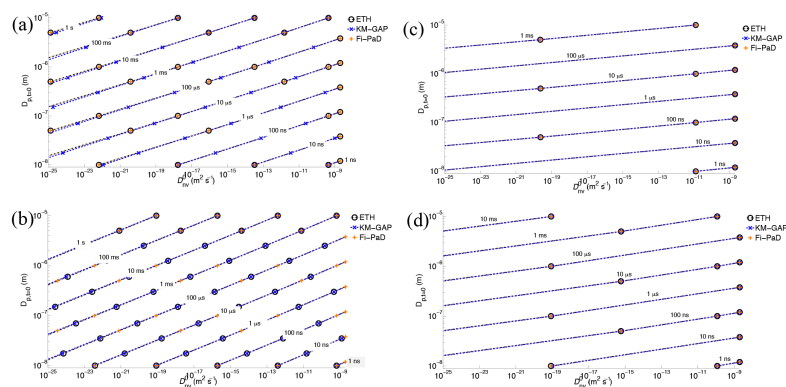


Figure A4. e -folding time contour plots for different instantaneous changes in the saturation ratio of the semi-volatile component (Δe_s) and different diffusion coefficient dependencies: (a) $\Delta e_s = 60$ – 80 % and logarithmic dependence, (b) $\Delta e_s = 80$ – 60 % and logarithmic dependence, (c) $\Delta e_s = 60$ – 80 % and sigmoidal dependence, and (d) $\Delta e_s = 80$ – 60 % and sigmoidal dependence. Models are given in the legend.

Table A1. Absolute tolerances used in KM-GAP whilst the self-diffusion coefficient of the semi-volatile component was held constant at $2.0 \times 10^{-9} \text{ m}^2 \text{ s}^{-1}$ and the saturation ratio of the semi-volatile component was increased and decreased from 1–90 and 90–1 %. The absolute tolerance required for stability depended on the self-diffusion coefficient of the non-volatile component (D_{nv}^0) and the initial particle diameter ($D_{p,t=0}$).

$D_{nv}^0 \text{ (m}^2 \text{ s}^{-1}\text{)}$	$D_{p,t=0} \text{ (m)}$			
	1.0×10^{-5}	1.0×10^{-6}	1.0×10^{-7}	1.0×10^{-8}
1.0×10^{-8} – 10^{-14}	1.0×10^{-12}	1.0×10^{-13}	1.0×10^{-14}	1.0×10^{-15}
1.0×10^{-16}	1.0×10^{-13}	1.0×10^{-14}	1.0×10^{-15}	1.0×10^{-16}
1.0×10^{-18}	1.0×10^{-14}	1.0×10^{-15}	1.0×10^{-16}	1.0×10^{-17}
1.0×10^{-20}	1.0×10^{-15}	1.0×10^{-16}	1.0×10^{-17}	1.0×10^{-18}
1.0×10^{-22}	1.0×10^{-16}	1.0×10^{-17}	1.0×10^{-18}	1.0×10^{-19}
1.0×10^{-24}	1.0×10^{-17}	1.0×10^{-18}	1.0×10^{-19}	1.0×10^{-20}
1.0×10^{-26}	1.0×10^{-18}	1.0×10^{-19}	1.0×10^{-20}	1.0×10^{-21}

the values of constant diffusion coefficient and initial particle diameter. In Fig. A4 are the e -folding times for changes of 60–80 and 80–60 % in the saturation ratio of the semi-volatile component using the logarithmic and sigmoidal dependencies of diffusion coefficient on semi-volatile component mole fraction.

Table A2. Number of shells used in each model for each change in the vapour-phase saturation ratio of the semi-volatile component (Δe_s) and for different values of non-volatile component self-diffusion coefficient (D_{nv}^0).

D_{nv}^0 ($\text{m}^2 \text{s}^{-1}$)	Δe_s					
	1–90 %	90–1 %	60–80 %	80–60 %	10–20 %	20–10 %
ETH model # shells						
1.0×10^{-8} – 10^{-14}	40	40	40	40	40	40
1.0×10^{-16} – 10^{-26}	300	300	40	40	40	40
KM-GAP # shells						
1.0×10^{-8} – 10^{-12}	40	40	40	40	40	40
1.0×10^{-14}	60	60	40	40	40	40
1.0×10^{-16}	100	100	40	40	40	40
1.0×10^{-18}	200	200	40	40	40	40
1.0×10^{-20}	250	250	100	100	40	40
1.0×10^{-22}	270	270	100	100	40	40
1.0×10^{-24}	300	300	100	100	40	40
1.0×10^{-26}	330	330	100	100	40	40
Fi-PaD # shells						
1.0×10^{-8} – 10^{-14}	40	40	40	40	40	40
1.0×10^{-16} – 10^{-26}	300	300	80	80	40	40

Author contributions. Simon O'Meara wrote the model codes, ran the simulations, created plots and tables and wrote the manuscript. David O. Topping and Gordon McFiggans provided substantial input to the method, model development and manuscript.

Acknowledgements. The Natural Environment Research Council has funded this work through the PhD studentship of Simon O'Meara, grant number NE/K500859/1, and through grant number NE/J02175X/1.

Edited by: M. Petters

References

- Crank, J.: *The Mathematics of Diffusion*, 2nd Edn., Clarendon Press, Oxford, 1975.
- Debenedetti, P. G. and Stillinger, F. H.: Supercooled Liquids and the Glass Transition, *Nature*, 410, 259–267, 2001.
- Haynes, W. M. (Ed.): *CRC Handbook of Chemistry and Physics*, 96th Edn., Internet Version 2016, available at: www.hbcpnetbase.com, 2015.
- He, X., Fowler, A., and Toner, M.: Water Activity and Mobility in Solutions of Glycerol and Small Molecular Weight Sugars: Implication for Cryo- and Lyopreservation, *J. Appl. Phys.*, 100, 074702, doi:10.1063/1.2336304, 2006.
- Kee, D. D., Liu, Q., and Hinestroza, J.: Viscoelastic (non-Fickian) Diffusion, *Can. J. Chem. Eng.*, 83, 913–929, 2005.
- Kolb, C. E., Cox, R. A., Abbatt, J. P. D., Ammann, M., Davis, E. J., Donaldson, D. J., Garrett, B. C., George, C., Griffiths, P. T., Hanson, D. R., Kulmala, M., McFiggans, G., Pöschl, U., Riipinen, I., Rossi, M. J., Rudich, Y., Wagner, P. E., Winkler, P. M., Worsnop, D. R., and O'Dowd, C. D.: An overview of current issues in the uptake of atmospheric trace gases by aerosols and clouds, *Atmos. Chem. Phys.*, 10, 10561–10605, doi:10.5194/acp-10-10561-2010, 2010.
- Krishna, R. and Wesselingh, J. A.: The Maxwell-Stefan Approach to Mass Transfer, *Chem. Eng. Sci.*, 52, 861–911, 1997.
- Lienhard, D. M., Huisman, A. J., Bones, D. L., Te, Y.F., Luo, B. P., Krieger, U. K., and Reid, J. P.: Retrieving the Translational Diffusion Coefficient of Water from Experiments on Single Levitated Aerosol Droplets, *Phys. Chem. Chem. Phys.*, 16, 16677–83, 2014.
- Lienhard, D. M., Huisman, A. J., Krieger, U. K., Rudich, Y., Marcolli, C., Luo, B. P., Bones, D. L., Reid, J. P., Lambe, A. T., Canagaratna, M. R., Davidovits, P., Onasch, T. B., Worsnop, D. R., Steimer, S. S., Koop, T., and Peter, T.: Viscous organic aerosol particles in the upper troposphere: diffusivity-controlled water uptake and ice nucleation?, *Atmos. Chem. Phys.*, 15, 13599–13613, doi:10.5194/acp-15-13599-2015, 2015.
- Murray, B. J. and Bertram, A. K.: Inhibition of Solute Crystallisation in Aqueous H^+ - NH_4^+ - SO_4^{2-} - H_2O Droplets, *Phys. Chem. Chem. Phys.*, 10, 3287–3301, 2008.
- Nowakowski, C. M., Aimutis, W. R., Helstad, S., Elmore, D. L., and Muroski, A.: Mapping Moisture Sorption Through Carbohydrate Composite Glass with Fourier Transform Near-Infrared (FT-NIR) Hyperspectral Imaging, *Food Biophys.*, 10, 207–216, doi:10.1007/s11483-014-9376-x, 2015.
- Pöschl, U.: *Atmospheric Aerosols: Composition, Transformation, Climate and Health Effects*, *Angew. Chem. Int. Edit.*, 44, 7520–40, 2005.
- Price, H. C., Murray, B. J., Mattsson, J., O'Sullivan, D., Wilson, T. W., Baustian, K. J., and Benning, L. G.: Quantifying water diffusion in high-viscosity and glassy aqueous solutions using a Raman isotope tracer method, *Atmos. Chem. Phys.*, 14, 3817–3830, doi:10.5194/acp-14-3817-2014, 2014.
- Seinfeld, J. H. and Pandis, S. N.: *Atmospheric Chemistry and Physics*, 2nd Edn., John Wiley & Sons Inc., Hoboken, NJ, USA, 2006.
- Shiraiwa, M., Pfrang, C., and Pöschl, U.: Kinetic multi-layer model of aerosol surface and bulk chemistry (KM-SUB): the influence of interfacial transport and bulk diffusion on the oxidation of oleic acid by ozone, *Atmos. Chem. Phys.*, 10, 3673–3691, doi:10.5194/acp-10-3673-2010, 2010.
- Shiraiwa, M., Pfrang, C., Koop, T., and Pöschl, U.: Kinetic multi-layer model of gas-particle interactions in aerosols and clouds (KM-GAP): linking condensation, evaporation and chemical reactions of organics, oxidants and water, *Atmos. Chem. Phys.*, 12, 2777–2794, doi:10.5194/acp-12-2777-2012, 2012.
- Smith, G. D., Woods, E., DeForest, C. L., Baer, T., and Miller, R. E.: Reactive Uptake of Ozone by Oleic Acid Aerosol Particles: Application of Single-Particle Mass Spectrometry to Heterogeneous Reaction Kinetics, *J. Phys. Chem. A*, 106, 8085–8095, 2002.
- Smith, G. D., Woods, E., Baer, T., and Miller, R. E.: Aerosol Uptake Described by Numerical Solution of the Diffusion – Reaction Equations in the Particle, *J. Phys. Chem. A*, 107, 9582–87, 2003.
- Starr, F. W., Sciortino, F., and Stanley, H. E.: Dynamics of Simulated Water under Pressure, *Phys. Rev. E*, 60, 6757–68, 1999.
- Thomas, N. L. and Windle, A. H.: A Theory of Case II Diffusion, *Polymer*, 23, 529–542, 1982.
- Vaden, T. D., Imre, D., Beranek, J., Shrivastava, M., and Zelenyuk, A.: Evaporation Kinetics and Phase of Laboratory and Ambient Secondary Organic Aerosol, *P. Natl. Acad. Sci. USA*, 108, 2190–2195, 2011.
- Vignes, A.: Diffusion in Binary Solutions, *Ind. Eng. Chem. Fund.*, 5, 189–199, 1966.
- Virtanen, A., Joutsensaari, J., Koop, T., Kannosto, J., Yli-Pirilä, P., Leskinen, J., Mäkelä, J. M., Holopainen, J. K., Pöschl, U., Kulmala, M., Worsnop, D. R., and Laaksonen, A.: An Amorphous Solid State of Biogenic Secondary Organic Aerosol Particles, *Nature*, 467, 824–27, 2010.
- Wesselingh, J. A. and Bollen, A. M.: Multicomponent Diffusivities from the Free Volume Theory, *T. I. Chem. Eng.-Lond.*, 75, 590–602, 1997.
- Zardini, A. A., Sjogren, S., Marcolli, C., Krieger, U. K., Gysel, M., Weingartner, E., Baltensperger, U., and Peter, T.: A combined particle trap/HTDMA hygroscopicity study of mixed inorganic/organic aerosol particles, *Atmos. Chem. Phys.*, 8, 5589–5601, doi:10.5194/acp-8-5589-2008, 2008.
- Zaveri, R. A., Easter, R. C., Fast, J. D., and Peters, L. K.: Model for Simulating Aerosol Interactions and Chemistry (MOSAIC), *J. Geophys. Res.*, 113, D13204, doi:10.1029/2007JD008782, 2008.
- Zaveri, R. A., Easter, R. C., Shilling, J. E., and Seinfeld, J. H.: Modeling kinetic partitioning of secondary organic aerosol and size distribution dynamics: representing effects of volatility, phase state, and particle-phase reaction, *Atmos. Chem. Phys.*, 14, 5153–5181, doi:10.5194/acp-14-5153-2014, 2014.

Zobrist, B., Soonsin, V., Luo, B. P., Krieger, U. K., Marcolli, C., Peter, T., and Koop, T.: Ultra-Slow Water Diffusion in Aqueous Sucrose Glasses, *Phys. Chem. Chem. Phys.*, 13, 3514–3526, 2011.

2.3 Paper 3

While numerical solutions to diffusion are generally applicable with respect to composition dependent diffusion and variable boundary conditions, no such analytical solution has been validated. An analytical solution would, in theory, provide a realistic simulation of particle-phase diffusion inside a regional model of aerosol transformation, accounting for other influential processes such as chemical reaction, nucleation, coagulation and variable meteorology. Implementing a numerical model inside such a framework is comparatively computationally expensive, while the analytical solution offers a relatively computationally efficient solution. For the limiting case of diffusion coefficient independent of composition, Zaveri *et al.* (2014) have verified an analytical solution to diffusion against a numerical solution. Therefore, the purpose of this paper is to investigate a correction for the Zaveri *et al.* (2014) solution to make it generally applicable to composition dependent diffusion. Such a solution would provide modellers with an ability to realistically assess the sensitivity of particulate transformation, such as number size distribution, to particle-phase diffusion in a regional model.

Paper 3

Implementing a more realistic efficient model for particle-phase diffusion, limitations to a general approach

Implementing a more realistic efficient model for particle-phase diffusion, limitations to a general approach

Simon O'Meara, David Topping, Rahul Zaveri, Gordon McFiggans

1 Abstract

Mounting evidence demonstrates that under certain conditions the rate of component partitioning between the gas- and particle-phase in atmospheric aerosol is limited by particle-phase diffusion. To date, however, particle-phase diffusion has not been incorporated to regional atmospheric models. An analytical rather than numerical solution to diffusion through particulate matter is desirable because of its comparatively small expense in regional models. Current analytical models assume diffusion to be independent of composition, and therefore use a constant diffusion coefficient. To realistically model diffusion, however, it should be composition dependent (e.g. due to the partitioning of components that plasticise, vitrify or solidify). This study assesses the modelling capability of an analytical solution to diffusion corrected to account for composition dependence, against a numerical solution. Results show reasonable agreement when the gas-phase saturation ratio of a partitioning component is constant and particle-phase diffusion limits partitioning rate ($< 10\%$ discrepancy in estimated radius change). However, when the saturation ratio of the partitioning component varies a generally applicable correction could not be found, indicating that existing methodologies are incapable of deriving a general solution. Until such time as a general solution is found, caution should be given to sensitivity studies that assume constant diffusivity. The correction was implemented in the polydisperse multi-process Model for Simulating Aerosol Interactions and Chemistry (MOSAIC), and is used to illustrate how the evolution of number size distribution may be accelerated by condensation of a plasticising component with a constant saturation ratio.

2 Introduction

The accurate simulation of atmospheric aerosol transformation has been identified as a key component of assessing aerosol impact on climate and health (Jacobson & Streets, 2009; Fiore *et al.*, 2012; Boucher *et al.*, 2013; Glotfelty *et al.*, 2016). However, comprehensive

modelling of the physicochemical processes that determine aerosol transformation across large spatial and temporal scales can be challenging due to the limitations of computer power (Zaveri *et al.*, 2008). While the majority of processes in large-scale models are solved by numerical methods, analytical solutions offer less computational expense. Particle-phase diffusion may be solved both analytically, under certain assumptions, or numerically (Crank, 1975).

The advantage of an analytical solution over a numerical one is the decreased computer expense (e.g. Smith *et al.*, 2003; Zobrist *et al.*, 2011; Shiraiwa *et al.*, 2012). The Euler forward step method of Zobrist *et al.* (2011) was observed to have the shortest computer time of three published numerical methods for diffusion estimation (O'Meara *et al.*, 2016). When a constant particle-phase diffusivity was assumed this method had a computer time approximately a factor of 20 greater than the analytical method presented in Zaveri *et al.* (2014) (with the numerical method using the minimum spatial resolution (20 shells) required for convergence of predicted equilibrium times, and the maximum change in component molecule number per time step recommended by Zobrist *et al.* (2011), while the analytical method used a conservative temporal resolution of 1×10^3 time steps). To rigorously investigate the role of composition dependent particle-phase diffusion a multi-process large-scale model is required. An analytical-solution to particle-phase diffusion would make this much more practical than a numerical solution with respect to computer time.

Unlike gas-phase diffusion, which is already accounted for in regional-scale models by equations of gas/particle partitioning (Seinfeld & Pandis, 2006; Zaveri *et al.*, 2008), particle-phase diffusion has not yet been included. Two outcomes of recent studies, however, indicate that particle-phase diffusion may pose a limitation to mass transfer. The first is field and laboratory observations that indicate the presence of airborne glassy phase state particulates (Zobrist *et al.*, 2008; Virtanen *et al.*, 2010; Vaden *et al.*, 2011; Saukko *et al.*, 2012). Second is the contribution of very low volatility organic compounds (Ehn *et al.*, 2014; Tröstl *et al.*, 2016) to particulate matter, since volatility and diffusivity show positive correlations (Kroll & Seinfeld, 2008; Koop *et al.*, 2011).

Whether particle-phase diffusion exerts a significant influence on particulate matter transformation remains an unanswered question. A major advance was the incorporation of an analytical solution to composition independent particle-phase diffusion into a growth equation for a spherical particle by Zaveri *et al.* (2014). In examples of constant particle-phase diffusion coefficients, it was shown that, with sufficiently low diffusivity, particle number size distributions could be greatly perturbed, though there was also a dependency on reaction rate and volatility. Using both analytical and numerical solutions to mass transfer equations, Mai *et al.* (2015) also report particle-phase diffusion being limiting under certain conditions, with a dependency on accommodation coefficient, particle size, and volatility.

While the results of Zaveri *et al.* (2014) and Mai *et al.* (2015) are highly beneficial, they have not accounted for the possibility of composition dependent diffusion (Vignes, 1966; Lienhard *et al.*, 2014; Price *et al.*, 2015; O’Meara *et al.*, 2016). This is particularly relevant when considering the role of water, which is important because of its comparatively high abundance and high self-diffusion coefficient (Starr *et al.*, 1999; O’Meara *et al.*, 2016). The potential for water exerting a plasticising effect on low diffusivity particles is particularly important because the constituent components are expected to be highly oxidised (Ehn *et al.*, 2014; Tröstl *et al.*, 2016) and therefore polar and likely water soluble (Zuend *et al.*, 2008; Topping *et al.*, 2013). While numerical solutions to composition dependent diffusion are available (Zobrist *et al.*, 2011; Shiraiwa *et al.*, 2012; O’Meara *et al.*, 2016), an analytical solution has not, to the author’s knowledge, yet been published. Indeed, Zaveri *et al.* (2014) state that the analytical solution requires incorporation of further complexity in the particle-phase: heterogeneously distributed reactant species, liquid-liquid phase separation and heterogenous (with regard to position) diffusivity.

How does radial heterogeneity of diffusivity arise? Atmospheric component concentrations and their partitioning coefficients will vary substantially in time and space (Donahue *et al.*, 2006), leading to concentration gradients through particles. With sufficient difference in the self-diffusivity of the component to the diffusivity of the particle bulk initially (in the case of condensation) or at equilibrium state (in the case of evaporation), and sufficient abundance of the component in the vapour phase (condensation) or particle-phase (evaporation), diffusion is likely to occur at a rate dependent on particle composition. An example would be a low diffusivity SOA-dominated particle formed during a comparatively low relative humidity afternoon and present in the boundary layer. Relative humidity increases as evening progresses and air temperature decreases. The resulting condensation of water onto the outside of the particle establishes a concentration gradient, thereby inducing diffusion. The increased concentration of water will act to increase diffusivity near the surface, whilst diffusivity in the particle core remains low (Zobrist *et al.*, 2011; Lienhard *et al.*, 2014; Price *et al.*, 2015; O’Meara *et al.*, 2016).

The analytical solution is strictly valid under the following conditions: constant concentration of the diffusing component at the particle surface, constant particle size and constant diffusion coefficient (diffusivity). In deriving a correction for varying diffusion coefficient, therefore, corrections to variable surface concentration and particle size may be implicit, depending on the scenario. Thus in the results below, the derivation of a correction is first studied for the relatively simple case of a constant surface mole fraction (determined through equilibration with a constant gas-phase saturation ratio). Second, the case of variable surface mole fraction (due to equilibration with a variable gas-phase saturation ratio) is studied. In addition, the effects of composition dependent diffusion on number size distribution are demonstrated.

3 Method

In the first part of the method the model setup will be described, including all assumptions made. A simple two component system was assumed, comprising one semi-volatile (*sv*) and one non-volatile component (*nv*) that were nonreactive. Both components were assigned a molecular weight of 100 g mol⁻¹ and a density of 1x10⁶ g m⁻³ (in the discussion it is shown that the model is sensitive to the ratio of the component molar volumes rather than absolute values of molecular weight or density). Ideality was assumed, therefore particle-phase volume was calculated by the addition of the product of each components' number of moles and molar volume. The initial particle-phase concentration was radially homogenous. For the purpose of deriving a solution to particle-phase diffusion independent of gas-phase diffusion the latter was assumed instantaneous. Therefore, in combination with the assumption of ideality, changes to the particle-phase surface mole fraction of the partitioning component implies equal changes to its gas-phase saturation ratio.

Fick's second law was solved by a numerical method; for a sphere, with spherical coordinates and with the diffusion coefficient (*D*) dependent on composition, this is (Crank, 1975):

$$\frac{\partial C_i(r, t)}{\partial t} = \frac{1}{r^2} \frac{\partial}{\partial r} \left(r^2 D_i(C_i) \frac{\partial C_i(r, t)}{\partial r} \right), \quad (1)$$

for component *i*, where *C* is concentration, *r* is radius and *t* represents time. In this study *D* followed a logarithmic dependence on the mole fraction of the semi-volatile component :

$$D(x_{sv}) = (D_{sv}^0)^{x_{sv}} (D_{nv}^0)^{(1-x_{sv})}, \quad (2)$$

where *D*⁰ is the self-diffusion coefficient and *x* is mole fraction. This equation fitted measurements reported in Vignes (1966) for ideal mixtures.

Equation 1 can be solved by several numerical methods (e.g. Zobrist *et al.* , 2011; Shiraiwa *et al.* , 2012), but here we use the initial-boundary problem approach (Fi-PaD) as presented in O'Meara *et al.* (2016). This model operates by splitting the particle into concentric shells, each assumed to be homogeneously mixed. The shell representation allows the radial profile of concentration (*C*) and therefore diffusion coefficient (*D*) to be realised. Increased steepness of the *D* gradient requires increased spatial resolution for accurate diffusion estimation. The volume of shells is revalued after every time step. Greater model temporal resolution is required with increased rates of volume change to account for the effect of particle size on diffusion rate. Therefore, as described in O'Meara *et al.* (2016), a

maximum radius change of 0.1% was allowed over a single time step, and the interval was iteratively shortened until this condition was met.

The analytical solution to diffusion is presented and described in Zaveri *et al.* (2014). For a non-reactive component with instantaneous gas-particle surface equilibration it is:

$$\frac{d\bar{C}_{a,i,m}}{dt} = 4\pi R_{p,m}^2 N_m K_{p,i,m} (\bar{C}_{s,i} - \bar{C}_{a,i,m} S_{i,m}), \quad (3)$$

where $K_{p,i,m}$ is the overall mass transfer coefficient:

$$\frac{1}{K_{p,i,m}} = \frac{R_{p,m}}{5D_i} \left(\frac{C_{g,i}^*}{\sum_j \bar{C}_{a,j,m}} \right), \quad (4)$$

and $S_{i,m}$ is the saturation ratio:

$$S_{i,m} = \frac{C_{g,i}^*}{\sum_j \bar{C}_{a,j,m}}, \quad (5)$$

where $_a$ and $_s$ represent the bulk and surface of the particle-phase, respectively, j is the index for all components, m is the index for size-section, R_p is particle radius and N is the particle number concentration ($\text{m}^{-3}(\text{air})$).

The analytical solution treats the particle as a single body, i.e., it cannot resolve radial heterogeneity of concentration and therefore diffusion coefficient (the $D-r$ profile). In order for the diffusion coefficient in the analytical method to respond to composition variation therefore, D was determined using eq. 2, which in turn used the bulk particle semi-volatile mole fraction ($x_{b,sv}$). Because D and the correction factor (derivation described below) varied with composition, the analytical solution was sensitive to temporal resolution. Analytical estimates were compared for a given scenario when the time steps of the Fi-PaD simulation were used and when a temporal resolution twice as fine was used. Results were identical, therefore the Fi-PaD resolution was considered sufficient for reliable analytical results.

Particles were assumed to initially have a radially homogenous concentration profile. Diffusion was then initiated by a change to the semi-volatile mole fraction at the particle surface ($\Delta x_{s,sv}$) to attain the equilibrium mole fraction $x_{s,sv,eq}$. The radial heterogeneity of D (in Fi-PaD) was therefore established through the setting of D_{sv}^0 and D_{nv}^0 and through the radial concentration gradient of the semi-volatile component resulting from diffusion. Since diffusion approaches equilibrium asymptotically, it is necessary to define an effective equilibrium point prior to complete equilibrium. We chose the e -folding state, which is when the absolute difference in component concentration at the surface and the bulk average (everything below the surface) decreases by a factor of e from its initial value.

Fi-PaD estimates of the time required to reach the e -folding state (the e -folding time) converged as its spatial resolution increased (O'Meara *et al.*, 2016). The spatial resolution required to attain a satisfactory degree of convergence increased with the gradient of the $D - r$ profile, which in turn was proportional to $\Delta x_{s,sv}$ and D_{nv}^0/D_{sv}^0 . The maximum acceptable change for e -folding time following the addition of a further shell was set at 0.1 %. Based on this condition, fig. 1 shows the shell resolution used for combinations of $\Delta x_{s,sv}$ and $\log_{10}(D_{nv}^0/D_{sv}^0)$. The majority of scenarios used a conservative shell resolution, and only where $|\Delta x_{s,sv}|$ and $|\log_{10}(D_{nv}^0/D_{sv}^0)|$ are both at a maximum for a given resolution was the convergence criteria neared.

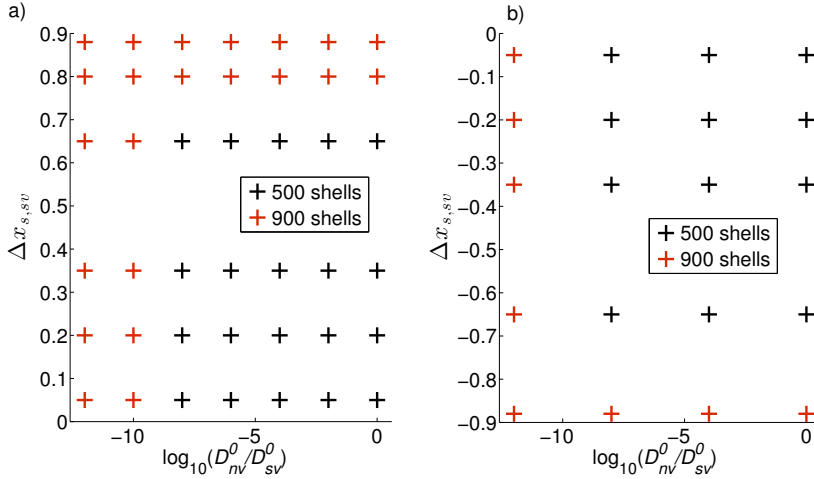


Figure 1: The shell resolution (given in the legend) distribution with $\Delta x_{s,sv}$ and $\log_{10}(D_{nv}^0/D_{sv}^0)$ used, for: a) +ve $\Delta x_{s,sv}$ and b) -ve $\Delta x_{s,sv}$.

As mentioned in the introduction, the correction of the analytical solution was for variation of not only the diffusion coefficient, but also particle size and surface concentration of the diffusing component. Consequently, corrections were derived and assessed for three scenarios of increasing complexity and generality. In the list of these scenarios below, the assumptions of ideality and instantaneous gas-phase diffusion mean that the condition of the surface mole fraction of the semi-volatile component also represents that of its gas-phase saturation ratio:

- i) constant $x_{s,sv,eq}$, with initial/equilibrium $x_{s,sv} = 0$ for +ve $\Delta x_{s,sv}$ / -ve $\Delta x_{s,sv}$
- ii) constant $x_{s,sv,eq}$, with initial/equilibrium $x_{s,sv} \neq 0$ for +ve $\Delta x_{s,sv}$ / -ve $\Delta x_{s,sv}$
- iii) variable $x_{s,sv,eq}$

For all scenarios the shell resolution distributions in fig. 1 were used to estimate the ap-

appropriate Fi-PaD spatial resolutions. $R_p - t$ profiles estimated by the analytical solution were fit by eye to those of Fi-PaD to derive correction equations. $\Delta x_{s,sv}$ and $\log_{10}(D_{nv}^0/D_{sv}^0)$ values across the ranges shown in fig. 1 were used, and the specific combinations shown in fig. 1 were used for the simplest derivation scenario (i) above). The analytical solution was found to have greater disagreement with the numerical solution for the condensation case than the evaporation case. Consequently fits were found for more combinations of $\Delta x_{s,sv}$ and $\log_{10}(D_{nv}^0/D_{sv}^0)$ for the condensation case, as shown in fig. 1. An interpolation method was developed to estimate parameters for the correction equation between the values of $\Delta x_{s,sv}$ and $\log_{10}(D_{nv}^0/D_{sv}^0)$ used for the equation derivation.

Finally, the following were incorporated into the Model for Simulating Aerosol Interactions and Chemistry (MOSAIC) (Zaveri *et al.*, 2014): eq. 2, the correction equations and the interpolation method (eqs. 3-5 were already implemented). The temporal evolution of number size distributions was found for the case of condensation of a plasticiser and compared against an assumption of constant diffusivity. For elucidation of the effect on number size distribution of composition dependent diffusion only the processes of gas/particle partitioning and particle-phase diffusion were modelled in MOSAIC.

4 Results

To begin, uncorrected analytical and Fi-PaD estimates of e -folding times were compared when D was dependent on composition (eq. 2). Estimates were made for the $\Delta x_{s,sv}$ and $\log_{10}(D_{nv}^0/D_{sv}^0)$ combinations in fig. 1, and the discrepancy is shown in fig. 2. For the case of +ve $\Delta x_{s,sv}$ (condensation) (fig. 2a), the analytical solution tends to underestimate diffusion rate, a result of being unable to resolve the plasticising effect of the semi-volatile component as it diffuses inward. Consequently, the discrepancy increases with increasing values of $|\Delta x_{s,sv}|$ and $|D_{nv}^0/D_{sv}^0|$, which together determine the plasticising effect. For -ve $\Delta x_{s,sv}$ (evaporation) (fig. 2b), this trend is reversed for comparatively high values of $|\Delta x_{s,sv}|$ and $|D_{nv}^0/D_{sv}^0|$ because the analytical solution is unable to resolve the solidifying effect of the non-volatile component as the semi-volatile component diffuses outward. The solidifying effect decreases with decreasing $|\Delta x_{s,sv}|$ and $|D_{nv}^0/D_{sv}^0|$, whereas the inaccuracy introduced to the analytical by changing particle size is unaffected by $|D_{nv}^0/D_{sv}^0|$, but increases with $|\Delta x_{s,sv}|$. The competing effects of these sources of inaccuracy produce the irregular contour layout at higher values of $|D_{nv}^0/D_{sv}^0|$.

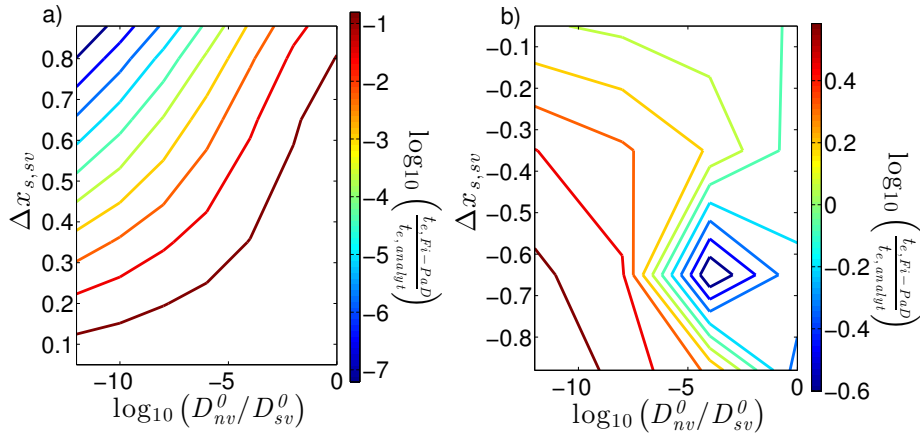


Figure 2: Ratio of Fi-PaD and analytical (*analyt*) estimated e -folding times (t_e) for: a) +ve $\Delta x_{s,sv}$ and b) -ve $\Delta x_{s,sv}$.

Generally the analytical solution is much more accurate for -ve $\Delta x_{s,sv}$, reaching a maximum absolute disagreement around 0.6 orders of magnitude compared to 7.0 for +ve $\Delta x_{s,sv}$. This is attributed to the different characteristics of diffusion between the -ve and +ve $\Delta x_{s,sv}$ cases. In the former, diffusion in Fi-PaD is limited by D near the particle surface, with a surface shell acting like a “crust”. During early stages, the plasticising effect of the semi-volatile component on this “crust” leads to comparatively rapid diffusion out of the particle, but the strength of this effect decreases with concentration of the semi-volatile component, so that the majority of the e -folding time is characterised by a gradual, relatively slow diffusion outward (see appendix for an example of the diffusion coefficient variation with radius for the evaporating case). The inability of the analytical solution to resolve the limiting diffusion near the surface leads to a greater rate of initial diffusion, however the consequent decrease in semi-volatile component concentration results in a D value that replicates the slow diffusion phase of Fi-PaD. In contrast, for +ve $\Delta x_{s,sv}$, diffusion is limited at the diffusion “front”, which is the shell boundary between shells with the greatest radial gradient of concentration. Modelling movement of the “front” requires knowledge of the concentration gradient there, however the only information available to the analytical approach is the particle bulk concentration, leading to the large discrepancies seen.

Next, the simplest scenario of a single and instantaneous change in $x_{s,sv}$ with the initial/final $x_{s,sv} = 0$ for +ve $\Delta x_{s,sv}$ / -ve $\Delta x_{s,sv}$ is investigated. The correction factor for D required to bring analytical R_p estimates into agreement with those of Fi-PaD was found at each time step used by the latter model. The correction factor was then plotted against a metric for proximity to equilibrium; for +ve $\Delta x_{s,sv}$ this was the ratio of surface to bulk average x_{sv} , while for -ve $\Delta x_{s,sv}$, this was the absolute difference between surface and bulk

average x_{sv} . This process was done for the model inputs shown in fig. 1 to determine whether a general equation form could be found that described the relationship between the D correction factor (C_D) and proximity to equilibrium. Examples are shown in fig. 3. The resulting general equations for +ve and -ve $\Delta x_{s,sv}$, respectively, are found to be:

$$C_D = (e^{-(x_{s,sv}/x_{b,sv}-p_1)^{p_2}/p_3} + p_4)^{-1}, \quad (6)$$

and

$$C_D = e^{((x_{b,sv}-x_{s,sv})^{p_1})^{p_2} - p_3}, \quad (7)$$

where p_n is a parameter value, dependent on $\Delta x_{s,sv}$ (the change in semi-volatile surface mole fraction from the initial value (equal to the initial bulk particle mole fraction)) and D_{nv}^0/D_{sv}^0 . Oscillations in C_D occur for the case of $\Delta x_{s,sv} = -0.88$ and $\log_{10}(D_{nv}^0/D_{sv}^0) = -12$. This is attributed to the competing effects of changing particle size, which for a shrinking particle, acts to overestimate diffusion rate, and of a composition dependent D , which for a solidifying particle acts to underestimate diffusion time. As diffusion proceeds, slight variations in the relative strengths of these effects causes C_D to oscillate. Nevertheless, an overall trend is discernible and can be described by eq. 7.

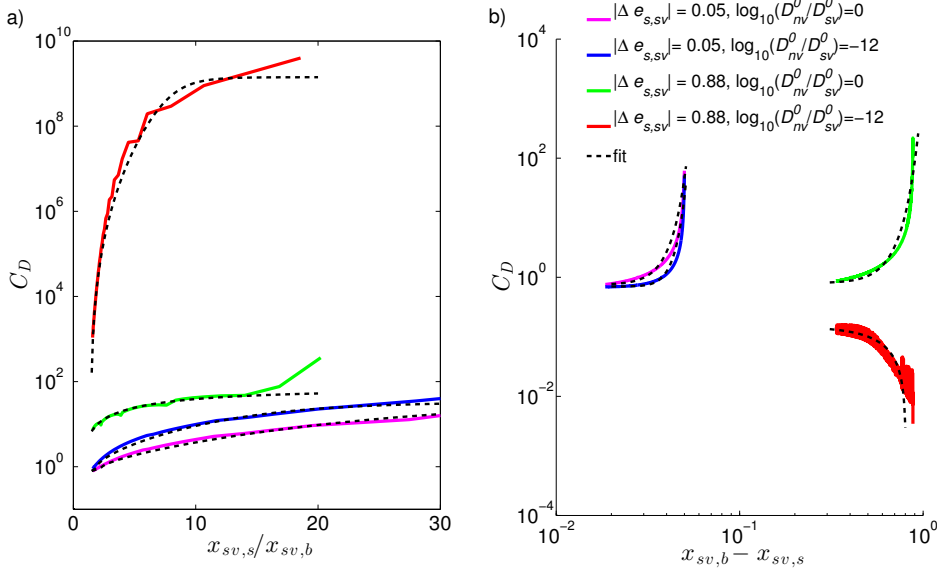


Figure 3: Examples of the correction factor for D in the analytical solution (C_D) required to give agreement with radius estimates in Fi-PaD as a function of proximity to equilibrium (for which the metric depends on the sign of $\Delta x_{s,sv}$), for: a) +ve $\Delta x_{s,sv}$ and b) -ve $\Delta x_{s,sv}$. The model scenario is described in the legend, which applies to both plots. Fits are plotted using eqs. 6 and 7 for a) and b), respectively.

Parameter values for eqs. 6 and 7 were found through fitting by eye analytical $R_p - t$ profiles with those of Fi-PaD for the model inputs shown in fig. 1 (values are provided in the appendix). To value the agreement between Fi-PaD and corrected analytical estimates, the following equation was used:

$$\% \text{ error} = \left(\frac{R_{p,Fi-PaD,t} - R_{p,analyt,t}}{|R_{p,Fi-PaD,t=t_e} - R_{p,Fi-PaD,t=0}|} \right) 100, \quad (8)$$

where *analyt* represents the corrected analytical model. Therefore, % error is the fraction of the total change in R_p comprised by the disagreement in model estimates of R_p at t .

For each marked $\Delta x_{s,sv}$ value in fig. 1, the marked $\log_{10}(D_{nv}^0/D_{sv}^0)$ scenario with greatest % error was identified. Of these scenarios, the four with greatest % error are shown in fig. 4 to demonstrate the cases of worst agreement. Fig. 4 shows that the disagreement between

analytical and Fi-PaD model estimates rarely exceeds $\pm 6\%$, even for cases representing the extremes of model disagreement.

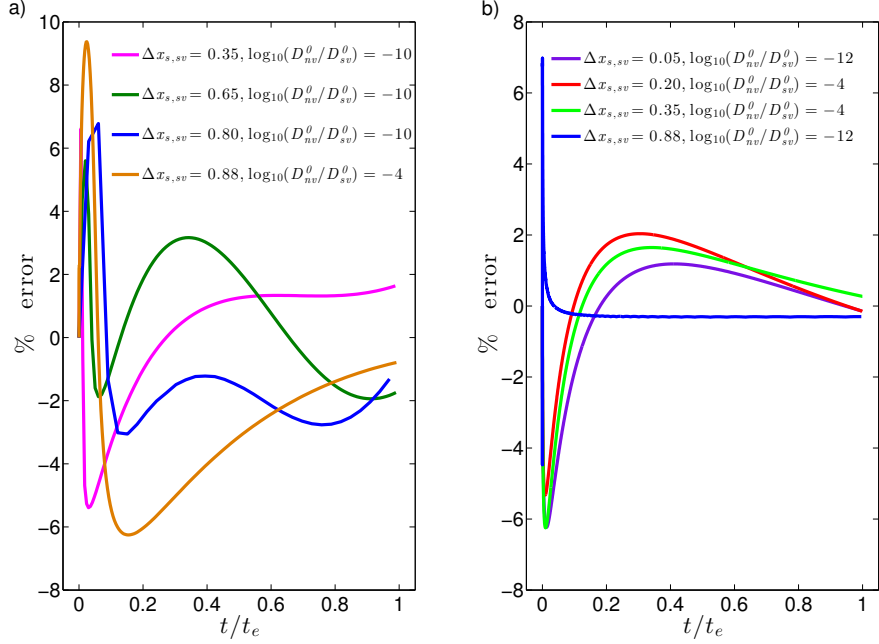


Figure 4: Examples of % error (eq. 8) of the analytical model with corrected D when diffusion is composition dependent (eq. 2), plotted against time normalised by the e -folding time. a) and b) are for +ve $\Delta x_{s,sv}$ and -ve $\Delta x_{s,sv}$, respectively, and scenarios are given in the legend.

In order to have general applicability, such good agreement must be reproducible for intermediate values of $\Delta x_{s,sv}$ and $\log_{10}(D_{nv}^0/D_{sv}^0)$, i.e., when parameter values are interpolated between the points of fig. 1. Parameter relationships with $\Delta x_{s,sv}$ and D_{nv}^0/D_{sv}^0 varied substantially, requiring separate interpolation methods for each parameter. The interpolation methods are presented in the appendix and were tested at $\Delta x_{s,sv}$ and $\log_{10}(D_{nv}^0/D_{sv}^0)$ comparatively far from those with known parameter values and spread across the variable space. Results are shown in fig. 5, again using the % error metric presented in eq. 8. They show that the low error produced for known parameter values is maintained when the interpolation method is applied.

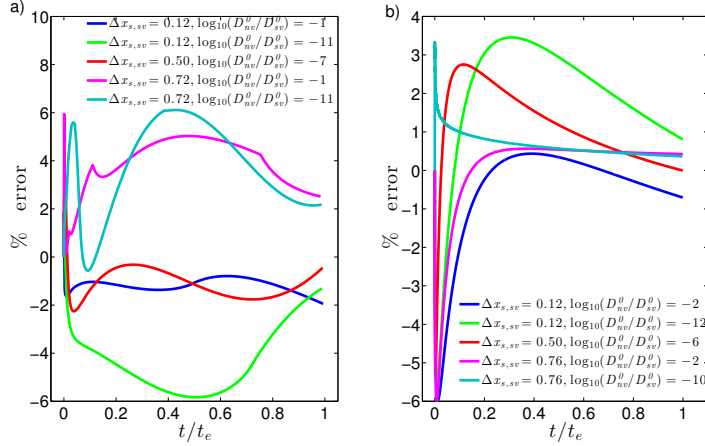


Figure 5: Examples of % error (eq. 8) of the analytical model with corrected D and composition dependent on diffusion (eq. 2), plotted against time normalised by the e -folding time. Parameter values for eqs. 6 and 7 were found through interpolation. a) and b) are for +ve $\Delta x_{s,sv}$ and -ve $\Delta x_{s,sv}$, respectively, and model setups are given in the legend.

Next, the case of a single and instantaneous change to $x_{s,sv}$ with the initial/final $x_{s,sv} \neq 0$ for +ve $\Delta x_{s,sv}$ / -ve $\Delta x_{s,sv}$ is studied. For the +ve $\Delta x_{s,sv}$ case, the correction method described above was found to be transferable to any starting $x_{s,sv}$ through transformation of the D dependence on x_{sv} . An effective self-diffusion coefficient of nv ($D_{nv,eff}^0$) is set as the D at the starting $x_{s,sv}$ (eq. 2), and the starting $x_{s,sv}$ for the analytical is set to 0. D_{sv}^0 is constant, but the equilibrium $x_{s,sv}$ ($x_{s,sv,eq}$) is changed to an effective value such that D at equilibrium gives the same change in D from the starting $x_{s,sv}$ as in the original scenario. Consistent with eq. 2 this effective $x_{s,sv,eq}$ is given by:

$$x_{s,sv,eq,eff} = \frac{(\log_{D_{nv,eff}^0} ((D_{nv}^0)^{(1-x_{s,sv,eq})} (D_{sv}^0)^{x_{s,sv,eq}}) - 1)}{(\log_{D_{nv,eff}^0} (D_{sv}^0) - 1)}, \quad (9)$$

where $x_{s,sv,eq}$ and D_{nv}^0 are the original values. An example transformation to this effective model setup is shown in fig. 6. It can be seen that, compared to the original setup, $\Delta x_{s,sv}$ is increased. Although the transformed D gradient with $x_{s,sv}$ is shallower than the original, therefore, this is offset in terms of diffusion rate by the increased radial gradient in sv concentration.

A similar method can be applied to the evaporation scenario when the final $x_{s,sv} \neq 0$. $D_{nv,eff}^0$ is set equal to that at the final $x_{s,sv}$, and the final $x_{s,sv}$ is set to 0. Whereas for the +ve $\Delta x_{s,sv}$ case we found $x_{s,sv,eq,eff}$, now an effective start $x_{s,sv}$ ($x_{s,sv,0,eff}$) is required.

The equation for this is the same as eq. 9, but with $x_{s,sv,eq,eff}$ replaced by $x_{s,sv,0,eff}$ and with $x_{s,sv,eq}$ replaced by $x_{s,sv,0}$. With regard to the transformed $D-x_{sv}$ profile (e.g. fig. 6), for a given pair of original start and finish $x_{s,sv}$ and a given pair of original self-diffusion coefficients, the transformation is the same for +ve and -ve $\Delta x_{s,sv}$.

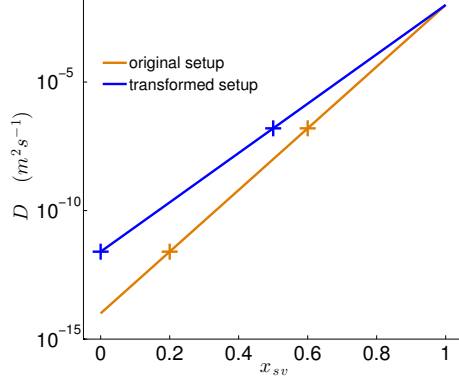


Figure 6: Example of the transformation of the D dependence on x_{sv} when the starting $x_{s,sv}$ (for condensation) or final $x_{s,sv}$ (for evaporation) $\neq 0$. In this example the original starting $x_{s,sv}$ was 0.2 and the equilibrium $x_{s,sv}$ was 0.6, while the original D_{nv}^0 was $1 \times 10^{-14} \text{ m}^2 \text{ s}^{-1}$ and D_{sv}^0 was $1 \times 10^{-2} \text{ m}^2 \text{ s}^{-1}$, as shown by the orange crosses. The effective starting and equilibrium $x_{s,sv}$ and effective D_{nv}^0 found by the transformation described in the main text are shown with blue crosses.

To exemplify the deviation in analytical (with correction) estimates of diffusion rate from those of Fi-PaD when this transformation is applied, the cases of $\Delta x_{s,sv} = 0.2$ and $= 0.5$, and a comparatively large $\log_{10}(D_{nv}^0/D_{sv}^0)$ of -12 were used. Estimates were compared using eq. 8. Results for +ve and -ve $\Delta x_{s,sv}$ are given in fig. 7, and demonstrate that the deviations are comparable to those when the transformation is not required (fig. 4).

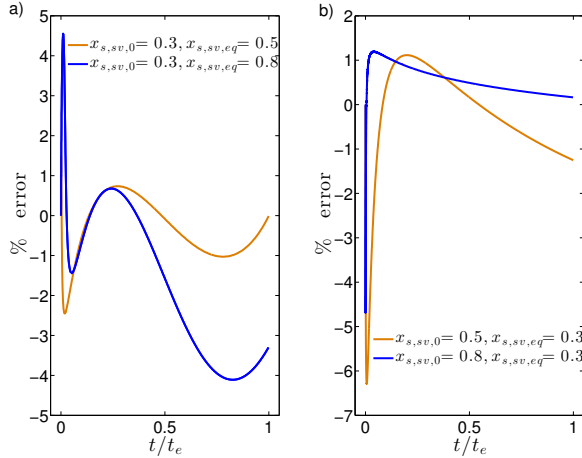


Figure 7: Agreement between corrected analytical and Fi-PaD estimates, using the metric given in eq. 8, for: a) +ve $\Delta x_{s,sv}$ and b) -ve $\Delta x_{s,sv}$, as shown in the legend. The start/finish $x_{s,sv} \neq 0$ for a)/b), therefore the transformation to an effective model setup (as described in the main text) was required. For both a) and b) $\log_{10}(D_{nv}^0/D_{sv}^0) = -12$.

Before moving onto a correction for the case of variable $x_{s,sv}$, the correction for constant $x_{s,sv}$ was implemented in MOSAIC to investigate the effect of composition dependent diffusion on number size distribution. The same initial number size distribution as presented in Zaveri *et al.* (2014) (their fig. 11) was used. Reactions, coagulation, nucleation, emission and deposition were all turned off to gain the clearest demonstration of the diffusion effect. To maintain $x_{s,sv}$, the gas-phase concentration of the semi-volatile component was held constant and low particle-phase self-diffusion coefficients were used to ensure that partitioning was not limited by diffusion in the vapour-phase. The model was run in Lagrangian mode to prevent numerical error due to rebinning and resultant loss of information about the initial particle size.

To test the effect on the timescale of number size distribution change during condensation of a plasticising semi-volatile component, $\Delta x_{s,sv}$ was set to +0.88, from an initial particle-phase mole fraction of 0. The number size distribution following diffusion was found for $\log_{10}(D_{nv}^0/D_{sv}^0)$ values of 0, -2 and -4, with D_{nv}^0 held constant at $1.0 \times 10^{-26} \text{ m}^2 \text{ s}^{-1}$. Simulations were run until the largest particle had reached its e -folding state. The distributions after one tenth and at the end of the run time for the $\log_{10}(D_{nv}^0/D_{sv}^0) = -4$ case are shown in fig. 8a and fig. 8b, respectively, along with the initial distribution.

As expected, fig. 8 shows that the condensing component can significantly increase the rate of diffusion and therefore the rate at which the number size distribution evolves.

For all values of $\log_{10}(D_{nv}^0/D_{sv}^0)$ the form of the number size distribution shows the same characteristic of initially narrowing as smaller particles grow more quickly before widening again as these particles equilibrate and larger particles grow. The degree of narrowing is similar between all cases, indicating that when a plasticising effect occurs, the resulting acceleration of diffusion is similar across all particle sizes (consistent with the results of O'Meara *et al.* (2016)).

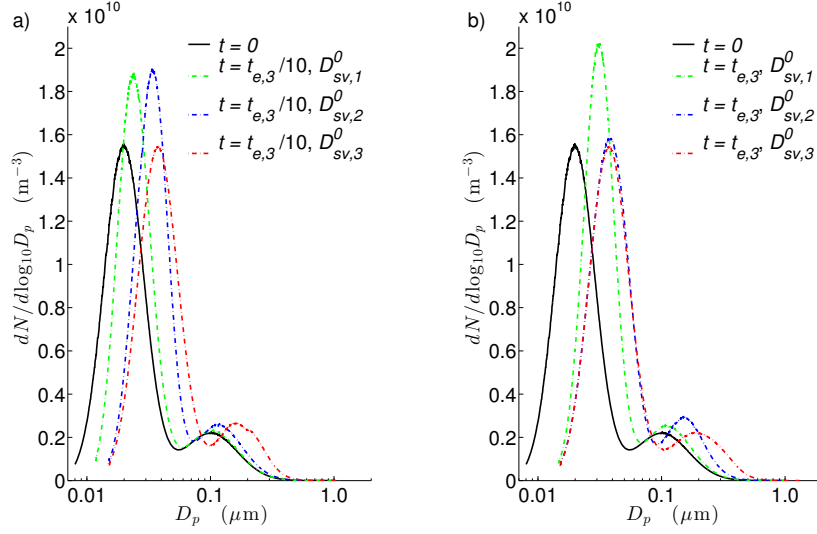


Figure 8: Number size distributions for $\log_{10}(D_{nv}^0/D_{sv}^0) = 0, -2$ and -4 , represented by $D_{sv,1}^0$, $D_{sv,2}^0$ and $D_{sv,3}^0$ respectively (D_{nv}^0 constant at $1.0 \times 10^{-26} \text{ m}^2 \text{ s}^{-1}$). $t_{e,3}$ is the time for the largest particle in the $\log_{10}(D_{nv}^0/D_{sv}^0) = -4$ run to attain e -folding state. a) is the distribution at one tenth of $t_{e,3}$ and b) is that at $t_{e,3}$. $x_{s,sv}$ was increased instantaneously from 0.00 to 0.88 and then held constant.

It is possible to set a constant diffusion coefficient in the analytical solution without correction that attains the same e -folding time as when the analytical solution with correction is used with a variable diffusion coefficient. For the case of $D_{nv}^0 = 1.0 \times 10^{-26}$ and $D_{sv}^0 = 1.0 \times 10^{-22} \text{ m}^2 \text{ s}^{-1}$ and $\Delta x_{s,sv} = 0.88$, the required constant diffusion coefficient was found to be $D_{con} = 4.4 \times 10^{-23} \text{ m}^2 \text{ s}^{-1}$. The % error (eq. 8) when the constant D treatment is used is shown in fig. 9a. This figure shows that although the constant D simulation does give the same e -fold time (agreement in radius estimate at $t/t_e = 1$), diffusion estimates about this point are different between the treatments of diffusion coefficient: beginning more quickly in the variable case before it slows relative to the constant case.

To test the effect of using a constant D on a polydisperse population, this treatment is used

to estimate number size distributions from MOSAIC and compared to estimates using the variable D treatment. Using the same model setup as for fig. 8, the comparison is shown in fig. 9b-d . Results are shown for three times since run start as described in the figure. As expected from fig. 9a, if one focusses on the smaller particle sizes it can be seen that growth is initially quickest in the variable D case (fig. 9b) but that growth in the constant D case catches and exceeds that for variable D , leading to increased narrowing of the distribution (fig. 9d). Note that while this demonstration focuses on the smallest sizes, the same effect is true for all sizes, indeed in fig. 9d for D_p around $0.1 \mu\text{m}$ it can be seen that particles are growing quicker in the variable treatment as diffusion initiates in these sizes. These discrepancies demonstrate the requirement for a correction to the analytical solution that is dependent on the proximity to equilibrium rather than a correction based on a constant D .

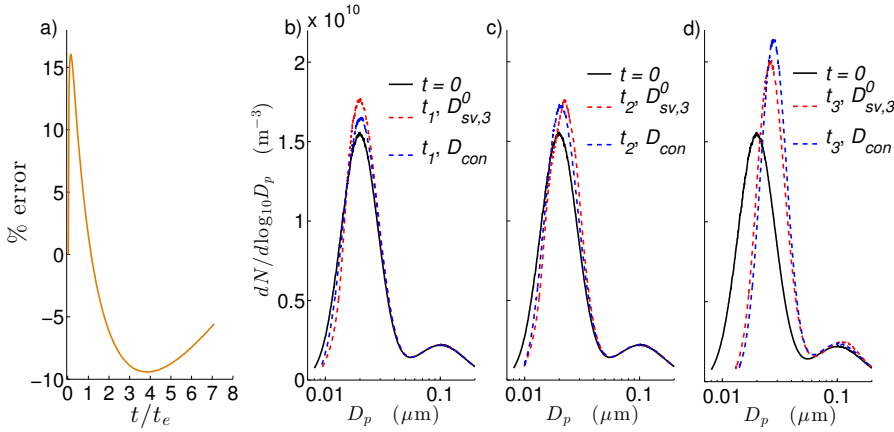


Figure 9: In a), the discrepancy (found using eq. 8) in estimated radius with model run time normalised to the e -folding time (t_e) when $x_{s,sv}$ is increased instantaneously from 0.00 to 0.88 for two diffusion coefficient treatments: i) $D_{nv}^0 = 1 \times 10^{-26}$ and $D_{sv}^0 = 1 \times 10^{-22} \text{ m}^2 \text{ s}^{-1}$ and ii) using the analytical without correction when D is constant at $4.4 \times 10^{-23} \text{ m}^2 \text{ s}^{-1}$. In later plots are the number size distributions for the same diffusion coefficient treatments, with red representing the former treatment (variable D) and blue the latter one (constant D). In b) $t = 1.80 \times 10^4$ s, c) $t = 4.50 \times 10^4$ s and in d) $t = 5.76 \times 10^5$ s since simulation start.

For the analytical solution to be generally applicable a correction when $x_{s,sv}$ varies prior to particle phase equilibration is required. Results shown to this point have been for a constant $x_{s,sv}$. Application of the correction presented above (eqs. 6 and 7) to the variable case is not straightforward as it is based on the difference between initial and equilibrium mole fractions and the particle is assumed to initially have a radially homogenous concentration profile. In the following passage is a description of a method to overcome this constraint

for a given time profile of $x_{s,sv}$. This serves as a basis to explain the limits of this correction method to general application.

$x_{s,sv}$ was decreased from 0.88 to 0.00 with a sinusoidal profile, as shown in fig. 10a. The initial particle radius was 1×10^{-4} m, $D_{nv}^0 = 1 \times 10^{-14}$ and $D_{sv}^0 = 1 \times 10^{-10}$ m^2s^{-1} . The resulting $R_p - t$ profile using Fi-PaD is shown in fig. 10b. For the analytical estimate to agree the correction equation was found to be:

$$C_D = e^{((v_1)^{p_1})p_2} - p_3, \quad (10)$$

where

$$v_1 = \frac{x_{sv,b}}{(\sin(\log_{10}(x_{r,t_n} - x_{r,t_{n-1}})/1.3 - 2.4)/4.6 + 1.1)}, \quad (11)$$

where x_r is the ratio of x_{sv} in the particle bulk to that at the surface. The ratios at the start of the time step being solved for (t_n) and at the start of the previous time step (t_{n-1}) are used. p_1 , p_2 and p_3 are the same as used for the original equation (eq. 7) and $\Delta x_{s,sv}$ was set equal to the particle bulk x_{sv} .

This correction gives excellent agreement with the Fi-PaD estimate (curve labelled analyt in fig. 10b). However, even a comparatively slight change to the temporal profile of $x_{s,sv}$ to the exponential profile given in fig. 10a (curve p_2), shows this correction to be over fitted. Eqs. 10 and 11, however, demonstrate that a correction is possible when knowledge of the rate of change of the ratio of semi-volatile component mole fraction in the particle bulk to that at the surface is attainable. If this rate is very low (instant equilibration) or very high (no diffusion), no correction is needed, but in between a correction dependent on the rate is required. We suggest that a generally applicable correction is only possible with an a priori estimate of the rate of change of bulk to surface mole fraction ratio for the current time step. However, the bulk mole fraction is the value being estimated, making a solution intractable using this methodology.

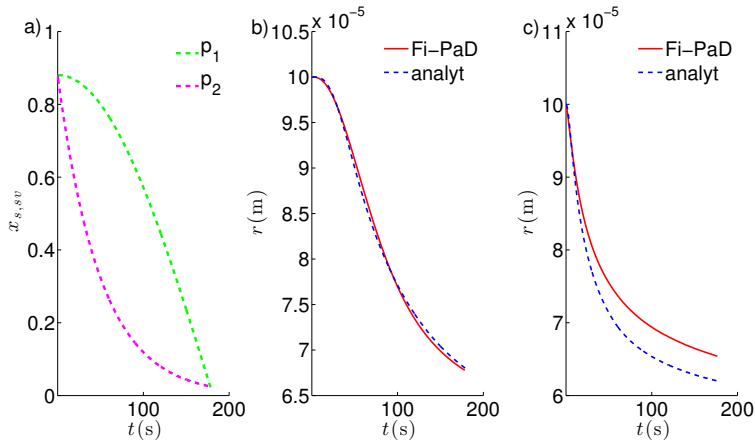


Figure 10: Plots demonstrating the limitation of the correction to cases of varying $x_{s,sv}$. In a) are the two temporal profiles of $x_{s,sv}$ used to test applicability, while b) and c) show Fi-PaD and analytical (analyt) estimates of radius (the latter corrected using eqs. 10 and 11) for $x_{s,sv}$ temporal profiles p_1 and p_2 , respectively. $D_{nv}^0 = 1 \times 10^{-14}$ and $D_{sv}^0 = 1 \times 10^{-10} \text{ m}^2 \text{ s}^{-1}$.

5 Discussion

As mentioned in the introduction, for a simple case of diffusion independent of composition, the computer time for the numerical solution is approximately 20 times as long as the analytical. However, this factor difference is expected to rise by 2-3 orders of magnitude for very steep gradients of diffusion coefficient with radius (O’Meara *et al.*, 2016). Therefore, implementation of composition dependent diffusion into a polydisperse multi-process aerosol model like MOSAIC through an analytical solution is highly preferable to a numerical one. Here, equilibration between the gas- and particle-phase was assumed instantaneous, so that the surface mole fraction of the partitioning component was equal to its gas-phase saturation ratio.

For the limiting case of constant surface mole fraction of a semi-volatile component, a correction to the analytical solution for when diffusivity is composition dependent has been derived and validated against estimates from the numerical solution. A method to interpolate correction parameters between values of $\Delta x_{s,sv}$ (change to surface mole fraction that initiates diffusion) and D_{nv}^0 / D_{sv}^0 (ratio of component self-diffusion coefficients) was also derived and validated. A similar derivation was attempted for the case of variable surface mole fraction, however this was found to be of narrow applicability. This issue, along with the limitations of the correction for constant $x_{s,sv}$ are discussed below.

In favour of the correction is its independence of particle size. In both solutions (numerical and analytical), diffusion rates have a square dependence on particle size, therefore the ratios of estimated diffusion rate are constant across sizes (all else being equal), as is the correction. Similarly, the correction is independent of absolute values of D_{nv}^0 and D_{sv}^0 and only dependent on the ratio of component self-diffusion coefficients: $\log_{10}(D_{nv}^0/D_{sv}^0)$.

Although the correction is applicable across particle sizes and values of D_{nv}^0 and D_{sv}^0 , it is specific to the ratio of component molar volumes used here, which is 1:1. The change in particle size due to partitioning depends on the molar volumes of components. The response of diffusion rate to a change in molar volume is different between the models and is non-linear in each. For quantifying model sensitivity to molar volume, a further complication is the variation of diffusivity with both molar mass and density (Koop *et al.*, 2011).

To gain an indication of the model disagreement arising from changing molar volume when the corrected analytical model is used, expected ranges of molar mass (M) and density (p) for atmospheric organic components were found. Barley *et al.* (2011) show that M is likely to be in the range 1×10^2 to 3×10^2 g mol⁻¹ and Topping *et al.* (2011) demonstrate that p is likely to be between 1.2×10^6 to 1.6×10^6 g m⁻³. The maximum expected molar volume for the semi-volatile component was therefore given by using $M = 3 \times 10^2$ g mol⁻¹ and $p = 1.2 \times 10^6$ g m⁻³. A relatively large effect from the changed molar volume was gained through using $\Delta x_{s,sv} = \pm 0.88$. Furthermore, the proportion of the correction attributed to particle size change rather than D composition dependence, is greatest for $\log_{10}(D_{nv}^0/D_{sv}^0) = 0$, therefore this was used to maximise the effect of varying molar volume on model agreement. For the +ve and -ve $\Delta x_{s,sv}$ cases, the maximum observed % error (eq. 8) was -58.0 and 29.0 %, respectively. Given this large discrepancy and the complexity of the model responses, we recommend further work to investigate correction dependence on molar volume.

A further limitation of the presented correction is its specificity to the D dependence on composition. Here we have assumed a logarithmic dependence on x_{sv} , however, measurements have reported sigmoidal and irregular dependencies resulting from changes to phase state and/or non-ideality (e.g. Vignes, 1966; Lienhard *et al.*, 2014; Price *et al.*, 2015). An indication of model disagreement generated by varying the D dependence was found by calculating the % error for several dependencies; all were based on a sigmoidal function, however, the steepness at the ‘‘cliff-edge’’ was varied, as shown in fig. 11a. Also shown here is the logarithmic dependence used to find the presented correction. A $\log_{10}(D_{nv}^0/D_{sv}^0) = -12$ and $\Delta x_{s,sv} = \pm 0.88$ were used because these provide the most stringent test of estimation capability. The dependencies were used in both the Fi-PaD and analytical model, with the latter using the correction method for the logarithmic dependence. The resulting discrepancies in estimated particle radius are shown in figs. 11b and 11c.

Fig. 11b shows that for +ve $\Delta x_{s,sv}$, the analytical method increasingly overestimates initial

diffusion with increasing sigmoidal function steepness, indicating the correction is too great when the ratio of surface to bulk x_{sv} is high. The reason is that, with the dependencies used, increased steepness causes increased resistance to inward semi-volatile diffusion at low x_{sv} . As surface to bulk x_{sv} ratio decreases in the analytical, so does the correction factor (fig. 3a), and Fi-PaD estimates begin to converge on the analytical. For the least steep sigmoidal dependence, diffusion in Fi-PaD overtakes the corrected analytical around $0.3 t/t_e$. This occurs after some initial diffusion and is therefore attributed to Fi-PaD diffusion occurring quickly relative to the logarithmic dependence once the bulk concentration of the semi-volatile has been raised. This is demonstrated in fig. 11a, where for the least steep sigmoidal dependence, above $x_{sv} \approx 0.3$ the same change in x_{sv} gives a greater increase in diffusivity than in the logarithmic dependence.

Results for -ve $\Delta x_{s,sv}$ are shown in fig. 11c, which shows that the analytical solution initially underestimates diffusion. This is attributed to the increasing plasticising effect of the semi-volatile on the surface crust of the particle with increasing steepness of the sigmoidal “cliff-edge”. Once x_{sv} has decreased however, the analytical shows a tendency to overestimate diffusion. The plasticising effect can quickly decrease (fig. 11a), and the surface crust imposes a greater impediment to diffusion. The correction factor (which acts to decelerate diffusion (fig. 3b)) found from the logarithmic dependence is insufficient to replicate this for the steepest dependency.

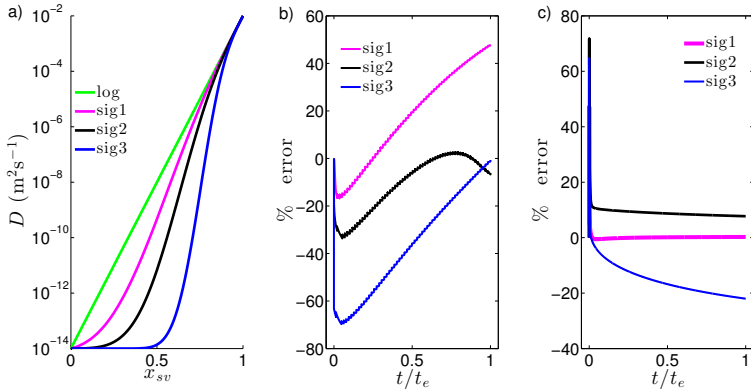


Figure 11: Plot a) shows the logarithmic dependency of diffusion coefficient on mole fraction on which the presented correction is derived and the sigmoidal dependencies for which it was tested. In b) and c) is the analytical model error (eq. 8) when the sigmoidal dependencies given in a) were used. b) +ve $\Delta x_{s,sv}$ and c) -ve $\Delta x_{s,sv}$, and for both plots $|\Delta x_{s,sv}| = 0.88$ and $\log_{10}(D_{nv}^0/D_{sv}^0) = -12$.

As fig. 11 shows, the presented correction is limited in its generality with regards to dif-

fusion coefficient dependence on composition. Along with the effect of molar volume on diffusion, however, it is conceivable that this could be overcome through a more advanced correction similar in approach to that presented. In contrast, deriving a correction with general applicability to changing particle surface mole fraction of the partitioning component appears impossible using the approach presented here. As shown in the results, under a variable surface mole fraction a correction based on the rate of change of bulk to surface mole fraction can be produced. However, this requires a priori knowledge of the diffusion rate (the value being estimated), making this approach redundant. An alternative approach is therefore required, and should be the focus of further work; a suggestion is decision tree learning.

Without a general analytical solution, thorough evaluation of particle-phase diffusion influence on particulate transformation remains limited. The correction for constant surface mole fraction of the semi-volatile component, however, offers greater ease of evaluating particle-phase diffusion effects, such as in Berkemeier *et al.* (2013) and Mai *et al.* (2015). It may also be of use for the inference of diffusivity from laboratory studies, if the rates of semi-volatile gas-phase saturation ratio change and gas-phase diffusion are much greater than the particle-phase diffusion rate (Zobrist *et al.* , 2011; Lienhard *et al.* , 2014; Steimer *et al.* , 2015).

6 Conclusion

For accurate simulation of particle phase evolution, the analytical solution to diffusion must account for composition dependent diffusion rate. To do this, a correction to the analytical solution was investigated based on estimates from the numerical solution of the partial differential equation for diffusion. A correction was derived for the limiting case of a constant surface mole fraction of the diffusing component (equal to a constant gas-phase saturation ratio when assuming equilibration between the gas- and particle-phase). The corrected analytical solution shows good agreement with the numerical one, rarely exceeding 8 % deviation in estimated particle radius change.

The verified correction is currently limited to conditions of similar molar volume between the partitioning component and the particle average, and of a logarithmic dependence of diffusion coefficient on partitioning component mole fraction. These limitations may be overcome through an advanced correction. However, a correction for the more general case of variable surface mole fraction of the diffusing component (e.g., due to varying gas-phase saturation ratio) was found to depend on the rate of change of the ratio of bulk to surface mole fraction. A correction based on the analytical approach presented here is therefore not viable because it requires a priori knowledge of the value to be estimated: the particle bulk mole fraction. A different approach to modifying the analytical solution to diffusion

is thus required to make it generally applicable.

To determine whether an expression for particle-phase diffusion is required in a regional model, an evaluation of regional model sensitivity to diffusion is desirable. This study builds on previous studies toward allowing such a sensitivity analysis, however, work remains to create a generally applicable realistic and efficient particle-phase diffusion model. Until this is achieved, studies of aerosol kinetic regimes conducted under limiting scenarios such as diffusion independent of composition, or constant gas-phase saturation ratios, should be interpreted cautiously because of their limited applicability to the real atmosphere. In particular, the comparatively high abundance and high self-diffusion coefficient of water means that its role in plasticising or vitrifying particles through condensation and evaporation, respectively, must be accounted for when assessing the effect of particle-phase diffusion on partitioning.

7 Appendix A

$\log_{10}(D_{nv}^0/D_{sv}^0)$	0	-2	-4	-6	-8	-10	-12
$\Delta x_{s,sv}$				p_1			
0.05	2.3000	2.1500	2.0000	1.9500	1.9100	1.8800	1.8800
0.20	1.8500	1.7800	1.7000	1.6400	1.6200	1.6000	1.5700
0.35	1.6000	1.5800	1.5700	1.5600	1.5600	1.5200	1.5200
0.65	1.4300	1.4500	1.4500	1.4700	1.4600	1.4500	1.4600
0.80	1.0696	1.3400	1.4300	1.4397	1.4348	1.4400	1.4550
0.88	0.0000	0.9300	1.0100	1.4238	1.4215	1.4400	1.4800
				p_2			
0.05	7.1430×10^{-1}	6.2500×10^{-1}	6.2500×10^{-1}	5.9170×10^{-1}	5.6820×10^{-1}	5.4050×10^{-1}	5.1280×10^{-1}
0.20	6.5070×10^{-1}	5.1900×10^{-1}	4.8950×10^{-1}	4.7990×10^{-1}	4.5000×10^{-1}	4.1930×10^{-1}	4.1670×10^{-1}
0.35	6.2500×10^{-1}	4.762×10^{-1}	4.348×10^{-1}	4.348×10^{-1}	3.7040×10^{-1}	3.7040×10^{-1}	3.7040×10^{-1}
0.65	4.2550×10^{-1}	3.9220×10^{-1}	3.7040×10^{-1}	3.4480×10^{-1}	3.3333×10^{-1}	3.1250×10^{-1}	3.1250×10^{-1}
0.80	2.6810×10^{-1}	3.0660×10^{-1}	2.9960×10^{-1}	2.9150×10^{-1}	2.8710×10^{-1}	2.8500×10^{-1}	2.8340×10^{-1}
0.88	3.0000×10^{-1}	4.8000×10^{-1}	6.0000×10^{-1}	2.9150×10^{-1}	2.8710×10^{-1}	2.6000×10^{-1}	2.7000×10^{-1}
				p_3			
0.05	3.0000	2.1500	2.0000	1.8000	1.6000	1.3600	1.2200
0.20	2.5346	1.3800	1.0000	7.4000×10^{-1}	6.2000×10^{-1}	4.9810×10^{-1}	4.1670×10^{-1}
0.35	2.1000	1.0000	6.2500×10^{-1}	4.4050×10^{-1}	3.3560×10^{-1}	2.7400×10^{-1}	2.2222×10^{-1}
0.65	1.1000	5.2630×10^{-1}	3.1150×10^{-1}	2.7140×10^{-1}	1.6450×10^{-1}	1.3230×10^{-1}	1.1170×10^{-1}
0.80	5.6500×10^{-1}	3.4500×10^{-1}	2.1700×10^{-1}	1.5700×10^{-1}	1.2200×10^{-1}	1.0100×10^{-1}	9.0500×10^{-2}
0.88	8.0000×10^{-1}	4.1000×10^{-1}	2.4000×10^{-1}	1.2950×10^{-1}	1.0300×10^{-1}	9.0500×10^{-2}	8.2000×10^{-2}
				p_4			
0.05	3.0000×10^{-2}						
0.20	2.5700×10^{-2}	1.9600×10^{-2}	1.1500×10^{-2}	1.5900×10^{-2}	3.2000×10^{-3}	1.4000×10^{-3}	1.5000×10^{-3}
0.35	2.2000×10^{-2}	1.0000×10^{-2}	5.0000×10^{-3}	3.5000×10^{-3}	4.0000×10^{-4}	1.0000×10^{-4}	9.0000×10^{-5}
0.65	1.700×10^{-2}	2.0000×10^{-3}	6.0000×10^{-4}	4.0000×10^{-5}	6.0000×10^{-6}	7.0000×10^{-7}	1.2000×10^{-7}
0.80	1.5600×10^{-2}	9.8400×10^{-4}	1.1000×10^{-4}	3.8000×10^{-6}	5.2700×10^{-7}	3.8000×10^{-8}	4.5000×10^{-9}
0.88	3.0000×10^{-2}	7.3100×10^{-4}	2.0000×10^{-4}	1.2100×10^{-6}	1.2200×10^{-7}	6.9900×10^{-9}	7.0700×10^{-10}

Table 1: Eq. 6 parameter values found for +ve $\Delta x_{s,sv}$.

$\log_{10}(D_{nv}^0/D_{sv}^0)$	0	-4	-8	-12
$\Delta x_{s,sv}$			p_1	
0.05	2.8100	2.8600	2.9200	3.0000
0.20	3.2300	3.5300	3.4600	2.0000
0.35	3.6500	4.4000	4.0000	2.0000
0.65	5.0000	8.0000	5.0000	2.0000
0.88	6.0000	1.1000×10^1	7.0000	1.9000
			p_2	
0.05	8.0000×10^3	8.0000×10^3	8.0000×10^3	8.0000×10^3
0.20	3.5000×10^2	3.0000×10^2	1.0000×10^2	-1.6000
0.35	1.0000×10^2	5.0000×10^1	-1.0000	-1.6000
0.65	2.3000×10^1	1.2000×10^1	-1.0000	-4.0000×10^{-1}
0.88	7.0000	3.0000	5.6000×10^{-1}	-2.0000×10^{-1}
			p_3	
0.05	4.0000×10^{-1}	4.2000×10^{-1}	4.0000×10^{-1}	4.2000×10^{-1}
0.20	3.2000×10^{-1}	4.1000×10^{-1}	5.0000×10^{-1}	5.2000×10^{-1}
0.35	2.5000×10^{-1}	4.0000×10^{-1}	5.8000×10^{-1}	6.2000×10^{-1}
0.65	0.0000	5.0000×10^{-1}	6.7000×10^{-1}	7.6000×10^{-1}
0.88	-1.0000×10^{-1}	5.8000×10^{-1}	7.8000×10^{-1}	8.5000×10^{-1}

Table 2: Eq. 7 parameter values found for -ve $\Delta x_{s,sv}$.

$\log_{10}(D_{nv}^0/D_{sv}^0)$	0	-2	-4	-6	-8	-10	-12
p_i	Method Code						
p_1	10L	10L	10S	10S	10S	10S	10S
p_2	10S	10S	01L	01L	01L	01L	01L
p_3	11L	11L	11S	11S	11S	11S	11S
p_4	10S	10S	10S	10S	10S	10S	10S
$\Delta x_{s,sv}$	< 0.12	$\geq 0.12 < 0.20$	$\geq 0.20 < 0.50$	$\geq 0.50 < 0.80$	≥ 0.80		
p_i	Method Code						
p_1	01S	01S	01L	01L	01L		
p_2	01S	01S	01L	01S	01L		
p_3	01S	01S	11L	01S	01S		
p_4	01S	01S	01L	11L	11L		

Table 3: Interpolation method for parameters in Eq. 6 (for +ve $\Delta x_{s,sv}$). Interpolation is done with respect to $\Delta x_{s,sv}$ and $\log_{10}(D_{nv}^0/D_{sv}^0)$ separately; the method for the former is given in the upper part of the table and for the latter see the lower part. The first number in each code represents whether the \log_{10} of parameter values was taken (1 for yes, 0 for no), the second number indicates whether the \log_{10} of the variable was taken (1 for yes, 0 for no), the final letter represents the form of the interpolation: L and S for linear and spline, respectively.

$\log_{10}(D_{nv}^0/D_{sv}^0)$	0	-4	-8	-12
p_i	Method Code			
p_1	00L	00L	00L	00L
p_2	11L	11L	1(2)1L	1(2)0L
p_3	00L	00L	00L	00L
$\Delta x_{s,sv}$	< 0.27	$\geq 0.27 < 0.65$	≥ 0.65	
p_i	Method Code			
p_1	01L	01L	01L	
p_2	1(2)1S ($D_r < -8$) 01L ($D_r \geq -8$)	1(2)1S ($D_r < -4$) 01L ($D_r \geq -4$)	1(1.1)1S ($D_r \geq -6$, $D_r \leq -4$) 1(2)1L ($D_r > -4$, $D_r < -6$)	
p_3	1(2)1S	1(2)1S	1(2)1S	

Table 4: Interpolation method for parameters in Eq. 7 (for -ve $\Delta x_{s,sv}$). Interpolation is done with respect to $\Delta x_{s,sv}$ and $\log_{10}(D_{nv}^0/D_{sv}^0)$ separately; the method for the former is given in the upper part of the table and for the latter see the lower part. The first number in each code represents whether the \log_{10} of parameter values was taken (1 for yes, 0 for no). Because parameters are sometimes negative, to gain a real result from the logarithm, a constant must be added to the parameters, if this is the case this constant is given in brackets beside the first code number (note that once interpolation is complete this constant is subtracted from the result). The second number indicates whether the \log_{10} of the variable was taken (1 for yes, 0 for no), the final element represents the form of the interpolation: L and S for linear and spline, respectively. For p_2 , when interpolating with respect to $\log_{10}(D_{nv}^0/D_{sv}^0)$, the interpolation method depends on the value of this variable, which is denoted D_r .

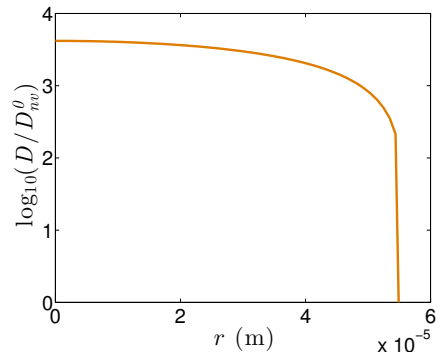


Figure 12: The logarithm of the ratio of the diffusion coefficient throughout an example particle to the self-diffusion coefficient of the non-volatile component, from the particle centre (at 0 m) to its surface. In this example, $\log_{10}(D_{nv}^0/D_{sv}^0) = -12$, and $x_{s,sv,eq} = 0$, and initial $x_{s,sv} = 0.88$.

References

- Barley, M.H., Topping, D., Lowe, D., Utembe, S., & McFiggans, G. 2011. The sensitivity of secondary organic aerosol (SOA) component partitioning to the predictions of component properties-Part 3: Investigation of condensed compounds generated by a near-explicit model of VOC oxidation. *Atmos. Chem. Phys.*, **11**, 13145–13159.
- Berkemeier, T., Huisman, A.J., Ammann, M., Shiraiwa, M., Koop, T., & Pöschl, U. 2013. Kinetic regimes and limiting cases of gas uptake and heterogeneous reactions in atmospheric aerosols and clouds: a general classification scheme. *Atmos. Chem. Phys.*, **13**, 6663–6686.
- Boucher, O., Randall, D., Artaxo, P., Bretherton, C., Feingold, G., Forster, P., Kerminen, V.-M., Kondo, Y., Liao, H., Lohmann, U., Rasch, P., Satheesh, S.K., Sherwood, S., Stevens, B., & Zhang, X.Y. 2013. Clouds and Aerosols. *In: Stocker, T.F., Qin, D., Plattner, G.-K., Tignor, M., Allen, S.K., Boschung, J., Nauels, A., Xia, Y., Bex, V., & Midgley, P.M. (eds), Climate Change 2013: The Physical Science Basis. Contribution of Working Group I to the Fifth Assessment Report of the Intergovernmental Panel on Climate Change.* Cambridge, United Kingdom and New York, NY, USA: Cambridge University Press.
- Crank, J. 1975. *The Mathematics of Diffusion*. 2 edn. Oxford: Clarendon Press.
- Donahue, N.M., Robinson, A.L., Stanier, C.O., & Pandis, S.N. 2006. Coupled partitioning, dilution and chemical ageing of semivolatile organics. *Environ. Sci. Technol.*, **40**, 2635–2643.
- Ehn, M., Thornton, J.A., Kleist, E., Sipilä, M., Junninen, H., Pullinen, I., Springer, M., Rubach, F., Tillmann, R., Lee, B., Lopez-Hilfiker, F., Andres, S., Acir, I., Rissanen, M., Jokinen, T., Schobesberger, S., Kangasluoma, J., Kontkanen, J., Nieminen, T., Kurtén, T., Nielsen, L. B., Jørgensen, S., Kjaergaard, H.G., Canagaratna, M., Maso, M.D., Berndt, T., Petäjä, T., Wahner, A., Kerminen, V., Kulmala, M., Worsnop, D.R., Wildt, J., & Mentel, T.F. 2014. A large source of low-volatility secondary organic aerosol. *Nature*, **506**, 476–479.
- Fiore, A.M., Naik, V., Spracklen, D.V., Steiner, A., Unger, N., Prather, M., Bergmann, D., Cameron-Smith, P.J., Cionni, I., Collins, W.J., Dalsøren, S., Eyring, V., Folberth, G.A., Ginoux, P., Horowitz, L.W., Josse, B., Lamarque, J., MacKenzie, I.A., Nagashima, T., O'Connor, F.M., Righi, M., Rumbold, S.T., Shindell, D.T., Skeie, R.B., Sudo, K., Szopa, S., Takemura, T., & Zeng, G. 2012. Global air quality and climate. *Chem. Soc. Rev.*, **41**, 6663–6683.
- Glotfelty, T., Zhang, Y., Karamchandani, P., & Streets, D.G. 2016. Changes in future

air quality, deposition, and aerosol-cloud interactions under future climate and emission scenarios. *Atmos. Environ.*

- Jacobson, M.Z., & Streets, D.G. 2009. Influence of future anthropogenic emissions on climate, natural emissions, and air quality. *J. Geophys. Res.*, **114**, D08118.
- Koop, T., Bookhold, J., Shiraiwa, M., & Pöschl, U. 2011. Glass transition and phase state of organic compounds: dependency on molecular properties and implications for secondary organic aerosols in the atmosphere. *Phys. Chem. Chem. Phys.*, **13**, 19238–19255.
- Kroll, J.H., & Seinfeld, J.H. 2008. Chemistry of secondary organic aerosol: formation and evolution of low-volatility organics in the atmosphere. *Atmos. Environ.*, **42**, 3593–3624.
- Lienhard, D.M., Huisman, A.J., Bones, D.L., Te, Y.F., Luo, B.P, Krieger, U.K., & Reid, J.P. 2014. Retrieving the translational diffusion coefficient of water from experiments of single levitated aerosol droplets. *Phys. Chem. Chem. Phys.*, **16**, 16677–16683.
- Mai, H., Shiraiwa, M., Flagan, R.C., & Seinfeld, J.H. 2015. Under what conditions can equilibrium gas-particle partitioning be expected to hold in the atmosphere? *Environ. Sci. Technol.*, **49**, 11485–11491.
- O’Meara, S., Topping, D.O., & McFiggans, G. 2016. The rate of equilibration of viscous aerosol particles. *Atmos. Chem. Phys.*, **16**, 5299–5313.
- Price, C., Mattsson, J., Zhang, Y., Bertram, A.K., Davies, J.F., Grayson, J.W., , Martin, S.T., O’Sullivan, D., Reid, J.P., Rickards, A.M.J., & Murray, B.J. 2015. Water diffusion in atmospherically relevant α -pinene secondary organic material. *Chem. Sci.*, **6**, 4876–4883.
- Saukko, E., Lambe, A.T., Massoli, P., Koop, T., Wright, J.P., Croasdale, D.R., Pedernera, D.A., Onasch, T.B., Laaksonen, A., Davidovits, P., Worsnop, D.R., & Virtanen, A. 2012. Humidity-dependent phase state of SOA particles from biogenic and anthropogenic precursors. *Atmos. Chem. Phys.*, **12**, 7517–7529.
- Seinfeld, J.H., & Pandis, S.N. 2006. *Atmospheric chemistry and physics: from air pollution to climate change*. 2 edn. Hoboken, N.J.: Wiley.
- Shiraiwa, M., Pfrang, C., Koop, T., & Pöschl, U. 2012. Kinetic multi-layer model of gas-particle interactions in aerosols and clouds (KM-GAP): linking condensation, evaporation and chemical reactions of organics, oxidants and water. *Atmos. Chem. Phys.*, **12**, 2777–2794.
- Smith, G.D., Woods, E., Baer, T., & Miller, R.E. 2003. Aerosol uptake described by numerical solution of the diffusion-reaction equations in the particle. *J. Phys. Chem. A*, **107**, 9582–9587.

- Starr, F.W., Sciortino, F., & Stanley, H.E. 1999. Dynamics of simulated water under pressure. *Phys. Rev. E*, **60**, 6757–6768.
- Steimer, S.S., Krieger, U.K., Te, Y.-F., Lienhard, D.M., Huisman, A.J., B.P.Luo, Ammann, M., & Peter, T. 2015. Electrodynamic balance measurements of thermodynamic, kinetic, and optical aerosol properties inaccessible to bulk methods. *Atmos. Meas. Tech.*, **8**, 2397–2408.
- Topping, D., Barley, M.H., & McFiggans, G. 2011. The sensitivity of Secondary Organic Aerosol (SOA) component partitioning to the predictions of component properties-Part 2: Determination of the particle hygroscopicity and its dependence on “apparent” volatility. *Atmos. Chem. Phys.*, **11**, 7767–7779.
- Topping, D.O., Barley, M., & McFiggans, G. 2013. Including phase separation in a unified model to calculate partitioning of vapours to mixed inorganic-organic aerosol particles. *Faraday Discuss.*, **165**, 273–288.
- Tröstl, J., Chuang, W.K., Gordon, H., Heinritzi, M., Yan, C., Molteni, U., Ahlm, L., Frege, C., Bianchi, F., Wagner, R., Simon, M., Lehtipalo, K., Williamson, C., Craven, J.S., Duplissy, J., Adamov, A., Almeida, J., Bernhammer, A-K., Breitenlechner, M., Brilke, S., Dias, A., Ehrhart, S., Flagan, R.C., Franchin, A., Fuchs, C., Guida, R., Gysel, M., Hansel, A., Hoyle, C.R., Jokinen, T., Junninen, H., Kangasluoma, J., Keskinen, H., Kim, J., Krapf, M., Kürten, A., Laaksonen, A., Lawler, M., Leiminger, M., Mathot, S., Möhler, O., Nieminen, T., Onnela, A., Petäjä, T., Piel, F.M., Miettinen, P., Rissanen, M.P., Rondo, L., Sarnela, N., Schobesberger, S., Sengupta, K., Sipilä, M., Smith, J.N., Steiner, G., Tomé, A., Virtanen, A., Wagner, A.C., Weingartner, E., Wimmer, D., Winkler, P.M., Ye, P., Carslaw, K.S., Curtius, J., Dommen, J., Kirkby, J., Kulmala, M., Riipinen, I., Worsnop, D.R., Donahue, N.M, & Baltensperger, U. 2016. The role of low-volatility organic compounds for initial particle growth in the atmosphere. *Nature*, **506**, 527–531.
- Vaden, T.D., Imre, D., Beránek, J., Shrivastava, M., & Zelenyuk, A. 2011. Evaporation kinetics and phase of laboratory and ambient secondary organic aerosol. *P. Natl. Acad. Sci. USA*, **108**, 2190–2195.
- Vignes, A. 1966. Diffusion in binary solutions. *Ind. Eng. Chem. Fund.*, **5**, 189–199.
- Virtanen, A., Joutsensaari, Koop, T., Kannosto, J., Yli-Pirilä, P., Leskinen, J., Mäkelä, J.M., Holopainen, J.K., Pöschl, U., Kulmala, M., Worsnop, D.R., & Laaksonen, A. 2010. An amorphous solid state of biogenic secondary organic aerosol particles. *Nature*, **467**, 824–827.
- Zaveri, R.A., Easter, R.C., Fast, J.D., & Peters, L.K. 2008. Model for Simulating Aerosol Interactions and Chemistry (MOSAIC). *J. Geophys. Res.*, **113**, D13204.

- Zaveri, R.A., Easter, R.C., Shilling, J.E., & Seinfeld, J.H. 2014. Modeling kinetic partitioning of secondary organic aerosol and size distribution dynamics: representing effects of volatility, phase state, and particle-phase reaction. *Atmos. Chem. Phys.*, **14**, 5153–5181.
- Zobrist, B., Marcolli, C., Pedernera, D.A., & Koop, T. 2008. Do atmospheric aerosols form glasses? *Atmos. Chem. Phys.*, **8**, 5221–5244.
- Zobrist, B., Soonsin, V., Luo, B.P., Krieger, U.K., Marcolli, C., Peter, T., & Koop, T. 2011. Ultra-slow water diffusion in aqueous sucrose glasses. *Phys. Chem. Chem. Phys.*, **13**, 3514–3526.
- Zuend, A., Marcolli, C., Luo, B.P., & Peter, T. 2008. A thermodynamic model of mixed organic-inorganic aerosols to predict activity coefficients. *Atmos. Chem. Phys.*, **8**, 4559–4593.

3 Summary

A conclusive overview of the thesis will be presented, including a summary of the objectives of each paper. After this a more detailed conclusion of each paper will be given, ideas for future research will be discussed, along with how this work responds to the motivation given in the introduction.

3.1 Thesis Overview

20-90 % of aerosol mass in the ambient atmosphere is expected to be composed of organic material, and of this approximately 70 % is expected to be secondary organic aerosol (SOA) (Kanakidou *et al.* , 2005; Hallquist *et al.* , 2009). The large uncertainty in climatic effects of aerosol is largely due to uncertainty in its number size distribution and composition (Boucher *et al.* , 2013). While large uncertainties in aerosol health effects is partly attributable to gaps in biochemical knowledge, again the aerosol number size distribution and composition is important (Krzyzanowski & Cohen, 2008; Baltensperger *et al.* , 2008; Ford & Heald, 2016). With these considerations it is important to improve our knowledge of aerosol properties through measurements and our ability to model aerosol through theory and comparison with measurements.

This thesis has focussed on improvements to the modelling approach to atmospheric aerosol, and specifically to simulating partitioning between the gas- and particle-phase. Several factors determine the fraction of a partitioning component in either phase at equilibrium. The factor investigated here is the pure component vapour pressure. While doubts remain over the ability of simplified treatments of volatility to simulate partitioning, such as the volatility basis set (Donahue *et al.* , 2006; Robinson *et al.* , 2007; Donahue *et al.* , 2009), a mechanistic approach in which component volatilities are individually employed, is required. The mechanistic approach is in theory applicable to any scenario, and would therefore provide a benchmark model to compare simpler treatments against. In the first paper presented here an assessment of vapour pressure estimation methods was conducted through a comparison with measurements. The main objective of this paper was to identify the most accurate estimation method, and therefore guide future mechanistic studies into aerosol transformation.

Although the equilibrium condensable fraction has traditionally been used to estimate the amount of a component in the particle-phase, the partitioning rate will also be influential. To estimate this rate, gas- and particle-phase diffusion in addition to surface accommodation requires modelling. While the gas-phase rate and surface accommodation has already been incorporated into partitioning calculations, a general particle-phase diffusion equation has not yet been implemented. The aim of current diffusion models is to solve Fick's

second law, and three numerical models have been proposed to do this. They had not been compared previously, and therefore the second paper presented here had the objective of comparing estimates from the three models, along with identification and explanation of any discrepancies.

While numerical solutions to diffusion can act as benchmarks for comparison with analytical models, they are more computationally demanding, requiring greater calculation time. Consequently, for practical solution of particle-phase diffusion in a regional model, an analytical solution is preferable. While such a solution has been found for the limiting case of diffusion independent of composition (constant diffusion coefficient), there is no analytical solution when the diffusion coefficient is dependent on composition. To overcome this, the third and final paper presented here investigated a correction to the previously presented analytical solution of Zaveri *et al.* (2014) that would make it applicable to composition dependent diffusion.

The main contributions of each paper to atmospheric science, specifically modelling of gas-particle partitioning, is summarised below:

paper 1: identification of the most accurate vapour pressure estimation method for use in mechanistic approaches to gas-particle partitioning modelling and indication of the sensitivity of estimated SOA concentration arising from vapour pressure estimation inaccuracy;

paper 2: confirmation of consistency between numerical solutions to Fickian diffusion and of the most effective methods to infer diffusion coefficients from mass transfer experiments;

paper 3: presentation of a correction to an analytical solution of particle-phase diffusion when diffusion is dependent on particle composition under limiting conditions, and explanation of why a general solution cannot be attained through a simple correction.

A more thorough conclusion from each paper is given next.

3.2 Conclusion of An assessment of vapour pressure estimation methods

The Lee-Kesler (Reid *et al.* , 1987) estimation method showed a range of advantageous properties over the other assessed methods. It is applicable to a relatively diverse range of chemical classes and produces comparatively low error and low bias estimates. For a subset of relatively low volatility compounds (vapour pressure at room temperature $< 10^{-2}$ Pa), the comparative accuracy of the Lee-Kesler method was even greater than for the entire test set of measurements: it had a mean average error of $10^{0.82}$ Pa com-

pared to $10^{0.97}$ Pa for the Nannoolal method (Nannoolal *et al.* , 2008), which was found to give best agreement in the previous assessment of Barley & McFiggans (2010). However, this recommendation is accompanied with a caution concerning the effect of vapour pressure inaccuracy on estimated SOA loading. Generally, the total (gas- and particle-phase) concentration of aerosol components decreases with decreasing vapour pressure (Donahue *et al.* , 2006; Cappa & Jimenez, 2010). Consequently, if comparable numbers of components have vapour pressures underestimated and overestimated (therefore giving a low overall bias), the result is an increase in particle-phase concentration from the measured vapour pressure case because the partitioning coefficients of relatively abundant and relatively scarce components are overestimated and underestimated, respectively. This is true even if similar fractions of components have vapour pressure overestimated and underestimated by a similar degree because the difference in their total concentrations means the exchange of total mass between volatility bins is unequal, acting to increase the total concentration in lower volatility (higher partitioning coefficient) bins.

The component concentration relationship with volatility meant the method with positive bias in vapour pressures (i.e. on average underestimated partitioning coefficients), Myrdal and Yalkowsky (Myrdal & Yalkowsky, 1997), gave best agreement with the SOA loading estimated using measured vapour pressures. When using the full set of components and assuming a non-polluted environment, the Myrdal and Yalkowsky method underestimated SOA loading by 30 %, compared to a 100 % overestimate by the Lee-Kesler method.

The EVAPORATION (Compernelle *et al.* , 2011) method had a mean average error of $10^{0.54}$ Pa for the 46 components it was applicable to, which was considerably lower than any other method, including Lee-Kesler with $10^{0.90}$ Pa. The EVAPORATION method cannot be applied to components with certain functional groups because contributions from these groups have not been calculated. The presented results, however, indicate that priority should be given to expanding this method so that it may be generally applicable.

The analysis of SOA loading sensitivity to vapour pressure estimation indicates the inaccuracy that may arise from using an estimation method in a regional model with a mechanistic approach to partitioning. Despite several of the methods having mean average errors close to an order of magnitude when compared to measurements, the estimated SOA loading is substantially less, around a factor of 2-3 different to the loading derived using measured vapour pressures. Although this is somewhat reassuring, it is still a substantial difference. There are major limitations to this assessment, however, such as the neglect of chemical reactions in either phase, and of new emission or deposition. In reality, processes such as these will influence partitioning and the components undergoing it. To address this issue, Li *et al.* (2015) test the response of a regional model, including chemical reactions, to a decrease in vapour pressure of two orders of magnitude. They report a factor of 2.5 increase in particulate loading, comparable to the estimated change

seen in the study here. However, the difference in estimated vapour pressure here was approximately one order of magnitude on average and included deviations of both signs (i.e. overestimating the vapour pressure of some components and underestimating for others). The comparison of the two studies, therefore, indicates a strong decrease in sensitivity of simulated SOA formation to vapour pressure when the model incorporates more partitioning dependent processes to be more realistic.

3.3 Conclusion of The rate of equilibration of viscous aerosol particles

In this paper it was shown that three published numerical solutions to Fick's second law gave consistent results, despite substantial variations in their model framework. They were rigorously tested through the introduction of relatively steep gradients of concentration with particle radius and of diffusion coefficient with partitioning component mole fraction. In addition, it was observed that for the same concentration and diffusion coefficient gradient and computer, the ETH model took approximately two orders of magnitude less time than the other two models. Consequently, the Euler forward step method used in the ETH model appears to be preferable.

The consistency between models allowed a reliable theoretical study on methods to optimise diffusion coefficient retrieval from mass transfer experiments (e.g. Zobrist *et al.*, 2011; Lienhard *et al.*, 2014; Steimer *et al.*, 2015). Using large changes in gas-phase saturation ratio of the partitioning component (which drives partitioning), can lead to poor constraint of the diffusion coefficient dependence on composition, because the response is dominated by the greatest diffusion coefficient encountered. For example, during condensation of a plasticiser, the diffusion coefficient is greatest at the highest gas-phase saturation ratio used, and this dominates the diffusion response, masking the diffusion coefficient value at lower saturation ratios. Use of small steps in gas-phase saturation therefore allows inference of the diffusion coefficient across a range of compositions. Furthermore, it was shown that the diffusion coefficient can be inferred with greatest certainty when the gas-phase saturation ratio changes quickly compared to the partitioning response.

Rapid equilibration times of less than 1 s were estimated by the diffusion models when the saturation ratio of water was increased to 90 %, even when the initial particle was comparatively large and had a relatively low diffusivity (characteristic of a glassy state according to the Stokes-Einstein relation). This shows the substantial impact an abundant plasticiser can have on particle-phase diffusion times, and that caution is required when diffusion or viscosity measurements obtained at low relative humidities are used to predict partitioning characteristics under more atmospherically relevant conditions. For example, several diffusion-based studies, including Vaden *et al.* (2011) and Abramson *et al.* (2013)

do not probe the effect of variable relative humidity, despite the relatively high and variable concentration of water vapour in the atmosphere.

3.4 Conclusion of Implementing a more realistic efficient model for particle-phase diffusion, limitations to a general approach

This paper showed that when the gas-phase concentration, and therefore particle surface mole fraction (assuming no partitioning rate limitation from gas-phase diffusion and surface accommodation), of a partitioning component is constant, a correction to the analytical solution of Zaveri *et al.* (2014) can simulate composition dependent diffusion with reasonable accuracy. The correction was implemented in a polydisperse model for aerosol transformation and used to confirm that increasing diffusion coefficient of the plasticising component compared to a non-volatile component increases rate of condensation and therefore particle number size transformation. However, the degree of narrowing of the number size distribution, indicative of particle-phase diffusion limited partitioning (Zaveri *et al.* , 2014), did not change with increasing plasticising effect.

The correction was shown to be specific to the ratio of component molar volumes and the dependence of diffusion coefficient on composition. However, it is expected that modification of the correction could overcome these limitations. It was found that to correct the solution for the more general case of a variable gas-phase saturation ratio of the partitioning component required estimation of the ratio of rate of partitioning component concentration change in the particle bulk to this rate at the particle surface. However, because the bulk particle concentration is the value being estimated, a general solution is intractable.

The MOSAIC model is already implemented inside regional models (Fry & Sackinger, 2012; Baklanov *et al.* , 2014) that account, among other influences on particle composition, for chemical reactions. Implementation of a realistic model for particle-phase diffusion in such models will allow assessment of conditions when particle-phase diffusion is important. Currently, identification of these conditions has been for limiting conditions, such as particle-phase diffusion independent of composition (Mai *et al.* , 2015), however, the theoretical framework for identifying kinetic regimes in general scenarios has been proposed (Berkemeier *et al.* , 2013; Shiraiwa *et al.* , 2014). With these frameworks and regional models already established, the result of this final paper provides a stepping stone toward a thorough assessment of the sensitivity of particle characteristics to particle-phase diffusion.

3.5 Future Work

While the discrepancies between even the most accurate vapour pressure estimation methods and measurements presented in the first paper appear large, it has not yet been determined what accuracy of estimated vapour pressure is required for a satisfactory simulation of gas-particle partitioning with a mechanistic approach. A simple test of particulate concentration sensitivity to vapour pressure accuracy was conducted by Li *et al.* (2015) in a regional model. They decreased the vapour pressure of all components by two orders of magnitude from a base case of estimated vapour pressures and compared estimated particulate concentration between the vapour pressure treatments. In the first paper here and in Barley *et al.* (2011), the average disagreement in vapour pressures between estimation methods is approximately one order of magnitude, and particulate concentration sensitivity to vapour pressure was assessed for a fixed set of components, without consideration of other processes, and therefore in a very simple model compared to that of Li *et al.* (2015). Despite vapour pressure varying by approximately one order of magnitude more in Li *et al.* (2015), the resulting sensitivity of particulate concentration is similar to or less than in the first paper here and in Barley *et al.* (2011). This indicates that with increased model complexity, accounting for such processes as chemical reaction, emission and deposition, sensitivity of gas-particle partitioning to vapour pressure estimation decreases. Therefore, in order to constrain the acceptable vapour pressure uncertainty, a systematic assessment of particulate concentration and composition sensitivity to vapour pressure similar to McFiggans *et al.* (2010) and Barley *et al.* (2011), but in a regional model such as Li *et al.* (2015) could be very useful. Once a mechanistic approach to partitioning is implemented in a regional model and component vapour pressures are estimated sufficiently accurately, it will allow assessment of the capability of simpler (and less computationally expensive) approaches to component representation and volatility, such as the volatility basis set (Donahue *et al.*, 2006; Robinson *et al.*, 2007; Donahue *et al.*, 2009).

There is also a demand for accurate vapour pressure measurements regardless of estimation method accuracy when used in regional models. As discussed in sects. 1.7 and 1.8, accurate vapour pressure measurements are required for accurate inference of deviations from non-ideality and surface accommodation. In turn, these measurements will contribute to our understanding and modelling of phase separation, partitioning coefficients and kinetic limitation of gas-particle partitioning due to interfacial transport. Improved models for these processes may then be implemented in regional models, allowing assessment of the sensitivity of aerosol properties to them.

The inclusion of particle-phase diffusion inside regional models has not yet been achieved. However, similar to a mechanistic approach to vapour pressures, the sensitivity of par-

ticulate properties to diffusion is most usefully assessed inside a model that accounts for other processes affecting particle properties, like chemical reaction. The third paper here shows that either a predictive correction (i.e. one based on prior knowledge of how variable surface concentrations affect diffusion through the particle bulk) to the analytical solution, or a numerical solution, may be required for estimating particle-phase diffusion under general conditions. The second paper shows that any of the numerical solutions presented to date may be used accurately, however, the Euler forward step method of the ETH model appears to be most computationally efficient.

One possible approach to deriving a generally applicable solution may be through decision tree learning, whereby a numerical solution is used to train a program to estimate diffusion rate for a given scenario, accounting for variables such as: the diffusion coefficient dependence on composition, the proximity to equilibrium, the particle bulk and surface concentration of diffusant, initial particle size and change in particle size due to partitioning. In practise the program would identify the most likely diffusion rate given these inputs, which should be more computationally efficient than using a numerical solution.

Alternatively, it may be possible to make a numerical solution more computationally efficient and implement this within a regional model. As discussed in both the second and third papers here, accuracy of the numerical solution is dependent on spatial and temporal resolution. The required resolutions are dependent on the steepness of concentration-radius gradients and diffusion coefficient-mole fraction gradients. Currently the spatial resolution is fixed throughout a numerical solution simulation, however it is plausible that as diffusion proceeds it could respond so that relatively high resolution is focussed where and when concentration gradients are strongest, allowing lower resolution elsewhere in the particle and when the concentration gradient flattens out. Since resolution is proportional to computer power, this approach would maximise computational efficiency. Adaptive spatial and temporal resolutions would be very useful for a generally applicable numerical solution so that it may respond to changes of environmental variables such as gas-phase saturation ratios and initial compositions of particulates.

Whether an analytical or numerical solution are developed and implemented in a regional model, under certain conditions, particle-phase diffusion (as well as gas-phase diffusion and interfacial transport) is unlikely to pose a significant kinetic limitation to partitioning. Rather, partitioning times compared to times for other processes like coagulation may be insignificant, in which case instantaneous equilibration is a valid assumption. Under such scenarios, the particle-phase diffusion calculations may be switched off. For a model to determine whether to solve diffusion, a decision process is required. Such a process is proposed in Berkemeier *et al.* (2013) and Shiraiwa *et al.* (2014). If these, or a similar system, could be implemented alongside gas- and particle-phase diffusion and interfacial

transport models in a regional model, computational efficiency could be optimised.

3.6 Implications for Climate and Air Quality

In the thesis introduction, the motivation for this work was to improve understanding of how aerosols affect climate and health. With increased certainty around their effects, policies to mitigate climate change and improve human health would be better informed, and have a greater likelihood of being effective.

The work presented here builds on a body of previous research toward improved understanding of aerosol effects. As discussed in sects. 3.1 to 3.4, the results here have contributed to our understanding of the mechanistic modelling of gas-particle partitioning. If done accurately, the mechanistic approach provides the most generally applicable and robust method to partitioning modelling. In theory, it allows thorough assessment of how determinants of partitioning affect particulate characteristics such as number size distribution, and when coupled with meteorological and chemical models over regional or global scales, therefore allows assessment of how these determinants affect climate and health. As yet such an assessment is theoretical because methods to accurately model partitioning have not yet been found. The results here help to narrow the search for some of these methods, specifically, estimating the partitioning coefficient through component vapour pressure estimates and modelling particle-phase diffusion. These results lay the foundation for the future work discussed in the previous section, which, combined with advances in other areas such as vapour pressure measurement and biochemical understanding, will progress aerosol modelling closer to the final aim of high certainty around the climatic and health effects of aerosol.

References for Introduction and Summary

- Abbasi, A., & Eslamloueyan, R. 2014. Determination of binary diffusion coefficients of hydrocarbon mixtures using MLP and ANFIS networks based on QSPR method. *Chemometr. Intell. Lab.*, **132**, 39–51.
- Abramson, E., Imre, D., Beránek, J., Wilson, J., & Zelenyuk, A. 2013. Experimental determination of chemical diffusion within secondary organic aerosol particles. *Phys. Chem. Chem. Phys.*, **15**, 2983–2991.
- Ahmadov, R., McKeen, S.A., Robinson, A.L., Bahreini, R., Middlebrook, A.M., de Gouw, J.A., Meagher, J., Hsie, E.-Y., Edgerton, E., Shaw, S., & Trainer, M. 2012. A volatility basis set model for summertime secondary organic aerosol over the eastern United States in 2006. *J. Geophys. Res.*, **117**, D06301.
- Aiken, A.C., DeCarlo, P.F., Kroll, J.H., Worsnop, D.R., Huffman, J.A., Docherty, K.S., Ulbrich, I.M., Mohr, C., Kimmel, J.R., Sueper, D., Sun, Y., Zhang, Q., Trimborn, A., Northway, M., Ziemann, P.J., Canagaratna, M.R., Onasch, T.B., Alfarra, M.R., Prevot, A.S.H., Dommen, J., Duplissy, J., Metzger, A., Baltensperger, U., & Jimenez, J.L. 2008. O/C and OM/OC ratios of primary, secondary, and ambient organic aerosols with high-resolution time-of-flight aerosol mass spectrometry. *Environ. Sci. Technol.*, **42**, 4478–4485.
- Allan, J. D., Williams, P.I., Najera, J., Whitehead, J.D., Flynn, M.J., Taylor, J.W., Liu, D., Darbyshire, E., Carpenter, L.J., Chance, R., Andrews, S.J., Hackenberg, S.C., & McFiggans, G. 2015. Iodine observed in new particle formation events in the Arctic atmosphere during ACCACIA. *Atmos. Chem. Phys.*, **15**, 5599–5609.
- Anenberg, S.C., Horowitz, L.W., Tong, D.Q., & West, J.J. 2010. An estimate of the global burden of anthropogenic ozone and fine particulate matter on premature human mortality using atmospheric modeling. *Environ. Health Perspect.*, **118**, 1189–1195.
- Arp, H.P.H., & Goss, K-U. 2009. Ambient gas/particle partitioning. 3. Estimating partition coefficients of apolar, polar and ionisable organic compounds by their molecular structure. *Environ. Sci. Technol.*, **43**, 1923–1929.
- Artaxo, P., Maenhaut, W., Storms, H., & Grieken, R.V. 1990. Aerosol characteristics and sources for the Amazon basin during the wet season. *J. Geophys. Res.*, **95(D10)**, 16971–16985.
- Asher, W.E., & Pankow, J.F. 2006. Vapour pressure prediction for alkenoic and aromatic organic compounds by a UNIFAC-based group contribution method. *Atmos. Environ.*, **40**, 3588–3600.
- Aumont, B., Szopa, S., & Madronich, S. 2005. Modeling the evolution of organic carbon

- during its gas-phase tropospheric oxidation: development of an explicit model based on a self generating approach. *Atmos. Chem. Phys.*, **5**, 2497–2517.
- Baklanov, A., Schlünzen, K., Suppan, P., Baldasano, J., Brunner, D., Aksoyoglu, S., Carmichael, G., Douros, J., Flemming, J., Forkel, R., Galmarini, S., Gauss, M., Grell, G., Hirtl, M., Joffre, S., Jorba, O., Kaas, E., Kaasik, M., Kallos, G., Kong, X., Korsholm, U., Kurganskiy, A., Kushta, J., Lohmann, U., Mahura, A., Manders-Groot, A., Maurizi, A., Moussiopoulos, N., Rao, S. T., Savage, N., Seigneur, C., Sokhi, R. S., Solazzo, E., Solomos, S., Sørensen, B., Tsegas, G., Vignati, E., Vogel, B., , & Zhang, Y. 2014. Online coupled regional meteorology chemistry models in Europe: current status and prospects. *Atmos. Chem. Phys.*, **14**, 317–398.
- Baltensperger, U., Dommen, J., Alfarra, M.R., Duplissy, J., Gaeggeler, K., Metzger, A., Facchini, M.C., Decesari, S., Finessi, E., Reinnig, C., Schott, M., Warnke, J., Hoffmann, T., Klatzer, B., Puxbaum, H., Geiser, M., Savi, M., Lang, D., Kalberer, M., & Geiser, T. 2008. Combined Determination of the Chemical Composition and of Health Effects of Secondary Organic Aerosols: The POLYSOA Project. *J. Aerosol Med. Pulm. D.*, **21(1)**, 145–154.
- Barley, M.H., & McFiggans, G. 2010. The critical assessment of vapour pressure estimation methods for use in modelling the formation of atmospheric organic aerosol. *Atmospheric Chemistry and Physics*, **10**, 749–767.
- Barley, M.H., Topping, D., Jenkin, M.E., & McFiggans, G. 2009. Sensitivities of the absorptive partitioning model of secondary organic aerosol formation to the inclusion of water. *Atmos. Chem. Phys.*, **9**, 2919–2932.
- Barley, M.H., Topping, D., Lowe, D., Utembe, S., & McFiggans, G. 2011. The sensitivity of secondary organic aerosol (SOA) component partitioning to the predictions of component properties-Part 3: Investigation of condensed compounds generated by a near-explicit model of VOC oxidation. *Atmos. Chem. Phys.*, **11**, 13145–13159.
- Barsanti, K.C., & Pankow, J.F. 2004. Thermodynamics of the formation of atmospheric organic particulate matter by accretion reactions-Part1: aldehydes and ketones. *Atmos. Environ.*, **38**, 4371–4382.
- Bergström, R., van der Gon, H.A.C. Denier, Prévôt, A.S.H., Yttri, K.E., & Simpson, D. 2012. Modelling of organic aerosols over Europe (2002-2007) using a volatility basis set (VBS) framework: application of different assumptions regarding the formation of secondary organic aerosol. *Atmos. Chem. Phys.*, **12**, 8499–8527.
- Berkemeier, T., Huisman, A.J., Ammann, M., Shiraiwa, M., Koop, T., & Pöschl, U. 2013. Kinetic regimes and limiting cases of gas uptake and heterogeneous reactions in

- atmospheric aerosols and clouds: a general classification scheme. *Atmos. Chem. Phys.*, **13**, 6663–6686.
- Berkemeier, T., Shiraiwa, M., Pöschl, U., & Koop, T. 2014. Competition between water uptake and ice nucleation by glassy organic aerosol particles. *Atmos. Chem. Phys.*, **14**, 12513–12531.
- Bi, X., Zhang, G., Li, L., Wang, X., Li, M., Sheng, G., Fu, J., & Zhou, Z. 2011. Mixing state of biomass burning particles by single particle aerosol mass spectrometer in the urban area of PRD, China. *Atmos. Environ.*, **45**, 3447–3453.
- Bian, F., & Bowman, F.M. 2002. Theoretical method for lumping multicomponent secondary organic aerosol mixtures. *Environ. Sci. Technol.*, **36**, 2491–2497.
- Bidleman, T.F. 1988. Atmospheric processes - wet and dry deposition of organic compounds are controlled by their vapor-particle partitioning. *Environ. Sci. Technol.*, **22(4)**, 361–367.
- Bilde, M., & Pandis, S.N. 2001. Evaporation Rates and Vapor Pressures of Individual Aerosol Species Formed in the Atmospheric Oxidation of α - and β -pinene. *Environ. Sci. Technol.*, **35**, 3344–3349.
- Bilde, M., Svenningsson, B., Mønster, J., & Rosenørn, T. 2003. Even-Odd Alteration of Evaporation Rates and Vapor Pressures of C3-C9 Dicarboxylic Acid Aerosols. *Environ. Sci. Technol.*, **37**, 1371–1378.
- Bilde, M., Barsanti, K., Booth, M., Cappa, C.D., Donahue, N.M., Emanuelsson, E.U., McFiggans, G., Krieger, U.K., Marcolli, C., Topping, D., Ziemann, P., Barley, M., Clegg, S., Dennis-Smith, B., Hallquist, M., Hallquist, Å.M., Khlystov, A., Kulmala, M., Mogensen, D., Percival, C.J., Pope, F., Reid, J.P., Silva, M.A.V. Ribeiro Da, Rosenoern, T., Salo, K., Soonsin, V.P., Yli-Juuti, T., Prisle, N.L., Pagels, J., Rarey, J., Zardini, A.A., & Riipinen, I. 2015. Saturation Vapor Pressures and Transition Enthalpies of Low-Volatility Organic Molecules of Atmospheric Relevance: From Dicarboxylic Acids to Complex Mixtures. *Chem. Rev.*, **115(10)**, 4115–4156.
- Bloss, C., Wagner, V., Jenkin, M. E., Volkamer, R., Bloss, W. J., Lee, J. D., Heard, D. E., Wirtz, K., Martin-Reviejo, M., Rea, G., Wenger, J. C., , & Pilling, M. J. 2005. Development of a detailed chemical mechanism (MCM v3.1) for the atmospheric oxidation of aromatic hydrocarbons. *Atmos. Chem. Phys.*, **5**, 641–664.
- Booth, A.M., Markus, T., McFiggans, G., Percival, C.J., McGillen, M.R., & Topping, D. 2009. Design and construction of a simple Knudsen Effusion Mass Spectrometer (KEMS) system for vapour pressure measurements of low volatility organics. *Atmos. Meas. Tech.*, **2**, 355–361.

- Booth, A.M., Barley, M.H., Topping, D.O., McFiggans, G., Garforth, A., & Percival, C.J. 2010. Solid state and sub-cooled liquid vapour pressures of substituted dicarboxylic acids using Knudsen Effusion Mass Spectrometry (KEMS) and Differential Scanning Calorimetry. *Atmos. Chem. Phys.*, **10**, 4879–4892.
- Booth, A.M., Murphy, B., Riipinen, I., Percival, C.J., & Topping, D.O. 2014. Connecting Bulk Viscosity Measurements to Kinetic Limitations on Attaining Equilibrium for a Model Aerosol Composition. *Environ. Sci. Tech.*, **48**, 9298–9305.
- Boucher, O., Randall, D., Artaxo, P., Bretherton, C., Feingold, G., Forster, P., Kerminen, V.-M., Kondo, Y., Liao, H., Lohmann, U., Rasch, P., Satheesh, S.K., Sherwood, S., Stevens, B., & Zhang, X.Y. 2013. Clouds and Aerosols. *In*: Stocker, T.F., Qin, D., Plattner, G.-K., Tignor, M., Allen, S.K., Boschung, J., Nauels, A., Xia, Y., Bex, V., & Midgley, P.M. (eds), *Climate Change 2013: The Physical Science Basis. Contribution of Working Group I to the Fifth Assessment Report of the Intergovernmental Panel on Climate Change*. Cambridge, United Kingdom and New York, NY, USA: Cambridge University Press.
- Bradley, R.S., & Cotson, S. 1953. The Vapour Pressure and Lattice Energy of Hydrogen-bonded Crystals. Part II. α - and β -Anhydrous Oxalic Acid and Tetragonal Pentaerythritol. *J. Chem. Soc.*, **Jun**, 1684–1688.
- Bruns, E.A., Greaves, J., & Finlayson-Pitts, B.J. 2012. Measurement of vapour pressures and heats of sublimation of dicarboxylic acids using atmospheric solids analysis probe mass spectrometry. *J. Phys. Chem. A*, **116**, 5900–5909.
- Cabada, J.C., Rees, S., Takahama, S., Khlystov, A., Pandis, S.N., Davidson, C.I., & Robinson, A.L. 2004. Mass size distributions and size resolved chemical composition of fine particulate matter at the Pittsburgh supersite. *Atmos. Environ.*, **38**, 3127–3141.
- Canagaratna, M.R., Jayne, J.T., Jimenez, J.L., Allan, J.D., Alfarra, M.R., Zhang, Q., Onasch, T.B., Drewnick, F., Coe, H., Middlebrook, A., Della, A., Williams, L.R., Trimborn, A.M., Northway, M.J., DeCarlo, P.F., Kolb, C.E., Davidovits, P., & Worsnop, D.R. 2007. Chemical and microphysical characterization of ambient aerosols with the aerodyne aerosol mass spectrometer. *Mass Spectrom. Rev.*, **26**, 185–222.
- Capouet, M., & Müller, J.-F. 2006. A group contribution method for estimating the vapour pressures of α -pinene oxidation products. *Atmos. Chem. Phys.*, **6**, 1455–1467.
- Cappa, C.D., & Jimenez, J.L. 2010. Quantitative estimates of the volatility of ambient organic aerosol. *Atmos. Chem. Phys.*, **10**, 5409–5424.
- Cappa, C.D., Lovejoy, E.R., & Ravishankara, A.. 2007. Determination of evaporation

- rates and vapour pressures of very low volatility compounds: a study of the C4-C10 and C12 dicarboxylic acids. *J. Phys. Chem. A*, **111**, 3099–3109.
- Carslaw, K.S., Clegg, S.L., & Brimblecombe, P. 1995. A thermodynamic model of the system HCL-HNO₃-H₂SO₄-H₂O, including solubilities of HBr, from <200 to 328 K. *J. Phys. Chem.*, **99**, 11557–11574.
- Chapman, C., Cowling, T.G., & Burnett, D. 1970. *The mathematical theory of non-uniform gases : an account of the kinetic theory of viscosity, thermal conduction and diffusion in gases*. 3 edn. London: Cambridge U.P.
- Charlson, R.J., Lovelock, J.E., Andreae, M.O., & Warren, S.G. 1987. Oceanic phytoplankton, atmospheric sulphur, cloud albedo and climate. *Nature*, **326**, 655–661.
- Chattopadhyay, S., & Ziemann, P.J. 2005. Vapor pressures of substituted and unsubstituted monocarboxylic and dicarboxylic acids measured using an improved thermal desorption particle beam mass spectrometry method. *J. Aerosol. Sci. Technol.*, **39(11)**, 1085–1100.
- Chenlo, F., Moreira, R., Pereira, G., & Ampudia, A. 2002. Viscosities of aqueous solutions of sucrose and sodium chloride of interest in osmotic dehydration processes. *J. Food. Eng.*, **54(4)**, 347–352.
- Chenyakin, Y., Ullmann, D.A., Evoy, E., Renbaum-Wolff, L., Kamal, S., & Bertram, A.K. 2016. Diffusion coefficients of organic molecules in sucrose-water solutions and comparison with Stokes-Einstein predictions. *Atmos. Chem. Phys.*, **submitted**.
- Chung, S.H., & Seinfeld, J.H. 2002. Global distribution and climate forcing of carbonaceous aerosols. *J. Geophys. Res.*, **107(D19)**, 4407.
- Ciobanu, V.G., Marcolli, C., Krieger, U.K., Weers, U., & Peter, T. 2009. Liquid-liquid phase separation in mixed organic/inorganic aerosol particles. *J. Phys. Chem. A*, **113**, 10966–10978.
- Clark, W.M., & Rowley, R.L. 1986. The mutual diffusion coefficient of methanol-n-hexane near the consolute point. *AICHE J*, **32(7)**, 1125–1131.
- Clegg, S., & Seinfeld, J.H. 2004. Improvement of the Zdanovskii-Stokes-Robinson model for mixtures containing solutes of different charge types. *J. Phys. Chem. A*, **108**, 1008–1017.
- Clegg, S., & Seinfeld, J.H. 2006. Thermodynamic models of aqueous solutions containing inorganic electrolytes and dicarboxylic acids at 298.15 K. 1. The acids as nondissociating components. *J. Phys. Chem. A*, **110**, 5692–5717.
- Clegg, S., Seinfeld, J.H., & Brimblecombe, P. 2001. Thermodynamic modelling of aqueous

- aerosols containing electrolytes and dissolved organic compounds. *Aerosol Sci.*, **32**, 713–738.
- Clegg, S.L., & Brimblecombe, P. 1998. Thermodynamic model of the system H^+ - NH_4^+ - NA^+ - SO_4^{2-} - NO_3^- - CL^- - H_2O at 298.15 K. *J. Phys. Chem. A*, **102**, 2155–2171.
- Clegg, S.L., Carslaw, K.S., & Wexler, A.S. 1998. Thermodynamic model of the system H^+ - NH_4^+ - SO_4^{2-} - NO_3^- - H_2O at tropospheric temperatures. *J. Phys. Chem. A*, **102**, 2137–2154.
- Clegg, S.L., Kleeman, M.J., Griffin, R.J., & Seinfeld, J.H. 2008. Effects of uncertainties in the thermodynamic properties of aerosol components in an air quality model - Part 1: Treatment of inorganic electrolytes and organic compounds in the condensed phase. *Atmos. Chem. Phys.*, **8**, 1057–1085.
- Clement, C.F., Kulmala, M., & Vesala, T. 1996. Theoretical consideration on sticking probabilities. *J. Aerosol Sci.*, **27(6)**, 869–882.
- Compernelle, S., Ceulemans, K., & Müller, J.-F. 2009. Influence of non-ideality on condensation to aerosol. *Atmos. Chem. Phys.*, **9**, 1325–1338.
- Compernelle, S., Ceulemans, K., & Müller, J.-F. 2011. EVAPORATION: a new vapour pressure estimation method for organic molecules including non-additivity and intramolecular interactions. *Atmos. Chem. Phys.*, **11**, 9431–9450.
- Corti, H.R., Frank, G.A., & Marconi, M.C. 2008. Diffusion-viscosity decoupling in supercooled aqueous trehalose solutions. *J. Phys. Chem. B.*, **112**, 12899–12906.
- Crank, J. 1975. *The Mathematics of Diffusion*. 2 edn. Oxford: Clarendon Press.
- Crouse, J.D., Nielsen, L.B., Jørgensen, S., Kjaergaard, H.G., & Wennberg, P.O. 2013. Autoxidation of organic compounds in the atmosphere. *J. Phys. Chem. Lett.*, **4(20)**, 3513–3520.
- da Silva, M.A.V. Ribeiro, & Monte, M.J.S. 1990. The construction, testing and use of a new knudsen effusion apparatus. *Thermochim. Acta.*, **171**, 169–183.
- da Silva, M.A.V. Ribeiro, Monte, M.J.S., & Ribeiro, J.R. 1999. Vapour pressures and the enthalpies and entropies of sublimation of five dicarboxylic acids. *J. Research of the National Bureau of Standards - A. Physics and Chemistry*, **80A(1)**, 35–39.
- da Silva, M.A.V. Ribeiro, Monte, M.J.S., & Ribeiro, J.R. 2001. Thermodynamic study on the sublimation of succinic acid and of methyl- and dimethyl-substituted succinic and glutaric acids. *J. Chem. Thermodynamics*, **33**, 23–31.
- Dahneke, B. 1983. *Theory of dispersed multiphase flow*. New York: Academic Press.

- Dall'Osto, M., & Harrison, R.M. 2006. Chemical characterisation of single airborne particles in Athens (Greece) by ATOFMS. *Atmos. Environ.*, **40**, 7614–7631.
- Davidovits, P., Kolb, C.E., Williams, L.R., Jayne, J.T., & Worsnop, D.R. 2006. Mass accommodation and chemical reactions at the gas-liquid interface. *Chem. Rev.*, **106**, 1323–1354.
- Davies, J.F., & Wilson, K.R. 2016. Raman Spectroscopy of Isotopic Water Diffusion in Ultraviscous, Glassy, and Gel States in Aerosol by Use of Optical Tweezers. *Analyt. Chem.*, **88**, 2361–2366.
- Davies, M., & Thomas, G.H. 1960. The lattice energies, infra-red spectra, and possible cyclization of some dicarboxylic acids. *Transactions of the Faraday Society*, **56(2)**, 185–192.
- Davis, E.J. 2006. A history and state-of-the-art of accommodation coefficients. *Atmos. Res.*, **82**, 561–578.
- de Wit, H.G.M., Bouwstra, J.A., Blok, J.G., & de Kruif, C.G. 1983. Vapor pressures and lattice energies of oxalic acid, mesotartaric acid, phloroglucinol, myoinositol, and their hydrates. *J. Chem. Physics*, **78(3)**, 1470–1475.
- Debenedetti, P.G., & Stillinger, F.H. 2001. Supercooled liquids and the glass transition. *Nature*, **410**, 259–267.
- DeCarlo, P.F., Dunlea, E.J., Kimmel, J.R., Aiken, A.C., Sueper, D., Crouse, J., Wennberg, P.O., Emmons, L., Shinozuka, Y., Clarke, A., Zhou, J., Tomlinson, J., Collins, D.R., Knapp, D., Weinheimer, A.J., Montzka, D.D., Campos, T., & Jimenez, J.L. 2008. Fast airborne aerosol size and chemistry measurements above Mexico City and Central Mexico during the MILAGRO campaign. *Atmos. Chem. Phys.*, **8**, 4027–4048.
- Decesari, S., Fuzzi, S., Facchini, M. C., Mircea, M., Emblico, L., Cavalli, F., Maenhaut, W., Chi, X., Schkolnik, G., Falkovich, A., Rudich, Y., Claeys, M., Pashynska, V., Vas, G., Kourtchev, I., Vermeylen, R., Hoffer, A., Andreae, M. O., Tagliavini, E., Moretti, F., & Artaxo, P. 2006. Characterization of the organic composition of aerosols from Rondônia, Brazil, during the LBA-SMOCC 2002 experiment and its representation through model compounds. *Atmos. Chem. Phys.*, **6**, 375–402.
- Deschout, H., Hagman, J., Fransson, S., Jonasson, J., Rudemo, M., Lorén, N., & Braeckmans, K. 2010. Straightforward FRAP for quantitative diffusion measurements with a laser scanning microscope. *Opt. Express*, **18(22)**, 22886–22905.
- Dockery, D.W., Pope, C.A., Xu, X., Spengler, J.D., Ware, J.H., Fay, M.E., Ferris, B.G., & Speizer, F.E. 1993. An association between air pollution and mortality in six U.S. cities. *N. Engl. J. Med.*, **329**, 1753–1759.

- Donahue, N.M., Robinson, A.L., Stanier, C.O., & Pandis, S.N. 2006. Coupled partitioning, dilution and chemical ageing of semivolatile organics. *Environ. Sci. Technol.*, **40**, 2635–2643.
- Donahue, N.M., Robinson, A.L., & Pandis, S.N. 2009. Atmospheric organic particulate matter: from smoke to secondary organic aerosol. *Atmos. Environ.*, **43**, 94–106.
- Donahue, N.M., Epstein, S.A., Pandis, S.N., & Robinson, A.L. 2011. A two-dimensional volatility basis set: 1. organic-aerosol mixing thermodynamics. *Atmos. Chem. Phys.*, **11**, 3303–3318.
- Ehn, M., Thornton, J.A., Kleist, E., Sipilä, M., Junninen, H., Pullinen, I., Springer, M., Rubach, F., Tillmann, R., Lee, B., Lopez-Hilfiker, F., Andres, S., Acir, I., Rissanen, M., Jokinen, T., Schobesberger, S., Kangasluoma, J., Kontkanen, J., Nieminen, T., Kurtén, T., Nielsen, L. B., Jørgensen, S., Kjaergaard, H.G., Canagaratna, M., Maso, M.D., Berndt, T., Petäjä, T., Wahner, A., Kerminen, V., Kulmala, M., Worsnop, D.R., Wildt, J., & Mentel, T.F. 2014. A large source of low-volatility secondary organic aerosol. *Nature*, **506**, 476–479.
- Erdakos, G.B., & Pankow, J.F. 2004. Gas/particle partitioning of neutral and ionizing compounds to single- and multi-phase aerosol particles. 2. Phase separation in liquid particulate matter containing both polar and low-polarity organic compounds. *Atmos. Environ.*, **38**, 1005–1013.
- Facchini, M.C., Decesari, S., Rinaldi, M., Carbone, C., Finessi, E., Mircea, M., Fuzzi, S., Moretti, F., Tagliavini, E., Ceburnis, D., & O’Dowd, C. 2008. Important source of marine secondary organic aerosol from biogenic amines. *Environ. Sci. Technol.*, **42**, 9116–9121.
- Fladerer, A., & Strey, R. 2003. Growth of homogeneously nucleated water droplets: a quantitative comparison of experiment and theory. *Atmos. Res.*, **65**, 161–187.
- Ford, B., & Heald, C.L. 2016. Exploring the uncertainty associated with satellite-based estimates of premature mortality due to exposure to fine particulate matter. *Atmos. Chem. Phys.*, **16**, 3499–3523.
- Fredenslund, A., Jones, R.L., & Prausnitz, J.M. 1975. Group-contribution estimation of activity coefficients in non ideal liquid mixtures. *AIChE J.*, **21**(6), 1086–1099.
- Fredenslund, A., Gmehling, J., & Rasmussen, P. 1977. *Vapor-liquid equilibria using UNI-FAC*. Amsterdam: Elsevier.
- Fry, J.L., & Sackinger, K. 2012. Model Investigation of NO₃ secondary organic aerosol (SOA) source and heterogenous organic aerosol (OA) sink in the western United States. *Atmos. Chem. Phys.*, **12**, 8797–8811.

- Fuchs, N.A., & Sutugin, A.G. 1971. *Highly dispersed aerosols*. Woburn, Mass: Butterworth Heinemann.
- Fukuta, N., & Walter, L.A. 1970. Kinetics of hydrometeor growth from a vapor-spherical model. *J. Atmos. Sci.*, **27**, 1160–1172.
- Fuzzi, S., Decesari, S., Facchini, M.C., Cavalli, F., Emblico, L., Mircea, M., Andreae, M.O., Trebs, I., Hoffer, A., Guyon, P., Artaxo, P., Rizzo, L.V., Lara, L.L., Pauliquevis, T., Maenhaut, W., Raes, N., Chi, X., Mayol-Bracero, O.L., Soto-García, L.L., Claeys, M., Kourttchev, I., Rissler, J., Swietlicki, E., Tagliavini, E., Schkolnik, G., Falkovich, A.H., Rudich, Y., Fisch, G., & Gatti, L.V. 2007. Overview of the inorganic and organic composition of size-segregated aerosol in Rondônia, Brazil, from the biomass-burning period to the onset of the wet season. *J. Geophys. Res.*, **112**, D01201.
- Ganbavale, G., Zuend, A., Marcolli, C., & Peter, T. 2015. Improved AIOMFAC model parameterisation of the temperature dependence of activity coefficients for aqueous organic mixtures. *Atmos. Chem. Phys.*, **15**, 447–493.
- Gao, Y., Hall, W.A., & Johnston, M.V. 2010. Molecular composition of monoterpene secondary organic aerosol at low mass loading. *Environ. Sci. Technol.*, **44**, 7897–7902.
- Goldstein, A.H., & Galbally, I.E. 2007. Known and unexplored organic constituents in the Earth’s atmosphere. *Environ. Sci. Technol.*, **41**(5), 1514–1521.
- Graham, B., Mayol-Bracero, O.L., P.Guyon, Roberts, G.C., Decesari, S., Facchini, M.C., Artaxo, P., Maenhaut, W., Köll, P., & Andreae, M.O. 2002. Water-soluble organic compounds in biomass burning aerosols over Amazonia 1. Characterization by NMR and GC-MS. *J. Geophys. Res.*, **107**(D20), 8047.
- Grayson, J.W., Zhang, Y., Mutzel, A., Renbaum-Wolff, L., Böge, O., Kamal, S., Herrmann, H., Martin, S.T., & Bertram, A.K. 2016. Effect of varying experimental conditions on the viscosity of α -pinene derived secondary organic material. *Atmos. Chem. Phys.*, **16**, 6027–6040.
- Grieshop, A.P., Miracolo, M.A., Donahue, N.M., & Robinson, A.L. 2009. Constraining the volatility distribution and gas-particle partitioning of combustion aerosol using isothermal dilution and thermodynamic measurement. *Environ. Sci. Technol.*, **43**, 4750–4756.
- Hallquist, M., Wenger, J.C., Baltensperger, U., Rudich, Y., Simpson, D., Claeys, M., Dommen, J., Donahue, N.M., George, C., Goldstein, A.H., Hamilton, J.F., Herrmann, H., Hoffmann, T., Iinuma, Y., Jang, M., Jenkin, M.E., Jimenez, J.L., Kiendler-Scharr, A., Maenhaut, W., McFiggans, G., Mentel, Th.F., Monod, A., Prévôt, A.S.H., Seinfeld, J.H., Surratt, J.D., Szmigielski, R., & Wildt, J. 2009. The formation, properties and

- impact of secondary organic aerosol: current and emerging issues. *Atmos. Chem. Phys.*, **9**, 5155–5236.
- Hanford, K.L., Mitchem, L., Reid, J.P., Clegg, S.L., Topping, D.O., & McFiggans, G.B. 2008. Comparative thermodynamic studies of aqueous glutaric acid, ammonium sulfate and sodium chloride at high humidity. *J. Phys. Chem. A*, **112**, 9413–9422.
- Heal, M.R., Kumar, P., & Harrison, R.M. 2012. Particles, air quality, policy and health. *Chem. Soc. Rev.*, **41**, 6606–6630.
- Heald, C.L., Kroll, J.H., Jimenez, J.L., Docherty, K.S., DeCarlo, P.F., Aiken, A.C., Chen, Q., Martin, S.T., Farmer, D.K., & Artaxo, P. 2010. A simplified description of the evolution of organic aerosol composition in the atmosphere. *Geophys. Res. Lett.*, **L08803**.
- Heintzenberg, J. 1989. Fine particles in the global troposphere. *Tellus*, **41B**, 149–160.
- Heitjans, P., & Kärger, J. 2005. *Diffusion in Condensed Matter*. 1 edn. Berlin, Heidelberg: Springer.
- Hepburn, C.J. 2016. *The Phases of Matter*. <http://www.splung.com/content/sid/6/page/phasesofm>
- Hilal, S.H., & Karickhoff, S.W. 2003. Prediction of the Vapor Pressure Boiling Point, Heat of Vaporization and Diffusion Coefficient of Organic Compounds. *QSAR Comb. Sci.*, **22**, 565–574.
- Hitchcock, D.R., Spiller, L.L., & Wilson, W.E. 1980. Sulfuric acid aerosols and HCl release in coastal atmospheres: evidence of rapid formation of sulphuric acid particulates. *Atmos. Environ.*, **14**, 165–182.
- Holdren, M.W., Westberg, H.H., & Zimmerman, P.R. 1979. Analysis of monoterpene hydrocarbons in rural atmospheres. *J. Geophys. Res.*, **84(C8)**, 5083–5088.
- Hopkins, R.J., Mitchem, L., Ward, A.D., & Reid, J.P. 2004. Control and characterisation of a single aerosol droplet in a single-beam gradient-force optical trap. *Phys. Chem. Chem. Phys.*, **6**, 4924–4927.
- Hosny, N. A., Fitzgerald, C., Vyšniauskas, A., Athanasiadis, A., Berkemeier, T., Uygur, N., Pöschl, U., Shiraiwa, M., Kalberer, M., Pope, F. D., & Kuimova, M. K. 2016. Direct imaging of changes in aerosol particle viscosity upon hydration and chemical aging. *Chem. Sci.*, **7**, 1357–1367.
- Jacob, D.J. 1999. *Introduction to atmospheric chemistry*. 1 edn. Chichester: Princeton University Press.
- Järvinen, E., Ignatius, K., Nichman, L., Kristensen, T. B., Fuchs, C., Hoyle, C. R., Höppel, N., Corbin, J. C., Craven, J., Duplissy, J., Ehrhart, S., Elä Haddad, I., Frege, C., Gordon, H., Jokinen, T., Kallinger, P., Kirkby, J., Kiselev, A., Naumann, K.-H., Petäjä,

- T., Pinterich, T., Prevot, A. S. H., Saathoff, H., Schiebel, T., Sengupta, K., Simon, M., Slowik, J. G., Tröstl, J., Virtanen, A., Vochezer, P., Vogt, S., Wagner, A. C., Wagner, R., Williamson, C., Winkler, P. M., Yan, C., Baltensperger, U., Donahue, N. M., Flagan, R. C., Gallagher, M., Hansel, A., Kulmala, M., Stratmann, F., Worsnop, D. R., Möhler, O., Leisner, T., & Schnaiter, M. 2016. Observation of viscosity transition in α -pinene secondary organic aerosol. *Atmos. Chem. Phys.*, **16**(7), 4423–4438.
- Jenkin, M. E. 2004. Modelling the formation and composition of secondary organic aerosol from α - and β -pinene ozonolysis using MCM v3. *Atmos. Chem. Phys.*, **4**, 1741–1757.
- Jenkin, M. E., Saunders, S. M., Wagner, V., & Pilling, M. J. 2003. Protocol for the development of the Master Chemical Mechanism, MCM v3 (Part B): tropospheric degradation of aromatic volatile organic compounds. *Atmos. Chem. Phys.*, **3**, 181–193.
- Jimenez, J. L., Canagaratna, M. R., Donahue, N. M., Prevot, A. S. H., Zhang, Q., Kroll, J. H., DeCarlo, P. F., Allan, J. D., Coe, H., Ng, N. L., Aiken, A. C., Docherty, K. S., Ulbrich, I. M., Grieshop, A. P., Robinson, A. L., Duplissy, J., Smith, J. D., Wilson, K. R., Lanz, V. A., Hueglin, C., Sun, Y. L., Tian, J., Laaksonen, A., Raatikainen, T., Rautiainen, J., Vaattovaara, P., Ehn, M., Kulmala, M., Tomlinson, J. M., Collins, D. R., Cubison, M. J., Dunlea, E. J., Huffman, J. A., Onasch, T. B., Alfarra, M. R., Williams, P. I., Bower, K., Kondo, Y., Schneider, J., Drewnick, F., Borrmann, S., Weimer, S., Demerjian, K., Salcedo, D., Cottrell, L., Griffin, R., Takami, A., Miyoshi, T., Hatakeyama, S., Shimono, A., Sun, J. Y., Zhang, Y. M., Dzepina, K., Kimmel, J. R., Sueper, D., Jayne, J. T., Herndon, S. C., Trimborn, A. M., Williams, L. R., Wood, E. C., Middlebrook, A. M., Kolb, C. E., Baltensperger, U., & Worsnop, D. R. 2009. Evolution of Organic Aerosols in the Atmosphere. *Science*, **326**(5959), 1525–1529.
- Joback, K.G., & Reid, R.C. 1987. Estimation of pure-component properties from group-contributions. *Chem. Eng. Comm.*, **57**, 233–243.
- Johnson, D., Jenkin, M.E., Wirtz, K., & Martin-Reviejo, M. 2004. Simulating the Formation of Secondary Organic Aerosol from the Photooxidation of Toluene. *Environ. Chem.*, **3**, 150–165.
- Johnson, D., Jenkin, M.E., Wirtz, K., & Martin-Reviejo, M. 2005. Simulating the Formation of Secondary Organic Aerosol from the Photooxidation of Aromatic Hydrocarbons. *Environ. Chem.*, **2**(1), 35–48.
- Johnson, D., Jenkin, M.E., Wirtz, K., & Martin-Reviejo, M. 2006. Simulating regional scale secondary organic aerosol formation during the TORCH 2003 campaign in the southern UK. *Atmos. Chem. Phys.*, **6**, 403–418.
- Julin, J., Winkler, P.M., Donahue, N.M., Wagner, P.E., & Riipinen, I. 2014. Near-unity

- mass accommodation coefficient of organic molecules of varying structure. *Environ. Sci. Technol.*, **48**, 12083–12089.
- Kalberer, M., Paulsen, D., Sax, M., Steinbacher, M., Dommen, J., Prevot, A. S. H., Fisseha, R., Weingartner, E., Frankevich, V., Zenobi, R., & Baltensperger, U. 2004. Identification of polymers as major components of atmospheric organic aerosol. *Science*, **303**, 1659–1662.
- Kamens, R., Jang, M., Chien, C-J., & Leach, K. 1999. Aerosol formation from the reaction of α -pinene and ozone using a gas-phase kinetics-aerosol partitioning model. *Environ. Sci. Technol.*, **33**, 1430–1438.
- Kanakidou, M., Seinfeld, J.H., Pandis, S.N., Barnes, I., Dentener, F.J., Facchini, M.C., Dingenen, R.V., Ervens, B., Nenes, A., Nielsen, C.J., Swietlicki, E., Putaud, J.P., Balkanski, Y., Fuzzi, S., Horth, J., Moortgat, G.K., Winterhalter, R., Myhre, C.E.L., Tsigaridis, K., Vignati, E., Stephanou, E.G., & Wilson, J. 2005. Organic aerosol and global climate modelling: a review. *Atmos. Chem. Phys.*, **5**, 1053–1123.
- Kawamura, K., & Sakaguchi, F. 1999. Molecular distributions of water soluble dicarboxylic acids in marine aerosols over the Pacific Ocean including tropics. *J. Geophys. Res.: Atmos.*, **104(D3)**, 3501–3509.
- Kawamura, K., Narukawa, M., Li, S-M., & Barrie, L.A. 2007. Size distributions of dicarboxylic acids and inorganic ions in atmospheric aerosols collected during polar sunrise in the Canadian high Arctic. *J. Geophys. Res.: Atmos.*, **112**, D10307.
- Kerminen, V-M., Mäkelä, T.E., Ojanen, C.H., Hillamo, R.E., Vilhunen, J.K., Rantanen, L., Havers, N., Bohlen, A., & Klockow, D. 1997. Characterization of the particulate phase in the exhaust from a diesel car. *Environ. Sci. Technol.*, **31(7)**, 1883–1889.
- Kolb, C.E., Cox, R.A., Abbatt, J.P.D., Davis, E.J., Donaldson, D.J., Garrett, B.C., George, C., Griffiths, P.T., Hanson, D.R., Kulmala, M., McFiggans, G., Riipinen, U., Pöschl I., Rossi, M.J., Rudich, Y., Wagner, P.E., Winkler, P.M., Worsnop, D.R., & O’Dowd, C.D. 2010. An overview of current issues in the uptake of atmospheric trace gases by aerosols and clouds. *Atmos. Chem. Phys.*, **10**, 10561–10605.
- Koop, T., Bookhold, J., Shiraiwa, M., & Pöschl, U. 2011. Glass transition and phase state of organic compounds: dependency on molecular properties and implications for secondary organic aerosols in the atmosphere. *Phys. Chem. Chem. Phys.*, **13**, 19238–19255.
- Koponen, A.K., Riipinen, I., Hienola, A., Kulmala, M., & Bilde, M. 2007a. Thermodynamic Properties of Malonic, Succinic, and Glutaric Acids: Evaporation Rates and Saturation Vapor Pressures. *Environ. Sci. Technol.*, **41**, 3926–3933.

- Koponen, I.K., Riipinen, I., Hienola, A., Kulmala, M., & Bilde, M. 2007b. Thermodynamic properties of malonic, succinic and glutaric acids: evaporation rates and saturation vapour pressures. *Environ. Sci. Technol.*, **41**, 3926–3933.
- Krieger, U.K., Marcolli, C., & Reid, J.P. 2012. Exploring the complexity of aerosol particle properties and processes using single particle techniques. *Chem. Soc. Rev.*, **41**, 6631–6662.
- Krishna, R., & Wesselingh, J.A. 1997. The Maxwell-Stefan approach to mass transfer. *Chem. Eng. Sci.*, **52**, 861–911.
- Kroll, J. H., Donahue, N.M., Jimenez, J.L., Kessler, S.H., Canagaratna, M.R., Wilson, K.R., Altieri, K.E., Mazzoleni, L.R., Wozniak, A.S., Bluhm, H., Mysak, E.R., Smith, J.D., Kolb, C.E., & Worsnop, D.R. 2011. Carbon oxidation state as a metric for describing the chemistry of atmospheric organic aerosol. *Nature Chem.*, **3**, 133–139.
- Kroll, J.H., & Seinfeld, J.H. 2008. Chemistry of secondary organic aerosol: formation and evolution of low-volatility organics in the atmosphere. *Atmos. Environ.*, **42**, 3593–3624.
- Krzyzanowski, M., & Cohen, A. 2008. Update of WHO air quality guidelines. *Air Qual. Atmos. Health*, **1**, 7–13.
- Lamb, B., Guenther, A., Gay, D., & Westberg, H. 1987. A national inventory of biogenic hydrocarbon emissions. *Atmos. Environ.*, **21(8)**, 1695–1705.
- Lanz, V.A., Prévôt, A.S.H., Alfarra, M.R., Weimer, S., Mohr, C., DeCarlo, P.F., Gianini, M.F.D., and J. Schneider, C. Hueglin, Favez, O., B.D’Anna, George, C., Baltensperger, U. 2010. Characterization of aerosol chemical composition with aerosol mass spectrometry in Central Europe: an overview. *Atmos. Chem. Phys.*, **10**, 10453–10471.
- Laskin, A., Gilles, M.K., Knopf, D.A., Wang, B., & China, S. 2016. Progress in the analysis of complex atmospheric particles. *Annu. Rev. Anal. Chem.*, **9**, 117–143.
- Lee, L.A., Reddington, C.L., & Carslaw, K.S. 2016. On the relationship between aerosol model uncertainty and radiative forcing uncertainty. *P. Natl. Acad. Sci. USA*, **113(21)**, 5820–5827.
- Lee-Taylor, J., Madronich, S., Aumont, B., Baker, A., Camredon, M., Hodzic, A., Tyn dall, G.S., Apel, E., & Zaveri, R.A. 2011. Explicit modelling of organic chemistry and secondary organic aerosol partitioning for Mexico City and its outflow plume. *Atmos. Chem. Phys.*, **11**, 13219–13241.
- Lei, T., Zuend, A., Wang, W.G., Zhang, Y.H., & Ge, M.F. 2014. Hygroscopicity of organic compounds from biomass burning and their influence on the water uptake of mixed organic ammonium sulfate aerosols. *Atmos. Chem. Phys.*, **14**, 11165–11183.

- Lesins, G., Chylek, P., & Lohmann, U. 2002. A study of internal and external mixing scenarios and its effect on aerosol optical properties and direct radiative forcing. *J. Geophys. Res.*, **107(D10)**.
- Lewis, W.G., & Whiteman, W.K. 1924. Principles of gas absorption. *Ind. Eng. Chem.*, **16(12)**, 1215–1220.
- Li, J., Cleveland, M., Ziemba, L.D., Griffin, R.J., Barsanti, K.C., Pankow, J.F., & Ying, Q. 2015. Modeling regional secondary organic aerosol using the Master Chemical Mechanism. *Atmos. Environ.*, **102**, 52–61.
- Li, Y., Pöschl, U., & Shiraiwa, M. 2016. Molecular corridors and parameterisations of volatility in the chemical evolution of organic aerosols. *Atmos. Chem. Phys.*, **16**, 3327–3344.
- Lienhard, D.M., Huisman, A.J., Bones, D.L., Te, Y.F., Luo, B.P, Krieger, U.K., & Reid, J.P. 2014. Retrieving the translational diffusion coefficient of water from experiments of single levitated aerosol droplets. *Phys. Chem. Chem. Phys.*, **16**, 16677–16683.
- Lienhard, D.M., Huisman, A.J., Krieger, U.K., Rudich, Y., Marcolli, C., Luo, B.P., Bones, D.L., Reid, J.P., Lambe, A.T., , Canagaratna, M.R., Davidovits, P., Onasch, T.B., Worsnop, D.R., Steimer, S.S., Koop, T., & Peter, T. 2015. Viscous organic aerosol particles in the upper troposphere: diffusivity-controlled water uptake and ice nucleation? *Atmos. Chem. Phys.*, **15**, 13599–13613.
- Liu, A.T., Zaveri, R.A., & Seinfeld, J.H. 2014. Analytical solution for transient partitioning and reaction of a condensing vapor species in a droplet. *Atmos. Env.*, **89**, 651–654.
- Mai, H., Shiraiwa, M., Flagan, R.C., & Seinfeld, J.H. 2015. Under what conditions can equilibrium gas-particle partitioning be expected to hold in the atmosphere? *Environ. Sci. Technol.*, **49**, 11485–11491.
- Mapes, M.K., Swallen, S.F., & Ediger, M.D. 2006. Self-Diffusion of Supercooled *o*-Terphenyl near the Glass Transition Temperature. *J. Phys. Chem. B.*, **110**, 507–511.
- Marcolli, C., & Krieger, U.K. 2006. Phase changes during hygroscopic cycles of mixed organic/inorganic model systems of tropospheric aerosols. *J. Phys. Chem. A*, **110**, 1881–1893.
- Marcolli, C., & Peter, Th. 2005. Water activity in polyol/water systems: new UNIFAC parameterization. *Atmos. Chem. Phys.*, **5**, 1545–1555.
- Marcolli, C., Peter, T., & Wienhold, F.G. 2004a. Internal mixing of the organic aerosol by gas phase diffusion of semivolatile organic compounds. *Atmos. Chem. Phys.*, **4**, 2593–2599.

- Marcolli, C., Luo, B., & Peter, T. 2004b. Mixing of the organic aerosol fractions: liquids as the thermodynamically stable phases. *J. Phys. Chem. A*, **108**, 2216–2224.
- Marshall, F.H., Miles, R.E.H., Song, Y.C., Ohm, P.B., Power, R.M., Reid, J.P., & Dutcher, C.S. 2016. Diffusion and reactivity in ultraviscous aerosol and the correlation with particle viscosity. *Chem. Sci.*, **7**, 1298–1308.
- Martin, S.T. 2000. Phase Transitions of Aqueous Atmospheric Particles. *Chem. Rev.*, **100**, 3403–3453.
- Matthiesen, J., Smith, R.S., & Kay, B.D. 2011. Mixing It Up: Measuring Diffusion in Supercooled Liquid Solutions of Methanol and Ethanol at Temperatures near the Glass Transition. *J. Phys. Chem. Lett.*, **2**, 557–561.
- McCormick, M.P., Thomason, L.W., & Trepte, C.R. 1995. Atmospheric effects of the Mt Pinatubo eruption. *Nature*, **373**, 399–404.
- McFiggans, G., Artaxo, P., Baltensperger, U., Coe, H., Facchini, M.C., Feingold, G., Fuzzi, S., Gysel, M., Laaksonen, A., Lohmann, U., Mentel, T.F., Murphy, D.M., O’Dowd, C.D., Snider, J.R., & Weingartner, E. 2006. The effect of physical and chemical aerosol properties on warm cloud droplet activation. *Atmos. Chem. Phys.*, **6**, 2593–2649.
- McFiggans, G., Topping, D.O., & Barley, M.H. 2010. The sensitivity of secondary organic aerosol component partitioning to the predictions of component properties - Part 1: a systematic evaluation of some available estimation techniques. *Atmos. Chem. Phys.*, **10**, 10255–10272.
- Migliori, M., Gabriele, D., Sanzo, R.D., Cindio, B., & Correr, S. 2007. Viscosity of multicomponent solutions of simple and complex sugars in water. *J. Chem. Eng.*, **52**, 1347–1353.
- Miles, R.E.H., Reid, J.P., & Riipinen, I. 2012. Comparison of approaches for measuring the mass accommodation coefficient for the condensation of water and sensitivities to uncertainties in thermophysical properties. *J. Phys. Chem. A*, **116**, 10810–10825.
- Miyazaki, Y., Kondo, Y., Shiraiwa, M., Takegawa, N., Miyakawa, T., Han, S., Kita, K., Hu, M., Deng, Z.Q., Zhao, Y., Sugimoto, N., Blake, D.R., & Weber, R.J. 2009. Chemical characterization of water-soluble organic carbon aerosols at a rural site in the Pearl River Delta, China, in the summer of 2006. *J. Geophys. Res.: Atmos.*, **114**, D14208.
- Moller, B., Rarey, J., & Ramjugernath, D. 2008. Estimation of the vapour pressure of non-electrolyte organic compounds via group contributions and group interactions. *J. Mol. Liq.*, **143**, 52–63.
- Mønster, J., Rosenørn, T., Svenningsson, B., & Bilde, M. 2004. Evaporation of methyl-

- and dimethyl-substituted malonic, succinic, glutaric and adipic acid particles at ambient temperatures. *J. Aerosol Science*, **35**, 1453–1465.
- Mutoru, J.W., & Firoozabadi, A. 2011. Form of multicomponent Fickian diffusion coefficients matrix. *J. Chem. Thermodyn.*, **43**, 1192–1203.
- Mutzel, A., Poulain, L., Berndt, T., Iinuma, Y., Rodigast, M., Böge, O., Richters, S., Spindler, G., Sipilä, M., Jokinen, T., Kulmala, M., & Herrmann, H. 2015. Highly Oxidized Multifunctional Organic Compounds Observed in Tropospheric Particles: A Field and Laboratory Study. *Environ. Sci. Technol.*, **49**, 7754–7761.
- Myhre, G., Bréon, F.-M., Collins, W., Fuglestedt, J., Huang, J., Koch, D., Lamarque, J.-F., Lee, D., Mendoza, B., Nakajima, T., Robock, A., Stephens, G., Takemura, T., & Zhang, H. 2013. Anthropogenic and Natural Radiative Forcing. *In: Stocker, T.F., Qin, D., Plattner, G.-K., Tignor, M., Allen, S.K., Boschung, J., Nauels, A., Xia, Y., Bex, V., & Midgley, P.M. (eds), Climate Change 2013: The Physical Science Basis. Contribution of Working Group I to the Fifth Assessment Report of the Intergovernmental Panel on Climate Change.* Cambridge, United Kingdom and New York, NY, USA: Cambridge University Press.
- Myrdal, P.B., & Yalkowsky, S.H. 1997. Estimating Pure Component Vapour Pressures of Complex Organic Molecules. *Ind. Eng. Chem. Res.*, **36**, 2494–2499.
- Nannoolal, Y., Rarey, J., Ramjugernath, D., & Cordes, W. 2004. Estimation of pure component properties Part 1. Estimation of the normal boiling point of non-electrolyte organic compounds via group contributions and group interactions. *Fluid Phase Equilib.*, **226**, 45–63.
- Nannoolal, Y., Rarey, J., & Ramjugernath, D. 2008. Estimation of pure component properties Part 3. Estimation of the vapour pressure of non-electrolyte organic compounds via group contributions and group interactions. *Fluid Phase Equilib.*, **269**, 117–133.
- Nannoolal, Y., Rarey, J., & Ramjugernath, D. 2009. Estimation of pure component properties. Part 4: Estimation of the saturated liquid viscosity of non-electrolyte organic compounds via group contributions and group interactions. *Fluid Phase Equilib.*, **281**, 97–119.
- Nel, A. 2005. Air Pollution-Related Illness: Effects of Particles. *Science*, **308(5723)**, 804–806.
- Ng, N.L., Canagaratna, M.R., Zhang, Q., Jimenez, J.L., Tian, J., Ulbrich, I.M., Kroll, J.H., Docherty, K.S., Chhabra, P.S., Bahreini, R., Murphy, S.M., Seinfeld, J.H., Hildebrandt, L., Donahue, N.M., DeCarlo, P.F., Lanz, V.A., Prévôt, A.S.H., Dinar, E., Rudich, Y., & Worsnop, D.R. 2010. Organic aerosol components observed in North-

- ern Hemispheric datasets from Aerosol Mass Spectrometry. *Atmos. Chem. Phys.*, **10**, 4625–4641.
- Nizkorodov, S.A., Laskin, J., & Laskin, A. 2011. Molecular chemistry of organic aerosols through the application of high resolution mass spectrometry. *Phys. Chem. Chem. Phys.*, **13**, 3612–3629.
- Nowakowski, C.M., Aimutis, W.R., Helstad, S., Elmore, D.L., & Muroski, A. 2015. Mapping Moisture Sorption Through Carbohydrate Composite Glass with Fourier Transform Near-Infrared (FT-NIR) Hyperspectral Imaging. *Food Biophys.*, **10**, 207–216.
- Noyes, W.A., & Wobbe, D.E. 1926. The Vapor Pressure of Anhydrous Oxalic Acid. *J. American Chem. Soc.*, **48**, 1882–1887.
- Odum, J.R., Hoffmann, T., Bowman, F., Collins, D., Flagan, R.C., & Seinfeld, J.H. 1996. Gas-particle partitioning and secondary organic aerosol yields. *Environ. Sci. Technol.*, **30**, 2580–2585.
- P. Papon, J. Leblond, P.H.E. Meijer. 2006. *The Physics of Phase Transitions: Concepts and Applications*. 2 edn. Berlin: Springer.
- Pajunoja, A., Malila, J., Hao, L., Joutsensaari, J., Lehtinen, K.E.J., & Virtanen, A. 2014. Estimating the viscosity range of SOA particles based on their coalescence time. *Aerosol. Sci. Tech.*, **48(2)**, i–iv.
- Pankow, J.F. 1987. Review and comparative analysis of the theories on partitioning between the gas and aerosol particulate phases in the atmosphere. *Atmos. Environ.*, **21(11)**, 2275–2283.
- Pankow, J.F. 1994. An absorption model of gas/particle partitioning of organic compounds in the atmosphere. *Atmos. Environ.*, **2**, 185–188.
- Pankow, J.F., & Asher, W.E. 2008. SIMPOL.1: a simple group contribution method for predicting vapour pressures and enthalpies of vaporization of multifunctional organic compounds. *Atmos. Chem. Phys.*, **8**, 2773–2796.
- Pfrang, C., Shiraiwa, M., & Pöschl, U. 2011. Chemical ageing and transformation of diffusivity in semi-solid multi-component organic aerosol particles. *Atmos. Chem. Phys.*, **11**, 7343–7354.
- Pierce, J.R., & Adams, P.J. 2007. Efficiency of cloud condensation nuclei formation from ultrafine particles. *Atmos. Chem. Phys.*, **7**, 1367–1379.
- Pitzer, K.S. 1991. *Activity coefficients in electrolyte solutions*. Boca Raton, FL, USA: CRC Press.

- Poling, B.E., Prausnitz, J.M., & O'Connell, J.P. 2004. *The properties of gases and liquids*. 5 edn. New York; London: McGraw-Hill.
- Pope, C.A., Burnett, R.T., Thun, M.J., Calle, E.E., Krewski, D., Ito, K., & Thurston, G.D. 2002. Lung cancer, cardiopulmonary mortality, and long-term exposure to fine particulate air pollution. *JAMA J. Am. Med. Assoc.*, **287**, 1132–1141.
- Pope, C.A., Hansen, M.L., Long, R.W., Nielsen, K.R., Eatough, N.L., Wilson, W.E., & Eatough, D.J. 2004. Ambient Particulate Air Pollution, Heart Rate Variability, and Blood Markers of Inflammation in a Panel of Elderly Subjects. *Environ. Health. Persp.*, **112**, 339–345.
- Pope, C.A., Burnett, R.T., Krewski, D., Jerrett, M., Shi, Y., Calle, E.E., , & Thun, M.J. 2009. Cardiovascular Mortality and Exposure to Airborne Fine Particulate Matter and Cigarette Smoke: shape of the exposure-response relationship. *Circulation*, **120**, 941–948.
- Pope, F.D., Tong, H., Dennis-Smith, B.J., Griffiths, P.T., Clegg, S.L., Reid, J.P., & Cox, R.A. 2010. Studies of Single Aerosol Particles Containing Malonic Acid, Glutaric Acid, and Their Mixtures with Sodium Chloride. II. Liquid-State Vapor Pressures of the Acids. *J. Phys. Chem. A*, **114**, 10156–10165.
- Pöschl, U. 2005. Atmospheric Aerosols: Composition, Transformation, Climate and Health Effects. *Angew. Chem. Int. Ed.*, **44**, 7520–7540.
- Pöschl, U., Rudich, Y., & Ammann, M. 2007. Kinetic model framework for aerosol and cloud surface chemistry and gas-particle interactions - Part 1: General equations, parameters, and terminology. *Atmos. Chem. Phys.*, **7**, 5989–6023.
- Power, R.M., Simpson, S.H., Reid, J.P., & Hudson, A.J. 2013. The transition from liquid to solid-like behaviour in ultrahigh viscosity aerosol particles. *Chem. Sci.*, **4**, 2597–2604.
- Pratt, K.A., & Prather, K.A. 2010. Aircraft measurements of vertical profiles of aerosol mixing states. *J. Geophys. Res.*, **115**, D11305.
- Price, C., Murray, B.J., Mattsson, J., O'Sullivan, D., Wilson, T.W., Baustian, K.J., & Benning, L.G. 2014. Quantifying water diffusion in high-viscosity and glassy aqueous solutions using a Raman isotope tracer method. *Atmos. Chem. Phys.*, **14**, 3817–3830.
- Price, C., Mattsson, J., Zhang, Y., Bertram, A.K., Davies, J.F., Grayson, J.W., , Martin, S.T., O'Sullivan, D., Reid, J.P., Rickards, A.M.J., & Murray, B.J. 2015. Water diffusion in atmospherically relevant α -pinene secondary organic material. *Chem. Sci.*, **6**, 4876–4883.
- Price, H.C., Mattsson, J., & Murray, B.J. 2016. Sucrose diffusion in aqueous solution. *Phys. Chem. Chem. Phys.*, **18**, 19207–19216.

- Putaud, J-P., Raes, F., Dingenen, R.V., Brüggemann, E., Facchini, M.C., Decesari, S., Fuzzi, S., Gehrig, R., Hüglin, C., Laj, P., Lorbeer, G., Maenhaut, W., Mihalopoulos, N., Müller, K., Querol, X., Rodriguez, S., Schneider, J., Spindler, G., Brink, H., Tørseth, K., & Wiedensohler, A. 2004. A European aerosol phenomenology-2: chemical characteristics of particulate matter at kerbside, urban, rural and background sites in Europe. *Atmos. Environ.*, **38**, 2579–2595.
- Qu, X., & Davis, A.J. 2001. Droplet evaporation and condensation in the near-continuum regime. *J. Aerosol. Sci.*, **32**, 861–876.
- Quintas, M., Brandão, T.R.S., Silva, C.L.M., & Cunha, R.L. 2006. Rheology of supersaturated sucrose solutions. *J. Food. Eng.*, **77**, 844–852.
- Reid, J.S., Koppmann, R., Eck, T.F., & Eleuterio, D.P. 2005. A review of biomass burning emissions part II: intensive physical properties of biomass burning particles. *Atmos. Chem. Phys.*, **5**, 799–825.
- Reid, R.C., Prausnitz, J.M., & Poling, B.E. 1987. *The properties of gases and liquids*. 4 edn. New York; London: McGraw-Hill.
- Riipinen, I., Koponen, I.K., Bilde, M., Hienola, A.I., & Kulmala, M. 2007. Evaporation Rates and Saturation Vapour Pressures of C3-C6 Dicarboxylic Acids. In: Dowd, C.D. O', & Wagner, P.E. (eds), *Nucleation and Atmospheric Aerosols*. Springer.
- Riipinen, I., Pierce, J.R., Donahue, N.M., & Pandis, S.N. 2010. Equilibration time scales of organic aerosol inside thermodenuders: Evaporation kinetics versus thermodynamics. *Atmos. Environ.*, **44**, 598–607.
- Robinson, A.L., Donahue, N.M., Shrivastava, M.K., Weitkamp, E.A., Sage, A.M., Grieshop, A.P., Lane, T.E., Pierce, J.R., & Pandis, S.N. 2007. Rethinking Organic Aerosols: Semivolatile Emissions and Photochemical Aging. *Science*, **315**, 1259–1262.
- Roth, C.M., Goss, K.U., & Schwarzenbach, R.P. 2005. Sorption of a diverse set of organic vapors to urban aerosols. *Environ. Sci. Tech.*, **39(17)**, 6638–6643.
- Rückerl, R., Schneider, A., Breitner, S., Cyrys, J., & Peters, A. 2011. Health effects of particulate air pollution: A review of epidemiological evidence. *Inhal. Toxicol.*, **23(10)**, 555–592.
- Saleh, R., Walker, J., & Khlystov, A. 2008. Determination of saturation pressure and enthalpy of vaporisation of semi-volatile aerosols: the integrated volume method. *J. Aerosol. Sci.*, **39**, 876–887.
- Saleh, R., Shihadeh, A., & Khlystov, A. 2009. Determination of evaporation coefficients of semi-volatile organic aerosols using an integrated volume-tandem differential mobility analysis (IV-TDMA) method. *J. Aerosol. Sci.*, **40**, 1019–1029.

- Saleh, R., Khlystov, A., & Shihadeh, A. 2010. Effect of Aerosol Generation Method on Measured Saturation Pressure and Enthalpy of Vaporization for Dicarboxylic Acid Aerosols. *Aerosol. Sci. Technol.*, **44**(4), 302–307.
- Salo, K., Jonsson, Å.M., Andersson, P.U., & Hallquist, M. 2010. Aerosol volatility and enthalpy of sublimation of carboxylic acids. *J. Phys. Chem.*, **114**, 4586–4594.
- Saukko, E., Lambe, A.T., Massoli, P., Koop, T., Wright, J.P., Croasdale, D.R., Pedernera, D.A., Onasch, T.B., Laaksonen, A., Davidovits, P., Worsnop, D.R., & Virtanen, A. 2012. Humidity-dependent phase state of SOA particles from biogenic and anthropogenic precursors. *Atmos. Chem. Phys.*, **12**, 7517–7529.
- Saunders, S. M., Jenkin, M. E., Derwent, R.G., & Pilling, M. J. 2003. Protocol for the development of the Master Chemical Mechanism, MCM v3 (Part A): tropospheric degradation of non-aromatic volatile organic compounds. *Atmos. Chem. Phys.*, **3**, 161–180.
- Saxena, P., & Hildemann, L.M. 1996. Water-soluble organics in atmospheric particles: a critical review of the literature and application of thermodynamics to identify candidate compounds. *J. Atmos. Chem.*, **24**, 57–109.
- Schnitzler, E.G., & McDonald, K.M. 2012. Characterization of low-temperature vapour pressure estimates for secondary organic aerosol applications. *Atmos. Environ.*, **56**, 9–15.
- Schröder, B., Fulem, M., & Martins, M.A.R. 2016. Vapor pressure predictions of multifunctional oxygen-containing organic compounds with COSMO-RS. *Atmos. Environ.*, **133**, 135–144.
- Schwarzenbach, R.P., Gschwend, P.M., & Imboden, D.M. 1993. *Environmental Organic Chemistry*. 1 edn. New York: Wiley.
- Seinfeld, J.H., & Pandis, S.N. 2006. *Atmospheric chemistry and physics: from air pollution to climate change*. 2 edn. Hoboken, N.J.: Wiley.
- Seinfeld, J.H., Bretherton, C., Carslaw, K.S., Coe, H., DeMott, P.J., Dunlea, E.J., Feingold, G., Ghan, S., Guenther, A.B., Kahn, R., Kraucunas, I., Kreidenweis, S.M., Molina, M.J., Nenes, A., Penner, J.E., Prather, K.A., Ramanathan, V., Ramaswamy, V., Rasch, P.J., Ravishankara, A. R., Rosenfeld, D., Stephens, G., & Wood, R. 2016. Improving our fundamental understanding of the role of aerosol?cloud interactions in the climate system. *P. Natl. Acad. Sci. USA*, **113**(21), 5781–5790.
- Serway, R.A., & Vuille, C. 2014. *College Physics: Volume 1*. 10 edn. Pacific Grove, Calif.; London: Brooks/Cole.

- Sharkey, T.D., Wiberley, A.E., & Donohue, A.R. 2008. Isoprene emission from plants: why and how. *Ann. Bot-London*, **101**, 5–18.
- Shilling, J.E., Chen, Q., King, S.M., Rosenoern, T., Kroll, J.H., Worsnop, D.R., DeCarlo, P.F., Aiken, A.C., Sueper, D., Jimenez, J.L., & Martin, S.T. 2009. Loading-dependent elemental composition of α -pinene SOA particles. *Atmos. Chem. Phys.*, **9**, 771–782.
- Shiraiwa, M., Kondo, Y., Iwamoto, T., & Kita, K. 2010. Amplification of Light Absorption of Black Carbon by Organic Coating. *Aerosol Sci. Tech.*, **44(1)**, 46–54.
- Shiraiwa, M., Ammann, M., Koop, T., & Pöschl, U. 2011. Gas uptake and chemical aging of semisolid organic aerosol particles. *P. NATL. ACAD. SCI. USA*, **108(27)**, 11003–11008.
- Shiraiwa, M., Pfrang, C., Koop, T., & Pöschl, U. 2012. Kinetic multi-layer model of gas-particle interactions in aerosols and clouds (KM-GAP): linking condensation, evaporation and chemical reactions of organics, oxidants and water. *Atmos. Chem. Phys.*, **12**, 2777–2794.
- Shiraiwa, M., L.D.Yee, Schilling, K.A., Loza, C.L., Craven, J.S., Zuend, A., Ziemann, P.J., & Seinfeld, J.H. 2013. Size distribution dynamics reveal particle-phase chemistry in organic aerosol formation. *P. Natl. Acad. Sci. USA*, **110**, 11746–11750.
- Shiraiwa, M., Berkemeier, T., Schilling-Fahnestock, K.A., Seinfeld, J.H., & Pöschl, U. 2014. Molecular corridors and kinetic regimes in the multiphase chemical evolution of secondary organic aerosol. *Atmos. Chem. Phys.*, **14**, 8323–8341.
- Shrivastava, M.K., Lipsky, E.M., Stanier, C.O., & Robinson, A.L. 2006. Modeling semivolatile organic aerosol mass emissions from combustion systems. *Environ. Sci. Technol.*, **40**, 2671–2677.
- Simpson, D., Yttri, K.E., Klimont, Z., Kupiainen, K., Caseiro, A., Gelencsér, A., Pio, C., Puxbaum, H., & Legrand, M. 2007. Modeling carbonaceous aerosol over Europe: Analysis of the CARBOSOL and EMEP EC/OC campaigns. *J. Geophys. Res.*, **112**, D23S14.
- Simpson, E., Connolly, P., & McFiggans, G. 2014. An investigation into the performance of four cloud droplet activation parameterisations. *Geosci. Model Dev.*, **7**, 1535–1542.
- Smith, G.D., (III), E. Woods, DeForest, C.L., Baer, T., & Miller, R.E. 2002. Reactive uptake of ozone by oleic acid aerosol particles: application of single-particle mass spectrometry to heterogenous reaction kinetics. *J. Phys. Chem. A*, **106**, 8085–8095.
- Smith, G.D., Woods, E., Baer, T., & Miller, R.E. 2003. Aerosol uptake described by numerical solution of the diffusion-reaction equations in the particle. *J. Phys. Chem. A*, **107**, 9582–9587.

- Song, M., Liu, P.F., Hanna, S.J., Martin, S.T., & Bertram, A.K. 2015. Relative humidity-dependent viscosities of isoprene-derived secondary organic material and atmospheric implications for isoprene-dominant forests. *Atmos. Chem. Phys.*, **15**, 5145–5159.
- Song, M., Liu, P.F., Hanna, S.J., Zaveri, R.A., Potter, K., You, Y., Martin, S.T., & Bertram, A.K. 2016. Relative humidity-dependent viscosity of secondary organic material from toluene photo-oxidation and possible implications for organic particulate matter over megacities. *Atmos. Chem. Phys.*, **16**, 8817–8830.
- Soonsin, V., Zardini, A.A., Marcolli, C., Zuend, A., & Krieger, U.K. 2010. The vapour pressures and activities of dicarboxylic acids reconsidered: the impact of the physical state of the aerosol. *Atmos. Chem. Phys.*, **10**, 11753–11767.
- Steimer, S.S., Krieger, U.K., Te, Y.-F., Lienhard, D.M., Huisman, A.J., B.P.Luo, Ammann, M., & Peter, T. 2015. Electrodynamic balance measurements of thermodynamic, kinetic, and optical aerosol properties inaccessible to bulk methods. *Atmos. Meas. Tech.*, **8**, 2397–2408.
- Stein, S.E., & Brown, R.L. 1994. Estimation of Normal Boiling Points from Group Contributions. *J. Chem. Inf. Comput. Sci.*, **34**, 581–587.
- Stokes, R.H., & Robinson, R.A. 1966. Interactions in aqueous nonelectrolyte solutions. *J. Phys. Chem.*, **70**(7), 2126–2131.
- Stone, E., J, Schauer, Quraishi, T.A., & Mahmood, A. 2010. Chemical characterization and source apportionment of fine and coarse particulate matter in Lahore, Pakistan. *Atmos. Environ.*, **44**(8), 1062–1070.
- Tao, Y., & McMurry, H. 1989. Vapor Pressures and Surface Free Energies of C14-C18 Monocarboxylic Acids and C5 and C6 Dicarboxylic Acids. *Environ. Sci. Technol.*, **23**, 1519–1523.
- Taylor, R., & Krishna, R. 1993. *Multicomponent Mass Transfer*. 1 edn. USA: Wiley.
- Telis, V.R.N., Telis-Romero, J., Mazzotti, H.B., & Gabas, A.L. 2007. Viscosity of aqueous carbohydrate solutions at different temperatures and concentrations. *Int. J. Food. Prop.*, **10**(1), 185–195.
- Tong, C., Clegg, S.L., & Seinfeld, J.H. 2008. Comparison of activity coefficient models for atmospheric aerosols containing mixtures of electrolytes, organics, and water. *Atmos. Environ.*, **42**, 5459–5482.
- Topping, D., Barley, M.H., & McFiggans, G. 2011. The sensitivity of Secondary Organic Aerosol (SOA) component partitioning to the predictions of component properties-Part 2: Determination of the particle hygroscopicity and its dependence on “apparent” volatility. *Atmos. Chem. Phys.*, **11**, 7767–7779.

- Topping, D.O., McFiggans, G., & Coe, H. 2005a. A curved multi-component aerosol hygroscopicity model framework: Part 1 - Inorganic compounds. *Atmos. Chem. Phys.*, **5**, 1205–1222.
- Topping, D.O., McFiggans, G., & Coe, H. 2005b. A curved multi-component aerosol hygroscopicity model framework: Part 2 - Including organic compounds. *Atmos. Chem. Phys.*, **5**, 1223–1242.
- Topping, D.O., Barley, M., & McFiggans, G. 2013. Including phase separation in a unified model to calculate partitioning of vapours to mixed inorganic-organic aerosol particles. *Faraday Discuss.*, **165**, 273–288.
- Tröstl, J., Chuang, W.K., Gordon, H., Heinritzi, M., Yan, C., Molteni, U., Ahlm, L., Frege, C., Bianchi, F., Wagner, R., Simon, M., Lehtipalo, K., Williamson, C., Craven, J.S., Duplissy, J., Adamov, A., Almeida, J., Bernhammer, A-K., Breitenlechner, M., Brilke, S., Dias, A., Ehrhart, S., Flagan, R.C., Franchin, A., Fuchs, C., Guida, R., Gysel, M., Hansel, A., Hoyle, C.R., Jokinen, T., Junninen, H., Kangasluoma, J., Keskinen, H., Kim, J., Krapf, M., Kürten, A., Laaksonen, A., Lawler, M., Leiminger, M., Mathot, S., Möhler, O., Nieminen, T., Onnela, A., Petäjä, T., Piel, F.M., Miettinen, P., Rissanen, M.P., Rondo, L., Sarnela, N., Schobesberger, S., Sengupta, K., Sipilä, M., Smith, J.N., Steiner, G., Tomé, A., Virtanen, A., Wagner, A.C., Weingartner, E., Wimmer, D., Winkler, P.M., Ye, P., Carslaw, K.S., Curtius, J., Dommen, J., Kirkby, J., Kulmala, M., Riipinen, I., Worsnop, D.R., Donahue, N.M., & Baltensperger, U. 2016. The role of low-volatility organic compounds for initial particle growth in the atmosphere. *Nature*, **506**, 527–531.
- Twohy, C.H., & Anderson, J.R. 2008. Droplet nuclei in non-precipitating clouds: composition and size matter. *Environ. Res. Lett.*, **3**(4), 045002.
- Vaden, T.D., Imre, D., Beránek, J., Shrivastava, M., & Zelenyuk, A. 2011. Evaporation kinetics and phase of laboratory and ambient secondary organic aerosol. *P. Natl. Acad. Sci. USA*, **108**, 2190–2195.
- Valorso, R., Aumont, B., Camredon, M., Raventos-Duran, T., Mouchel-Vallon, C., Ng, N.L., Seinfeld, J.H., Lee-Taylor, J., & Madronich, S. 2011. Explicit modelling of SOA formation from α -pinene photooxidation: sensitivity to vapour pressure estimation. *Atmos. Chem. Phys.*, **11**, 6895–6910.
- Vesala, T., Kulmala, M., Rudolf, R., Vrtala, A., & Wagner, P. 1997. Models for condensational growth and evaporation of binary aerosol particles. *J. Aerosol. Sci.*, **28**, 565–598.
- Vignes, A. 1966. Diffusion in binary solutions. *Ind. Eng. Chem. Fund.*, **5**, 189–199.

- Virtanen, A., Joutsensaari, Koop, T., Kannosto, J., Yli-Pirilä, P., Leskinen, J., Mäkelä, J.M., Holopainen, J.K., Pöschl, U., Kulmala, M., Worsnop, D.R., & Laaksonen, A. 2010. An amorphous solid state of biogenic secondary organic aerosol particles. *Nature*, **467**, 824–827.
- Wagner, P., & Kuttler, W. 2014. Biogenic and anthropogenic isoprene in the near-surface urban atmosphere – A case study in Essen, Germany. *Sci. Total. Environ.*, **475**, 104–115.
- Wexler, A.S., & Seinfeld, J.H. 1990. The distribution of ammonium salts among a size and composition dispersed aerosol. *Atmos. Environ.*, **24A(5)**, 1231–1246.
- Wexler, A.S., & Seinfeld, J.H. 1991. Second-generation inorganic aerosol model. *Atmos. Environ.*, **25A(12)**, 2731–2748.
- Yan, W., Topphoff, M., Roe, C., & Gmehling, J. 1999. Prediction of vapor-liquid equilibria in mixed-solvent electrolyte systems using the group contribution concept. *Fluid Phase Equilib.*, **162**, 97–113.
- Yatawelli, R.L.N., & Thornton, J.A. 2010. Particulate Organic Matter Detection Using a Micro-Orifice Volatilization Impactor Coupled to a Chemical Ionization Mass Spectrometer (MOVI-CIMS). *Aerosol. Sci. Technol.*, **44(1)**, 61–74.
- Yokouchi, Y., & Ambe, Y. 1988. Diurnal Variations of Atmospheric Isoprene and Monoterpene Hydrocarbons in an Agricultural Area in Summertime. *J. Geophys. Res.*, **93(D4)**, 3751–3759.
- Zardini, A.A., Krieger, U.K., & Marcolli, C. 2006. White light Mie resonance spectroscopy used to measure very low vapour pressures of substance in aqueous solution aerosol particles. *Opt. Express*, **14(15)**, 6951–6962.
- Zaveri, R.A., Easter, R.C., Fast, J.D., & Peters, L.K. 2008. Model for Simulating Aerosol Interactions and Chemistry (MOSAIC). *J. Geophys. Res.*, **113**, D13204.
- Zaveri, R.A., Easter, R.C., Shilling, J.E., & Seinfeld, J.H. 2014. Modeling kinetic partitioning of secondary organic aerosol and size distribution dynamics: representing effects of volatility, phase state, and particle-phase reaction. *Atmos. Chem. Phys.*, **14**, 5153–5181.
- Zhang, Q., Jimenez, J.L., Canagaratna, M.R., Allan, J.D., Coe, H., Ulbrich, I., Alfarra, M.R., Takami, A., Middlebrook, A.M., Sun, Y.L., Dzepina, K., Dunlea, E., Docherty, K., DeCarlo, P.F., Salcedo, D., Onasch, T., Jayne, J.T., Miyoshi, T., Shimojo, A., Hatakeyama, S., Takegawa, N., Kondo, Y., Schneider, J., F, Drewnick, Borrmann, S., S, Weimer and K. Demerjian, Williams, P., Bower, K., Bahreini, R., Cottrell, L., Griffin, R.J., Rautiainen, J., Sun, J.Y., Zhang, Y.M., & Worsnop, D.R. 2007. Ubiquity and

- dominance of oxygenated species in organic aerosols in anthropogenically-influenced Northern Hemisphere midlatitudes. *Geophys. Res. Lett.*, **34**, L13801.
- Ziemann, P.J., & Atkinson, R. 2012. Kinetics, products, and mechanisms of secondary organic aerosol formation. *Chem. Soc. Rev.*, **41**, 6582–6605.
- Zobrist, B., Marcolli, C., Pedernera, D.A., & Koop, T. 2008. Do atmospheric aerosols form glasses? *Atmos. Chem. Phys.*, **8**, 5221–5244.
- Zobrist, B., Soonsin, V., Luo, B.P., Krieger, U.K., Marcolli, C., Peter, T., & Koop, T. 2011. Ultra-slow water diffusion in aqueous sucrose glasses. *Phys. Chem. Chem. Phys.*, **13**, 3514–3526.
- Zuend, A., Marcolli, C., Luo, B.P., & Peter, T. 2008. A thermodynamic model of mixed organic-inorganic aerosols to predict activity coefficients. *Atmos. Chem. Phys.*, **8**, 4559–4593.
- Zuend, A., Marcolli, C., Peter, T., & Seinfeld, J.H. 2010. Computation of liquid-liquid equilibria and phase stabilities: implications for RH-dependent gas/particle partitioning of organic-inorganic aerosols. *Atmos. Chem. Phys.*, **10**, 7795–7820.
- Zuend, A., Marcolli, C., Booth, A.M., Lienhard, D.M., Soonsin, V., Krieger, U.K., Topping, D.O., McFiggans, G., Peter, T., & Seinfeld, J.H. 2011. New and extended parameterization of the thermodynamic model AIOMFAC: calculation of activity coefficients for organic-inorganic mixtures containing carboxyl, hydroxyl, carbonyl, ether, ester, alkenyl, alkyl, and aromatic functional groups. *Atmos. Chem. Phys.*, **11**, 9155–9206.